

REPORT DOCUMENTATION PAGE				Form Approved OMB No. 0704-0188	
Public reporting burden for this collection of information is estimated to average 1 hour per response, including the time for reviewing instructions, searching existing data sources, gathering and maintaining the data needed, and completing and reviewing the collection of information. Send comments regarding this burden estimate or any other aspect of this collection of information, including suggestions for reducing the burden, to Department of Defense, Washington Headquarters Services, Directorate for Information Operations and Reports (0704-0188), 1215 Jefferson Davis Highway, Suite 1204, Arlington, VA 22202-4302. Respondents should be aware that notwithstanding any other provision of law, no person shall be subject to any penalty for failing to comply with a collection of information if it does not display a currently valid OMB control number. PLEASE DO NOT RETURN YOUR FORM TO THE ABOVE ADDRESS.					
1. REPORT DATE (DD-MM-YYYY) 02-09-2004		2. REPORT TYPE Final Report		3. DATES COVERED (From – To) 20 July 2001 - 20-Jul-04	
4. TITLE AND SUBTITLE Simulation of Ductile Failure in Metals Under Dynamic Loading Conditions Using Advanced Material Damage Modeling			5a. CONTRACT NUMBER F61775-01-C0003		
			5b. GRANT NUMBER		
			5c. PROGRAM ELEMENT NUMBER		
6. AUTHOR(S) Dr. Nicola Bonora and Pietro Paolo Milella			5d. PROJECT NUMBER		
			5d. TASK NUMBER		
			5e. WORK UNIT NUMBER		
7. PERFORMING ORGANIZATION NAME(S) AND ADDRESS(ES) University of Cassino Via G. Di Biasio 43 Cassino 03043 Italy				8. PERFORMING ORGANIZATION REPORT NUMBER N/A	
9. SPONSORING/MONITORING AGENCY NAME(S) AND ADDRESS(ES) EOARD PSC 802 BOX 14 FPO 09499-0014				10. SPONSOR/MONITOR'S ACRONYM(S)	
				11. SPONSOR/MONITOR'S REPORT NUMBER(S) SPC 01-4054	
12. DISTRIBUTION/AVAILABILITY STATEMENT Approved for public release; distribution is unlimited.					
13. SUPPLEMENTARY NOTES					
14. ABSTRACT This report results from a contract tasking University of Cassino as follows: The contractor shall investigate the the issue of advanced failure prediction and design by means of innovative material failure modeling and computational techniques. The specific tasks include: - the use and implementation of advanced material modeling incorporating damage, strain rate and temperature effects, in an extensive number of numerical simulations; - verification of the model effective predictive capabilities in a number of applications; - extension of the material model in order to incorporate advanced features needed in penetration mechanics simulations; - development of analytical tools to measure material response to high strain rates loadings using a simple instrumented Charpy pendulum.					
15. SUBJECT TERMS EOARD, Failure Mechanisms, Metals & alloys, High Strain Rate					
16. SECURITY CLASSIFICATION OF:			17. LIMITATION OF ABSTRACT UL	18, NUMBER OF PAGES 218	19a. NAME OF RESPONSIBLE PERSON KEVIN J LAROCHELLE, Maj, USAF
a. REPORT UNCLAS	b. ABSTRACT UNCLAS	c. THIS PAGE UNCLAS			19b. TELEPHONE NUMBER <i>(Include area code)</i> +44 (0)20 7514 3154



DiMSAT, Dipartimento di
Meccanica, Strutture
Ambiente e Territorio
Facoltà di Ingegneria

*Università di Cassino
via Di Biasio 43, 03043
Cassino (FR), Italy*

RESEARCH CONTRACT

SPC 01-4054 N° F61775-01-C0003

**SIMULATION OF DUCTILE FAILURE IN METALS
UNDER DYNAMIC LOADING CONDITIONS USING
ADVANCED MATERIAL DAMAGE MODELING**

FINAL REPORT

To: AFRL/EOARD, 223/231 Marylebone Rd., London
NW1 5TH – England

Authors: **Nicola Bonora and Pietro Paolo Milella**

July, 2004

Contents

CONTENTS.....	1
STATEMENT	3
LISTS OF FIGURES	5
LIST OF TABLES.....	17
EXECUTIVE SUMMARY.....	19
ACKNOWLEDGMENT.....	21
1. INTRODUCTION.....	23
1.1. REFERENCES.....	24
2. MATERIAL MODELING	27
2.1. REFERENCES.....	35
3. DUCTILE DAMAGE MODELING.....	37
3.1. DUCTILE DAMAGE FORMULATION: EXTENSION TO COMPRESSIVE STATE OF STRESS.....	40
3.2. DUCTILE DAMAGE FORMULATION: STRAIN RATE AND TEMPERATURE EFFECTS	45
3.3. REFERENCES.....	47
4. CDM MODEL NUMERICAL IMPLEMENTATION	49
5. DYNAMIC ANALYSIS IN MSC/MARC	51
5.1. DIRECT INTEGRATION	51
5.2. TECHNICAL BACKGROUND.....	52
5.3. DAMPING	54
6. FLYING PLATE IMPACT TEST ANALYSIS.....	57
6.1. FLYING PLATE IMPACT TEST FINITE ELEMENT SIMULATION	69
6.2. PRELIMINARY VERIFICATION AND THEORY ASSESSMENT.....	71
6.3. SPALL FEATURES ASSESSMENT	74
Parametric Study on Damping and Mesh Effect	75
Spall Fracture Process.....	80
OHFC 99.9 Copper.....	81
Armco Iron.....	87
Tungsten 93W	88
6.4. SPALL SIGNAL ANALYSIS.....	90
6.5. GEOMETRIC EFFECTS ON SPALL FRACTURE INITIATION AND PROPAGATION ..	96

6.6.	FLYING PLATE IMPACT TEST SIMULATION USING HYDROCODE.....	109
	Damage model implementation benchmark test	110
	Damage evolution in Flying plate impact test	112
6.7.	REFERENCES	121
7.	TAYLOR IMPACT TEST	123
7.1.	FINITE ELEMENT MODELING	124
7.2.	ROD-ON-ROD (ROR) IMPACT TEST	132
7.3.	REFERENCES	139
8.	NUMERICAL INVESTIGATION OF ADVANCED DYNAMIC TESTING TECHNIQUES FOR HIGH STRAIN RATES MATERIAL TESTING	141
8.1.	HOPKINSON PRESSURE BAR FINITE ELEMENT SIMULATION	142
8.2.	FINITE ELEMENTS MODELING OF FLYING WEDGE DEVICE	158
8.3.	ADVANCED USE OF CHARPY TEST FOR STRAIN RATE EFFECT MEASUREMENTS. 168	
8.3.1.	GENERAL YIELDING OF CHARPY V-N SPECIMENS	171
8.3.2.	2D FE STATIC ANALYSIS.....	178
8.3.3.	3D FE STATIC ANALYSIS.....	186
8.3.4.	SUMMARY OF 2D-3D FE STATIC RESULTS	189
8.3.5.	3D FE DYNAMIC ANALYSIS.....	192
8.3.5.1.	PLAIN STRAIN CONDITION.....	192
8.3.5.2.	REAL CONDITIONS.....	202
8.3.5.3.	STRAIN RATE ASSESSMENT	205
8.3.6.	CONCLUSIONS.....	210
8.4.	REFERENCES	211
9.	CONCLUSIONS.....	215

Statement

In accordance with Defense Federal Acquisition Regulation 252.227-7036, Declaration of Technical Data Conformity (Jan 1997), the contractor, Nicola Bonora, DiMSAT - University of Cassino, hereby declares that, to the best of his knowledge and belief, the technical data delivered herewith under contract n° F61775-01-C0003 is complete, accurate and complies with all requirements of the contract.

Date: July 15, 2004

Name, Title and Signature of Authorized Official:

Nicola Bonora, Professor, Primary Investigator, _____



In accordance with the requirements in Federal Acquisition Regulation 52.227-13 Patent Rights- Acquisition by the U.S. Government (Jun 1999):

Disclosure of all subject inventions as defined in FAR 52.227-13 have been reported in accordance with this clause

I certify that there were no subject inventions to declare as defined in FAR 52.227-13, during the performance of this contract.

Date: July 15, 2004

Nicola Bonora, Professor, Primary Investigator, _____



Lists of Figures

Figure 2.1 - Strain rate effect on commercial aluminum under shear load	27
Figure 2.2- Temperature effect on strength of β -titanium	28
Figure 2.3- Yield strength variation with strain rate and temperature for a low alloy steel	29
Figure 2.4- Scheme of strain rate and temperature effect and associated mechanisms for the Milella unified model.	30
Figure 2.5 - Comparison of Milella unified strength model and experimental data relative to several metals.....	31
Figure 2.6 - Ductility reduction as a function of TF for a SA537 steel	33
Figure 3.1 - Sketch of the Reference Volume element, RVE, nominal section area, A_0 , and effective resisting area, A_{eff}	37
Figure 3.2 - Microvoids formation in impacted 1145 aluminum plate (Ref.3.3)	41
Figure 3.3 - Particle matrix interaction inside a RVE under compressive deformation state: a) under weak and b) under strong confinement of the ductile matrix.....	41
Figure 3.4- Outline of the mechanical behavior expected when an initial compressive load ramp is followed by tension loading (scenario A).....	42
Figure 3.5- Outline of the mechanical behavior expected when an initial tensile loading ramp is followed by compression and again by tension loading (scenario B).	43
Figure 3.6 - Strain rate, $\dot{\epsilon}_f$ and diameter at fracture in smooth and notched tensile bar in steel, (Ref.3.8).....	46
Figure 3.7 - Simulated strain rate effect on damage evolution law	46
Figure 4.1 - Logical scheme for damage calculation in fem code. The procedure is started at the end of each load increment when global variables have been calculated and it is repeated for each gauss-point of each active element.	49
Figure 6.1 - Graphical representation of the relations found for the uniaxial strain condition for an ideally elastic-fully plastic material (no-hardening)	59

Figure 6.2 - Lagrange diagram for plate impact test	60
Figure 6.3 - Stress wave system at moderate impact velocity	62
Figure 6.4 - Strain rate variation at the material point when invested by the stress wave: when the stress reaches the plateau strain remain constant and $\dot{\epsilon}$ drops to zero.	62
Figure 6.5 - Uniaxial strain stress-strain curve showing concave-up typical behavior ...	63
Figure 6.6 - Shock wave profile.....	63
Figure 6.7 - State diagram and Hugoniot representation for solids.....	65
Figure 6.8 - Hugoniot representation on U (u_s , impact velocity) u_p (particle velocity) plot.	67
Figure 6.9 - Velocity profile at the free surface of target plate in flying plate impact test showing signal modification due to the occurrence of spall.	67
Figure 6.10 - SSM scheme	70
Figure 6.11 - Finite element mesh for the fine grid SSM and zoomed detail at the impact region	70
Figure 6.12 - Two stress wave system in moderate impact in copper 99.9 OHFC.	72
Figure 6.13 - Shock wave in copper 99.9 OHFC.	72
Figure 6.14 - Uniaxial stress-strain response of fem model in copper flying plate impact test at 185 m/s.	73
Figure 6.15 - Close up of uniaxial stress-strain response of fem model in copper flying plate impact test at 185 m/s: verification of dynamic yield strength and elasticity modulus	73
Figure 6.16 - Uniaxial stress-strain curve showing concave up behavior.....	74
Figure 6.17 - Work hardening data for A533B at low strain rate.....	76
Figure 6.18 - Damping effect on free surface velocity with time	77
Figure 6.19 - Comparison between damping factor in MARC and AUTODYN.....	77
Figure 6.20 - Mesh sensitivity: stress pulse profile	78
Figure 6.21 - Mesh sensitivity: free velocity profile	79

Figure 6.22 - Stress pulse traveling into the target plate: fine mesh	79
Figure 6.23 - Spall time determination in A533B steel	81
Figure 6.24 - Velocity profile for OFHC copper at 185 m/s	83
Figure 6.25 - Stress triaxiality evolution with time along target thickness	83
Figure 6.26 - Damage evolution with time along target thickness.....	84
Figure 6.27 - Microvoid distribution at the spall plane in pure aluminum.....	84
Figure 6.28 - Void volume fraction distributions in copper under different impact pressure.	85
Figure 6.29 - Velocity profile for ARMCO iron at 500 m/s	87
Figure 6.30 - Velocity profile for 93W at 247.8 m/s	89
Figure 6.31 - Velocity profile for 93W at 410 m/s.....	89
Figure 6.32 - Spall signal comparison for OFHC copper	90
Figure 6.33 - Different secondary separation mechanisms for spall plane faces	92
Figure 6.34- Shape effect on the non-linear spring response for tractions across spall separation plane.....	94
Figure 6.35- Evolution of the normalized area associated to the force-displacement diagram for different choices of ?.....	94
Figure 6.36 - Spring element simulations for dissipation in spall plane separation	95
Figure 6.37 - Schematic sketch of the different flyer geometries investigated.....	97
Figure 6.38: a) Deformed view at spall time of obtained with AUTODYN simulation for an impact velocity of 185m/s and D/h=16. b) same plot obtained with MSC/MARC and damage model at the same velocity 185m/s and D/h=13, here contours indicate damage extension: min D:0.005 max D=0.85.	98
Figure 6.39 - Pressure distribution (negative means tension) at the time of spall in 99.9 OFHC at 185 m/s impact: dash lines indicate the possible spall extension using a p=1.85 GPa failure criterion.	99
Figure 6.40 - Active plastic strain and stress triaxiality distribution along the plate thickness at the time of spall at the first spall location.	100

Figure 6.41 - Stress triaxiality distribution along the plate thickness at the spall time for both symmetry axis and first spall locations	100
Figure 6.42 - Comparison of free surface velocity profiles versus time for flying plate configuration $D/h=16$ obtained using both MSC/MARC fem code and AUTODYN.....	101
Figure 6.43 -Comparison of free surface velocity profiles versus time for flying plate configuration $D/h=8$ obtained using both MSC/MARC fem code and AUTODYN.....	101
Figure 6.44 - Comparison of free surface velocity profiles versus time for flying plate configuration $D/h=4$ obtained using both MSC/MARC fem code and AUTODYN.....	102
Figure 6.45 - Comparison of free surface velocity profiles versus time for flying plate configuration $D/h=2$ obtained using both MSC/MARC fem code and AUTODYN.....	102
Figure 6.46 - Damage area in $D/h=8$ impact configuration using both maximum pressure criterion (AUTODYN) and CDM.....	104
Figure 6.47 - Damage area in $D/h=4$ impact configuration using both maximum pressure criterion (AUTODYN) and CDM.....	105
Figure 6.48 - Damage area in $D/h=2$ (a-b) and $D/h=1$ (c-d) impact configuration using both maximum pressure criterion (AUTODYN) and CDM.....	106
Figure 6.49 - Schematic plot of the edge effect on first spall location	107
Figure 6.50 - Boundary line definition	107
Figure 6.51 - Stress pulse at two locations: along the symmetry axis (blue), along the upper flyer edge (blue).....	109
Figure 6.52 – Sketch of the single cell for damage model implementation benchmark	111
Figure 6.53 – Damage evolution under different imposed stress triaxiality levels: uniaxial ($TF=0.333$) and shear ($TF=0.0$).....	111
Figure 6.54 – Rear target surface velocity plot as a function of time calculated with CDM model implemented in AUTODYN: comparison with experimental data and MSC-MARC FEM code.	113
Figure 6.55 – Velocity plot calculated with Autodyn and the proposed damage model for two impact velocity conditions.	114

Figure 6.56 – Normalized velocity plot for 185 an 150 m/s impact in OFHC copper. ..	114
Figure 6.57 – Damage evolution during spall plane formation for 185 m/s impact in OFHC copper	116
Figure 6.58 – Stress wave profile along flyer plate thickness at different radial locations.	117
Figure 6.59 – Damage evolution during spall plane formation in OHFC copper. Impact velocity. 150 m/s.....	119
Figure 6.60 – Damage extension though flyer thickness along the symmetry axis (distance from the impact plane) at v=185 m/s.....	120
Figure 6.61– Damage extension though flyer thickness along the symmetry axis (distance from the impact plane) at v=150 m/s.....	120
Figure 7.1- Definition of the segment for yields stress determination in the Taylor cylinder impact test	124
Figure 7.2- Semi-infinite elements used in modeling the infinite target wall.....	125
Figure 7.3 - Sketch of the finite and unbounded portions	125
Figure 7.4 - Detail of the mesh at the impact surface: a) undeformed and b) deformed mesh for copper. Here, severe element distorsion is clearly visible in the near impact region	126
Figure 7.5 - Comparison of post impact deformation with experimental data for ARMCO iron ($l_0=12,6\text{mm}$; $V_0=279\text{m/s}$): a) strain rate sensitive material, b) strain rate and temperature sensitive material.	128
Figure 7.6 - Comparison of post impact deformation with experimental data for AISI steel ($l_0=8,1\text{mm}$; $V_0=343\text{m/s}$): a) strain rate sensitive material, b) strain rate and temperature sensitive material.	129
Figure 7.7 - Comparison of post impact deformation with experimental data for OFHC copper ($l_0=24.5\text{mm}$; $V_0=190\text{ m/s}$): a) strain rate sensitive material, b) strain rate and temperature sensitive material.	130
Figure 7.8 - Damage map in Taylor cylinder post impact test for copper	132
Figure 7.9 – Compressive wave formation and fading due to free boundary release wave incoming.	134
Figure 7.10- Compressive wave fading scheme in ROR impact test.	135

Figure 7.11- Evolution of damage threshold as a function of grain size.....	136
Figure 7.12 – Elongation to failure in nanocrystalline metals.....	137
Figure 7.13 – Damage threshold strain fit as a function of grain size	138
Figure 7.14- Experimental [Ref.7.3] and calculated deformed microstructure of 40?m OFE copper impacted at 233m/s.	138
Figure 8.1- Sketch of the Hopkinson pressure bar apparatus.....	142
Figure 8.2- Scheme of the theoretical expected signal outputted from the Hopkinson bar	144
Figure 8.3- Schematics of the Hopkinson bar in tension	145
Figure 8.4 – Detail of the mesh at the specimen location.....	146
Figure 8.5- Strain signals in simulated SHPBC for three different impact velocites....	146
Figure 8.6- SHPBC derived stress diagram for $v=15$ m/s	147
Figure 8.7 – Comparison of stress vs distance from impact with Newmark and Humbolt integration algorithms.....	149
Figure 8.8- Detailed mesh for the SHPBT near the specimen section change	149
Figure 8.9- Stress pulses in SHPBT.....	150
Figure 8.10- Simulated strain rate versus time signal for different strain values	151
Figure 8.11- Stress-strain curve for OFHC copper using SHPBT at different strain rates	151
Figure 8.12- Strain rate as function increasing strain along the specimen in SHPBT using different gauge lengths	152
Figure 8.13- Sketch of the simulated dynamic fracture with SHPBT in copper	153
Figure 8.14- Evolution of the necking in a SHPB test.....	153
Figure 8.15- Calibration of numerical damping for ARMCO iron SHPBT test	154
Figure 8.16- Comparison of the calculated reduction of area in the necking region as a function of time, with experimental measurements	155
Figure 8.17- Simulated fracture in SHPBT test on ARMCO iron	156

Figure 8.18 – Strain rate versus strain along the specimen: comparison between calculated and experimental data.	157
Figure 8.19- Comparison of the calculated temperature rise along the specimen with experimental data.	157
Figure 8.20 - Flying Wedge device conceptual scheme	158
Figure 8.21 - FEM modeling of flying wedge device.....	160
Figure 8.22 – Strain rate versus time in round smooth specimen using different whorkholder materials (steel and aluminum) and constrain condition (touching or full constrained).	161
Figure 8.23 – Engineering stress-strain in round smooth specimen using different whorkholder materials (steel and aluminum) and constrain condition (touching or full constrained).	162
Figure 8.24 – Strain rate evolution with time in flying wedge test with different wedge impact velocities	162
Figure 8.25 – Resulting stress-strain curves for different wedge impact velocities.	163
Figure 8.26 – $1/d$ effect on strain rate in flying wedge test	164
Figure 8.27 – FEM model for the flying wedge test with $d=10$ mm specimen	164
Figure 8.28 – Stress –strain response for smaller specimen dimensions at different impact velocities	166
Figure 8.29 – Strain rate response in round specimen with smaller dimensions.	166
Figure 8.30 - Smooth round bar: double neck feature	167
Figure 8.31- Smooth round bar: single neck feature.....	167
Figure 8.32– (a) the Charpy pendulum, (b) CharpyV-N specimen dimensions and (c) schematic of the three-point bend loading arrangement with the specimen set on its anvil and the tup indenter.	168
Figure 8.33 – Fracture appearance of Charpy-VN specimens broken at different temperatures (Milella).	170
Figure 8.34 – Experimental load-displacement record obtained on a Charpy V-N specimen of A 508 Cl.B steel (Milella).	171

- Figure 8.35 – Slip-line field solution for a Charpy V-N specimen loaded under quasi-static conditions by pure moment (four-point bending). It can be seen the plastic hinge and a detail of the stress field just behind the notch [17]. .. 172
- Figure 8.36 - Progression of slip-lines in a Charpy V-N type specimen subjected at room temperature to quasi-static pure bending equal to (a) 0.92, (b) 0.94, (c) 0.96 and (d) 1.00 fold the general yielding (Rif. 8.20). In (d) the plastic lines emanating from the notch tip merge those formed on the opposite face creating the plastic hinge. 173
- Figure 8.37 – Slipline field solution for a Charpy V-N specimen loaded under quasi-static three-point bending. It can be seen the plastic hinge emanating from the notch and the opposite point, as well. 173
- Figure 8.38 – Plastic hinge formed at different temperatures in a Charpy V-N specimen of mild steel, loaded under three-point bending, evidenced by etching with Fry’s reagent (Rif. 8.20). 174
- Figure 8.39 – Schematic of the internal reaction on the notched cross section that balances the external moment M_{nt} 174
- Figure 8.40 – The first formation of the plastic hinge occurs when the load-displacement diagram loses its linearity (Rif. 8.21). 177
- Figure 8.41 – Working matrix followed in this study. 177
- Figure 8.42 – Schematic of the mesh used in the 2D FE static analysis to simulate one half of the Charpy V-N specimen. 179
- Figure 8.43 – Load vs displacement for the half Charpy specimen analyzed having either ideal rigid/plastic behavior (dashed line). 179
- Figure 8.44 – Trend of the equivalent stress (von Mises) and shear stress at general yielding on the mid-section of un-notched Charpy specimen having ideally rigid-plastic behavior. 180
- Figure 8.45 – Stress distribution on the mid-section of the un-notched Charpy specimen where the tup indenter is acting, at the moment of first plastic hinge formation. 181
- Figure 8.46 – FE results obtained for a Charpy V-N specimen of elastic-plastic material having different strain hardening. The picture shows the points (full circles) where the plastic hinge was first formed. 181

Figure 8.47 – Trend of the constraint factor C vs the hardening of the material obtained for $E = 196,000$ MPa.	182
Figure 8.48 – FE results obtained for a Charpy V-N specimen of elastic-plastic material having different strain hardening, yield strength of 492 MPa and Young's modulus equal to 71,000 MPa. The picture shows the points (full circles) where the plastic hinge was first formed.	183
Figure 8.49 – Trend of the constraint factor C_{tpb} vs the hardening of the material obtained for $E = 71,000$ MPa compared to that for $E = 200,000$ MPa. ..	184
Figure 8.50 – Mesh used in the 3D static analysis. Only 1/4 of the specimen has been considered ($\frac{1}{2}$ thickness).....	184
Figure 8.51 – 3D FE results obtained for $n = 0.0, 0.1, 0.2$ and 0.3 , respectively. For comparison, the 2D plain strain results are also shown.	185
Figure 8.52 – Trend of plastic constraint factors vs strain hardening in FE 2D and 3D analyses.	185
Figure 8.53 – $n = 0.0$. Plastic hinge formation on the external face of the Charpy V-N specimen (b). At the same load step the plastic hinge is not completely formed on the mid-thickness plane (a).....	187
Figure 8.54 – $n = 0.3$. Plastic hinge formation on the external face of the Charpy V-N specimen (b). At the same load step the plastic hinge is not completely formed on the mid-thickness plane (a).....	187
Figure 8.55 – Trend of the constraint factors versus strain hardening n under 2D and 3D conditions. As to the latter case, it is shown the trend of the C factors on both the external surface and the inner face (center of specimen).....	188
Figure 8.56 – 3D analysis. The closure of the plastic hinge on the external face and on the center face of the Charpy V-N specimen is shown on the load-displacement curves for n equal to $0.0, 0.1, 0.2$ and 0.3 , respectively.	188
Figure 8.57 – Schematic of half thickness FE mesh.	193
Figure 8.58 – Schematic of FE mesh used in the analysis (one quarter of the structure).	193
Figure 8.59 – Record of load versus time obtained in the dynamic analysis with $n = 0.0$ on the contact surface between tup indenter and Charpy V-N specimen and on the anvil as total reaction.	194

Figure 8.60 – Rigid body acceleration showing first and second mode of vibration.....	195
Figure 8.61 – Plot of external forces.	195
Figure 8.62 – Record of load versus time obtained in the dynamic analysis with $n = 0.1$ on the contact surface between tup indenter and Charpy V-N specimen and on the anvil as total reaction.	196
Figure 8.63 – Dynamic curves obtained in the FE analysis.	196
Figure 8.64 – Sequence of plastic hinge formation in a Charpy V-N specimen loaded dynamically by a tup indenter having an impact speed of 5 m/s.....	198
Figure 8.65 – Inertia and external forces that balance the reaction moment by internal stresses on the notch section.	199
Figure 8.66– Comparison between static equivalent and dynamic forces exerted by the tup indenter on the Charpy V-N specimen, for the four values of n considered in this analysis.	200
Figure 8.67 – Comparison between static and static equivalent forces at the tup indenter-specimen surface contact.	200
Figure 8.68 – Comparison between 3D plain strain conditions and 3D real conditions, for the tup force vs time and $n = 0.0$	201
Figure 8.69 – Comparison between 3D plain strain conditions and 3D real conditions, for the tup force vs displacement and $n = 0.0$	201
Figure 8.70 – Comparison between static equivalent tup forces under 3D plain strain conditions and 3D real conditions. The closed points indicate the moment in which the plastic hinge is formed.	203
Figure 8.71 – Comparison between 3D static equivalent force (derived from the 3D dynamic calculations) on the tup and the corresponding 3D static, for the case $n = 0.0$	203
Figure 8.72 – Comparison between 3D static equivalent force (derived from the 3D dynamic calculations) on the tup and the corresponding 3D static, for the case $n = 0.1, 0.2$ and 0.3	204
Figure 8.73 – Trend of the tup force during the transient. From about 44 μs to about 49 μs the plastic hinge closes on the external and internal face, respectively.	204

Figure 8.74 – Growth of the plastic hinge on the internal face of the Charpy V-N specimen. Till about 0.05 ms the two lobes are separated by an elastic strain field (denoted with the A letter). From about 0.05 to 0.06 ms the hinge is formed with a growing strain field afterwards it remains constant up to about 0.08 ms, during which the strain field extends towards the upper and lower part of the specimen.	206
Figure 8.75 – Trend of the effective plastic strain in the plastic hinge. The letter caption is presented in Figure 8.76.	207
Figure 8.76 – Location of the points where the effective plastic strain of Figure 8.75 has been computed.	207
Figure 8.77 – Letters indicate the points in the plastic hinge where the effective plastic strain has been assessed.	208
Figure 8.78 – Trend of the effective plastic strain in the plastic hinge. The letter caption is presented in Figure 8.77.	208
Figure 8.79 – Trend of the effective plastic strain in the plastic hinge. The letter caption is presented in Figure 8.76.	209
Figure 8.80 – Trend of the plastic strain rate $\dot{\epsilon}$ in points A, D and G of the plastic hinge.	209
Figure 8.81 – Trend of the plastic strain rate $\dot{\epsilon}$ in points B and F of the plastic hinge (see Figure 8.77).	210

List of Tables

Table 6.1 - Material properties for A533B steel.....	76
Table 6.2 - Predicted and calculated spall time	80
Table 6.3 - Material properties for OFHC copper.....	82
Table 6.4 - J&C parameters for OHFC copper	82
Table 6.5 - Damage parameters for OFHC copper	82
Table 6.6 - Material properties for Armco Iron	86
Table 6.7 - J&C parameters for Armco iron	86
Table 6.8 - Damage parameters for ARMCO iron	87
Table 6.9 - Material Properties for W93 tungsten alloy.....	88
Table 6.10 - J&C parameters for W93 tungsten alloy	88
Table 6.11 - Damage parameters for W93 tungsten alloy	88
Table 6.12 - Geometrical co-ordinates of first spall location	108
Table 7.1 - Comparison of predicted length reduction after impact and experimental data for different strength models	131
Table 7.2. Computed and experimental impact section diameter.	135
Table 8.1 Time, displacement and forces at the moment when plastic hinge first for ($E = 196,000$ MPa).....	182
Table 8.2 - Time, displacement and forces with $E = 71,000$ MPa, at the moment when plastic hinge first forms.....	183
Table 8.3 - Displacement, force and constraint factor at the moment when plastic hinge forms on the external face and on the central one. ($E = 196,000$ MPa)...	189
Table 8.4- Time, displacement and forces at the moment when plastic hinge first forms, ($E = 196,000$ MPa)	197

Executive Summary

Advanced design of components requires that failure conditions can be accurately predicted in order to define operative safety limits. The definition of failure imply a dimensional scale at which the capability to perform or to achieve a predetermined task is no longer assured. At the material level, failure can occurs in a very high number of modes as a result of the material type, the nature of loading condition, the characteristic time of the phenomenon and the operative environment. In metals, all the failure modes can be ascribed to five micromechanisms (cleavage, fatigue, creep, ductile deformation and corrosion) that occur at the material meso/micro scale. The ability to predict failure in real components/structures depends on the capability to describe and account for the effects associated to these micromechanisms through the use of advanced constitutive modeling tools in the design.

The objective of the work is to demonstrate the possibility to simulate and predict, with high degree of reliability, failure in dynamically loaded ductile metals by means of an advanced damage model developed by the authors in the framework of continuum damage mechanics (CDM).

The research addresses a number of dynamic impact reference cases where the proposed model predicting capabilities are tested through extensive finite element analyses. Numerical simulations are always compared with experimental data available in the literature. Often, a review of the theoretical background is given in order to give clarity to the exposition of the results. In some cases, theoretical solutions are used to benchmark finite element models. The following dynamic loading configurations, for which experimental data are available could be retrieved from the literature, have been investigated studied by means of numerical simulations incorporating the proposed damage modeling:

Flying plate impact test

Taylor cylinder impact test

Rod-on-Rod impact test

Hopkinson pressure bar (tension and compression)

Wedge impact test

Charpy impact test

Flying plate impact test. An extensive study of the symmetric impact configuration has been performed using both implicit and explicit finite element codes. Aim of this study is the comparison of the predicted response, in terms of free surface velocity, spall plane location, stress pulse at the spall plane, etc., with the experimental data available in the literature. Since dynamic simulations involving contact between deformable bodies are

strongly sensible to the choice of several numerical parameters, such as damping, integration time step, contact formulation and release, etc., a parametric study on their associated effects on the global response has been performed. In addition, the study addresses the edge effect in flying plate impact with plates with different diameters as well as the issue related to the fracture work dissipation in the separation process under complete spall loading conditions.

Taylor Cylinder and ROR Impact Test. The Taylor cylinder impact test is a very well known configuration that would allow one to get reliable information about material dynamic yield stress. Experimental tests on a number of materials under different temperature are available. In some cases, measurements of deformed shaped, that can be used for comparison with numerical simulations, are also reported. Following the investigation scheme used for the plate impact plate, a detailed fem study has been performed on standard Taylor impact test and rod-on-rod configuration. The results of this study highlighted the possibility to correlate the damage parameters to the material microstructure in a multiscale description of damage.

Hopkinson pressure bar. The Hopkinson pressure bar is probably the most common and widely accepted experimental technique to determine dynamic material response under high strain rate loading conditions. The functionality of this equipment has strong theoretical bases. An extensive finite element analysis of this testing technique has been performed in order to validate the numerical results and procedures with the theory. Both split compression and pure tension Hopkinson bars have been simulated. The role of the specimen geometry and the occurrence of plastic instability on the effective strain rate generated in the specimen have been pointed out. These analyses have been used to design a Hopkinson pressure bar in pure tension at the University of Cassino.

Flying Wedge Impact Test. The University of Leeds has developed a so-called "flying wedge" testing facility in order to perform dynamic tensile test under controlled strain rate and stress state conditions. This experimental configuration has the major advantages with respect to other traditional techniques to simultaneously apply true tensile loading at the both end of the test piece. Additionally, the use of notched specimen seems to be a simple and effective way to amplify nominal strain rate. In this study a numerical investigation of the conceptual wedge test configuration has been performed.

Charpy impact test. The Charpy impact test is used to measure the material toughness and to assess brittle to ductile transition temperature. Here, the Charpy impact test has been proposed as a simple and cheap experimental technique to provide material response at high strain rates at different temperatures. An extensive and systematic 2D and 3D finite element investigation has been performed in order to determine the correlation between the dynamic material yield strength and the applied force, as well as the reference strain rate.

Acknowledgment

This work was supported by U.S. Air Force Research Laboratory (AFRL) - EOARD. Lt. Col. C. Ward was the program manager and Dr. D. Belk at Munitions Directorate, Eglin AFB was the program monitor. The authors want to acknowledge Dr. R. Sierakowski, MN/AF Chief Scientist, Dr. J. House, Dr. M. Schmidt, M. Nixon, Dr. J. Wilson of Munitions and Armor Directorate for the support given in the discussion of several technical aspects of the research. The help and contribution of Dr. Andrew Ruggiero at the University of Cassino is also acknowledged.

1. Introduction

Computational techniques can be profitably used in designing critical experiments for the assessment of mechanical response of materials and structures. This is particularly interesting for those advanced applications involving dynamic loading, such as blast loads, projectile impact, etc.

Nowadays, a number of advanced numerical tools and techniques are available in order to simulate components performance under the action of loads of different nature (mechanical, thermal, electromagnetic, etc.) and the coupled effects associated to their action.

Since 1982, Ref.1.1 pointed out that the most serious limitation to an extensive use of computational techniques in simulating and predicting structures and components behavior under dynamic loading was given by the inadequacy of constitutive models to fairly represent failure process.

The knowledge of the actual metal behavior and performance under dynamic loading still remains a critical issue. Metals response under severe dynamic loading is the result of the concurrent action of the modification in the constitutive response (stress-strain), due to the strain rate and temperature, and the effects associated to the occurrence of irreversible damage processes in the material microstructure. Both need to be well understood and incorporated into constitutive models in order to obtain reliable predictions.

Ductile metals are dynamically loaded at temperatures where they are allowed to flow and fail in a ductile manner, in general. Many models to simulate ductile failure in metals have been proposed in the literature. Basically, they can be organized in three groups: abrupt failure criteria, porosity and continuum damage mechanics (CDM) based models, (Ref. 1.2, Ref.1.3). All of them usually show major limitations such as material dependence, the need of a large number of material parameters, inaccurate account for stress triaxiality effect, etc. These limitations become more evident when the formulations are used to predict material performance under severe dynamic loading conditions involving complex failure phenomena such as spallation or high velocity impact and target penetration. In 1997, Bonora (Ref. 1.4) proposed a non-linear damage model, based on CDM approach, that overcame some of the limitations. The model has been successfully verified in a large number of applications and loading conditions (Ref. 1.5). At the same time, Milella (Ref. 1.6), developed an innovative equation of state to describe the effect of the strain rate and temperature on the material constitutive response. Recently, Bonora and Milella (Ref. 1.7) proposed a constitutive model that incorporates both strain rates, temperature, damage and

accounts for stress triaxiality without the complexities that usually characterizes similar formulations.

Failure under dynamic loading can involve anything from complete material separation or disintegration to changes in material stiffness or flow properties. In metals, dynamic failure due to spallation has been widely investigated by many authors (Ref. 1.8, Ref. 1.9).

Spallation is defined as tensile failure due to the reflection of a short duration compressive pulse from a free surface. At present, two general types of model to simulate spallation in metals have been proposed. The first type assumes that failure occurs when an internal variable (i.e. spall stress criterion) or state variable reaches a critical value. Alternatively, empirical criteria based on critical strain, plastic work, etc. has been also proposed. The second approach is based on the microstructural evolution of the damage process.

Barbee et al. (Ref.1.11) and Seaman et al. (Ref. 1.10) simulated spalling in flying impact plate test using nucleation and growth (NAG) models. In most of the cases, NAG models have been used in post-test analysis to match experimental results. Notwithstanding the use of ad hoc damage parameters, they have shown limited predictive capability. In addition, these models, based on the growth of cavities, cannot be used to predict the formation of micro and macro shear bands that is the other critical failure process observed in penetration mechanics. Here, void sheeting process, instead of void growth, and plastic flow localization effect due to thermal softening are usually not taken into account in the formulations.

The aim of the present research is to demonstrate the potential and the performance of the damage model given in Ref. 1.4 through a detailed numerical analysis of a number of dynamic impact loading configurations. Since any constitutive model requires the determination of some parameters specific for the material, part of the work has been also devoted to the examination of the current and updated dynamic testing experimental techniques proposed as alternative to for material testing at high strain rates. As a result of this, the standard Charpy test has been reviewed and an innovative procedure has been determined to use this experimental technique in order to generate, quickly and at low cost, yield strength material database at moderately high strain rates at different temperatures.

1.1. References

- 1.1 Zuckas, J., A., Nicholas, T., Swift, F. H., Greszczuk, L. B., and Curran, D. R., Impact Dynamics, Wiley- New York, 1982

- 1.2 Lemaitre, J., A Course on Damage Mechanics, Springer-Verlag, Berlin, 1992
- 1.3 Gurson, A.L., J. Engn. Mat. Tech.,(1977), 99, pp. 2-15
- 1.4 Bonora, N., (1997), International Journal of Fracture, 88, 359-371
- 1.5 Bonora, N., and Newaz, M.G. ,(1998) Int. J. Solids Struct., 35, pp. 1881-1894.
- 1.6 Milella P.P., Proceedings of at TMS Fall Meeting 1998, Chicago, Illinois, Oct. 11-15
- 1.7 Bonora, N., and Milella, P.P., (2001), Int. J. of Impact Engineering,
- 1.8 Johnson, G.R., (1981) J. Appl. Phys, 52, pp. 2812-2825
- 1.9 Davidson, L., Stevens, A. L., and Kipp, M.E., (1977) J. Mech. Phys. Sol., 25, pp.11-28.
- 1.10 Seaman L., Curran, D.R., and Shockey, D.A., (1976) J. Appl. Phys., 47, p. 4814.
- 1.11 Barbee, Jr., T. W., Seaman, L., Crewdson, R., and Curran, D. R., (1972), J. Mat. Sci., 7, pp. 393-401.

2. Material Modeling

The capability to model material behavior under high strain rates, temperatures and pressure is a critical issue for the numerical simulation and prediction performance of dynamically loaded structures. Material modeling requires accurate description of the interaction between material strength and damage processes, which are inherently linked to the deformation processes.

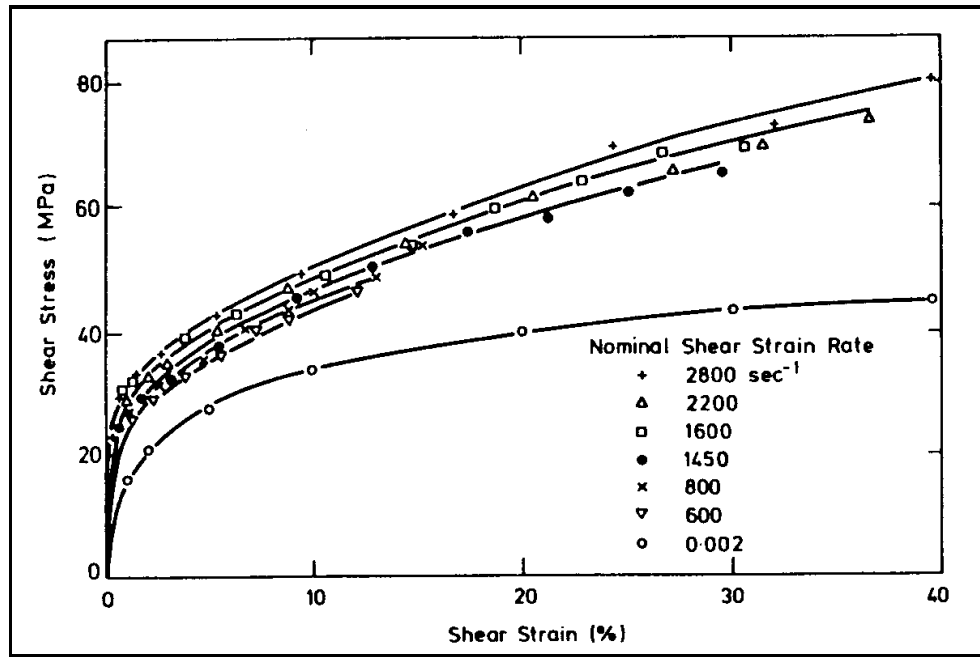


Figure 2.1 - Strain rate effect on commercial aluminum under shear load

In the past, strength and damage have been studied separately and material strength has received much more attention. A number of models have been developed following two different approaches: a physical description of material lattice mechanics, such as energy activation based or dislocation mechanics, or, alternatively, an empiric approach.

Many metals and alloy show a great sensibility to strain rates and temperature. In most of the cases strain rate has the major effect to increase material strength as shown in figure Figure 2.1 - Strain rate effect on commercial aluminum under shear load where the shear stress-strain response for commercial aluminum is given for a strain rate ranging between 600 and 2800 s^{-1} as well as the reference quasi-static curve at $2.0 \cdot 10^{-3} \text{ s}^{-1}$.

Temperature, on the contrary, softens material response, as shown for an α -titanium in Figure 2.2, where the different stress-strain curves, at the same strain rate, are given for temperature ranging between 77- 288 K.

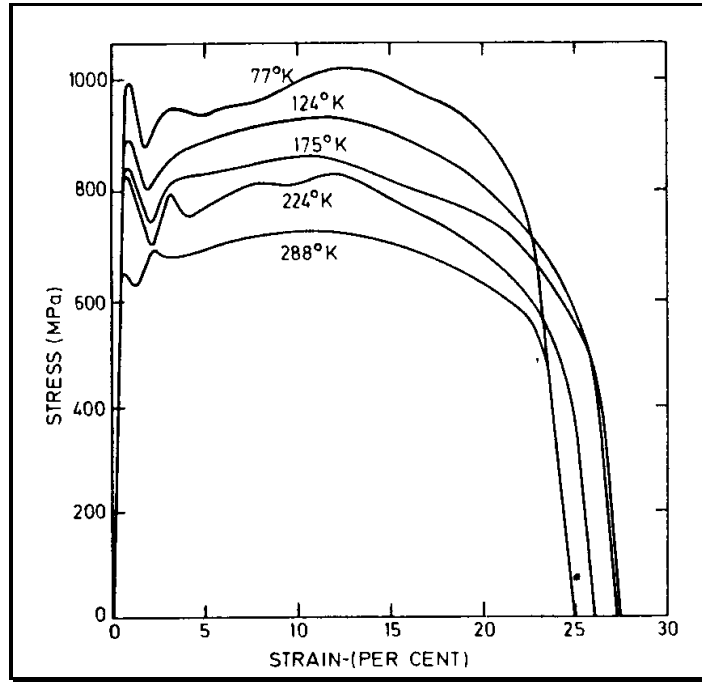


Figure 2.2- Temperature effect on strength of α -titanium

Today is known that the sensitivity of the material to the strain rate and temperature is related to the atomic structure. In particular, metals with body-centered cubic (BCC) lattice, such as α -iron, ferritic steels, niobium, tantalum etc., show a strong variation of the yield strength with temperature, T , and strain rate, $\dot{\epsilon}$. On the contrary, metals having a face-centered cubic (FCC) structure, such as austenitic steels, nickel, aluminum, copper, and silver, do not show the same sensitivity especially with respect to temperature. Finally, closely-packed hexagonal (HCP) lattice metals, like titanium and zinc, exhibit a behavior that is in between that of BCC and FCC metals.

It is rather difficult to describe the inelastic behavior of all metals through a generalized process that leads to a unified theory. Many attempts have been made in the past to establish a relation between the yield strength σ_y and the temperature T and the strain rate $\dot{\epsilon}$:

$$\sigma_y = f(\epsilon, \dot{\epsilon}, T) \quad (2.1.1)$$

Many authors proposed a number of different equations, Ref. 2.1-2.3. Even though, in many cases, the proposed equations were not consistent at all, it has been found that, in general, there is an exponential dependence of the yield strength σ_y on the temperature and equivalence between temperature and strain rate effects.

This feature finds confirmation in the experimental data, as shown in Figure 2.3, where the variation of yield strength with both temperature and strain rate is given for a low

alloy steel. This plot clearly shows how the yield strength linearly increases, in the log-plot, with the increasing of strain rates in the range below 10^4 s^{-1} .

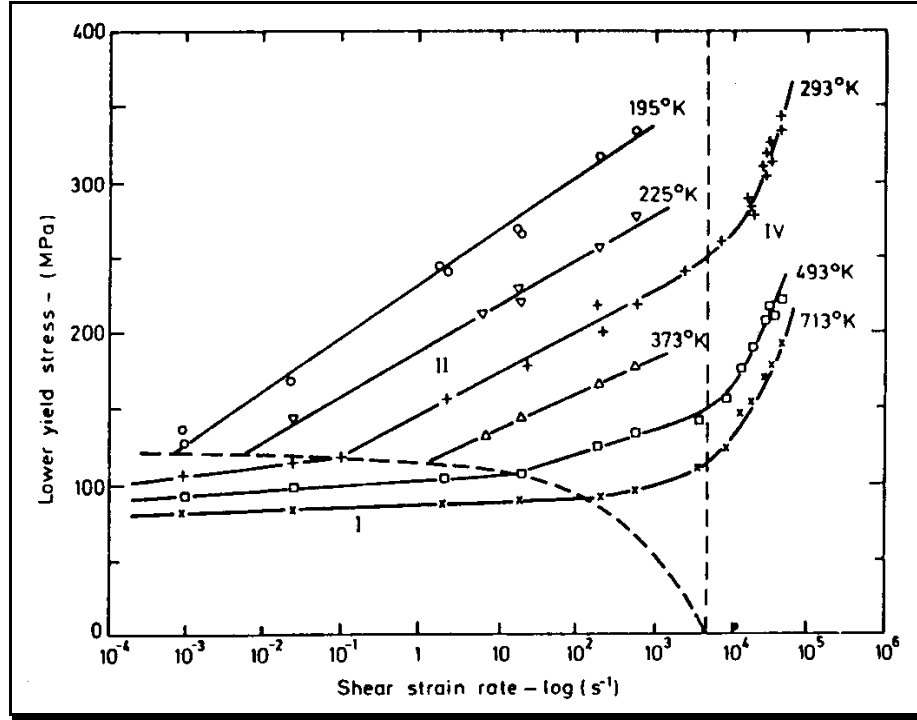


Figure 2.3- Yield strength variation with strain rate and temperature for a low alloy steel

This latter aspect, in particular, is well shown by the Zener and Hollomon relation:

$$\sigma_y = f(\dot{\epsilon} \cdot e^{Q/RT}) \quad (2.1.2)$$

where Q is the activation energy and R the universal gas constant.

The Johnson and Cook (J&C) model, in particular, has enjoyed much success because of its simplicity. The J&C model is an empirical five parameters constitutive equation that takes the following form:

$$\sigma_y = (A + B\varepsilon_p^n) \cdot (1 + C \cdot \ln \dot{\epsilon}^*) \cdot (1 - T^{*m}) \quad (2.1.3)$$

where σ_y and ε_p are the von Mises flow stress and the equivalent plastic strain, respectively, $\dot{\epsilon}^* = \dot{\epsilon} / \dot{\epsilon}_o$ is a dimensionless strain rate with $\dot{\epsilon}_o$ equal to 1.0 s^{-1} , and T^* is the homologous temperature defined as:

$$T^* = \frac{T - T_r}{T_m - T_r} \quad (2.1.4)$$

where T_r is a reference temperature (normally the room temperature, RT) and T_m the melting temperature of the material. A, B, n, C and m are the five material constants. In Eqn. (2.1.3), the first set in brackets gives the dependence of the flow stress on strain, while the second and third one provides the dependence on strain rate and temperature, respectively.

At variance, the Zerilli-Armstrong constitutive equation is a physically based model. It is a three parameters model that has a very good capability to fit experimental results. It is based on thermally activated dislocation motion, focusing on the relevant difference between BCC and FCC metal response, for which the predicted evolution of the material yield strength with the strain rates and temperatures becomes:

$$\begin{aligned} BCC : \quad \sigma_y &= C_1 \exp(-C_3 T + C_4 T \ln \dot{\varepsilon}) \\ FCC : \quad \sigma_{flow} &= C_2 \varepsilon^{1/2} \exp(-C_3 T + C_4 T \ln \dot{\varepsilon}) \end{aligned} \quad (2.1.5)$$

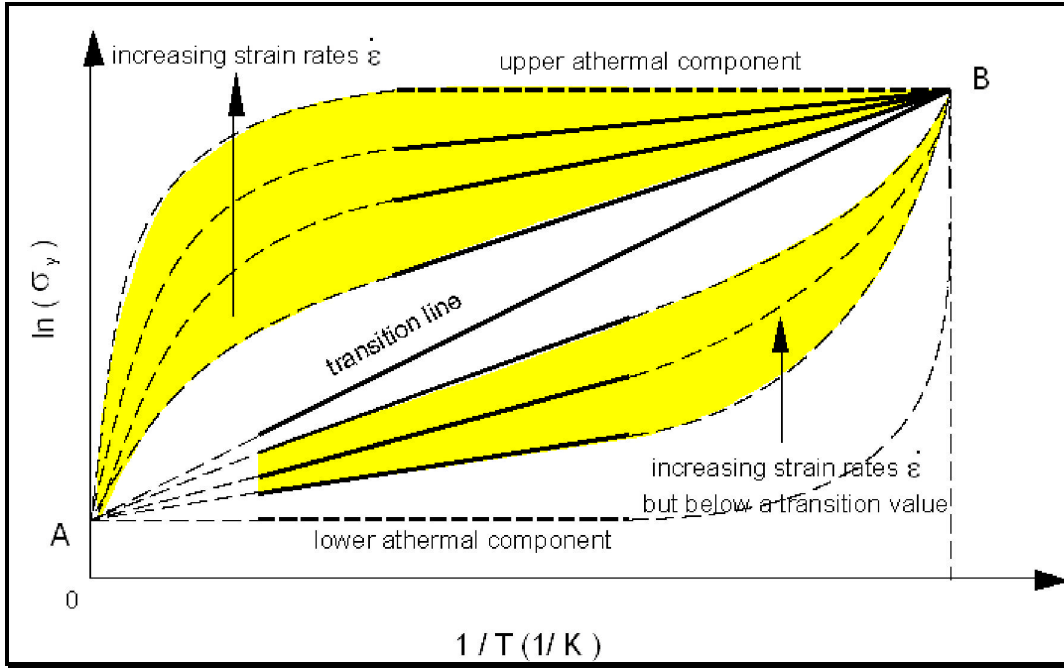


Figure 2.4- Scheme of strain rate and temperature effect and associated mechanisms for the Milella unified model.

More recently Milella (Ref. 2.4) derived a unified relation for both BCC and HFC metals, physically based on the dynamics of Cottrell atmosphere. Starting from the observation that different metal lattices are localized in specific zones of the $\ln(\sigma_y)$ - $1/T$ diagram, Figure 2.4, the following relation that accurately describes the transition from one regime to the other, has been proposed:

$$\frac{\sigma_y - \sigma_o}{\sigma_{\max} - \sigma_o} = 1 - \left[1 - \frac{\ln(t/t_{\min})}{\ln(t_{\max}/t_{\min})} \right]^m \quad (2.1.6)$$

where m is a strain rate exponent, σ_{\max} the maximum value of the yield strength achievable at any strain rate at the minimum temperature T_{\min} , σ_o the athermal component of the yield strength, $t = 1/T$, $t_{\max} = 1/T_{\min}$ and $t_{\min} = 1/T_{\max}$. In Figure 2.5 the comparison of the model prediction together with a number of experimental data for different metals is reported.

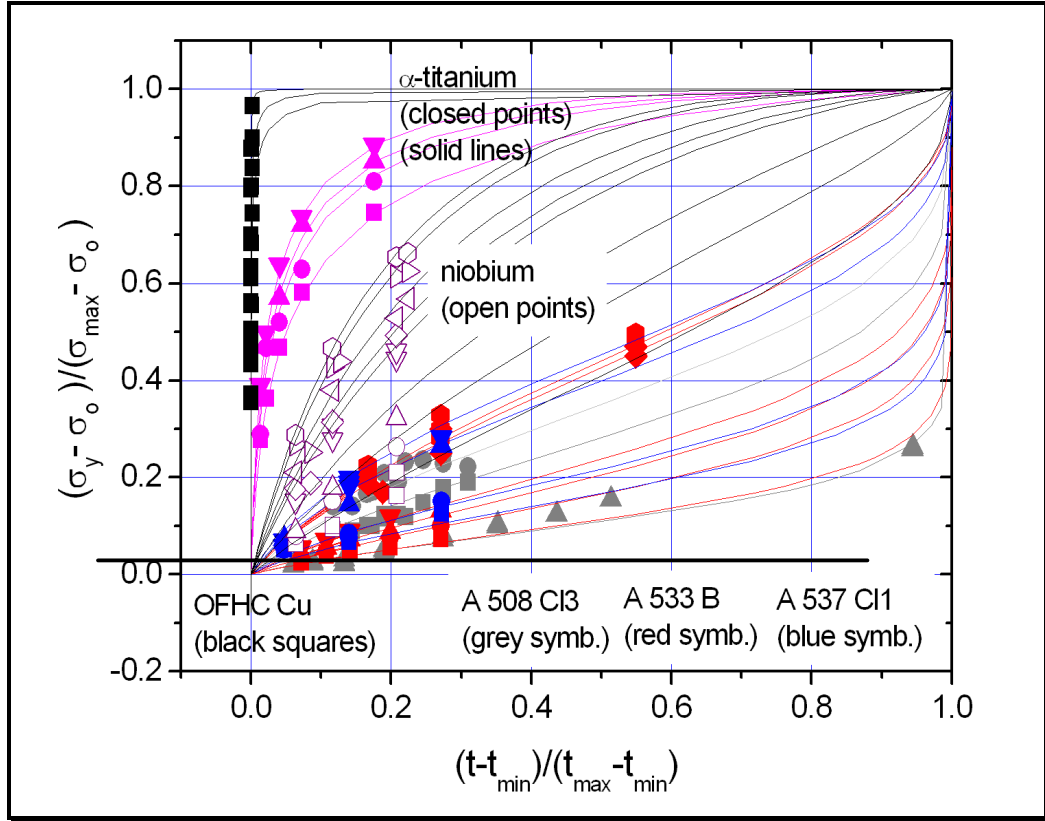


Figure 2.5 - Comparison of Milella unified strength model and experimental data relative to several metals

In comparison to strength modeling, damage has received less attention in the past. For decades failure has been conceptualized as a phenomenon independent from the material or structure stress/deformation process history in the sense that no material modification would occur in the material until, for some reasons, it suddenly becomes incapable to sustain loads. Failure theories, for instance, are the tentative to understand and predict the occurrence of rupture in terms of material maximum allowable without addressing the specific material failure mechanisms.

Even if brittle fracture in metals has received large attention since the beginning of the 20th century, ductile failure has been investigated in details only starting from the 60's.

McClintock (Ref. 2.5) and Rice and Tracy (Ref. 2.6) were the first to identify in the formation and growth of micropores, resulting from increasing strain levels, the micro-mechanism responsible for ductile failure.

Since then, several failure models have been proposed. Basically, they can be grouped into so called abrupt criteria and nucleation and growth (NAG) models. In the first group, failure occurs instantaneously in the material when an internal variable or a state variable reaches a critical value at the material point. In these models, even though the damage accumulates during the deformation history, there is no coupling with other constitutive variables. This is typical of modeling of brittle materials in which failure occurs when a critical stress or stress field intensity is reached. In the NAG models the activation of damage mechanisms results in the modification of material properties. Here, failure is seen as the result of progressive deterioration of material load carrying capability. The variable that accounts for this deterioration is commonly addressed as damage, which is usually coupled with other internal variables and requires the definition of a kinetic evolution law.

Abrupt failure criteria are usually simple to implement in numerical codes but transferability can suffer of both size and geometry effects. In impact dynamics the use of these criteria has been often preferred to on the assumption that deformation phenomena occurs so rapidly that the associated effects remain confined in limited volumes and eventual damage coupling could be neglected in the computations. On the contrary, since these criteria are phenomenological in nature, they often need a post-test material parameters calibration that strongly reduces the effective predicting capability.

For instance, in this framework, the maximum pressure in tension is commonly used to match spall fracture in simulation of flying impact test. Here, failure is assumed to occur when the hydrostatic pressure, somewhere in the target, exceeds a critical tensile value. The determination of this critical value, characteristic for the material under investigation, need a number of tests at different velocities and matching is performed comparing the resulted spall signal, in term of free target surface velocity profile, with the computed one. In the case of soft spall, this criterion does not account for the role of stress triaxiality in the ductile failure process.

Hancock and Mackenzie (Ref. 2.7) and Thomson and Hancock (Ref. 2.8) recognized that stress triaxiality plays a major role in reducing material capability to deform. They proposed that failure would occur when the critical strain is reached at the material point. The value of the critical strain depends on the complexity of multiaxial state of stress and can be given in the form:

$$\varepsilon_f = \alpha \exp\left(-\frac{3}{2} \frac{\sigma_m}{\sigma_{eq}}\right) \quad (2.1.7)$$

where \mathbf{s}_m is the hydrostatic pressure, \mathbf{s}_{eq} is the equivalent Mises stress, and α is a material constant determined inferring the material ductility under uniaxial state of stress condition ($TF = \mathbf{s}_m / \mathbf{s}_{eq} = 1/3$). Similar expression has been determined independently by Manjoine (Ref. 2.9) fitting the experimental results for a number of steels:

$$\varepsilon_f = \varepsilon_f^{uniaxial} 2^{(1-3\sigma_m/\sigma_{eq})} \quad (2.1.8)$$

In Figure 2.6 the comparison of the different equations for the ductility reduction, as a function of the increasing stress triaxiality, is given together with the experimental data relative to a SA537 steel tested at different load rates, (Ref. 2.10).

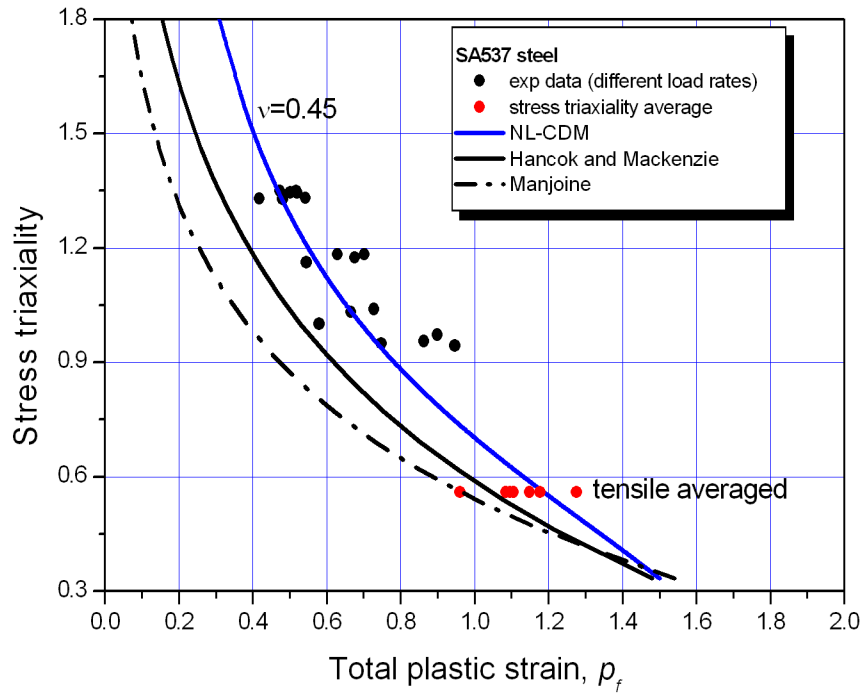


Figure 2.6 - Ductility reduction as a function of TF for a SA537 steel

Johnson and Cook (Ref. 2.11) proposed a critical strain based criterion incorporating stress triaxiality, strain rate and temperature effect:

$$\varepsilon_f = \left(D_1 + D_2 \exp D_3 \frac{\sigma_m}{\sigma_{eq}} \right) \left(1 + D_4 \ln \frac{\dot{\varepsilon}}{\dot{\varepsilon}_0} \right) \left(1 + D_5 \frac{T - T_0}{T_{melt} - T_0} \right) \quad (2.1.9)$$

In order to account for the strain history, they proposed a cumulative criterion where failure it is assumed to occur when the normalized cumulated strain increment becomes equal to one:

$$D = \sum \frac{\Delta \varepsilon_i}{\varepsilon_f^i} \quad (2.1.10)$$

Usually these abrupt criteria are time independent, in the sense that time does not appear explicitly in the expressions. Tuler and Butcher (Ref. 2.12), starting from the observation that the stress that causes failure in a long-duration pulse is lower than the one for a short-duration pulse, proposed the following expression:

$$\int_0^{t_f} (\sigma - \sigma_0)^\lambda dt \geq K_c \quad (2.1.11)$$

σ_0 is the threshold value over which the criterion is activated and t_f is the total time for failure completion. Fracture will occur at the material point when the integral of Eqn. (2.1.11) exceeds the reference value K_c . Even though this criterion showed good predicting performance in the case of triangular pulse in plate impact tests, it neglects material volumes and stress triaxiality effects.

In NAG models it is assumed that the occurrence of some irreversible phenomena during the deformation process modify the material response and its capability to sustain loads. To model this, the material constitutive equations need to be redefined. In the past, two main approaches have been proposed. The porosity-based models accounts for damage through the introduction of an artificial porosity variable, related to the formation of microcavities in the material due to plastic deformation, which softens the material yield function. Here, the constitutive equations for the material at the macro scale are the same as for the standard elastic-plastic material, but the yield criterion is modified by the porosity: when porosity reaches its critical value the yield function implodes to a point at zero stress. This approach has been initially formulated by Gurson (Ref. 2.13) and subsequently has been modified by Tvergaard and Needleman (Ref. 2.14) in order to account for rapid increase of porosity due to microvoids coalescence. Needleman and Rice (Ref. 2.15) modified the model in order to account for new void family nucleation during the deformation process. Even though this model has been widely used in a large number of applications and it is available in several commercial codes, it suffers from two major limitations: the requirement of an extensive number of material parameters (up to 9) and the lacking of transferability to different geometry and constraint conditions (Ref. 2.16, 2.17)

Similarly, Curran et al. (Ref. 2.18) proposed a different form for the evolution of porosity assuming an exponential distribution of voids with respect to void size. Seaman et al. (Ref. 2.19) proposed a nucleation distribution function of tensile pressure.

Alternatively to porosity models, continuum damage mechanics defines the constitutive set of equation for the damaged material. Here, damage is one of the thermodynamics variables. Assuming the existence of a damage dissipation potential, the kinetic law of damage evolution is obtained. Lemaitre (Ref. 2.20) defined the constitutive framework

for a ductile damage material. Later authors (as Ref. 2.21) provided different forms for the damage dissipation potential that resulted in specific shape of the damage evolution law with strain characteristic of some classes of metals. Recently Bonora (Ref. 2.22) proposed a new and more general form for the damage dissipation potential capable to describe damage evolution in different metals and to correctly account for stress triaxiality effects.

Accurate and reliable simulation of impact phenomena requires that the material model incorporates both strength and damage advanced modeling capabilities. A unified model in which damage and material constitutive response are fully embedded is not still available and if it was it would probably require a large number of material parameters difficult to calibrate or measure. However a model of this kind is not really needed if it is possible to come up to the same results merging together one strength and a damage model. For instance this is the numerical strategy used in AUTODYN code in which the user has available a wide choice of material models and erosion criteria for material failure.

From the theoretical point of view merging would be possible if damage effects are uncoupled from the strength model and if there are enough clues that confirm a lacking of coupling or mutual interference between the parameters of each model. In particular this is the case of damage parameters that can be eventually sensible to pressure, strain rate or temperature.

In this research the following approach to simulate and predict material failure under different dynamic conditions has been followed. A strength model where both strain rate and temperature effects are incorporated has been used to simulate material response. Since the compressive pressure range investigated in all the applications is of the order of 1-10 time the yield stress, no specific equation of state (EOS) is used or prescribed. More specifically, the Johnson and Cook strength model has been implemented in the calculations since material parameters are available for different classes of metals. A CDM model, in the formulation developed by Bonora, has been used to account for ductile damage evolution. As discussed in the next section, this damage formulation is strain rate independent while temperature effects are accounted for updating material damage parameters.

2.1. References

- 2.1 Zener C., and Hollomon J.H., (1944), J. Appl. Ph., 15, pp. 22-32
- 2.2 Cottrell A.H., (1957) Proc. of Conference on Property of Materials at High Rates of Strain, pp. 1-12.
- 2.3 Hollomon J. H., (1947), Trans. AIME, 171, pp. 535-545

- 2.4 Milella, P.P. , (2001), Proc. of Shock Compression of Condensed Matter, AIP Conf. Proc. 620, Atlanta.
- 2.5 McClintock, F.A., (1968), J. Appl. Mech., 35, pp. 363-371.
- 2.6 Rice, J.R., and Tracy, D.M., (1969), J. Mechanics Physics Solids, 17, 210-217.
- 2.7 Hancock, J.W. and Meckenzie, A.C., (1976), J. of Mech. Phy. Sol., 24, pp. 147-169
- 2.8 Thomson, R.D., and Hancock, J.W., (1984), Int. J. Frac. 26, pp.99-112.
- 2.9 Manjoine, M.J., (1982), Welding Research Supplement, 50s-57s.
- 2.10 Bonora, N., and Milella, (2000) P.P., USAF/AFRL Contract n° F61775-00-WE029 Final Report.
- 2.11 Johnson G.R. and Cook W.H., (1983), Proc. 7th Inter. Symp. Ballistic, Am. Def. Prep. Org. (ADPA), Netherlands.
- 2.12 Tuler, F.R., and Butcher,B.M., (1968), Int. J. Fract. Mech., 4, pp. 431-437
- 2.13 Gurson, A.L., J. Engr. Mat. Tech.,(1977), 99, pp. 2-15
- 2.14 Tvergaard, V. and Needleman, A., (1984), Acta Metall., 32, p.157-169
- 2.15 Needleman, A., and Rice, J. R., (1978), Limits to ductility by plastic flow localization in Mechanics of Sheet Metal Forming, Koistinen and Wang Eds., Plenum Publ. Company, New York, pp. 237-265.
- 2.16 Gao, X., Faleskog, J., Shih, C.F., and Dodds, R. H., (1998), Eng. Fracture Mechanics, 59, N 6, pp. 761-777
- 2.17 Brocks, W., Klingbeil, D., Kunecke, G., and Sun, D.Z., (1994), in Constraint Effects in Fracture: Theory and Application, ASTM STP 1244, Kirk and Bakker Eds., American Society for Testing and Materials, Philadelphia.
- 2.18 Curran, D. R., Seaman, L., Shockey, D.A., in Shock Waves and High Strain Rates Phenomena in Metals, Ed. Meyers M.A. and Murr L.E., Plenum, New-York
- 2.19 Seaman L., Curran, D.R., and Shockey, D.A., (1976) J. Appl. Phys., 47, p. 4814.
- 2.20 Lemaitre, J., A Course on Damage Mechanics, Springer-Verlag, Berlin, 1992
- 2.21 Chandrakanth, S. and Pandey, P.C., (1993), Int. J. Fracture, 60, R73-R76.
- 2.22 Bonora, N., (1997), Int. J. of Fracture, 88, 359-371

3. Ductile damage Modeling

Damage represents the progressive material deterioration and it can be defined in terms of relative reduction of the net resisting section of a reference volume element (RVE) as:

$$D_{(n)} = 1 - \frac{A_{eff}^{(n)}}{A_0^{(n)}} \quad (3.1)$$

where, for a given normal n , $A_0^{(n)}$ is the nominal cross section area and $A_{eff}^{(n)}$ is the truly resisting one reduced by the presence of flaws, microvoids, etc., and their mutual interactions, as sketched in Figure 3.1.

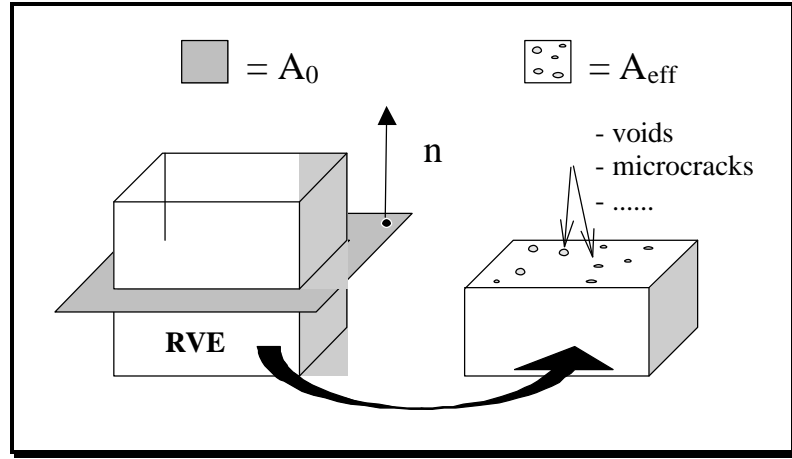


Figure 3.1 - Sketch of the Reference Volume element, RVE, nominal section area, A_0 , and effective resisting area, A_{eff} .

With the additional assumption of isotropic damage, the damage tensor can be conveniently reduced to a scalar D for which a practical definition, using the effective stress concept introduced by Rabotnov, can be given:

$$D = 1 - \frac{\tilde{E}}{E_0} \quad (3.2)$$

where E_0 and \tilde{E} are the Young's modulus of the undamaged and damaged material, respectively. Since plasticity can occur without damage but ductile damage requires the presence of plastic deformations, damage variable has to depend on plastic strain.

On the other hand, since the damage presence affects the elastic strain only, the damage and the plastic dissipation potentials can be assumed to be uncoupled. According to this, the entire set of constitutive equations for the damaged material can be written as

follows. Total strain decomposition in elastic and plastic contribution is assumed. Elastic strain tensor is given as a function of the effective stress:

$$\varepsilon_{ij}^e = \frac{1 + \nu}{E} \frac{\sigma_{ij}}{1 - D} - \frac{\nu}{E} \frac{\sigma_{kk}}{1 - D} \delta_{ij} \quad (3.3)$$

Standard isotropic plasticity, associated with a Von Mises yield criterion, leads to the following expression for the plastic potential F_p ,

$$F_p(\sigma, R, X; D) = \left(\frac{s}{1 - D} - X' \right)_{eq} - R(r) - \frac{3}{4X_\infty} \mathbf{x}'_{ij} X'_{ij} - \sigma_y \quad (3.4)$$

where s_{ij} and X'_{ij} are the deviatoric part of the stress and kinematic hardening tensor, respectively; σ_y is the initial uniaxial yield stress, and the equivalent operator is:

$$\left(\frac{s}{1 - D} - X' \right)_{eq} = \left[\frac{3}{2} \left(\frac{s_{ij}}{1 - D} - X'_{ij} \right) \left(\frac{s_{ij}}{1 - D} - X'_{ij} \right) \right]^{\frac{1}{2}} \quad (3.5)$$

The plastic strain components and the internal variables associated to R and X_{ij} , can be derived from F_p through from the normality rule,

$$\dot{\varepsilon}_{ij}^p = \dot{\lambda} \frac{\partial F_p}{\partial \sigma_{ij}} = \frac{3}{2} \frac{\dot{\lambda}}{1 - D} \left(\frac{s_{ij}}{1 - D} - X'_{ij} \right) \frac{1}{\left(\frac{s}{1 - D} - X' \right)_{eq}} \quad (3.6)$$

$$\dot{\alpha}_{ij} = -\dot{\lambda} \frac{\partial F_p}{\partial X'_{ij}} = \dot{\varepsilon}_{ij}^p (1 - D) - \frac{3}{2X_\infty} X'_{ij} \dot{\lambda} \quad (3.7)$$

$$\dot{r} = -\dot{\lambda} \frac{\partial F_p}{\partial R} = \dot{\lambda} = \dot{p} (1 - D) \quad (3.8)$$

where \mathbf{I} is the plastic multiplier and p is the equivalent accumulated plastic strain. The kinematic back stress increases with the plastic strain and tends to saturate to a value, characteristic for the material, X_∞ . More detailed description on the kinematic back stress formulation can be found elsewhere, (Ref. 3.1). The kinetic law of damage evolution is then given by:

$$\dot{D} = -\dot{\lambda} \frac{\partial F_D}{\partial Y} \quad (3.9)$$

where F_D is the damage dissipation potential that need to be determined and Y is the variable associated to damage. The choice of the damage dissipation potential is a key point of every CDM model. In Ref. 3.1 it was proposed the following expression:

$$F_D = \left[\frac{1}{2} \left(-\frac{Y}{S_0} \right)^2 \cdot \frac{S_0}{1-D} \right] \cdot \frac{(D_{cr} - D)^{\frac{\alpha-1}{\alpha}}}{p^{\frac{2+n}{n}}} \quad (3.10)$$

that was proven to match well the damage evolution for different classes of metals and to be effective in describing the decrease of ductility (i.e. strain to failure) with increasing stress triaxiality exhibited by ductile metals. The substitution in Eq. (9) leads to:

$$\dot{D} = -\dot{\lambda} \frac{\partial f_D}{\partial Y} = \alpha \cdot \frac{(D_{cr} - D_0)^{\frac{1}{\alpha}}}{\ln(\varepsilon_f / \varepsilon_{th})} \cdot f \left(\frac{\sigma_H}{\sigma_{eq}} \right) \cdot (D_{cr} - D)^{\frac{\alpha-1}{\alpha}} \cdot \frac{\dot{p}}{p} \quad (3.11)$$

where

$$f \left(\frac{\sigma_H}{\sigma_{eq}} \right) = \frac{2}{3} (1 + \nu) + 3 \cdot (1 - 2\nu) \cdot \left(\frac{\sigma_H}{\sigma_{eq}} \right)^2 \quad (3.12)$$

account for stress triaxiality effect on damage evolution law. In standard CDM framework, Ref. 3.2, damage affects internal associated variables, such as strain, the yield condition and the Khun-Tucker complementary conditions as a result of the substitution of the stress tensor with the effective one.

According to this, there are two major consequences consequently to the accumulation of damage: i) material stiffness reduction and ii) material softening. When damage reaches its critical value the material stiffness is reduced to zero and the yield surface implodes to a point.

Softening is the cause of a number of well-known numerical problems, such as plastic flow localization, mesh dependency and numerical instability. Anyway, as noted in Ref. 3.1, one of the underlying hypotheses in the Lemaitre formulation is that damage affects elastic strains only, consequently the substitution of the effective stress in the yield condition is questionable.

As a matter of fact, the plastic flow curve measured experimentally is the result of the concurring action of both hardening and damage effects that cannot be separated. In other words, it is not possible to measure directly the plastic flow curve for a metal without damage. Moreover, the macroscopic tensile stress-strain curves of most metals do not exhibit softening even when applying Bridgman correction for necking. Therefore, it is necessary to rewrite Eqn. (3.4) in the following way:

$$F_p(\sigma, R, X) = \sigma_{eq} - f(R, X; D) = 0 \quad (3.13)$$

where $f(R, X; D)$ is the experimentally determined material flow curve where damage effects on R and X are already taken into account but cannot be analytically explicated. In this way, softening is no longer present and the analytical model formulation is consistent with the experimental evidence. The complete set of constitutive equation can be rewritten as follows:

$$\varphi = F_p(\sigma, R, X; D) + F_D(Y; p, D) = [\sigma_y - f(R, X; D)] + F_D(Y; p, D) = 0 \quad (3.14)$$

$$\varepsilon_{ij}^e = \frac{1 + \nu}{E} \frac{\sigma_{ij}}{1 - D} - \frac{\nu}{E} \frac{\sigma_{kk}}{1 - D} \delta_{ij} \quad (3.15)$$

$$\dot{\varepsilon}_{ij}^p = \dot{\lambda} \frac{\partial F_p}{\partial \sigma_{ij}} = \frac{3}{2} \dot{\lambda} \frac{(s_{ij} - X'_{ij})}{(s - X')_{eq}} \quad (3.16)$$

$$\dot{\alpha}_{ij} = -\dot{\lambda} \frac{\partial F_p}{\partial X'_{ij}} = \dot{\varepsilon}_{ij}^p - \frac{3}{2X_\infty} X'_{ij} \dot{\lambda} \quad (3.17)$$

$$\dot{r} = -\dot{\lambda} \frac{\partial F_p}{\partial R} = \dot{\lambda} = \dot{p} \quad (3.18)$$

$$\dot{D} = -\dot{\lambda} \frac{\partial f_D}{\partial Y} = \alpha \cdot \frac{(D_{cr} - D_0)^{\frac{1}{\alpha}}}{\ln(\varepsilon_f / \varepsilon_{th})} \cdot f\left(\frac{\sigma_H}{\sigma_{eq}}\right) \cdot (D_{cr} - D)^{\frac{\alpha-1}{\alpha}} \cdot \frac{\dot{p}}{p} \quad (3.19)$$

where Eqn. (3.15)-(3.18) are the standard associative plasticity equations.

3.1. Ductile Damage Formulation: Extension to Compressive State of Stress

From the microscopic point of view, ductile damage associated with plastic deformation can be regarded mainly as voids nucleation, growth, coalescence and their mutual interaction. The occurrence of this mechanism is demonstrated for dominating tensile stress conditions. Even in the case of shear band formation the presence of microvoids, whose dimensions are smaller than in the tensile case, has been also observed. Here, the only difference is given by the fact that voids do not increase their dimensions but stretch and eventually coalesce by internal ligament necking (known as microvoid sheeting) under increasing loading. The same mechanism of damage has been found in dynamic impact failure phenomena, such as spall fracture, as shown in Figure 3.2, where microvoids formation, due to the combination of reversed compressive pulse and release wave, occurs.

If the state of stress is compressive and plastic strain occurs, it is not clear if microvoids damage mechanism changes or simply remains inactive. In Ref. 3.2, it was postulated that compressive state of stress could partially close back formerly formed voids, resulting in a different value of damage in tension and in compression. There, it was also assumed that damage accumulates in the same way under tensile and compressive state of stress.

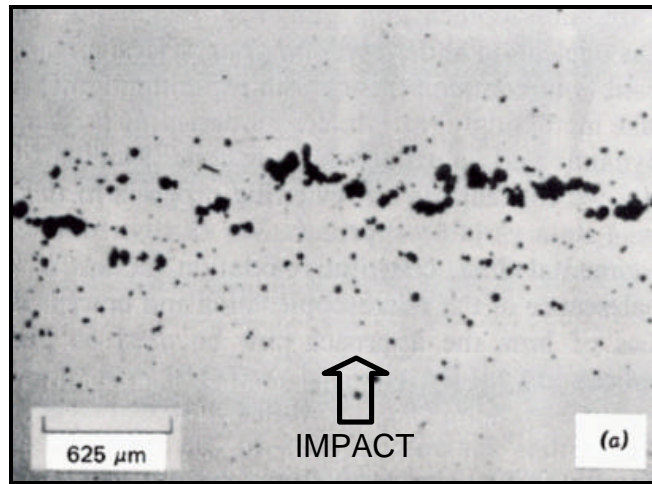


Figure 3.2 - Microvoids formation in impacted 1145 aluminum plate (Ref.3.3)

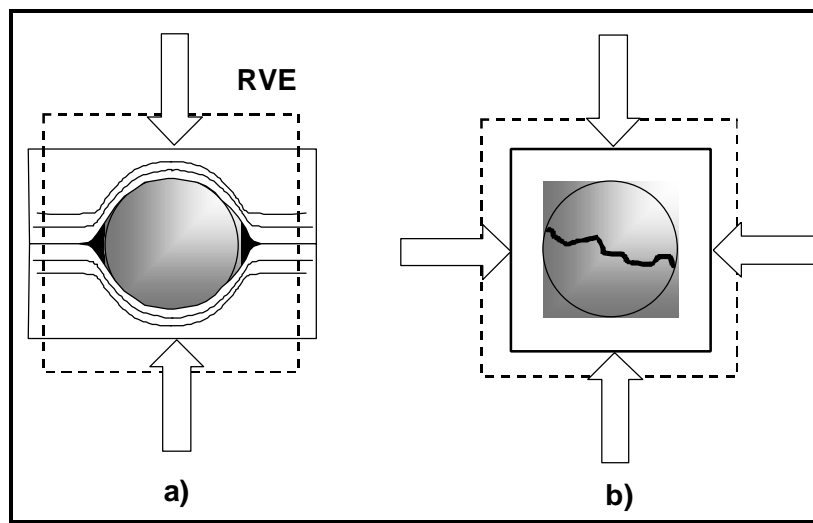


Figure 3.3 - Particle matrix interaction inside a RVE under compressive deformation state: a) under weak and b) under strong confinement of the ductile matrix.

In both previously cited models, the constitutive framework remains unchanged, i.e. damage accumulates with the equivalent accumulated plastic strain. Anyway, when applied to real components, these models may result in very short predicted lives due to a very rapid accumulation of plastic strain.

In the present study it has been observed that, even under limited plastic deformation levels, intense triaxial compressive pulses, resulting from dynamic impact, can potentially break the included brittle particles reducing the material damage threshold strain down to the inelastic limit (i.e. ~ 0.002).

In order to extend the CDM model to compressive state of stress and to complex load histories, one needs to understand the microstructural modification (i.e. damage) of the material during the deformation process and the related effect on the constitutive response. Because of the limited knowledge about ductile damage produced in compression and the associated effects, two scenarios have been speculated.

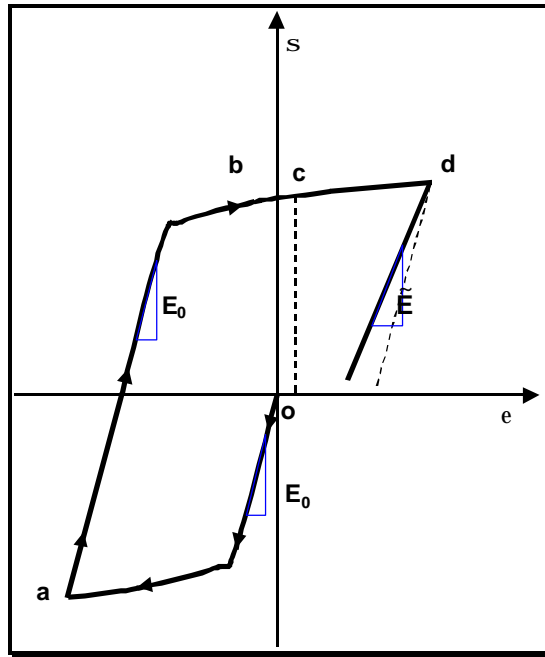


Figure 3.4- Outline of the mechanical behavior expected when an initial compressive load ramp is followed by tension loading (scenario A).

Scenario A

Let us assume that the material is in its initial and stress-free state. Let us start to load the material under monotonic compressive loading, avoiding any buckling phenomena, and to focus the attention to the modification occurring in the RVE. The sketch in Figure 3.3 shows how the ductile matrix can either: a) flow around the particle, eventually resulting in the failure of the interface, if the confinement is weak (low triaxiality) or, b) it can be compressed around the particle, if the confinement is strong (high triaxiality), eventually resulting in the particle fracture if local stress overcomes its strength. This kind of damage should not affect material stiffness since no reduction of the net resisting area is occurred. The only effect that it would be expected is probably an anticipated microvoids nucleation when the stress state is reversed in tension (i.e. a lower strain threshold value), due to an early void opening since the

particle-matrix interface is damaged and/or the particle is broken. Even though an irreversible process such as particle breaking would eventually occur under compressive loads, the stiffness should remain unaffected indicating no damage in compression.

When the stress is reversed in tension, damage would eventually start to accumulate, as soon as the plastic strain overcomes the actual damage threshold value, according to the proposed damage evolution law. No effect due to the previous compressive half-cycle, even though severe, should be observed on both material stiffness and plastic flow curve until ductile damage in tension will occur, Figure 3.4.

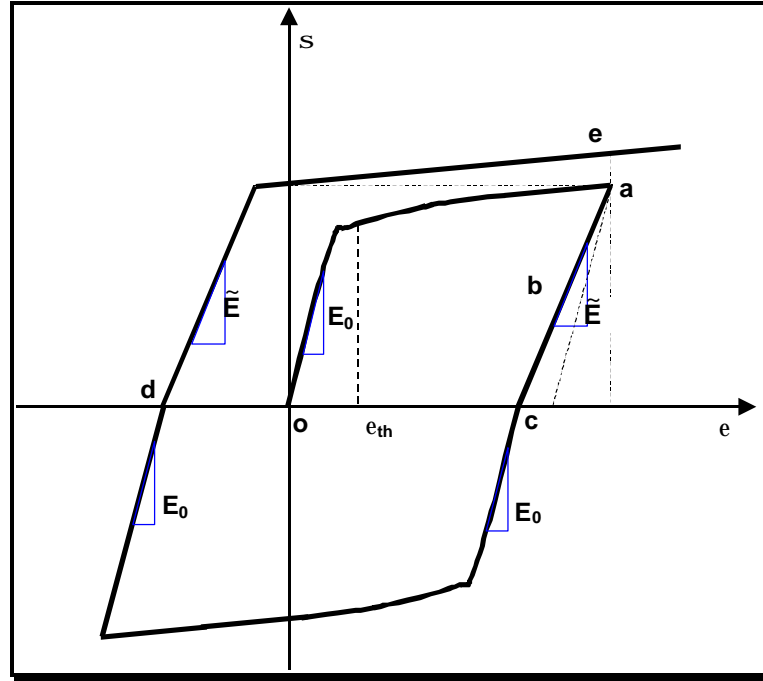


Figure 3.5- Outline of the mechanical behavior expected when an initial tensile loading ramp is followed by compression and again by tension loading (scenario B).

Scenario B

Let us consider the RVE initially loaded in tension, above the material threshold strain value, where some damage is generated, (Figure 3.5, point a). If the load is reversed at this point, the unloading will follow a slope determined by the effective modulus $\tilde{E} = E_0(1 - D)$, as shown in Figure 3.5, point b. During the unloading down to the zero state of stress, at the RVE scale the ductile matrix is forced back to its initial configuration. Microvoids, whose shape is controlled by the matrix deformation, are therefore squeezed back to the particles from which they nucleated. Potential microvoid buckling is not considered at this stage. Complete void closure can eventually occur when stresses come back to zero at the macroscale, point c in Figure 3.5. At this point the initial nominal section area of the RVE is restored and material stiffness should be back to its initial value E_0 . Further increase of compression should not generate

additional damage and consequently the actual stiffness will remain unchanged. If the load is reversed again, damage will remain inactive until stress will become positive again, Figure 3.5, point d. Here, since damage was previously generated, the actual threshold strain is reduced to zero and material stiffness is given by the effective modulus. Damage will start to accumulate only if the previous plastic strain level reached during the first loading in tension is exceeded, Figure 3.5, point e.

Formulation

According to those two scenarios, damage model formulation should be modified as follows:

Damage accumulates if and only if stress triaxiality is positive:

$$\text{if } \sigma_m / \sigma_{eq} \geq 0 \ \& \ \varepsilon \geq \varepsilon_{th} \mapsto \dot{D} > 0, D \neq 0 \ \& \ \tilde{E} = E_0(1 - D)$$

Damage affect material stiffness by means of effective modulus definition. Damage effects are active if and only if stress triaxiality is positive.

Under compressive state of stress (i.e. $\sigma_m / \sigma_{eq} < 0$) damage does not accumulate and its effects are inactive:

$$\text{if } \sigma_m / \sigma_{eq} < 0 \ \& \ D > 0 \mapsto \dot{D} = 0 \ \& \ \tilde{E} = E_0$$

It has to be noticed that since the damage D is a thermodynamics variable, it has to increase monotonically due to the irreversible nature of the deformation process that it represents and its evolution as a function of the associated variable Y has to be a continuous function. It follows that damage cannot depend on the equivalent accumulated plastic strain p , tout court. In fact, the total accumulated plastic strain accumulates both in tension and compression while damage does it only in the tension part, resulting in a sudden jump and a discontinuous damage evolution law that has no physical sound.

Here a new internal variable p^+ , called active accumulated plastic strain, is introduced. It is the equivalent plastic strain accumulated if and only if the actual stress triaxiality is greater than zero. Similarly, an active damage D^+ is defined and Eqn. (3.18) and Eqn. (3.19) can be rewritten as follows:

$$\dot{p}^+ = \dot{\lambda} \cdot H \langle f(\sigma_m / \sigma_{eq}) \rangle \quad (3.1.1)$$

$$\dot{D}^+ = -\dot{\lambda} \frac{\partial f_D}{\partial Y} = \alpha \cdot \frac{(D_{cr} - D_0)^{\frac{1}{\alpha}}}{\ln(\varepsilon_f / \varepsilon_{th})} \cdot f\left(\frac{\sigma_H}{\sigma_{eq}}\right) \cdot (D_{cr} - D^+)^{\frac{\alpha-1}{\alpha}} \cdot \frac{\dot{p}^+}{p^+} \quad (3.1.2)$$

and

$$\tilde{E} = E(1 - D^+)H \langle f(\sigma_m / \sigma_{eq}) \rangle \quad (3.1.3)$$

where:

$$H \langle f(\sigma_m / \sigma_{eq}) \rangle = \begin{cases} 0 & \sigma_m / \sigma_{eq} < 0 \\ 1 & \sigma_m / \sigma_{eq} \geq 0 \end{cases} \quad (3.1.4)$$

3.2. Ductile damage formulation: strain rate and temperature effects

In the literature, very little attention has been given to possible effects on damage evolution due to dynamic loading. Ping (Ref. 3.5) analyzed the modification resulting from dynamic loading onto the growth rate of cavities in a ductile matrix including inertial effect but without the support of experimental evidences. Strain rate effect onto porosity accumulation resulted from the strain rate sensibility of the matrix in the theoretical formulation.

In order to assess possible strain rates effect on damage evolution Bonora and Milella (Ref. 3.6) performed damage measurements in the low strain rate range ($\sim 0.1 \text{ s}^{-1}$) observing no effect on damage evolution law. Experimental observations confirm that the formation and growth of microcavities, independently of both temperature and strain rate, always control ductile failure mechanism, Bonora and Milella (Ref. 3.6) came to the conclusion that the damage potential should remain unchanged and should not depended explicitly on strain rate and temperature.

Due to the great difficulty to make direct damage measurements at high strain rates, some indirect indications, on at least two of the four damage material parameters, i.e. ε_{th} and ε_f , can be obtained from dynamic tensile tests at different strain rates on smooth and notched round bars specimens.

Johnson and Cook (Ref. 3.7) investigated the behavior of several classes of metals under intense load rates and different temperatures, coming to the conclusion that material strain to failure would change according to

$$\varepsilon_f = \left[D_1 + D_2 \exp \left(D_3 \frac{\sigma_m}{\sigma_{eq}} \right) \right] \left(1 + D_4 \ln \frac{\dot{\varepsilon}}{\dot{\varepsilon}_0} \right) \left(1 + D_5 \frac{T - T_0}{T_{melt} - T_0} \right) \quad (3.2.1)$$

Consequently, for a given a stress state, temperature strongly affects failure strain while strain rate has minor role and its effect could be eventually neglected in the simulations. A clear example of this is given by OHFC copper in which temperature can cause an

increase of ductility of the order of 112% at 0.5 of the homologous temperature, while strain rates increases ductility of 20% only at 10^4 s^{-1} . Following these considerations it has been postulated that an analogous effect would be eventually found on damage threshold strain.

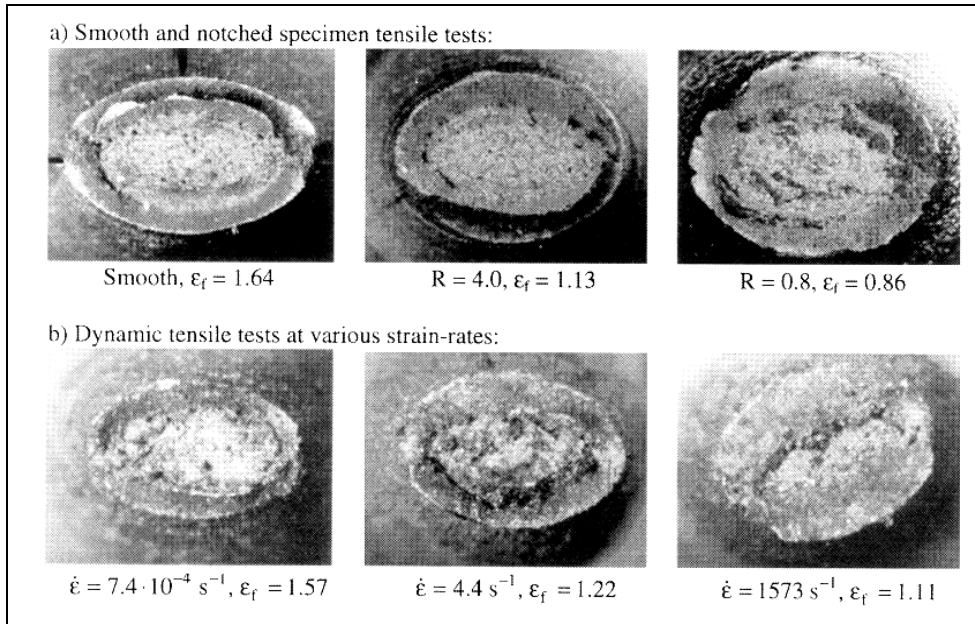


Figure 3.6 - Strain rate, ϵ_f and diameter at fracture in smooth and notched tensile bar in steel, (Ref.3.8)

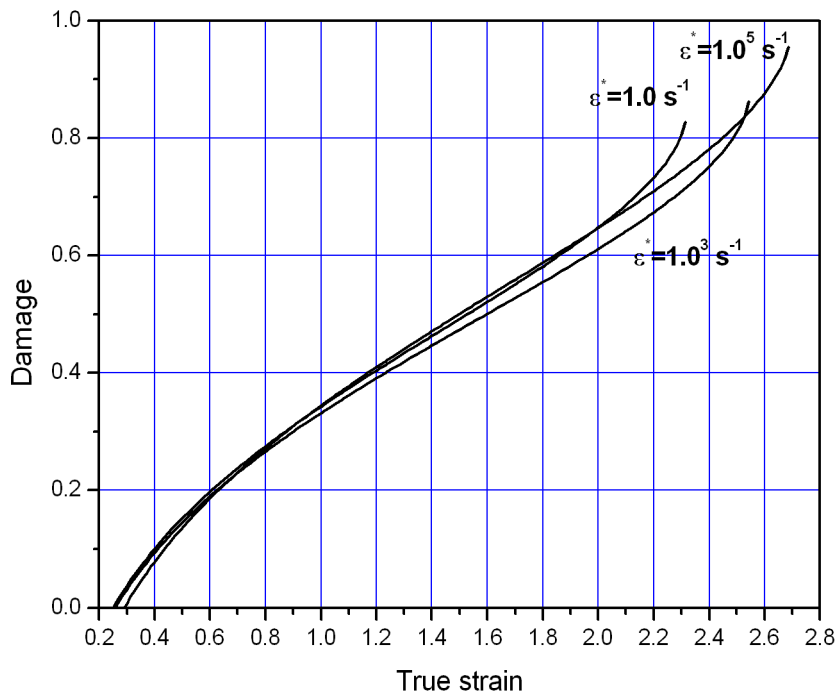


Figure 3.7 - Simulated strain rate effect on damage evolution law

Even for the critical damage, D_{cr} , which is directly related to the effective net resisting area at fracture, it has been found similar behavior, (Ref. 3.8). This seems to confirm that stress triaxiality effects could be uncoupled from those associated to strain rates and temperature in determining failure in the material, see Figure 3.7.

Temperature should have a different effect on each damage parameters. For example, an increase of temperature would eventually weaken the bond between the ductile matrix and the included particles reducing the threshold strain.

From these considerations, it is possible to suppose that strain rate affects all damage parameters in the same way. Thus an empirical expression, as that proposed by J&C, can be written as:

$$\begin{bmatrix} \tilde{\varepsilon}_{th} \\ \tilde{\varepsilon}_f \\ \tilde{D}_{cr} \end{bmatrix} = \begin{bmatrix} \varepsilon_{th} \\ \varepsilon_f \\ D_{cr} \end{bmatrix} \left(1 + D_4 \ln \frac{\dot{\varepsilon}}{\dot{\varepsilon}_0} \right) \left(1 + \begin{bmatrix} D_7 \\ D_5 \\ D_6 \end{bmatrix} \frac{T - T_0}{T_{melt} - T_0} \right) \quad (3.2.2)$$

ε_{th} , ε_f and D_{cr} are the quasi static damage parameters at room temperature and D_7 and D_6 are other two material constants to be determined experimentally.

3.3. References

- 3.1 Bonora, N., (1997), Int. J. of Fracture, 88, 359-371
- 3.2 Lemaitre, J., A Course on Damage Mechanics, Springer-Verlag, Berlin, 1992
- 3.3 Zuckas, J., A., Nicholas, T., Swift, F. H., Greszczuk, L. B., and Curran, D. R., Impact Dynamics, Wiley- New York, 1982
- 3.4 Bonora, N., and Newaz, M.G. ,(1998) Int. J. Solids Struct., 35, pp. 1881-1894.
- 3.5 Ping, Wang-Ze, (1994), Int. J. of Sol. Struc., 31, no. 15, pp. 2139-2150.
- 3.6 Bonora, N., and Milella, (2000) P.P., USAF/AFRL Contract n° F61775-00-WE029 Final Report.
- 3.7 Johnson G.R. and Cook W.H., (1983), Proc. 7th Inter. Symp. Ballistic, Am. Def. Prep. Org. (ADPA), Netherlands.
- 3.8 Borvik, T., Langseth, M., Hopperstad, O.S., Malo, K.A., (1999), Int. J. of Impact Engineering, 22, pp.855-886.

4. CDM Model Numerical Implementation

The numerical implementation of the proposed material modeling is simple and straightforward. The J&C strength model and the Bonora non-linear CDM model have been implemented on both implicit and explicit finite element code.

The J&C model has been implemented in the finite element code MSC/MARC release 2000. Subsequent release MSC/MARC 2001, as recently received, has the J&C model built-in. The implementation is performed through user subroutines linked directly to the main program. One of the major features of the MSC/MARC code is the possibility to access via user subroutine to all the major parameters and the numerical procedures allowing the user incorporate his modifications as needed.

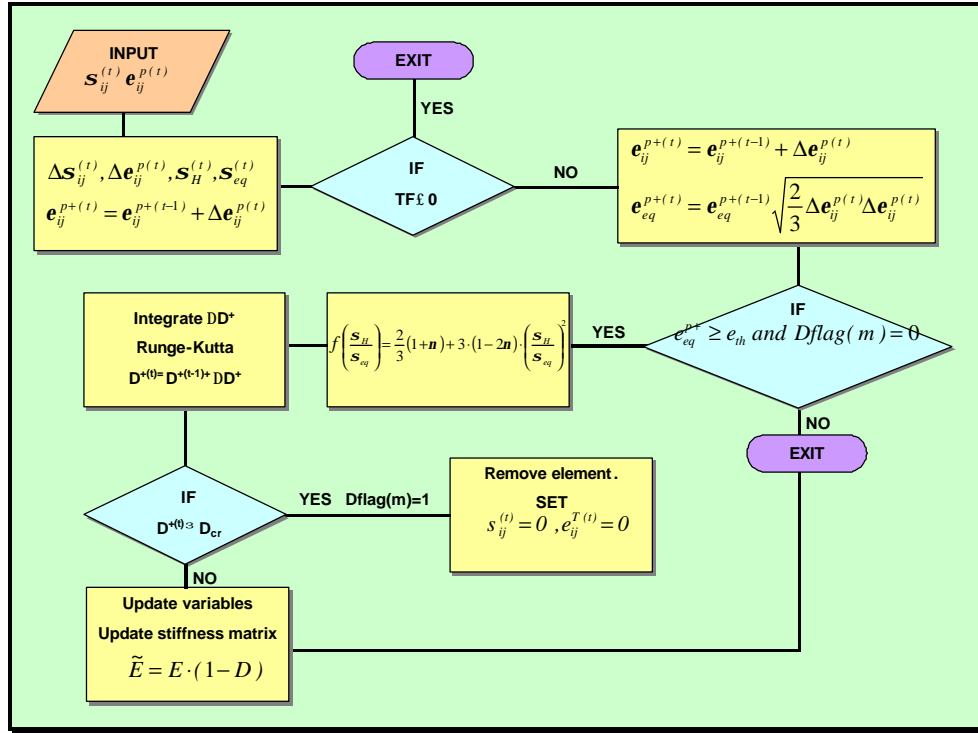


Figure 4.1 - Logical scheme for damage calculation in fem code. The procedure is started at the end of each load increment when global variables have been calculated and it is repeated for each gauss-point of each active element.

The damage model has been implemented in very simple way. As formulated in Section 3, there is no need to solve back, for each total strain increment, the entire set of equations given in Eqn. (3.14)-(3.19). Since there is no coupling between the plastic and damage dissipation potentials, the equivalent plastic strain and the effective one coincides in this formulation. Moreover, since the damage rate equation, given in Eqn. (3.19), is function of the actual damage amount, the accumulated plastic strain, and stress triaxiality, it has to be integrated over the plastic strain increment. Standard

integration procedure using Runge-Kutta scheme has been used. Damage calculations are performed for each time steps, at every element gauss-point. When the element reaches the critical damage in all the gauss-points, the element is removed and the frozen stresses and strain are relieved. At this stage, no automatic sub-cycling procedure for a progressive element removal technique is available. Previous benchmark tests showed that the damage calculation procedure is robust enough to be insensitive to reasonable variation of the loading step size. In order to have a good stability of the solution during crack growth simulation it has been found that a load step for which the removal of a single element occurs, usually leads to better results since the code has time to reestablish equilibrium in the subsequent steps without error propagation. The logical scheme followed is given in Figure 4.1.

5. Dynamic Analysis in MSC/MARC

MARC has a dynamic analysis capability that allows one to perform the following calculations:

Eigenvalue Analysis

Transient Analysis

Harmonic Response

Spectrum Response

The program contains two methods for eigenvalue extraction and three time integration operators. Nonlinear effects, including material nonlinearity, geometric nonlinearity, and boundary nonlinearity, can be incorporated. Linear problems can be analyzed using modal superposition or direct integration. All nonlinear problems should be analyzed using direct integration methods. In addition to distributed mass, the user can also attach concentrated masses associated with each degree of freedom of the system. Damping can be included in either the modal superposition or the direct integration methods. Non-uniform displacement and/or velocity as an initial condition, and apply time-dependent forces and/or displacements as boundary conditions can be included

5.1. Direct Integration

Direct integration is a numerical method for solving the equations of motion of a dynamic system. It is used for both linear and nonlinear problems. In nonlinear problems, the nonlinear effects can include geometric, material, and boundary nonlinearities. For transient analysis, the MARC program offers three direct integration operators listed below.

Newmark-beta Operator

Houbolt Operator

Central Difference Operators

Direct integration techniques are imprecise; this is true regardless of which technique is used. Each technique exhibits at least one of the following problems:

conditional stability

artificial damping

phase errors.

Newmark- β Operator

This operator is probably the most popular direct integration method used in finite element analysis. For linear problems, it is unconditionally stable and exhibits no numerical damping. The Newmark- β operator can effectively obtain solutions for linear and nonlinear problems for a wide range of loadings. The procedure allows for change of time step, so it can be used in problems where sudden impact makes a reduction of time step desirable. This operator can be used with adaptive time step control. Although this method is stable for linear problems, instability can develop if nonlinearities occur. By reducing the time step and/or adding (stiffness) damping, allows one to overcome these problems.

Houbolt Operator

This operator has the same unconditional stability as the Newmark- β operator. In addition, it has strong numerical damping characteristics, particularly for higher frequencies. This strong damping makes the method very stable for nonlinear problems as well. In fact, stability increases with the time step size. The drawback of this high damping is that the solution can become inaccurate for large time steps. Hence, the results obtained with the Houbolt operator usually have a smooth appearance, but are not necessarily accurate. The Houbolt integration operator, implemented in MARC as a fixed time step procedure, is particularly useful in obtaining a rough scoping solution to the problem.

Central Difference Operators

These explicit operators are only conditionally stable. The program automatically calculates the maximum allowable time step. This method is not very useful for shell or beam structures because the high frequencies result in a very small stability limit. This method is particularly useful for analysis of shock-type phenomena. In this procedure, since the operator matrix is a diagonal mass matrix, no inverse of operator matrix is needed. However, this fact also implies that it cannot be used in problems having degrees of freedom with zero mass. This restriction precludes use of the Herrmann elements, gap-friction elements, the pipe bend element. The mass is updated in lagrangian update formulation or contact problem. The elastomer capability can be used with explicit dynamics in an updated Lagrange framework where the pressure variables are condensed out before going into the solver.

5.2. Technical Background

Consider the equations of motion of a structural system:

$$M a + C v + K u + F = 0 \quad (5.2.1)$$

where M, C, and K are mass, damping, and stiffness matrices, respectively, and a, v, u, and F are acceleration, velocity, displacement, and force vectors. Various direct integration operators can be used to integrate the equations of motion to obtain the dynamic response of the structural system. The technical background of the three direct integration operators available in MARC is described below.

Newmark-**b** Operator

The generalized form of the Newmark-beta operator is

$$\begin{aligned} u^{n+1} &= u^n + \Delta t \cdot v^n + \left(\frac{1}{2} - \beta\right) \Delta t^2 \cdot a^n + \beta \cdot \Delta t^2 \cdot a^{n+1} \\ v^{n+1} &= v^n + (1 - \gamma) \Delta t \cdot a^n + \gamma \cdot \Delta t \cdot a^{n+1} \end{aligned} \quad (5.2.2)$$

where superscript n denotes a value at the nth time step and u, v, and a take on their usual meanings. The particular form of the dynamic equations corresponding to the trapezoidal rule

$$\gamma = \frac{1}{2} \quad \beta = \frac{1}{4}$$

results in

$$\left(\frac{4}{\Delta t^2} M + \frac{2}{\Delta t} C + K\right) \Delta u = F^{n+1} - R^n + M \left(a^n + \frac{4}{\Delta t} v^n\right) + C v^n \quad (5.2.3)$$

where R is the internal force given by:

$$R = \int_V \beta^T \sigma dV \quad (5.2.4)$$

Eqn. (5.2.3) allows the implicit solution of the problem in the form:

$$u^{n+1} = u^n + \Delta u \quad (5.2.5)$$

Notice that the operator matrix includes K, the tangent stiffness matrix. Hence, any nonlinearity results in a reformulation of the operator matrix. Additionally, if the time step changes, this matrix must be recalculated because the operator matrix also depends on the time step. The operator γ plays also the role of artificial damping.

Houbolt Operator

The Houbolt operator is based on the use of a cubic fitted through three previous points and the current (unknown) in time. This results in the equations

$$v^{n+1} = \left(\frac{11}{6}u^{n+1} - 3u^n + \frac{3}{2}u^{n-1} - \frac{1}{3}u^{n-2} \right) \cdot \frac{1}{\Delta t} \quad (5.2.6)$$

and

$$a^{n+1} = \left(2u^{n+1} - 5u^n + 4u^{n-1} - u^{n-2} \right) \frac{1}{\Delta t^2} \quad (5.2.7)$$

Substituting Eqn (5.2.6) and (5.2.7) into the equation of motion we get:

$$\begin{aligned} & \left(\frac{2}{\Delta t^2}M + \frac{11}{6\Delta t}C + K \right) \Delta u = \\ & = F^{n+1} - R^n + \frac{(3u^n - 4u^{n-1} + u^{n-2})M}{\Delta t^2} + \frac{C}{\Delta t} \left(\frac{7}{6}u^n - \frac{3}{2}u^{n-1} + \frac{1}{3}u^{n-2} \right) \end{aligned} \quad (5.2.8)$$

This equation provides an implicit solution scheme. By solving the above for Δu , Eqn. (5.2.1) is obtained, and so obtain v^n and a^n .

5.3. Damping

In a transient dynamic analysis, damping represents the dissipation of energy in the structural system. It also retards the response of the structural system. MARC allows you to enter two types of damping in a transient dynamic analysis: modal damping and Rayleigh damping. Use modal damping for the modal superposition method and Rayleigh damping for the direct integration method. During time integration, the program associates the corresponding damping fraction with each mode. The program bases integration on the usual assumption that the damping matrix of the system is a linear combination of the mass and stiffness matrices, so that damping does not change the modes of the system.

For direct integration damping, the damping matrix, as a linear combination of the mass and stiffness matrices of the system, can be specified and damping coefficients can be given on an element basis.

Numerical damping is used to damp out unwanted high-frequency chatter in the structure. If the time step is decreased (stiffness damping might cause too much damping), use the numerical damping option to make the damping (stiffness) coefficient proportional to the time step. Thus, if the time step decreases, high-frequency response can still be accurately represented. This type of damping is particularly useful in problems where the characteristics of the model and/or the response change strongly during analysis (for example, problems involving opening or closing gaps).

Element damping uses coefficients on the element matrices and is represented by the equation:

$$C = \sum_{i=1}^n \left\{ \alpha_i M_i + \left(\beta_i + \gamma_i \frac{\Delta t}{\pi} \right) K_i \right\} \quad (5.3.1)$$

Where:

C is the global damping matrix

M_i is the mass matrix of i th element

K_i is the stiffness matrix of the i th element

α_i is the mass damping coefficient on the i th element

β_i is the usual stiffness damping coefficient on the i th element

γ_i is the numerical damping coefficient on the i th element

Δt is the time increment

If the same damping coefficients are used throughout the structure, Equation (5.3.1) is equivalent to Rayleigh damping.

The damping coefficients associated with springs (stiffness and numerical damping) and with mass points (mass damping) are zero. The damping on elastic foundations is the same as the damping on the element on which the foundation is applied. For springs, a dashpot can be added for nonlinear analysis.

6. Flying Plate Impact Test Analysis

The theory of stress wave propagation, resulting from the dynamic impact of two bodies, is a very complex issue in general. At low velocity impact the resulting stresses can be below the dynamic material yield strength so that only elastic stress waves are generated. At higher velocities the yield stress can be exceeded and both elastic and inelastic stress waves will be generated. Detailed theoretical formulations are available for unbounded media, (Ref.6.1, Ref.6.2). When dealing with bounded media, the formulation can be extremely complex and impossible to be approached analytically. In this case two basic situations can be analyzed in a simple way: waves of uniaxial stress and uniaxial strain.

The uniaxial stress wave condition is usually obtained for those a geometrical configuration in which target (or projectile) lateral dimension is very small compared with its longitudinal one, as in the case of long rods impacting an infinite target.

The uniaxial strain wave condition is obtained when the target (or projectile) longitudinal dimension is small compared with its lateral one. This is the case of plate impacts. Here the time for propagation of longitudinal stress waves is small compared with the time needed by the longitudinal one resulting in fully constrained deformation field for the region far from the plate ends. This configuration provides pure uniaxial strain loading condition that in real experiments is not subjected to assumptions or approximations providing only the condition of planar impact.

In practical tests one disk with elevated diameter to thickness ratio ($D/h \geq 5$) is shot against another disk, made of the same or different material, with same diameter but higher thickness. The target plate can be either simply supported or clamped. Alignment and impact planarity are critical for the quality and understanding of the material response.

A state of uniaxial strain is defined as:

$$\varepsilon_x \neq 0 \quad \varepsilon_y = \varepsilon_z = \varepsilon_{xy} = \varepsilon_{yz} = \varepsilon_{zx} = 0 \quad (6.1)$$

In order to derive some useful expressions the following hypotheses are made:

I. total strain decomposition:

$$\varepsilon_{ij}^T = \varepsilon_{ij}^e + \varepsilon_{ij}^p \quad (6.2)$$

II. Incompressible plastic flow:

$$\varepsilon_x^p + \varepsilon_y^p + \varepsilon_z^p = 0 \quad (6.3)$$

III. Von Mises (or Tresca) yield criterion:

$$\sigma_{eq} = \sqrt{\frac{3}{2} s_{ij} s_{ij}} \quad i, j = x, y, z \quad (6.4)$$

The Hook law for an elastic isotropic material can be written as follow:

$$\varepsilon_{ij} = \frac{1 + \nu}{E} \sigma_{ij} + \frac{\nu}{E} \sigma_{kk} \delta_{ij} \quad (6.5)$$

imposing the condition in Eqn. (6.1) and solving with respect to σ_x , Eqn (6.5) leads to:

$$\begin{aligned} \sigma_y &= \frac{\nu}{1 - \nu} \sigma_x \\ \sigma_z &= \frac{\nu}{1 - \nu} \sigma_x \end{aligned} \quad (6.6)$$

Since the hydrostatic pressure is given by:

$$p = \frac{\sigma_x + \sigma_y + \sigma_z}{3} \quad (6.7)$$

(defined positive for compressive state of stress), substituting Eqn.(6.6), we get that in the case of uniaxial strain the pressure can be written as:

$$p = \left(\frac{1}{3} \frac{1 + \nu}{1 - \nu} \right) \sigma_x \quad (6.8)$$

While the equivalent yield stress is given by:

$$\sigma_{eq} = \sigma_x \left(1 - \frac{\nu}{1 - \nu} \right) = \sigma_x - \sigma_y = Y_0 \quad (6.9)$$

If the stress amplitude σ_x is less than $Y_0 (1 - \nu)/(1 - 2\nu)$, the hydrostatic pressure is equal to $p \approx 0.62\sigma_x$. If the stress amplitude exceed the yield limit, pressure $p = \sigma_x$ (from Eqn. (6.8), imposing $\nu=0.5$) it follows that under uniaxial strain loading condition the pressure and the longitudinal stress wave, i.e. the one parallel to the impact direction, are coincident.

If Eqn. (6.6) is substituted into Eqn. (6.5), we get:

$$\sigma_x = \frac{E(1 - \nu)}{(1 - 2\nu)(1 + \nu)} \varepsilon_x \quad (6.10)$$

that is the dynamic linear stress-strain law. For analogy with the quasi-static elastic Hook law, the modulus

$$\bar{E} = \frac{E(1-\nu)}{(1-2\nu)(1+\nu)} \quad (6.11)$$

can be take as the dynamic elasticity modulus

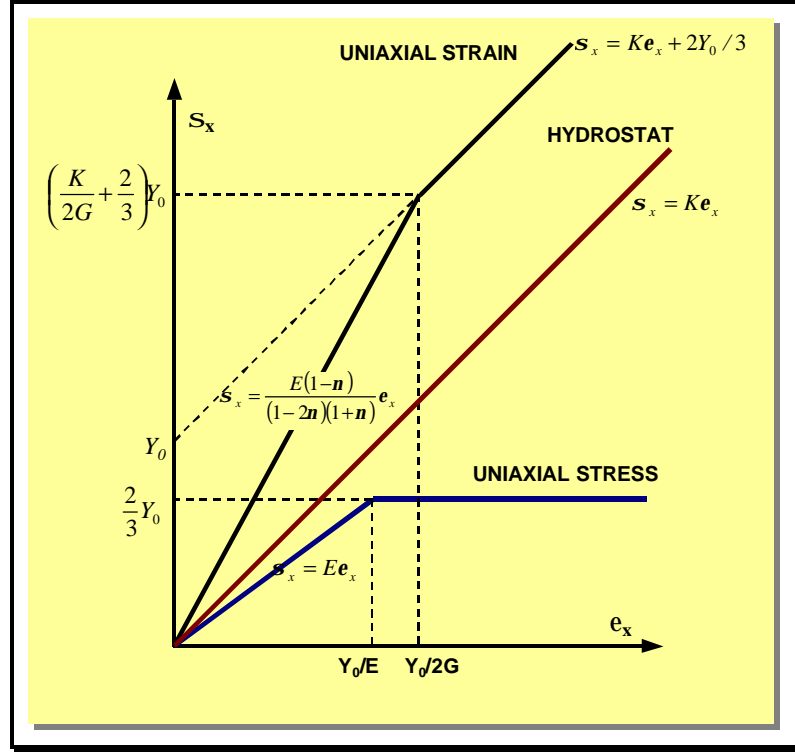


Figure 6.1 - Graphical representation of the relations found for the uniaxial strain condition for an ideally elastic-fully plastic material (no-hardening)

Introducing the bulk modulus, K , and the shear modulus, G , Eqn. (6.10) can be written as:

$$\sigma_x = \left(K + \frac{4}{3}G \right) \varepsilon_x \quad (6.12)$$

where:

$$K = \frac{E}{3(1-2\nu)} \quad (6.13)$$

$$G = \frac{E}{2(1+\nu)}$$

Under uniaxial strain condition the value of σ_x at which the yield criterion is met is commonly indicated has Hugoniot Elastic Limit (HEL) that from Eqn. (6.9) is given as:

$$\sigma_{HEL} = Y_0 \left(\frac{1 - \nu}{1 - 2\nu} \right) = Y_0 \left(\frac{K}{2G} + \frac{2}{3} \right) \quad (6.14)$$

For an ideal elastic-perfectly plastic material, beyond the yield point the stress-strain curve becomes:

$$\sigma_x = K \varepsilon_x + \frac{2}{3} Y_0 \quad (6.15)$$

The relationships for the uniaxial strain conditions are depicted in Figure 6.1.

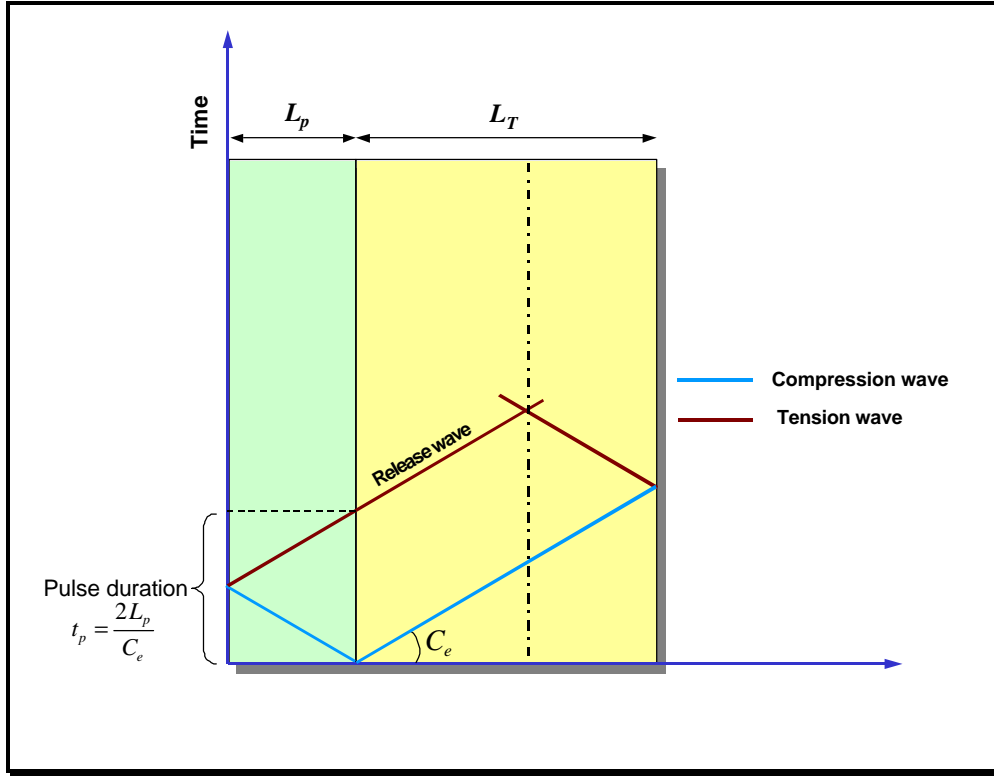


Figure 6.2 - Lagrange diagram for plate impact test

Stress wave structure depends on material constitutive response. Under the assumption of ideally elastic-perfectly plastic material a two-wave structure is generated into the target plate. An elastic wave, usually indicated as elastic precursor, is generated first and starts to travel through the target thickness with a velocity given by:

$$C_e = \sqrt{\frac{K + 4G/3}{\rho}} \quad (6.16)$$

The stress magnitude of this wave depends on the impact velocity and it is bounded up by the HEL. If the impact velocity is strong enough to overcome the HEL, a plastic wave will follow the elastic precursor with a lower velocity given by

$$C_p = \sqrt{\frac{K}{\rho}} \quad (6.17)$$

It has to be noted that elastic stress wave travel faster than plastic wave. The duration of the pulse is directly related to the flying plate thickness as simply shown in the Lagrange diagram reported in Figure 6.2,

$$t_p = \frac{2L_p}{C_e} \quad (6.18)$$

When t_p is reached after impact, separation between the projectile and the target will occur. Pressure induced by the impact is related to the velocity of the flying plate and the velocity transmitted to the target particle. In the case of symmetric impact, that is same material for both target and flyer, the pressure intensity is given by:

$$p = \frac{1}{2} \rho_0 C_e V_0 \quad (6.19)$$

In Figure 6.3 a reference plot of the wave system for symmetric impact, at moderate impact velocity, is given.

Real materials not only show a constitutive response that is far from the elastic-perfectly plastic assumption, i.e. hardening effect cannot be neglected, but also can exhibit a strain rate dependency as discussed in the previous sections. This latter aspect is the most crucial for the modeling purposes. In fact, the material point along the traveling path of the compressive pulse generated during the impact is subjected to a progressive straining that does not occur at constant rate. In Figure 6.4, an example of the uniaxial deformation evolution with time is given. This implies a deformation process that occurs with variable strain rate during the rising (and similarly during the downloading) stress pulse ramp.

The material point at any given time frame behaves as showing a different strength. This results in the concave-up uniaxial stress-strain curve often reported in the literature, Figure 6.5.

It is worth to anticipate here that the concavity of the stress-strain curve in the uniaxial strain condition is obtained in numerical simulations that use strength model with strain rate sensitivity.

Clearly, the capability to reproduce the effective material curve is related to the model capability to account for strain rate effects. In fact, concavity becomes more evident at high pressures, usually so high that the first elastic part of the curve can be neglected.

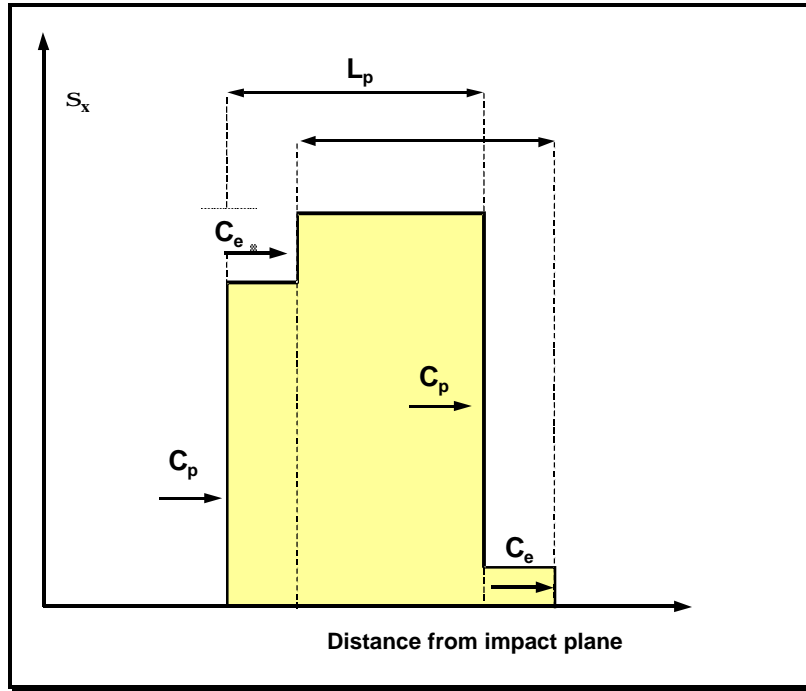


Figure 6.3 - Stress wave system at moderate impact velocity

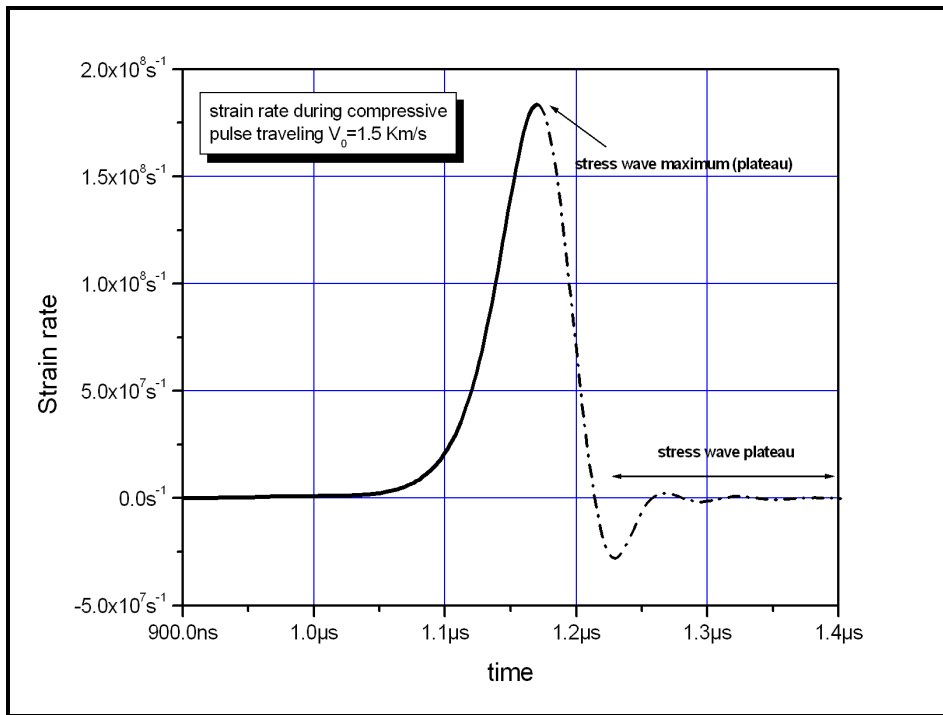


Figure 6.4 - Strain rate variation at the material point when invested by the stress wave: when the stress reaches the plateau strain remain constant and $\dot{\epsilon}$ drops to zero.

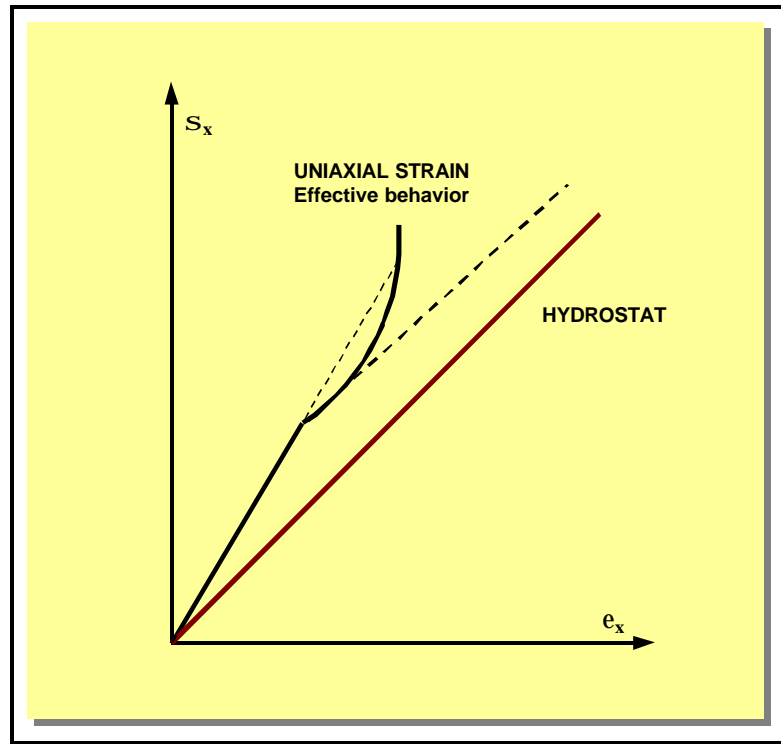


Figure 6.5 - Uniaxial strain stress-strain curve showing concave-up typical behavior

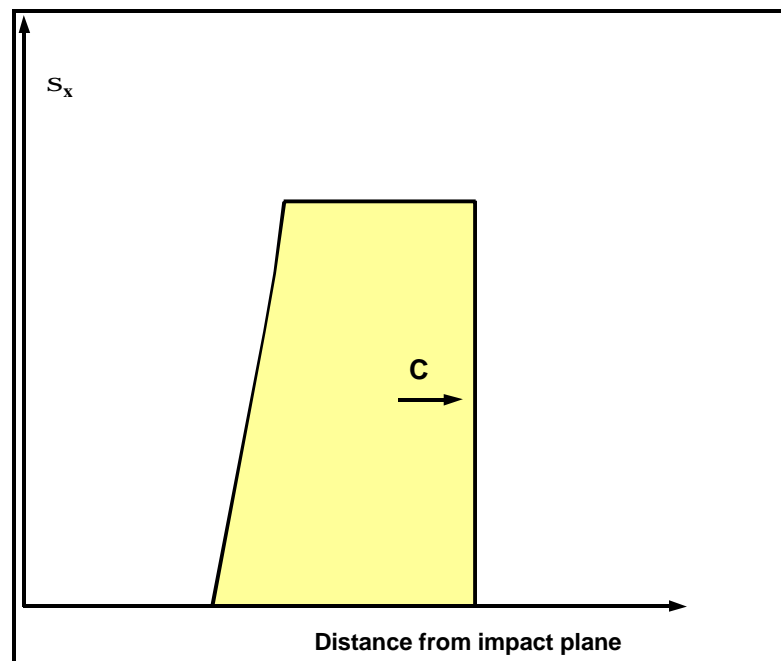


Figure 6.6 - Shock wave profile

One of the major consequences of the material strain rate sensitivity is the possibility to generate shock waves into solids. Here, if the impact velocity is strong enough to

generate an impact pressure several order higher than HEL, a shock wave traveling with a velocity given by

$$C = \sqrt{\frac{\sigma_x / \varepsilon_x}{\rho}}$$

is produced in the material, as depicted in Figure 6.6, without any elastic precursor. Contrarily to elastic waves, shock waves can either strengthen or disperse.

In flying impact test configuration, for a given material, pressure is related to the target velocity as given in Eqn. (6.19). Increasing the impact velocity also the strain rate increases as well. In figure 6.4 the strain rate variation at the material point for an impact at 1.5 Km/s in OHFC copper has been computed. This plot shows a maximum strain rate of the order of 10^8 , already in the velocity range in which the yield strength linearly depends on $\dot{\varepsilon}$, as given in Figure 6.3. In this specific case, the J&C model would underestimate the effective strain rate effect on the strength model since only the $\ln(\dot{\varepsilon})$ dependence of σ_y is accounted in the model.

The main purpose of flying plate impact tests in the experimental practice is the determination of the equation of state for a given material. The equation of state, together with the constitutive relation, is needed to solve the Rankine-Hugoniot relations or jump conditions:

- Mass conservation:

$$\frac{\rho_1}{\rho_0} = \frac{U - u_0}{U - u_1} \quad (6.20)$$

- Momentum conservation

$$\sigma_1 - \sigma_0 = \rho_0 (u_1 - u_0)(U - u_0) \quad (6.21)$$

- Energy conservation

$$E_1 - E_0 = \frac{1}{2}(\sigma_1 + \sigma_0) \left(\frac{1}{\rho_0} - \frac{1}{\rho_1} \right) \quad (6.22)$$

These are three equations function of five variables: density, ρ , stress in the direction of propagation, σ , internal energy, E , wave velocity, U , and particle velocity, u .

The equation of state, also indicated as Hugoniot, can relate U and u or, simply, P and V , as in the equation of state for gas: $PV=RT$.

The role of the equation of state in the computations becomes important for high pressure values at which the material compressibility and the associated temperature

increase are so severe that the material behaves more as a fluid than a solid. In these cases a material state change can also occurs.

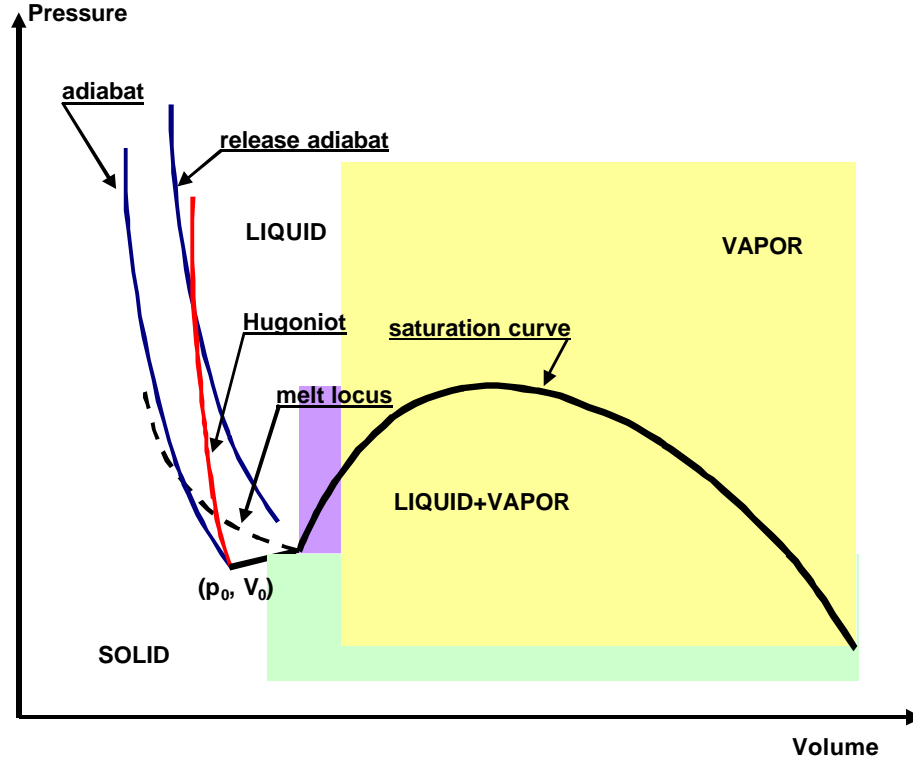


Figure 6.7 - State diagram and Hugoniot representation for solids

The Hugoniot represents the locus of the equilibrium states that can be obtained under uniaxial strain wave conditions. It is important to recall that each flying impact test provides a single point of the Hugoniot and, consequently, several shots at progressively increasing impact velocities are necessary to trace the curve. The representation of the Hugoniot curve, with respect to the adiabat, can be given in a reference diagram of state in which, at least in theory, it should be possible to follow all the material transformation phases, from solid to vapor, Figure 6.7.

From the computational point of view, equations of state can be easily inferred simply decomposing the stress tensor into its deviatoric and volumetric part. To this purpose, the total strain tensor is usually decomposed into the elastic and plastic portions as,

$$\dot{\epsilon}_{ij}^T = \dot{\epsilon}_{ij}^e + \dot{\epsilon}_{ij}^p \quad (6.23)$$

both elastic and plastic strain tensors can be seen as the sum of their respective deviatoric and volumetric portion:

$$\dot{\epsilon}_{ij}^T = \frac{1}{3} \dot{\epsilon}_{kk}^e \delta_{ij} + \dot{\epsilon}_{ij}^e + \frac{1}{3} \dot{\epsilon}_{kk}^p \delta_{ij} + \dot{\pi}_{ij}^p \quad (6.24)$$

where \mathbf{p}_{ij} and \mathbf{e}_{ij} are deviatoric part of the plastic and elastic strain tensor, respectively. Due to plastic strain incompressibility, $\dot{\varepsilon}_{kk}^p$ is zero and (6.24) can be rewritten as:

$$\dot{\varepsilon}_{ij}^T = \frac{1}{3} \dot{\varepsilon}_{kk}^e \delta_{ij} + (\dot{e}_{ij}^e + \dot{\pi}_{ij}^p) = \frac{\dot{V}}{3V} \delta_{ij} + \dot{\varepsilon}_{ij}^{D,T} \quad (6.25)$$

For sake of simplicity let us consider a material in the elastic regime, then the Hook law can be rewritten as:

$$\begin{aligned} \varepsilon_{ij}^e &= \frac{1+\nu}{E} \sigma_{ij} - \frac{\nu}{E} \sigma_{kk} \delta_{ij} = \\ &= \frac{1+\nu}{E} s_{ij} + \frac{\sigma_{kk} \delta_{ij}}{3} \frac{(1-2\nu)}{E} = \\ &= 2Gs_{ij} + \frac{p}{3K} \delta_{ij} \end{aligned} \quad (6.26)$$

where $s_{ij} = \sigma_{ij} - \sigma_{kk} \delta_{ij} / 3$ is the deviatoric stress tensor and p is the volumetric part (hydrostatic pressure).

Combining the right side term of Eqn. (6.25) and (6.26) we get that total deformation can be treated separately as the sum of an hydrostatic pressure tem,

$$\dot{p} = K \frac{\dot{V}}{V_0} = K \dot{\mu} \quad (6.27)$$

that in the classical Von Mises plasticity theory does not provide contribution to strength, and a deviatoric term that accounts for volume distortion and actively contribute to strength calculation. Eqn. (6.27) provides the simplest equation of state already built in the constitutive model. For material under severe dynamic loading condition K become sensitive to pressure. To this purpose appropriate equation of state can be inferred modifying Eqn. (6.27). The identification of the equation of state with flying plate impact tests is performed through the measure of the velocity of the target free surface, opposite to the impact face, as a function of time. The velocity profile provides a direct measure of the particle and shock velocity that can be used to determine the Hugoniot through a number of repeated tests at different impacting velocities, Figure 6.8.

The free surface velocity profile is usually recorded by means of VISAR technique, laser interferometry. A typical response is given in Figure 6.9. Here, the history of the traveling stress pulse in the target plate can be traced back. Point A indicates the arrival of the first elastic wave characterized by low strain amplitude. The subsequent arrival of relatively slow plastic wave are indicated by A'. Here, this point identifies the reaching of HEL. The visualization of the elastic precursor arrival is in the time range of

ns and depends, other than VISAR resolution, on the material internal damping that can smear the signal making the identification of HEL very difficult.

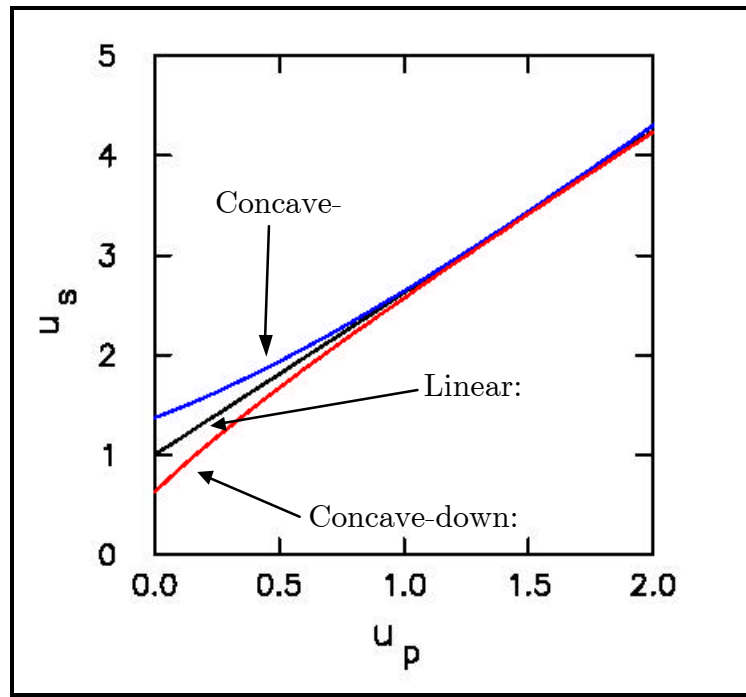


Figure 6.8 - Hugoniot representation on U (u_s , impact velocity) u_p (particle velocity) plot.

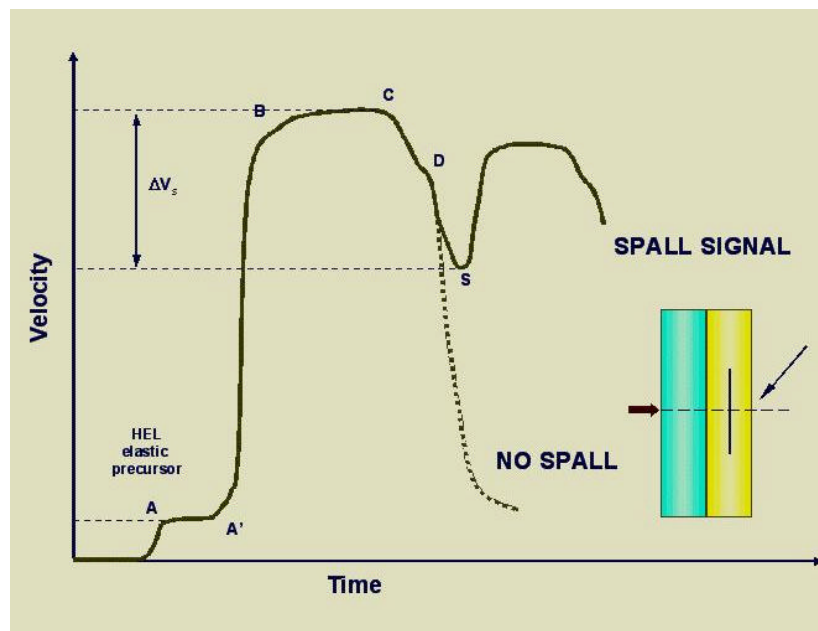


Figure 6.9 - Velocity profile at the free surface of target plate in flying plate impact test showing signal modification due to the occurrence of spall.

When the plastic wave arrives, the velocity at the free surface jumps from A' to B, indicating the arrival of the stress pulse plateau. Then, the velocity remains constant since the stress is constant. In C the stress wave at the free surface and the incident release wave start to combine. Tensile stress wave superposition occurs until point D with consequent reduction of particle velocity. At this point if spall does not occur, i.e. the tensile stress generated by the superposition of both reflected and release wave is not critical, the reflected tensile wave continues to travel backward while the release wave dies at the free surface.

If spall occurs other two compressive waves will be generated at the spall free surface and will start to travel toward both the target surfaces. The stress wave will reach the target free surface at time indicated by S in Figure 6.9. The velocity profile that will follow is indicated as spall signal.

Spall failure is a fracture process that can strongly differ according to the material. If the material is brittle, spall will occur instantaneously forming a clear fracture plane and eventually resulting in fragmentation. On the other hand if the material is ductile, ductile or soft spall will occur. Here, the piling up of the tensile stress, due to the reversed compressive pulse at the free surface and the arriving release wave, activates microvoid nucleation and rapid growth that result in material catastrophic failure. High stress triaxiality, due to the uniaxial strain condition, dramatically reduces the material ductility at the spall plane. Due to material variability, spall occurrence is not an on-off process. As a matter of fact, a range of impact velocity exists in which material can exhibit from incipient spall, i.e. few void growth and coalescence but no plane separation, to intermediate and complete spall, where the complete separation of in the target has occurred.

Since the point S at time t_c indicate the arrival of the spall wave to the free surface, the exact time for spall occurrence can be calculated as:

$$t_s = t_c - \frac{L_t}{C_e} \quad (6.28)$$

An estimation of the pressure at which spall occurs the following expression is traditionally used for engineering purposes:

$$p = \frac{1}{2} \rho_0 C_e \Delta V_s \quad (6.29)$$

It is worth to anticipate here that spall failure occurrence and spall signal simulation are two separate issues. In fact for the first one only a simple failure criterion is needed while for the latter one, an understanding of the physical process associated to the spall plane formation and separation is needed.

6.1. Flying Plate Impact Test Finite Element Simulation

The simulation of flying plate impact test has been performed with the major purpose to verify the effectiveness of the proposed damage model in predicting ductile failure induced by dynamic loading. Parallel to this, the attention has been focused in a systematic verification of the fem model response with the theory illustrated above.

As a first step, the flying plate impact test has been simulated with the finite implicit element code MSC/MARC. Dynamic transient has been solved using Newmark- β integrating algorithm, that is the default procedure used in the result showed here unless stated differently.

Since flying plate impact geometry and loading establish uniaxial strain condition, there is no need to model the entire impacting disks size. At this stage possible influence of the free boundaries is neglected. To this purpose a simple mesh, indicated hereafter as single strip model (SSM) has been developed a follows, see Figure 6.10.

A single strip representative of the plate section along the symmetry axis has been modeled for both target and flying plate. Different element type has been used in order to test element formulation associated effects. If not stated differently, the element used is a four node, isoparametric, arbitrary quadrilateral written for axisymmetric applications. As this element uses bilinear interpolation functions, the strains tend to be constant throughout the element. This element is preferred over higher-order elements when used in a contact analysis. The stiffness of this element is formed using four-point Gaussian integration. For nearly incompressible behavior, including plasticity or creep, constant dilatation method, which eliminates potential element locking, has been used. Updated Lagrangian procedure, together with finite strain and large displacement formulation has been used in all simulations. The SSM height is conditioned by the element size in order to have square element mesh.

Impact between the flyer and the target plate has been modeled through contact algorithm developed in MSC/MARC for both 2D and 3D problem. Both bodies have been considered deformable. This feature can be responsible of inducing some shear deformation in the impacted strip. In order to avoid this problem and to simulate a pure planar impact, the displacement in the impact direction of each upper node has been tied to the one of lower corresponding one. In order to ensure a stable contact between

the two bodies during the impact, a finer vertical mesh for the flyer has been used as given in figures Figure 6.11. To be consistent with the CDM length scale, the mesh size has been taken of the order of 100 μm and time increment has been determined on the basis of the element characteristic time. The initial condition has be set imposing an initial prescribed velocity to the node of the flyer. The material behavior has been modeled, at this stage, using the J&C formulation incorporating in all the simulations

both strain rate and temperature effects. It is assumed that the 90% of the plastic work is converted in heat and, due to the short time duration of the phenomenon, adiabatic conditions have been postulated.

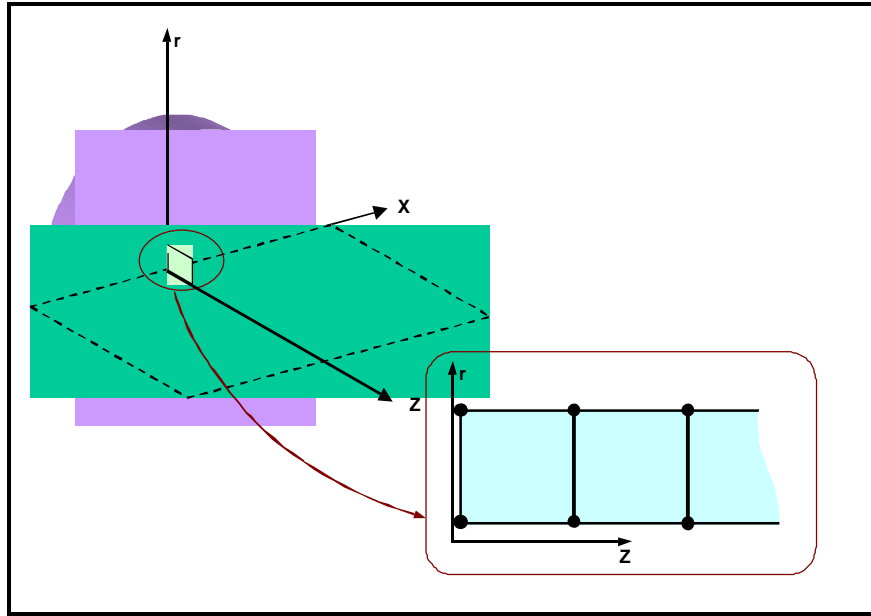
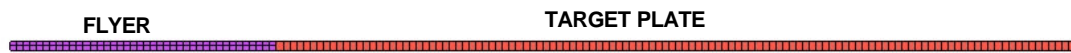
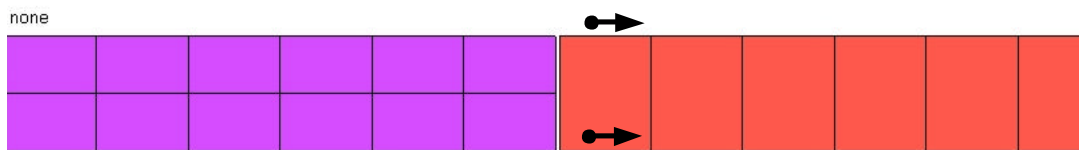


Figure 6.10 - SSM scheme



a)



b)

Figure 6.11 - Finite element mesh for the fine grid SSM and zoomed detail at the impact region

Four materials (copper OHFC, A533B steel, W93 tungsten alloy, and Armco iron), for which experimental spall data were available in the literature, have been investigated.

For those materials for which damage parameters were not available, they have been identified a posteriori matching the velocity profiles. Successively, the effects associated to the impact of plates with different diameters have been also investigated. Here, a parametric study on flyer with different height to diameter ratio has been developed in order to quantify the free boundary effect on rear surface velocity profiles.

6.2. Preliminary Verification and Theory Assessment

Prior to proceed to investigate damage model performance in predicting spalling in flying impact test, fem model assessment has been performed comparing the major problem features with the theoretical solutions. Firstly, the capability to reproduce the stress wave system into the target plate has been checked. In Figure 6.12 and Figure 6.13 the stress profile for a reference OHFC 99.9% pure copper plate with a thickness of 9 mm impacted by a flyer plate 2 mm thick at $V=185$ m/s and 1.5 km/s are shown, respectively. In Figure 6.12 the typical two-wave system is clearly shown. The elastic precursor is visible even though damping smoothes its front. However, both pulse duration and stress wave velocity match the predicted theoretical values. The stress pulse shows an initial oscillatory behavior in the early stage of the impact. At $V_0=185$ m/s, after 1.0 μ s both the numerical damping and the internal damping due to plasticity smoothes the stress wave resulting in a clear sharp stress plateau.

Same behavior is obtained at different velocities. If the velocity range is in the range below 1.0 km/s, there is no need to update the numerical damping that can be taken constant for all calculations.

In Figure 6.13 the possibility to simulate shock wave with the same finite element model is shown. Here, due to the high velocity impact, a larger values of the numerical damping has been used to filter very high frequency signal in the model response and to smooth the stress plateau after 1.0 μ s.

In this latter figure the shock wave is clearly visible showing a sharp pressure front without no elastic precursor or elastic release features. The intensity of the stress pulse obtained is in a very good agreement with the theoretical expected value. At 185 m/s impact, the pressure predicted by Eqn. 6.19 is 3.16 GPa while the fem simulation gives a plateau stress of 3.2 GPa, with an error of 1.2%. Similarly, the uniaxial strain material response has been verified for a generic material point along the stress wave path. In the close up of the elastic-plastic transition is given together with the fitting curve to determine the effective yield strength Y_0 and the dynamic modulus In Figure 6.15.

The reference yield strength for the material is 90 MPa that, according to the J&C model, is increased by strain rate effect at 92 MPa, approximately.

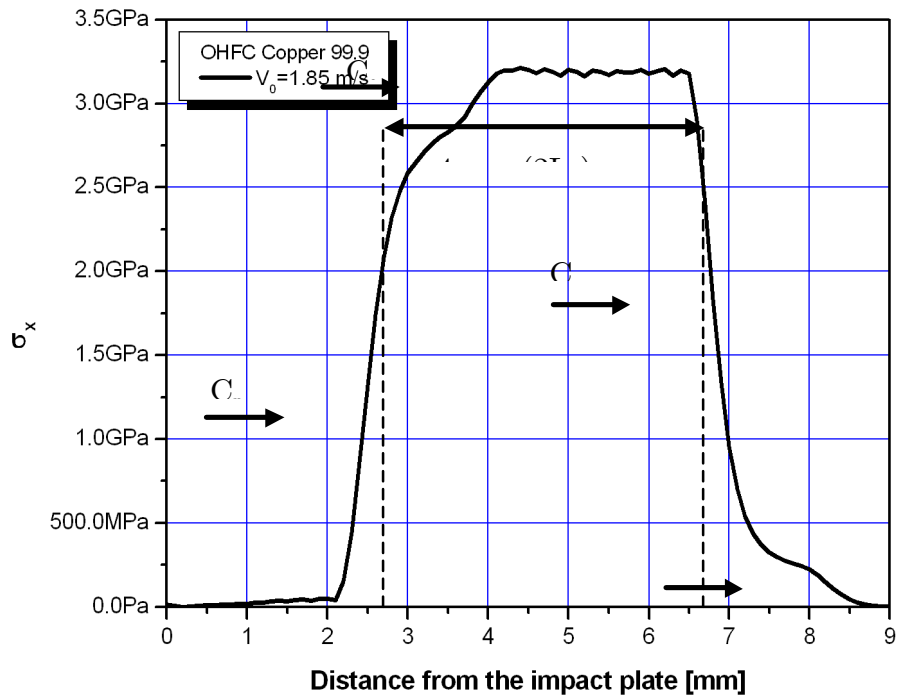


Figure 6.12 - Two stress wave system in moderate impact in copper 99.9 OHFC.

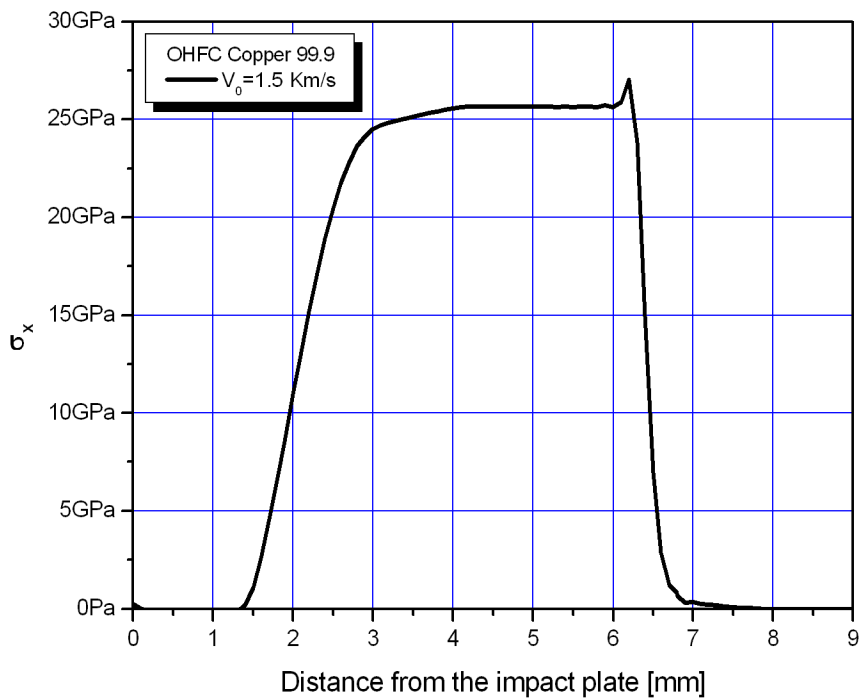


Figure 6.13 - Shock wave in copper 99.9 OHFC.

Figure 6.14 the global stress-strain plot showing both the elastic-plastic transition during loading and the unloading after the stress wave transit is given.

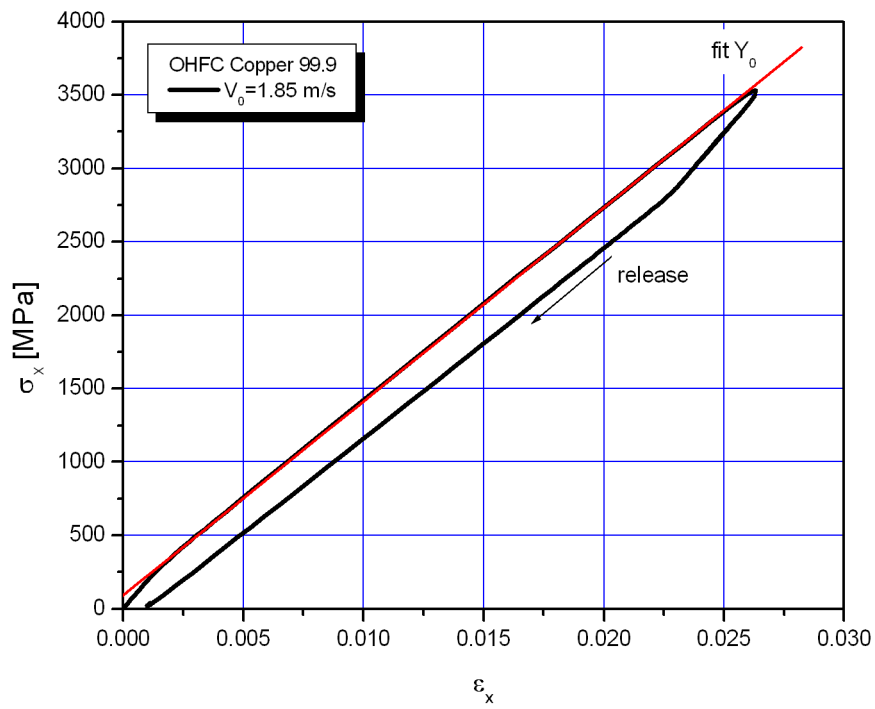


Figure 6.14 - Uniaxial stress-strain response of fem model in copper flying plate impact test at 185 m/s.

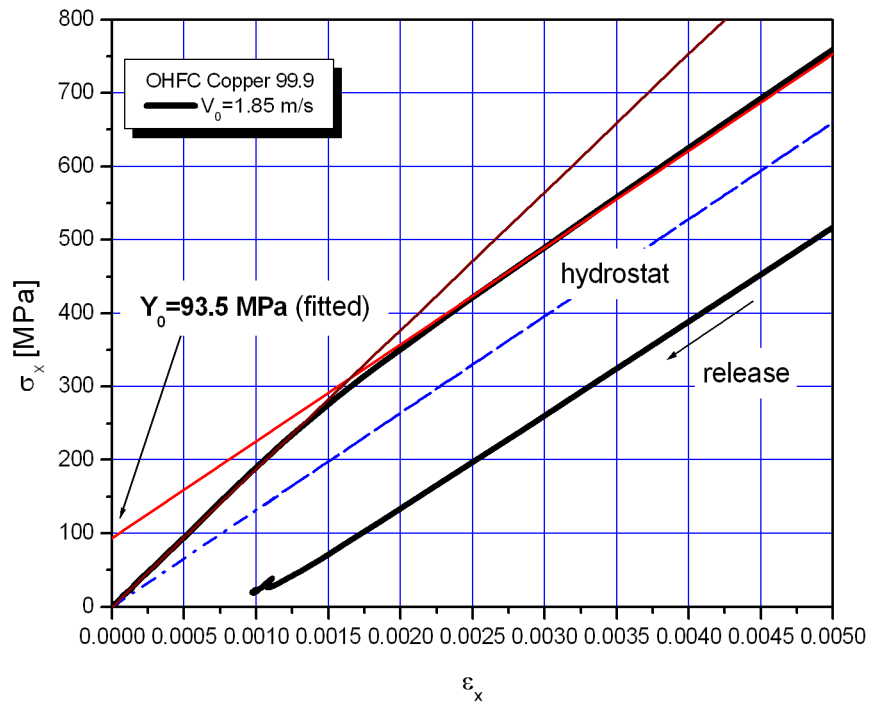


Figure 6.15 - Close up of uniaxial stress-strain response of fem model in copper flying plate impact test at 185 m/s: verification of dynamic yield strength and elasticity modulus

The fit from the data obtained by fem confirms an extrapolated value of 93.5 MPa. Similarly same good agreement with the theory is obtained for the dynamic elasticity modulus. Here, the expected value is 190.858 MPa ($E=125.000$ and $\nu=0.34$) while the extrapolated value from fem data is 188.385 MPa with an error of 0.13%, only.

Concave-up behavior of the stress-strain curve is not visible at this stage since the pressure is of the order the material yield strength and no EOS is used. At higher pressure impact, 25GPa, a slight concavity is found as depicted in Figure 6.16 where both slope of HEL and at high pressure are given.

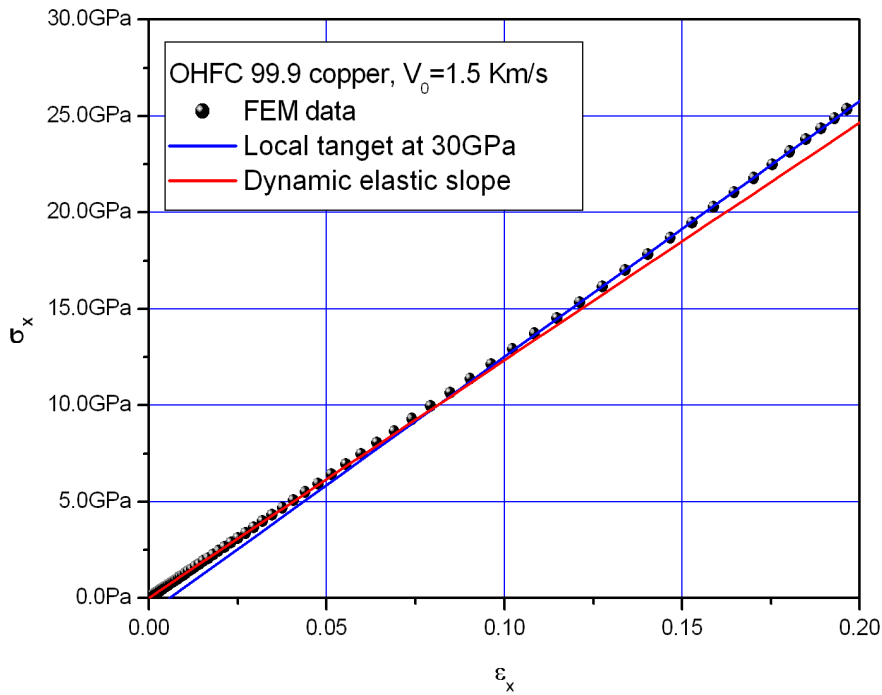


Figure 6.16 - Uniaxial stress-strain curve showing concave up behavior

6.3. Spall Features Assessment

Once verified that the fem model is capable to reproduce all the major features predicted by the theory, spall process has been simulated in the material. The damage calculation, with the model described in the previous sections, has been performed simulating fracture process by element removal technique. When the damage reaches the critical value for the material under investigation, the elastic stiffness matrix is reduced to zero, the element is removed and frozen stresses and strain are released with consequent separation of the mesh. The formation of two free surfaces generates the

stress pulse that will be recorded at the rear target plate free surface as the spall signal. Since failure implies the loss of elements both conservation of mass and momentum laws are violated. For those cases examined in this work it has been found that, since spall plane formation usually does not involve more than 4 elements out of 90 or more elements in the target plate, the loss of mass and associated momentum has been found to be still acceptable. Under planar impact, damage evolution with plastic strain is very limited due to the high stress triaxiality generated under uniaxial strain conditions. Stress triaxiality reduces material ductility close to threshold strain. In this case CDM model results to be similar to critical strain based abrupt failure criteria. The substantial difference is that here failure derives from coupled geometrical and material considerations and does not require post-test calibration procedure.

Parametric Study on Damping and Mesh Effect

Damping plays a critical role in the numerical simulation of dynamic phenomena. Damping is needed in order to simulate the effective material viscosity, the associated effect on the stress wave propagation and to wipe out unwanted high frequency waves that otherwise take place in the finite element mesh. How to model effective material damping is still an open issue. Johnson (Ref. 6.3) has recently published a very interesting study on two possible damping formulations to be implemented in explicit fem code for impact study. In MSC/MARC code the standard damping formulation, as given in the previous section, is available. In the present analysis only the numerical damping has been used ($\alpha=\beta=0$ and $\gamma\neq 0$). Damping effect spatially de-localizes any signal (stress, strain, damage, etc.). As a consequence of this both the elastic precursor and the constant stress pulse plateau are affected. Since this parameter has to be assumed by the user, a parametric study has been performed in order to quantify the effect associated to the choice of the damping factor and to determine, if possible, a good value to be used in all following analyses.

A reference flying plate impact case, where the material is a A533B steel for which material plastic flow curve and damage parameters have been previously determined and verified, has been simulated. Material parameters are summarized in Table 6.1. The work hardening curve at low strain rate (nominally 1.0 sec^{-1} for the Johnson and Cook constitutive law) has been given in the form of power law according to:

$$\sigma = [1 + C \ln(\dot{\epsilon} / \dot{\epsilon}_0)] 400(1 + 56\epsilon_p)^{0.22}$$

In Figure 6.17 the plastic flow curve at different strain rates for the material under investigation is given. In Figure 6.18, the rear free surface velocity signal is given for 4 different damping values ranging from 0.04 to 2.0, for a reference impact velocity of $V_0=300 \text{ m/s}$ at which spall occurs.

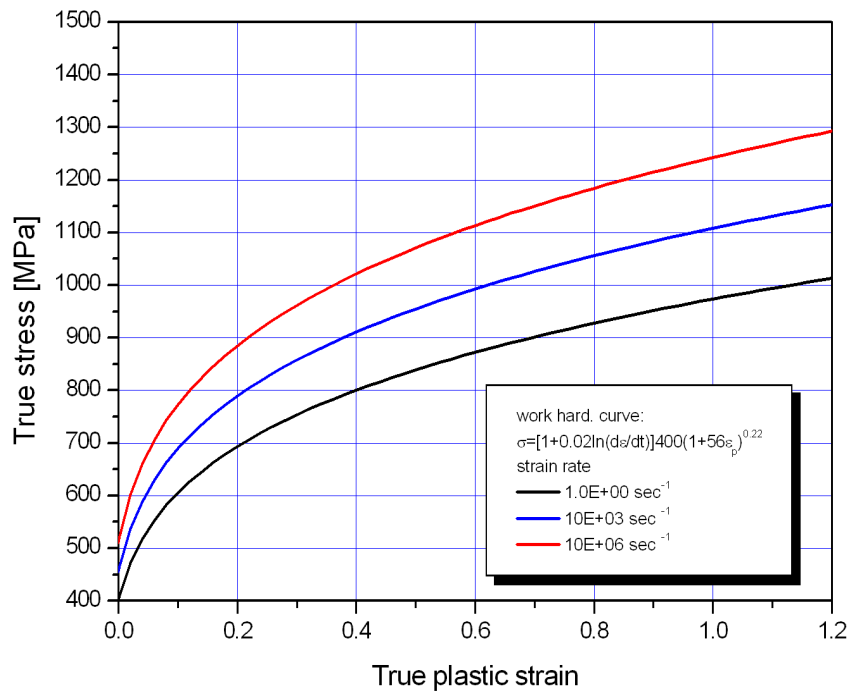


Figure 6.17 - Work hardening data for A533B at low strain rate

Table 6.1 - Material properties for A533B steel

Young modulus [MPa]	Poisson ratio	Yield strength [MPa]	True failure strain
210000	0.3	400	1.3

Damage parameters

ϵ_{th}	ϵ_f	D_{cr}	α
0.0125	1.3	0.75	0.53

With very low damping factor, higher frequency waves are clearly visible in the response resulting in a very blurry velocity plateau. Increasing the damping factor, these disturbances fade away. For larger damping values (>0.8) the amplitude of the spall wave decreases together with a slight shift in frequency.

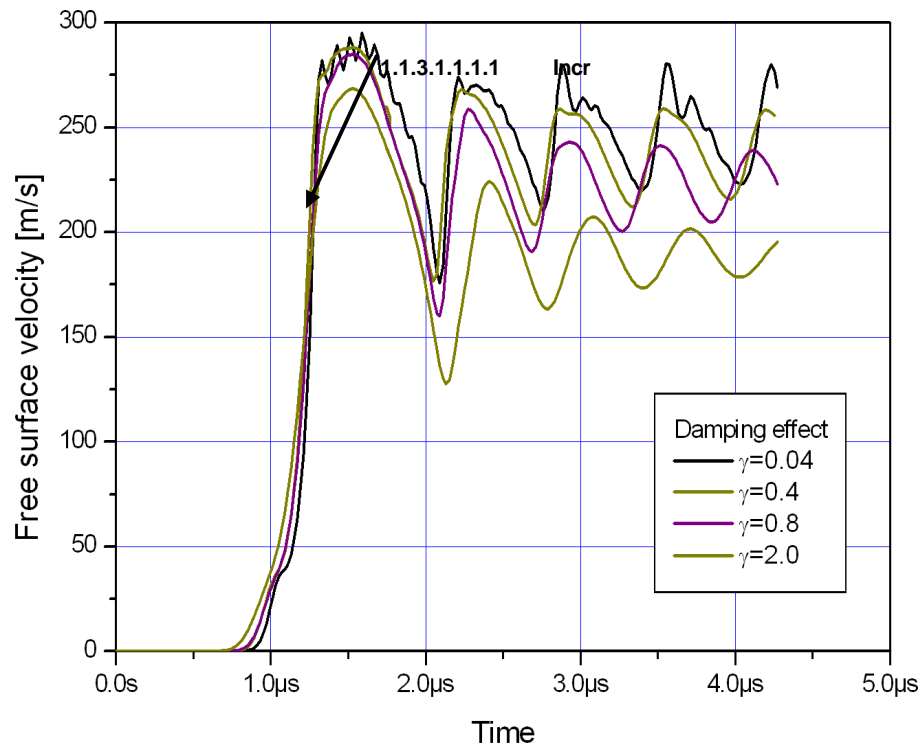


Figure 6.18 - Damping effect on free surface velocity with time

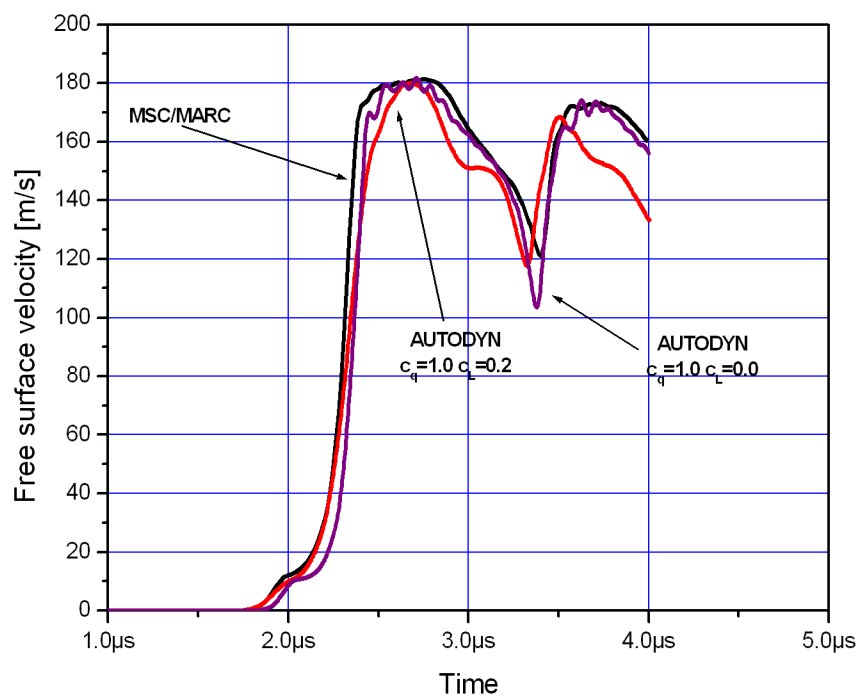


Figure 6.19 - Comparison between damping factor in MARC and AUTODYN

It has been found that, even though the damping is characteristic of the material under investigation, it can be assumed independently of the impact velocity over a reasonable velocity range. The reference value of 0.4 worked pretty fairly for almost all materials investigated in this study. In the simulation performed with AUTODYN it has been found that the suggested initial damping values (for both linear and viscous damping) are too high. In Figure 6.19 the comparison of the predicted free surface signal obtained with MARC and AUTODYN (default damping values) is given together with the experimental results for pure OFHC copper.

Parallel to this, a parametric study on the possible influence of the mesh size and time step has been also performed. The reference mesh size is 100x100 μm as discussed previously. A test case with a mesh size 25x25 μm (four times denser) has been analyzed. In Figure 6.20 and Figure 6.21 the comparison of the stress pulse generated in the target plate together with the free surface velocity profile, is given.

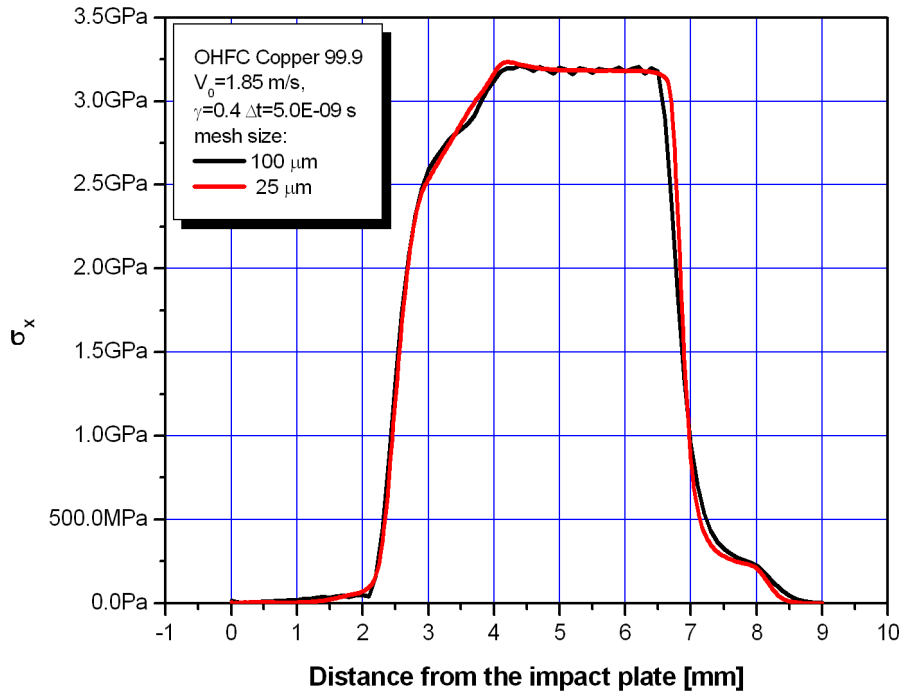


Figure 6.20 - Mesh sensitivity: stress pulse profile

These results show that there are no major effects associated to the mesh size confirming that 100 μm is a scale consistent for both dynamic phenomena and damage process. In Figure 6.21 the time evolution of the traveling pulse for the 25 μm mesh is also given. Here, the stress pulse generated by the impact for three subsequent timeframes is given. It is clearly shown how an accurate spatial discretization is needed together with the time range of interest in order to accurately reproduce the stress wave immediately after impact.

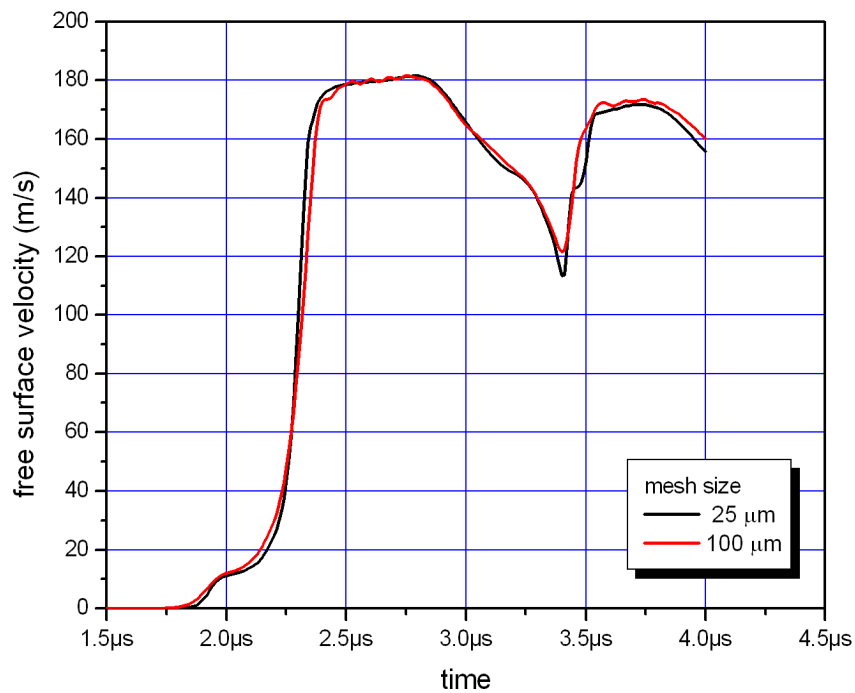


Figure 6.21 - Mesh sensitivity: free velocity profile

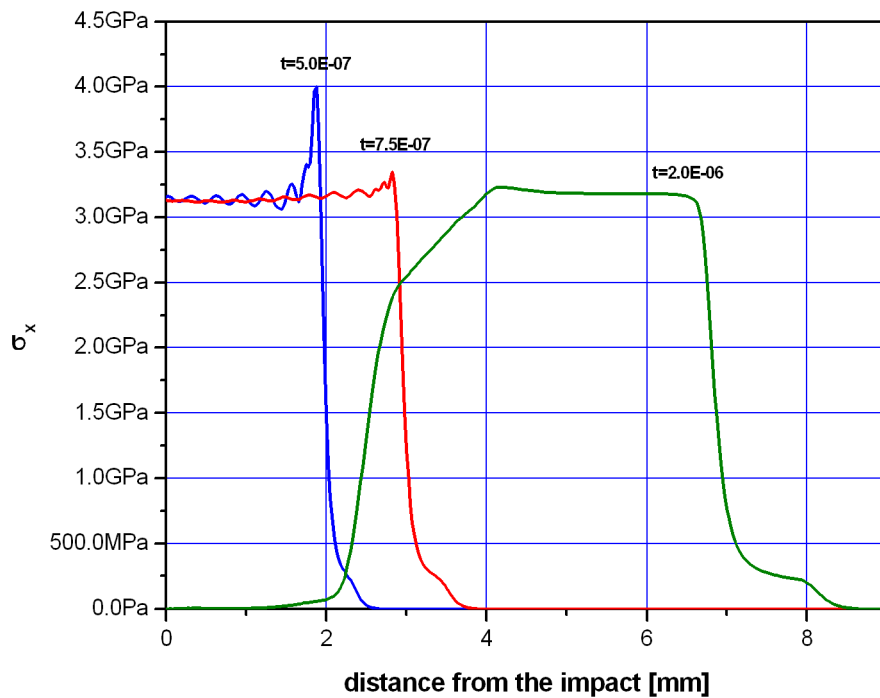


Figure 6.22 - Stress pulse traveling into the target plate: fine mesh

In Figure 6.22, the stress wave profile at $5.0 \cdot 10^{-7}$ s after impact shows behavior similar to shock wave even though no real shock occurs in the material for such velocity impact. This is due to the fact that stress wave has invested few elements only at that given

time. Here, the plastic and the elastic wave are very close since they are just generated in the material. Separation between elastic and plastic wave components becomes more and more visible as time goes on. At the same time, local numerical fluctuations, responsible for the first stress peak, are wiped out by the action of damping. Spall time assessment has been performed comparing time at which spall occurs in the target with those predicted by theory. The results are plotted in Figure 6.23 for A533B steel. Here, black dots indicate the initiation and termination of damage process that result in spall process. In Table 6.2, the values of different predicted spall time at different velocities are given together with the calculated ones. The comparison shows a very good agreement with theory with a relative error below 4%. Once again, it is worth to underline that with the CDM model used here spall time is a result and the user does not infer it. The damage parameter that mostly influences the spall time determination is the damage threshold strain. Failure strain and other damage parameters play a minor role since damage evolution with strain is limited by the severe stress triaxiality due to almost pure hydrostatic state of stress.

Spall Fracture Process

Spall fracture in different metal has been studied and compared, where possible, with experimental data retrieved from the literature. Since flying plate impact test is generally used to build the hughonot, even though several papers report experimental impact test measurements, a limited number of them reports the target rear free surface velocity profile together with detailed material properties description necessary for the numerical simulations. Most of the numerical studies focusing on spall signal and spall prediction very often refer to the same experimental data sets. In these cases, the experimental measurements performed by Curran et al. (Ref. 6.1) and Rajandran (Ref. 6.2) are often used for comparison. Here, together with these experimental results for copper and iron, measurements performed by Dattatraya et al. (Ref. 6.3) on tungsten have been used to verify the CDM model performance and predictions.

Critical time t_c [s]	Impact velocity [m/s]	Numerical predicted spall time t_s [s]	Theoretical predicted spall time t_s [s]	Relative Error [%]
2.0725E-6	300	1.751E-6	1.68582E-6	3.86
2.1525E-6	250	1.7725E-6	1.76582E-6	0.37
2.2125E-6	225	1.8925E-6	1.82582E-6	3.65

Table 6.2 - Predicted and calculated spall time

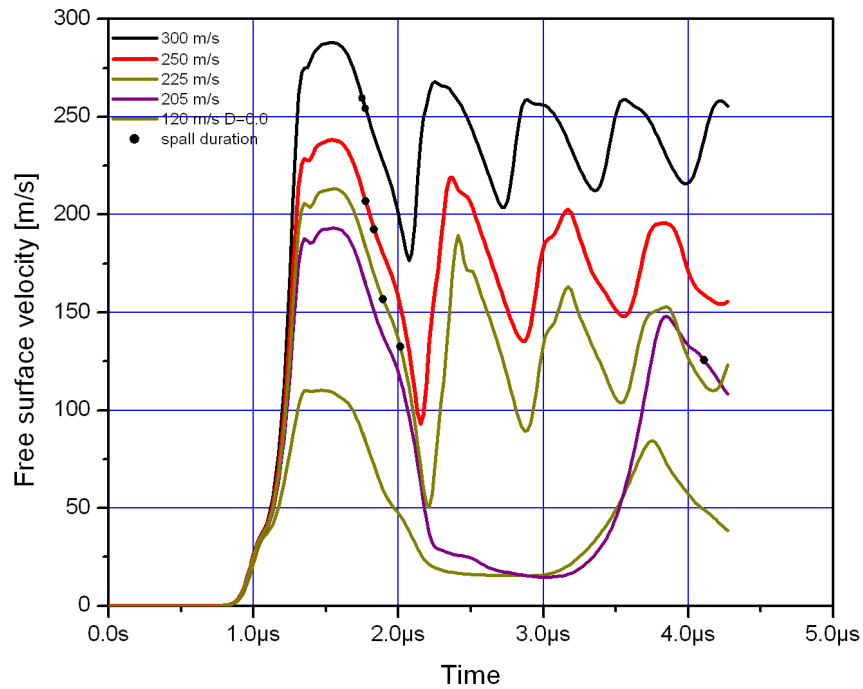


Figure 6.23 - Spall time determination in A533B steel

OHFC 99.9 Copper

Experimental data are taken from Ref. 6.5. Material properties and strength are taken from Ref. 6.4 and are summarized in the following tables. The reference mesh size is $100\ \mu\text{m}$ and the impact velocity is $185\ \text{m/s}$. Flyer and target plate are 2.0 and $9.0\ \text{mm}$ thick, respectively. In Figure 6.24 the velocity profile is given together with experimental data. Here, even though damage parameters approximated values were known for copper, threshold damage strain has been calibrated on t_c . Damping factor $\gamma=0.4$ has been found to give good prediction of the velocity plateau at $180\ \text{m/s}$. The damage parameters are summarized in the following table.

Table 6.3 - Material properties for OFHC copper

Material properties	
Elastic modulus	124 GPa
Poisson ratio	0.34
Shear modulus	46 GPa
Bulk modulus	129 GPa
Density	8960 kg/m ³
Conductivity	389 W/mK
Specific heat, c_p	383 J/kgK
Expansion coef. α	0.00005 K ⁻¹
Melting temperature	1356 K

Table 6.4 - J&C parameters for OFHC copper

J&C parameters	
A	90 MPa
B	292 MPa
C	0.025
M	1.09
N	0.31

Table 6.5 - Damage parameters for OFHC copper

ϵ_{th}	ϵ_f	D_{cr}	α
0.0095	3.2	0.85	0.63

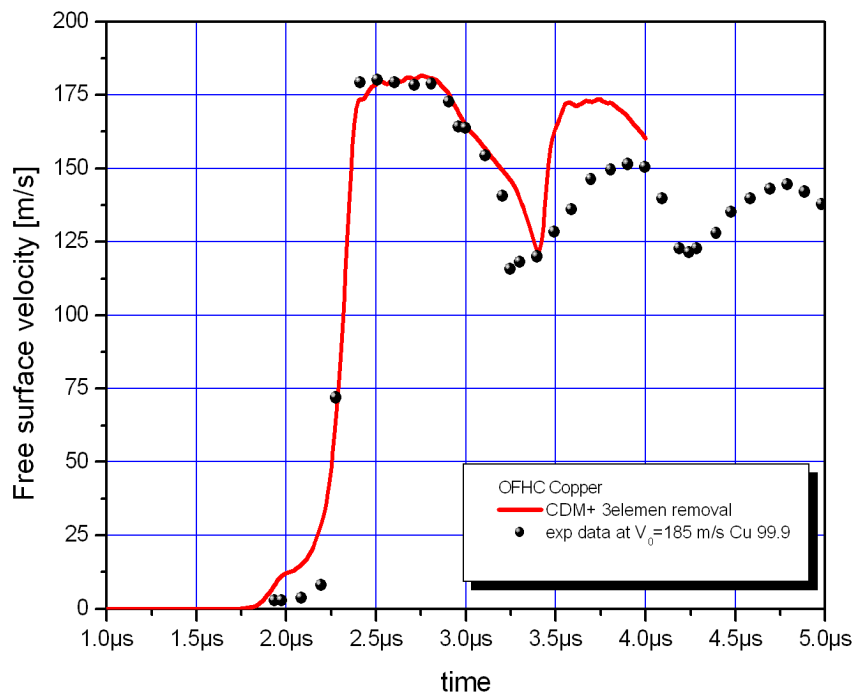


Figure 6.24 - Velocity profile for OFHC copper at 185 m/s

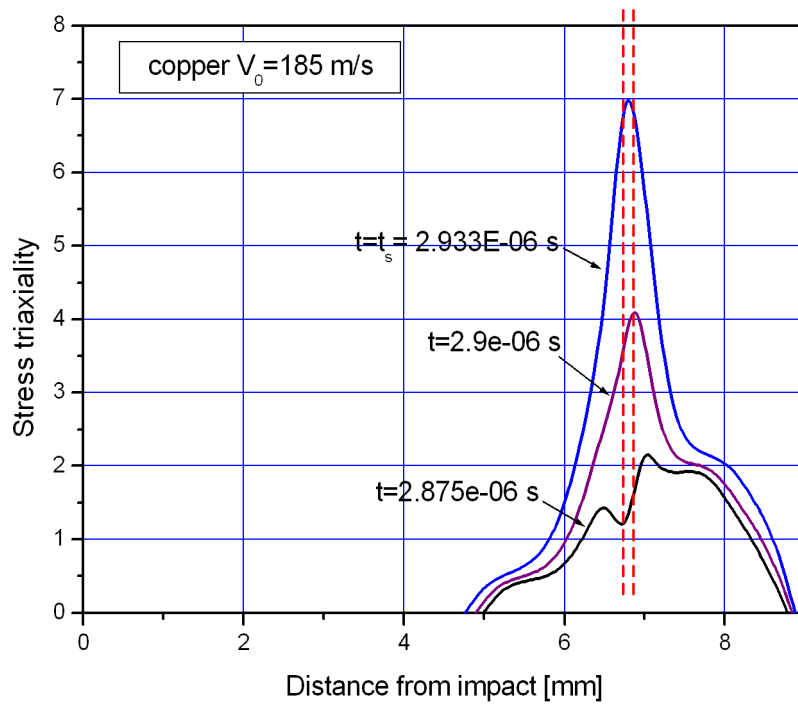


Figure 6.25 - Stress triaxiality evolution with time along target thickness

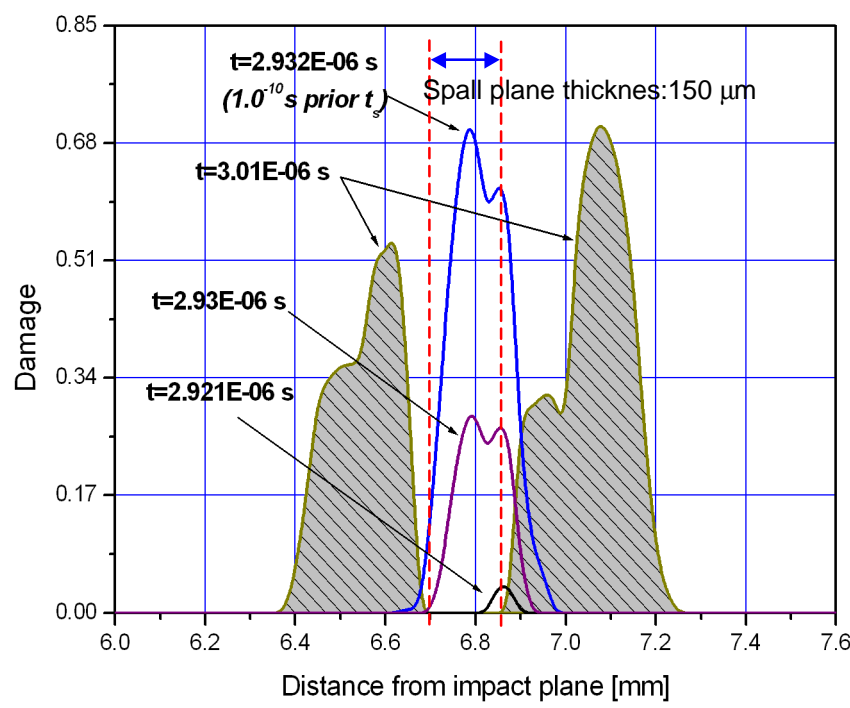


Figure 6.26 - Damage evolution with time along target thickness

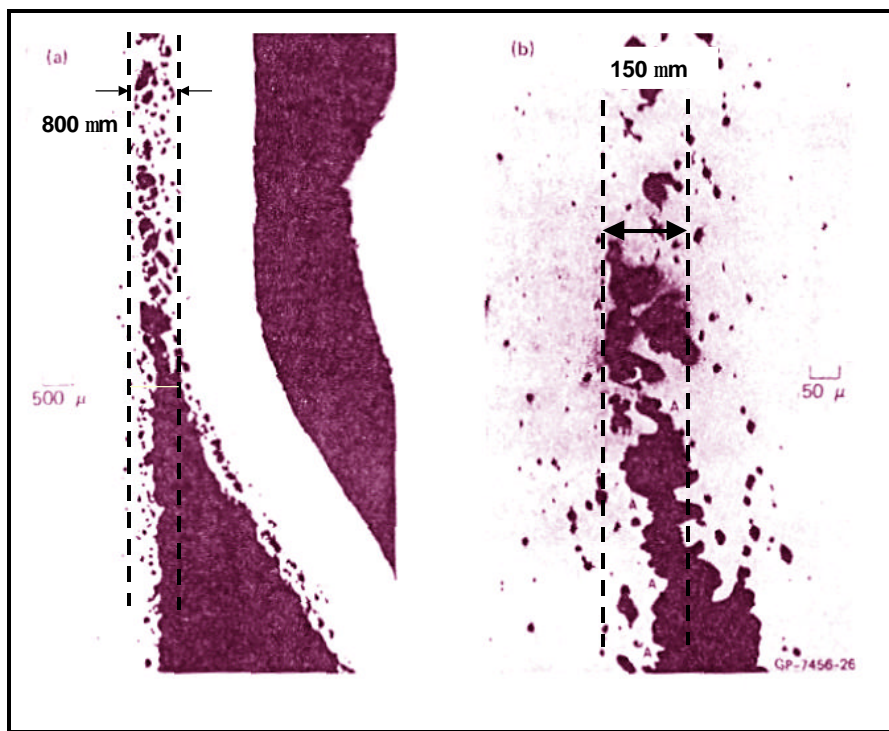


Figure 6.27 - Microvoid distribution at the spall plane in pure aluminum

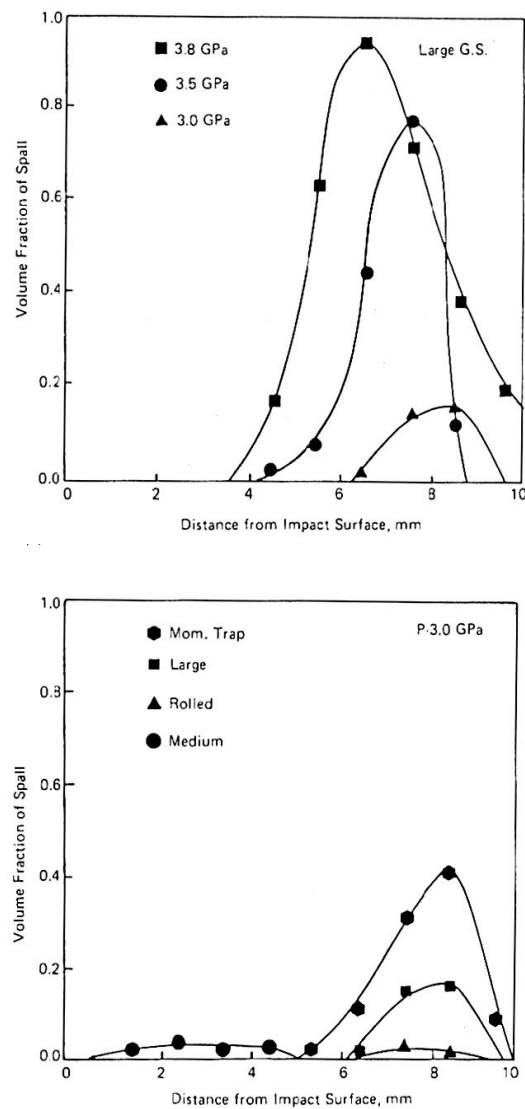


Figure 6.28 - Void volume fraction distributions in copper under different impact pressure.

Stress triaxiality distribution along the target plate thickness, during stress wave travel, is a clear indicator for the location of spall fracture process and gives some clues on the spatial width of spall plane. To this purpose the evolution of stress triaxiality during release wave and reflected stress wave superposition is given in Figure 6.25. It has been found that, even though stress triaxiality values are very high, in general, spall will occur only for those material elements interested by the stress triaxiality peak as indicated in the plot. In Figure 6.26 the correspondent damage evolution is given from the incipient damage formation up to the first point failure. The complete spall formation is given by the damage plot distribution at the end of the element removal process, as given by the shaded area, which indicates the extension of the damaged area where some void growth could be found. A confirmation of this process is found in Ref.

6.4, in Figure 6.27 the picture of the morphology at the spall plane is given. Here, microvoids density rapidly decreasing from the spall plane is clearly visible. Sizes given in the picture are of the same order of the one predicted with CDM model. Similar results have been obtained by Christy et al. (Ref. 6.5) on OFHC copper. In Figure 6.28 the microvoids distribution in terms of volume fraction along the target thickness are given for several impact pressures.

Table 6.6 - Material properties for Armco Iron

Material properties	
Elastic modulus	207 GPa
Poisson ratio	0.29
Shear modulus	80 GPa
Bulk modulus	164 GPa
Density	7890 kg/m ³
Conductivity	73 W/mK
Specific heat, c_p	452 J/kgK
Expansion coef. α	0.000032 K ⁻¹
Melting temperature	1811 K

Table 6.7 - J&C parameters for Armco iron

J&C parameters	
A	175 MPa
B	380 MPa
C	0.06
M	0.55
N	0.32

Armco Iron

The same impact configuration has been simulated in case of Armco iron. Experimental data are taken from Al-Hassani et al. (Ref. 6.6). The material properties are taken from Johnson and Cook and reported in the tables 6.6-6.8.

Based on the reference value for the strain to failure, damage parameters have been identified matching the spall time. Damage parameters used in the simulation for ARMCO iron are summarized in Table 6.8. The test case is relative to a 1.5 mm flyer and 3.0 mm target plate impacted at 500 m/s.

Table 6.8 - Damage parameters for ARMCO iron

ϵ_{th}	ϵ_f	D_{cr}	α
0.02	1.88	0.85	0.53

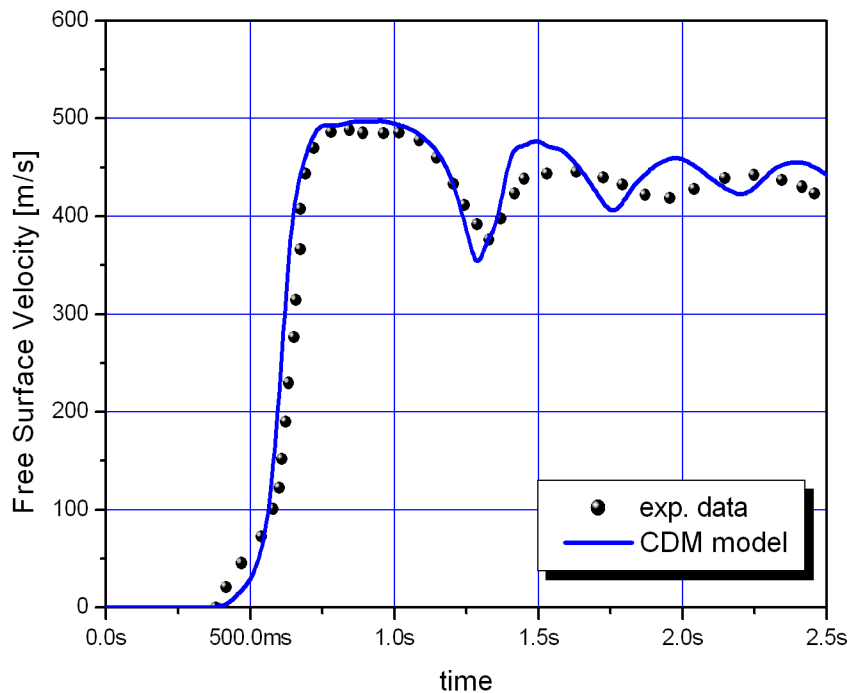


Figure 6.29 - Velocity profile for ARMCO iron at 500 m/s

Tungsten 93W

An extensive experimental study on spall behavior in tungsten alloy can be found in Ref. 6.6. The material properties are not reported in the paper and they have been adapted from reference values given by Johnson and Cook.

Table 6.9 - Material Properties for W93 tungsten alloy

Material properties	
Elastic modulus	476.2 GPa
Poisson ratio	0.28
Density	18260 kg/m ³

Table 6.10 - J&C parameters for W93 tungsten alloy

J&C parameters	
A	100 MPa
B	177 MPa
C	0.016
m	1.0
n	0.12

Table 6.11 - Damage parameters for W93 tungsten alloy

ϵ_{th}	ϵ_f	D_{cr}	α
0.002	0.2	0.18	0.75

The impact case examined is relative to 2.9 mm flyer against 6.1 mm plate at 247.8 m/s and 410 m/s. Results are given in Figure 6.30 and 6.31. Here, damping factor used is $\gamma=0.5$.

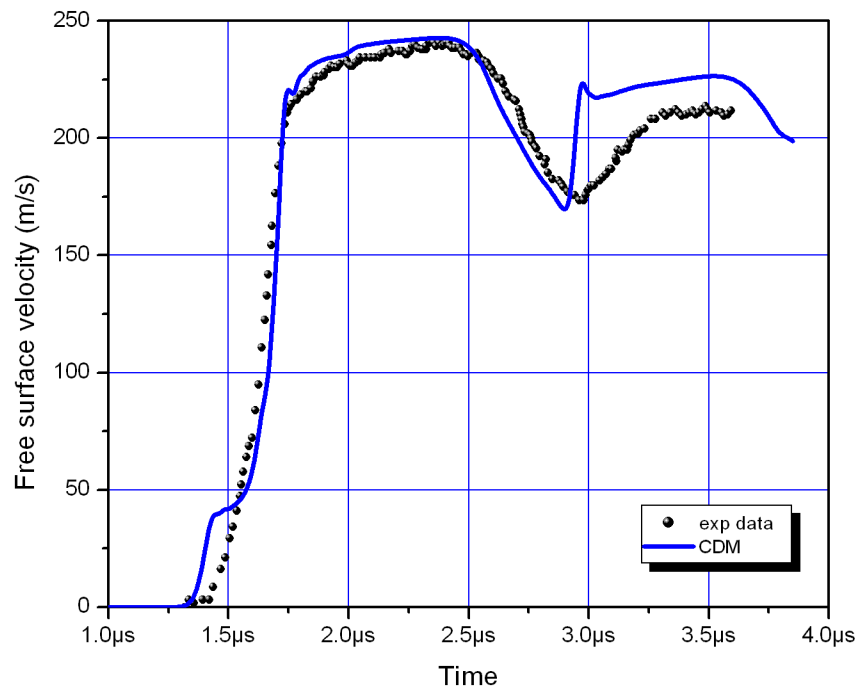


Figure 6.30 - Velocity profile for 93W at 247.8 m/s

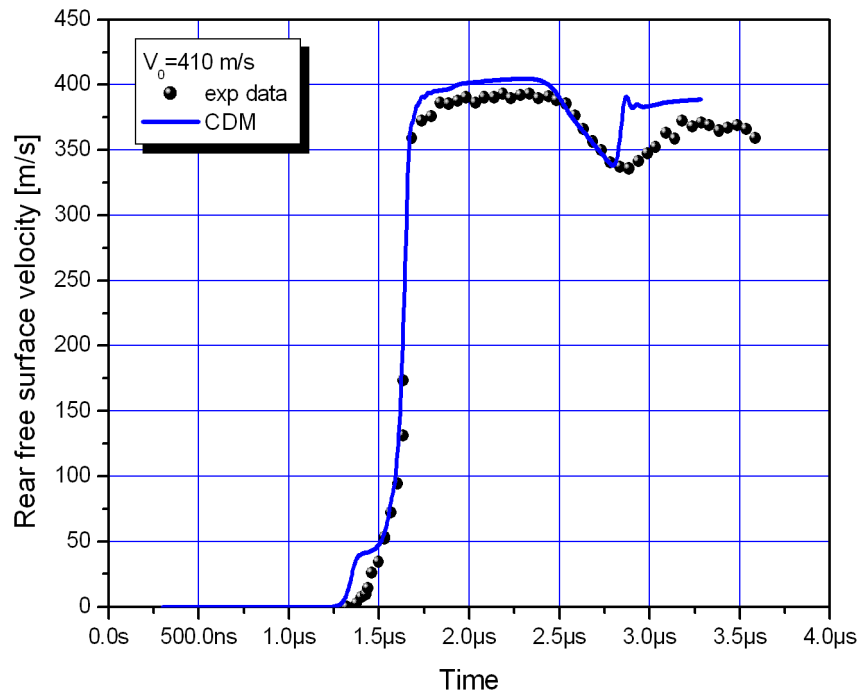


Figure 6.31 - Velocity profile for 93W at 410 m/s

6.4. Spall Signal Analysis

As discussed in the previous section, spall signal is the velocity curve as a function of time measured at the target rear free surface starting from the time at which spall stress wave reaches the free surface. The difference in velocity between the first and the second peak amplitude in the velocity profile is commonly used to define the material spall strength as:

$$\sigma = \frac{1}{2} \rho \Delta v \cdot c \quad (6.4.1)$$

This value defines the conditions for damage nucleation but it does not account exhaustively for additional energy spent in damage evolution, growth of flaw, or spall plane separation. In the numerical simulation performed here, and in similar calculations reported in the literature using different damage models, it has been found that the calculated second velocity peak has a higher slope with respect to the experimental measured signal.

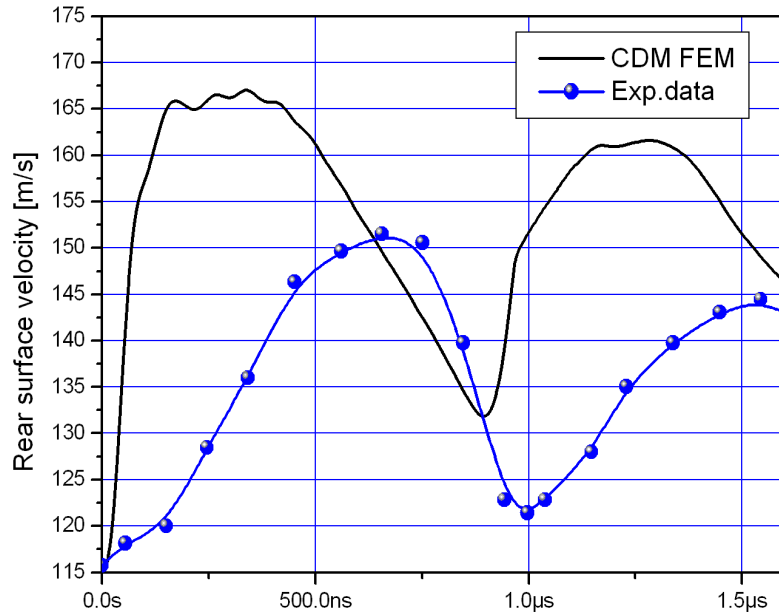


Figure 6.32 - Spall signal comparison for OFHC copper

In Figure 6.32 the calculated spall signal for copper is compared with the experimental measurements. Here, the time scale has been reset to zero for the time of arrival on the free surface of the first spall wave. Since the slope of the curve is a measure of the acceleration at the material point, a lower slope in the spall signal is indicative of a loss of momentum due to irreversible processes. In the literature, matching the spall signal with those from simulations is commonly used to calibrate and verify numerical model predictions. Very often the calculated spall signal is adjusted modifying opportunely the

damping factor. It is opinion of the authors that this approach is incorrect since numerical damping is necessary to get rid of higher frequency disturbances only. Once the damping value has been calibrated, obtaining an appropriate correspondence between the computed and measure first part (i.e. HEL, and velocity plateau) of the rear velocity curve, it has to be kept constant since there are no physical reasons why it would change in the due course of the process. Numerical simulations presented in the previous section, using the proposed CDM models, always show a steeper velocity increases in the spall signal portion even though the plateau and the HEL are accurately predicted. In addition, the maximum velocity of the second peak is always higher than the measured one. Simulations for copper, for instance, show the larger difference between the first and the second velocity peak.

In order to understand the cause of these differences, it has been initially suspected that the steeper increase of velocity just after the spall in the signal could be produced by the element removal technique implemented in the code. As previously described, once the critical damage value is reached over all element Gauss-points this is removed instantaneously and the frozen stress and strain are suddenly released, eventually resulting in a spurious stress wave.

In order to avoid this, an alternative element removal technique has been implemented. Here a progressive or delayed element killing procedure has been developed imposing zero stiffness at failure and removing the failed element in a used prescribed number of increments. Results, not reported here, showed no difference in the spall signal with respect to the sudden death element removal technique indicating that the observed differences should be due to different phenomenon.

At this point, it has been thought that an additional dissipative process in the separation of the surfaces at the spall plane could be the cause of the discrepancies between the computed and experimental signal.

From a physical point of view, the separation between the spall plane faces should occur differently according to the material microstructure and its fracture mode. For instance, even though microvoids develops in both in copper and pure aluminum during plastic deformation, the coalescence process can be considerably different. In the case of pure aluminum, complete separation due to coalescence occurs by voids ligament sheeting. This failure mode is substantially "brittle" in the sense that it requires low strain energy. In copper, similar voids as for aluminum, would coalesce by inter-void ligament necking that is a more "ductile" process requiring larger energy amount. In Figure 6.33 a schematic plot of both mechanisms is given.

Since the formation of the spall plane is analogous to the formation of a ductile crack in the material, using fracture mechanics concepts it is possible to estimate the work required to generate two free surfaces and to compare it with the amount of surplus energy in the calculated spall signal, responsible of higher secondary velocity peak.

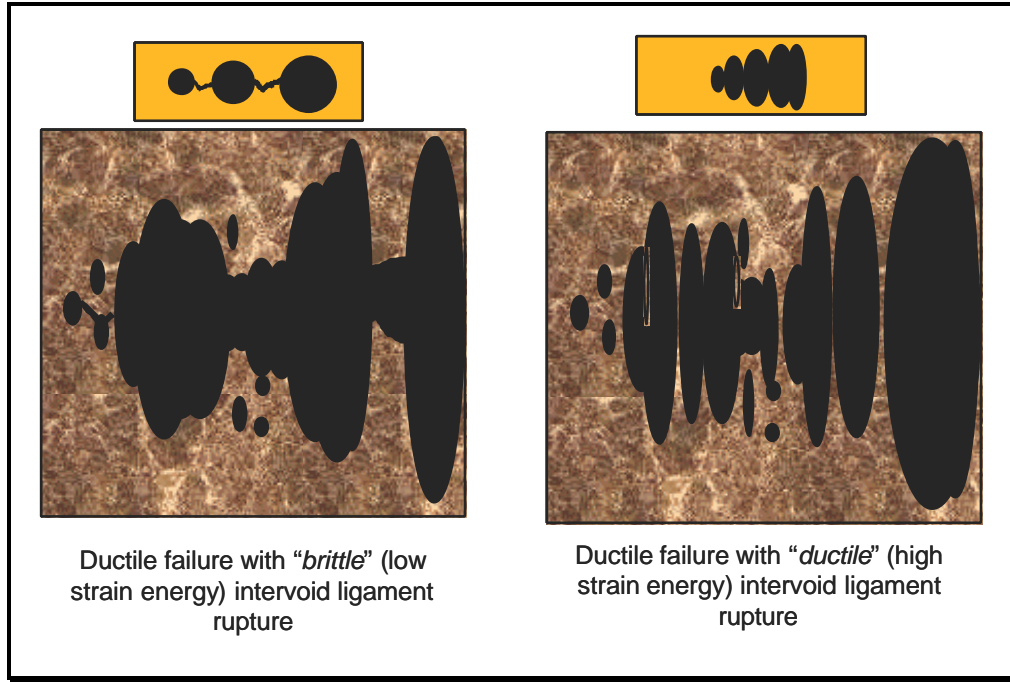


Figure 6.33 - Different secondary separation mechanisms for spall plane faces

From Griffith theory, the energy required to generate two free surfaces in a material is given by:

$$G = 2\Gamma \quad (6.4.2)$$

where Γ is the total free surface energy comprehensive of both elastic and plastic contributions. The strain energy release rate G can be directly related to the material fracture toughness, K_{Ic} , that even though is a pure linear-elastic concept, can still be taken as a reference value since plastic deformation along the spall plane is usually very contained in absolute value and confined to a thin layer across the separation, plane. Thus it follows:

$$\Gamma = \frac{1}{2}\alpha \frac{K_{Ic}^2}{E} \quad (6.4.3)$$

Since $K_{Ic} = 60 \text{ MPa} \sqrt{m}$ is a reasonable value for copper, assuming pure plane strain conditions $\alpha = (1-\nu^2)$ and recalling that there is a factor of 2π due to axial-symmetry, we finally get $\Gamma \simeq 2000 \text{ J/m}^2$, approximately, that is the energy amount dissipated due to the formation of new surface energy in copper.

The comparison of calculated and experimental spall signal as a function of time can be used to estimate the excess in kinetic energy that numerical simulation is not spent in other dissipative process such as new surface formation. As a matter of fact, it is

possible to subtract to the calculated velocity, at each time instant, the experimental correspondent value. The resulting plot as a function of time given the difference velocity evolution for which the mean square root value can be defined as follows:

$$\Delta v_{eff} = \sqrt{\frac{1}{T} \int_0^T [v_{fem}(t) - v_{exp}(t)]^2 dt} \quad (6.4.4)$$

The surplus of kinetic work per unit surface can be then calculated as follows:

$$\frac{\Delta W}{\Delta S} = \frac{1}{2} \rho \Delta v_{eff}^2 h_f \left(1 - \frac{h_f}{h_t} \right) = 3842 \frac{J}{m^2} \quad (6.4.5)$$

where h_f and h_t are the flyer and target thickness respectively. Dividing by a factor of 2 the result of Eqn.(6.4.5) due to the two formed surfaces, we get the calculated value for Γ , i.e 1921 J/m², which is in a very good agreement with the value estimated with fracture mechanics concepts.

It has to be noted that similar behavior would also be expected for Armco iron that is substantially pure ductile material. On the contrary differences between the first and the second peak velocity are much less pronounced than for copper. This can be explained in a stronger strain rate material sensitivity that under dynamic loading fails in a brittle manner at least for pressure lower than 13 GPa at which transformation phase occurs.

A verification of this has been performed implementing the tractions dissipation mechanism in the finite element simulation. This has been done adding a couple of non-linear springs in the one dimensional SSM. Spring stiffness is progressively reduced to zero with the increasing spall plane separation distance. When the critical opening u_0 is exceeded the separation force becomes zero. In order to avoid arbitrary choice of the force-displacement law, an expression similar to the crystalline plane bond has been assumed in the following form:

$$f = K \sin \left(\pi \left(\frac{u}{u_0} \right)^\alpha \right) \exp \left(- \left(\frac{u}{u_0} \right)^m \right) \quad (6.4.6)$$

where K is the amplitude, u_0 is the maximum separation gap at which the traction goes to zero, α is the shape exponent. The exponential term has the role to keep zero the traction for separation values higher than u_0 and in a user subroutine can eventually be omitted and replaced by an IF instruction. In any case a choice of $m=10$ or higher is good enough. Thus, the choice of u_0 , α and K is performed imposing that the area below the curve is equal to the dissipated separation work. The calculated new spall signal for copper is given in Figure 6.36. It is important to note that the action of the non linear spring in the early stage of spall faces separation has an effect on the following evolution of the entire spall signal in both amplitude and phase.

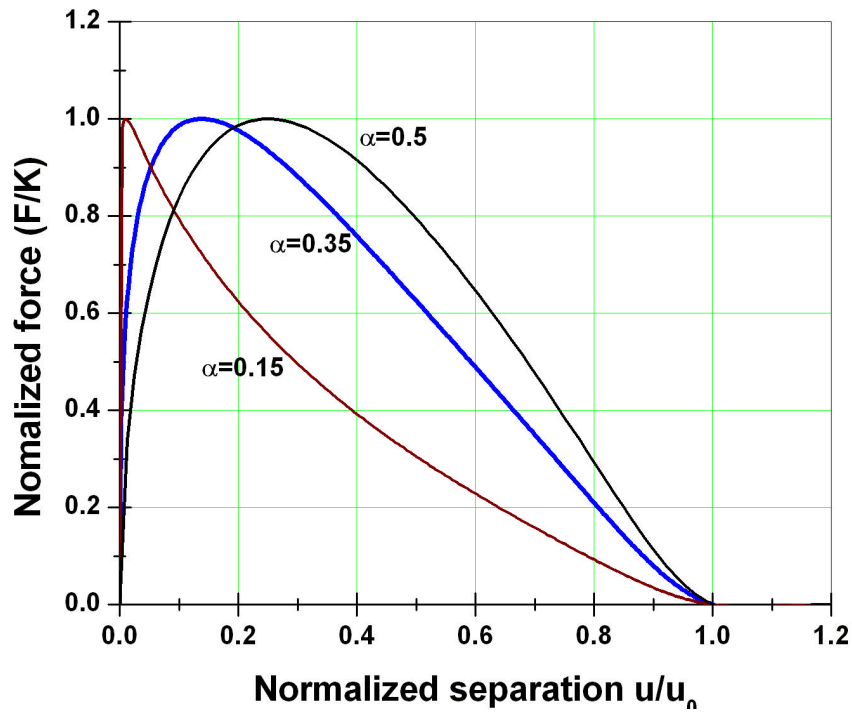


Figure 6.34- Shape effect on the non-linear spring response for tractions across spall separation plane

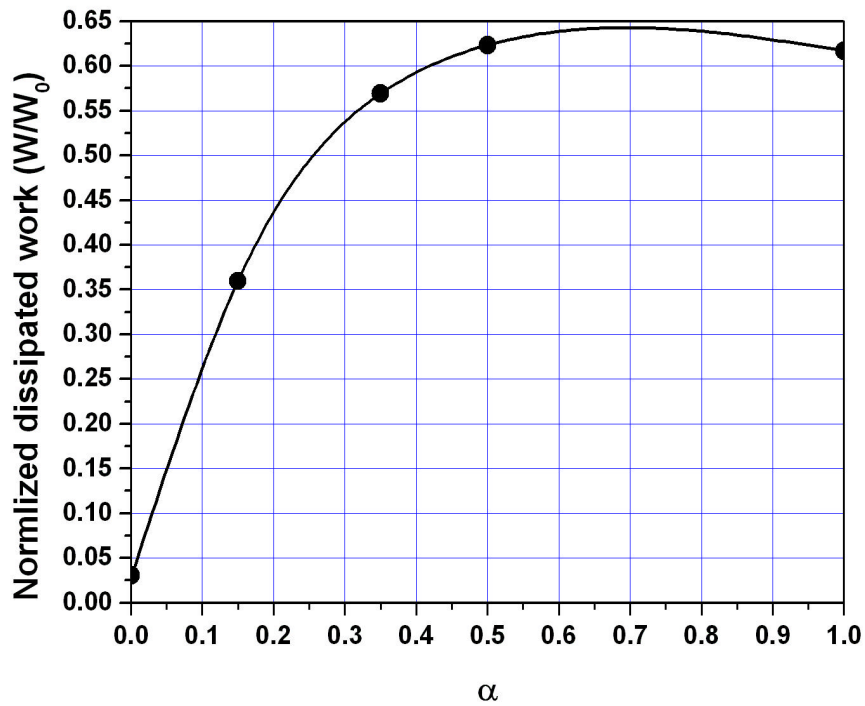


Figure 6.35- Evolution of the normalized area associated to the force-displacement diagram for different choices of **a**.

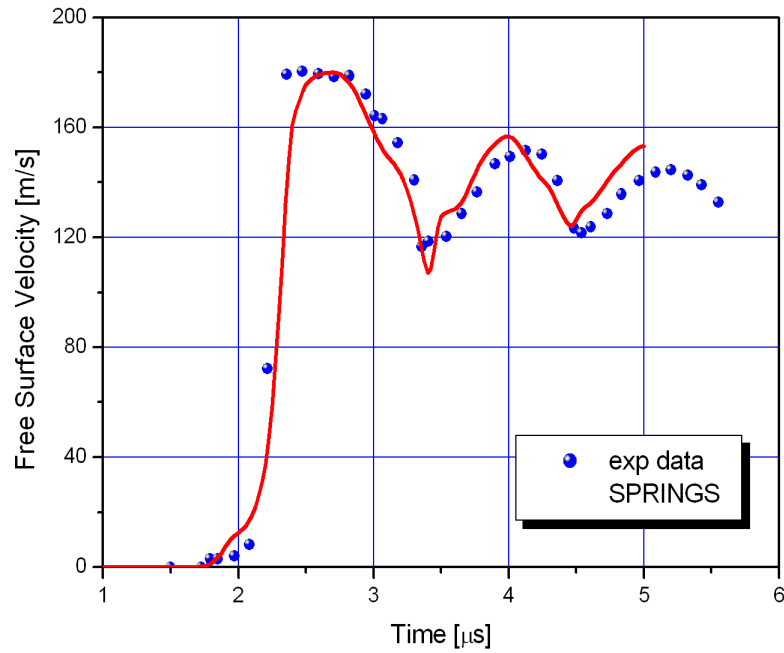


Figure 6.36 - Spring element simulations for dissipation in spall plane separation

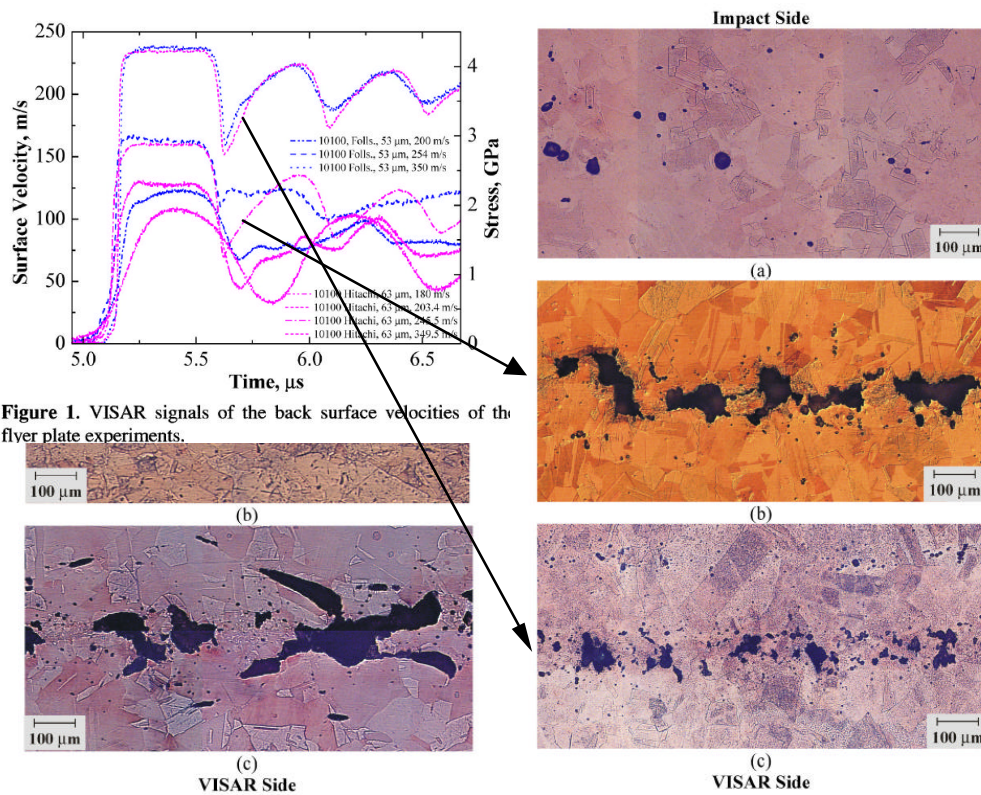


Figure 1. VISAR signals of the back surface velocities of the flyer plate experiments.

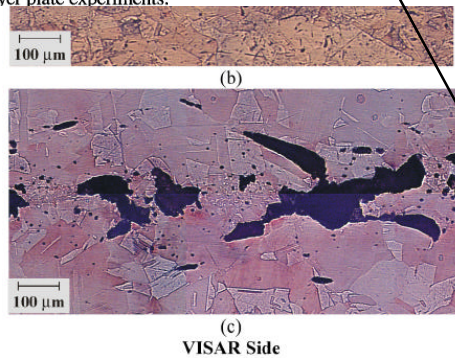


Figure 2. Optical micrographs of the region of spallation in the Follansbee plate samples. (a) 2.26 GPa, (b) 2.86 GPa, (c) 4.28 GPa.

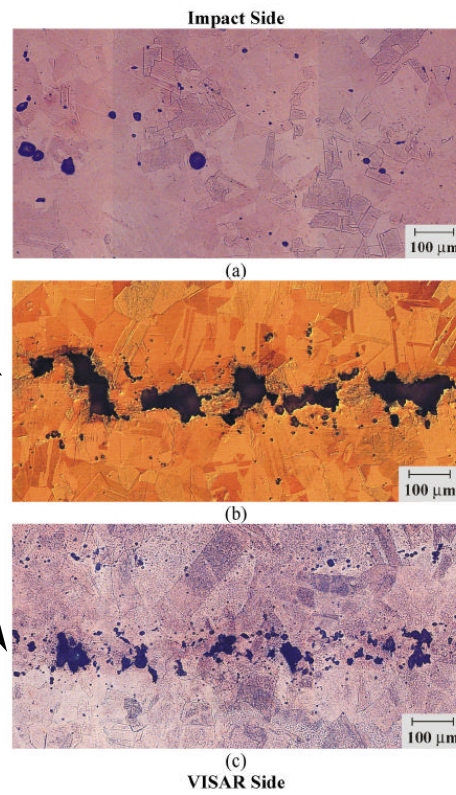


Figure 3. Optical micrographs of the Hitachi plate impact tests. (a) 2.27 GPa, (b) 2.88 GPa, and (c) 4.23 GPa.

In Figure 6.35, the resulting force-displacement diagram for the non linear spring, for reference as a function of the shape parameter α , is given. In Figure 6.34 the evolution of the normalized dissipated work associated to the choice of the α parameter is also given. More recently, Thissel et al. (Rif. 6.13) investigated the effect of material cleanness in copper on the spall response. The reported microscopy investigation of the features of the fracture surface along the spall plane, reported above, seems to confirm the proposed mechanism described in Figure 6.33.

6.5. Geometric Effects on Spall Fracture Initiation and Propagation

In experimental testing and simulation of flying plate impact test a very little attention is usually given to the possible effect induced by the free boundaries of both flying and target plate. It is common assumed that, in order to generate planar impact, plate diameter has to be large with respect to thickness and that, as a result of axial-symmetry, spall fracture would occur along the symmetry axis first. Additionally, it is implicit, and regularly not expressed, that for the flyer and the target plates with same diameters, planar impact would occur under perfectly aligned conditions.

A very little attention has been given in the literature to the effect, on stress wave propagation and spall occurrence in flying plate tests, associated to the impact of disks with different diameters. Nemes and Eftis (Ref. 6.7, Ref. 6.8) simulated the planar impact of disks with different diameters pointing the attention to the variation of the stress states induced by the flyer free edge. Analogous study can be found in Ref. 6.9.

Here, an extensive study on planar impacts with different size disks has been performed using both MSC/MARC finite element and AUTODYN lagrangian code. The aim of the work is to understand stress wave propagation and interaction due to free boundaries; to try to identify possible criteria to predict spall plane initiation and its location; to define, if possible, limit conditions and validity dimensional range for planar impact and to correlate spall signal modification with fracture modes.

The study has been performed starting from the reference impact configuration of flyer and target plate with same diameter (64 mm) and 2 and 9 mm thickness, respectively. Successively, a parametric study has been performed keeping constant the target plate dimensions and flyer thickness, and progressively reducing its diameter. Several flyer diameter thickness ratios ($D/h=32, 16, 8, 4, 2$, and 1) have been investigated as sketched in Figure 6.37.

All simulations have been performed for a reference impact velocity of 185 m/s and in symmetric impact condition (same material for both flyer and target). The material used in this study is OFHC copper 99.9%. As in the previous sections, the strength model is given in the form of J&C formulation. The damage model has been used in the simulations performed with finite element code MSC/MARC while a maximum pressure criterion has been used in the simulation performed with AUTODYN.

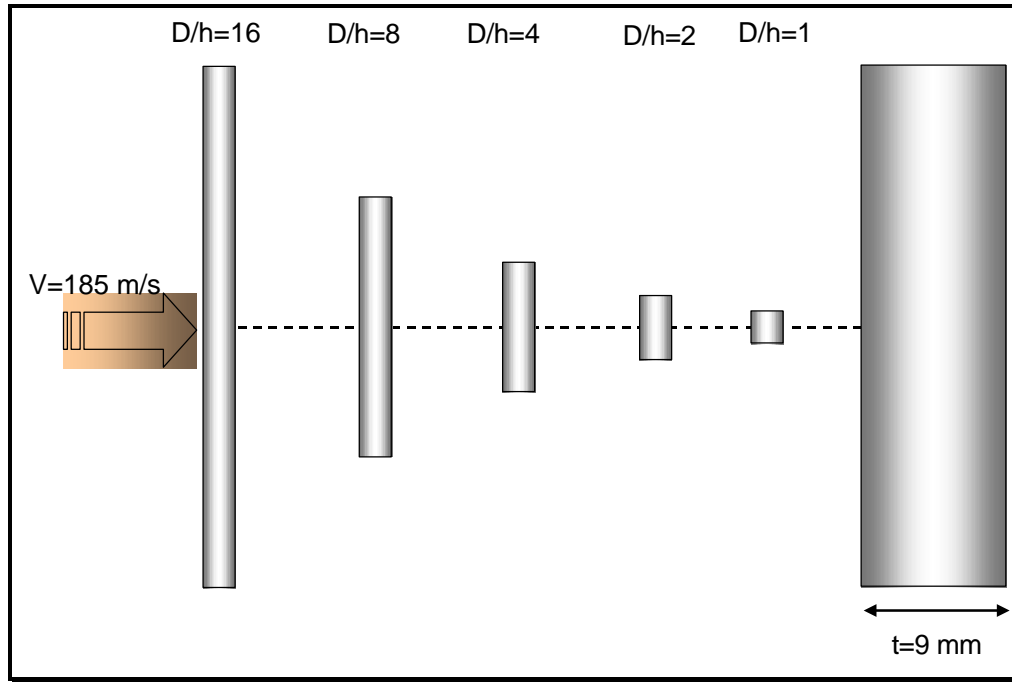
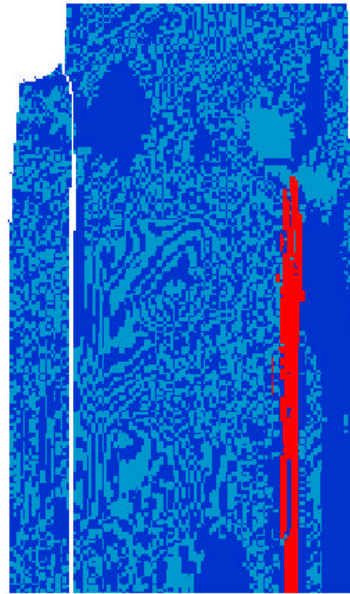


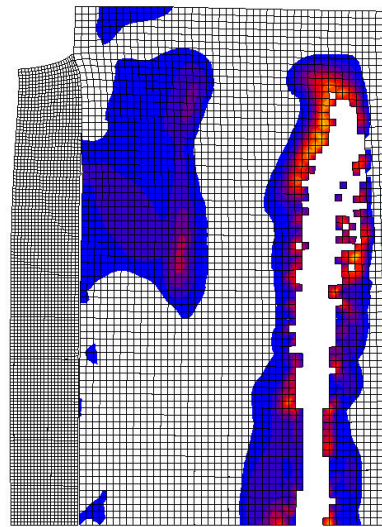
Figure 6.37 - Schematic sketch of the different flyer geometries investigated.

The maximum pressure has been determined from damage calculations performed with the proposed model. More specifically, relatively to the reference case and using the single strip fem model, the critical maximum pressure has been measured as the pressure that correspond at the time at which the first element fails by damage accumulation. This approach leads to very similar results with both code formulations. Maximum pressure and damage are intimately related variables since pressure is accounted in the damage model by stress triaxiality function. Once again, when using damage modeling, failure is predicted on the basis of material properties only. On the contrary, when using abrupt criterion such as maximum pressure, numerical predictions require post test calibration procedures that have to be repeated each time a single basic feature is changed. In figure 6.38a and 6.38b, a qualitative comparison between spall zones obtained for the reference configuration is given. Here, both predicted shape

and damage area locations are very similar. On the contrary, some differences in the damage area extension are found.



a)



b)

Figure 6.38: a) Deformed view at spall time of obtained with AUTODYN simulation for an impact velocity of 185m/s and $D/h=16$. b) same plot obtained with MSC/MARC and damage model at the same velocity 185m/s and $D/h=13$, here contours indicate damage extension: min $D:0.005$ max $D=0.85$.

This can be explained taking into account that, as far as concern the AUTODYN simulations, maximum pressure criterion requires that failure would occur only in those

cells where the maximum pressure in tension exceed a critical value. The maximum pressure has been determined looking at the pressure distribution prior spall in fem simulation and a peak value of 1.85 GPa has been taken as depicted in Figure 6.36.

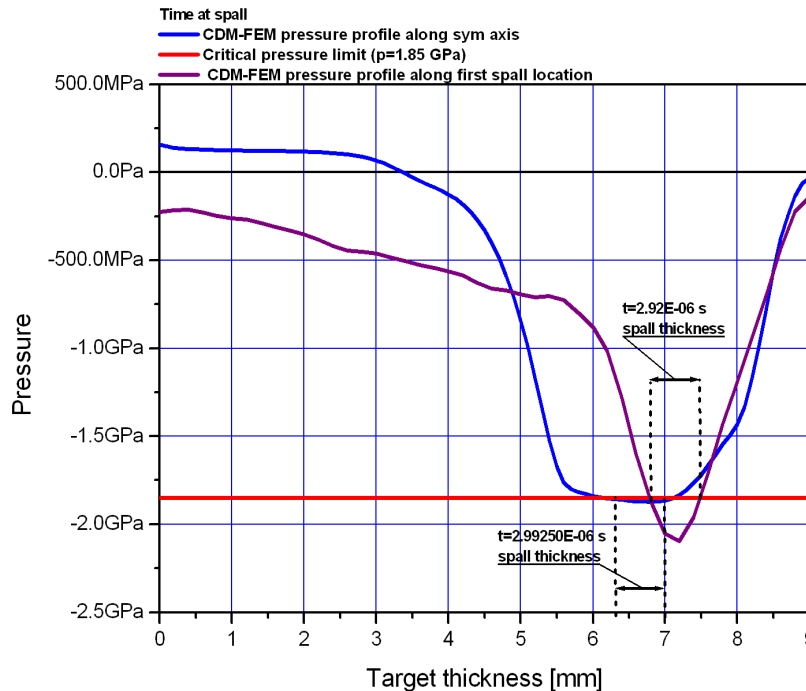


Figure 6.39 - Pressure distribution (negative means tension) at the time of spall in 99.9 OFHC at 185 m/s impact: dash lines indicate the possible spall extension using a $p=1.85$ GPa failure criterion.

In Figure 6.37, pressure distribution along the symmetry axis and along the plate thickness at the first spall location (approximately 90% of the flyer radius), shows that, at the respective spall time, the region in which the maximum pressure is exceeded is approximately the same. Consequently, the spall plane thickness predicted with this criterion has to be constant along the entire spall plane length as found in the AUTODYN simulation.

CDM based calculations, that account for the concurrent action of active plastic strain and stress triaxiality, predict larger damaged area at the location where spall firstly occurs. In Figure 6.38 the distribution of the stress triaxiality together with active plastic strain at the time of spall, are given for this location. Here, stress triaxiality subdivides the plate thickness in two regions: a first low triaxiality region where some damage occurs due to the flyer corner action, and the remaining thickness portion at higher stress triaxiality where damage threshold strain is exceeded only for a limited zone where spall will develop. A comparison of the stress triaxiality distribution along the plate thickness at the symmetry axis and first spall shows a larger zone at higher

stress triaxiality in the latter case, Figure 6.39, which explain an expected larger damaged area at that location.

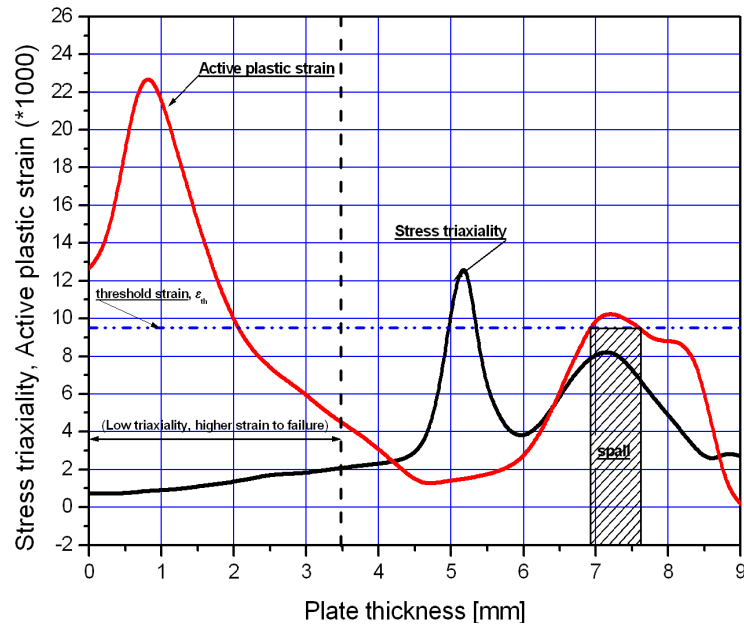


Figure 6.40 - Active plastic strain and stress triaxiality distribution along the plate thickness at the time of spall at the first spall location.

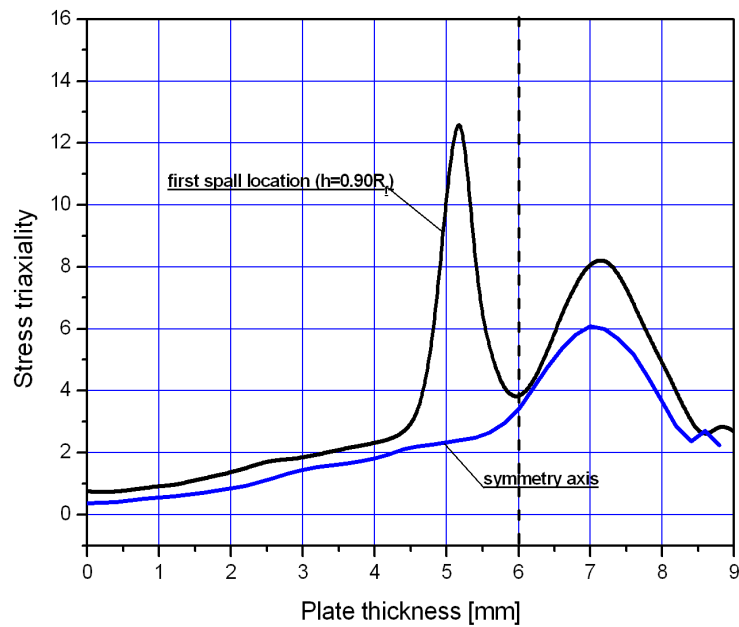


Figure 6.41 - Stress triaxiality distribution along the plate thickness at the spall time for both symmetry axis and first spall locations

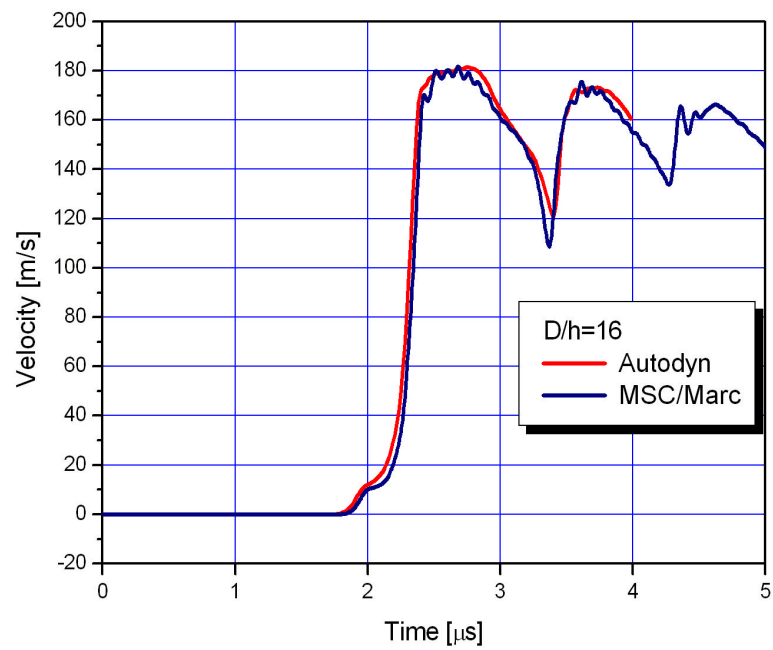


Figure 6.42 - Comparison of free surface velocity profiles versus time for flying plate configuration $D/h=16$ obtained using both MSC/MARC fem code and AUTODYN

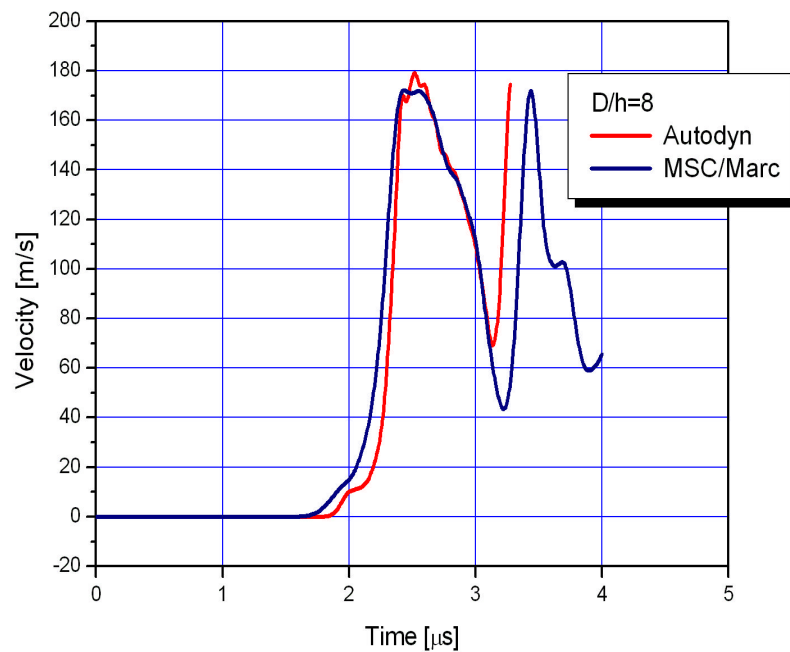


Figure 6.43 - Comparison of free surface velocity profiles versus time for flying plate configuration $D/h=8$ obtained using both MSC/MARC fem code and AUTODYN

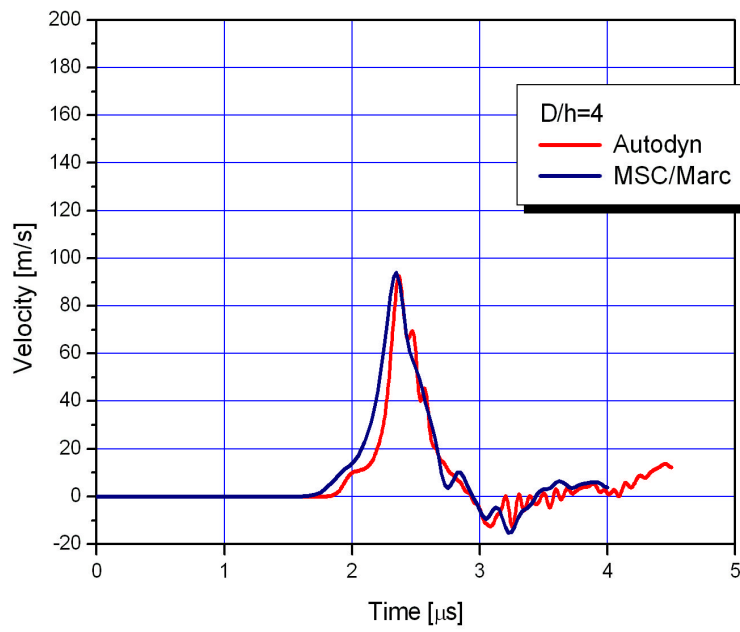


Figure 6.44 - Comparison of free surface velocity profiles versus time for flying plate configuration $D/h=4$ obtained using both MSC/MARC fem code and AUTODYN

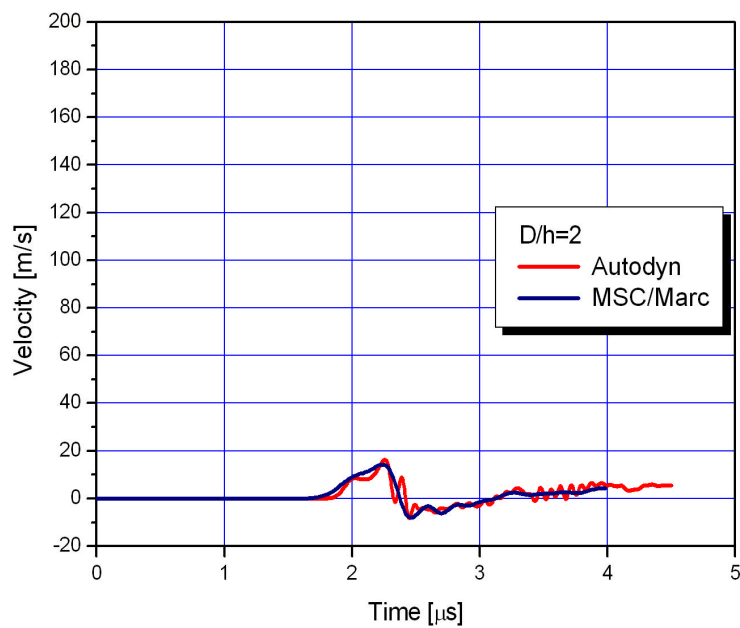


Figure 6.45 - Comparison of free surface velocity profiles versus time for flying plate configuration $D/h=2$ obtained using both MSC/MARC fem code and AUTODYN

As far as concern the free surface velocity profile measured for the point on the symmetry axis, the ratio D/h higher than 16 is large enough to realize full planar impact condition and to avoid any free edge effect coming from the free boundary. In Figure 6.40 the comparison for the free velocity profile is given for both MSC/MARC and AUTODYN calculations.

Comparison shows a very good agreement between solutions obtained with different codes. As also discussed in the previous sections, numerical damping plays an important role. It has been found that suggested values given in AUTODYN are usually too high over-dumping the effective material response. It has to be observed that all basic features such as the HEL, constant velocity plateau and the spall signal as well as spall time, matches for both simulations.

Progressive reduction of flyer diameter results in a modification of the free surface velocity signal as given in the following Figures 6.41-6.43

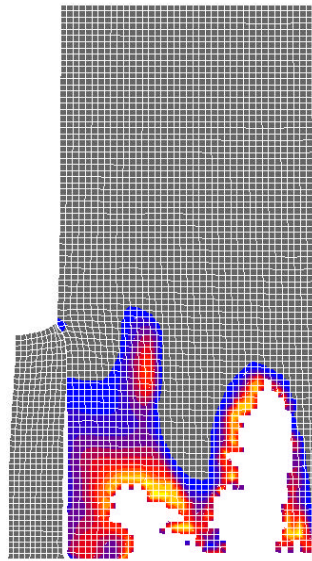
For $D/h=8$ the free velocity signal sees a reduction of the plateau and an increase of the velocity drop at the spall occurrence. In this case, main feature of spall signal can still be recognized. The contour plots for this configuration at spall time show that even though spall still occurs at the predicted location, damage develops in larger target section prior spall plane. This damaging process has been found, at least in its general feature, in both calculations using MARC and AUTODYN. In figure 6.44 and 6.46 the comparison of the failed areas is given.

With further reduction of the flyer aspect ratio, spall characteristics in the free surface velocity signal are completely lost. The only feature that is still preserved is the HEL. The dramatic modification of the signal is a clear indicator that uniaxial strain loading condition, basic feature of planar impact, is no longer verified. Damage starts to develop into the flyer and for a ratio $D/h < 4$ no spall would occur in the target. Here, some sort of different failure mechanism such as target penetration would eventually start to occur.

For D/h ratio lower than 2, the geometrical configuration is closer to the one of a Taylor impact test than a plate impact. The deformed view of the flyer shows typical mushrooming and an extensive damage development. It has to be anticipated here, that mesh size used for this configuration is inadequate to follow the effective deformation process. Computational analyses reveal that there is a correspondence between the flyer diameter and the location of the first spall along the spall plane. This location also indicates the maximum extension of spall fracture. If we draw for a given diameter/thickness configuration a theoretical line starting from the flyer corner and intersecting the spall plane at the first spall location, this line will have a slope that is independent of the flyer diameter length. In Figure 6.47 the sketch of the proposed criterion is given.



a)

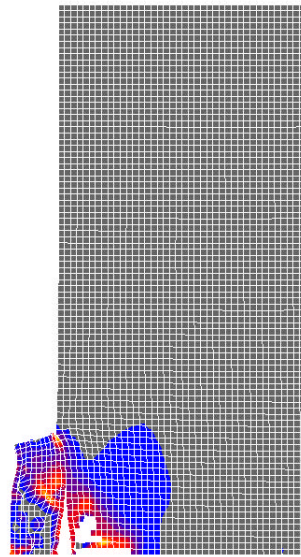


b)

Figure 6.46 - Damage area in $D/h=8$ impact configuration using both maximum pressure criterion (AUTODYN) and CDM



a)



b)

Figure 6.47 - Damage area in $D/h=4$ impact configuration using both maximum pressure criterion (AUTODYN) and CDM

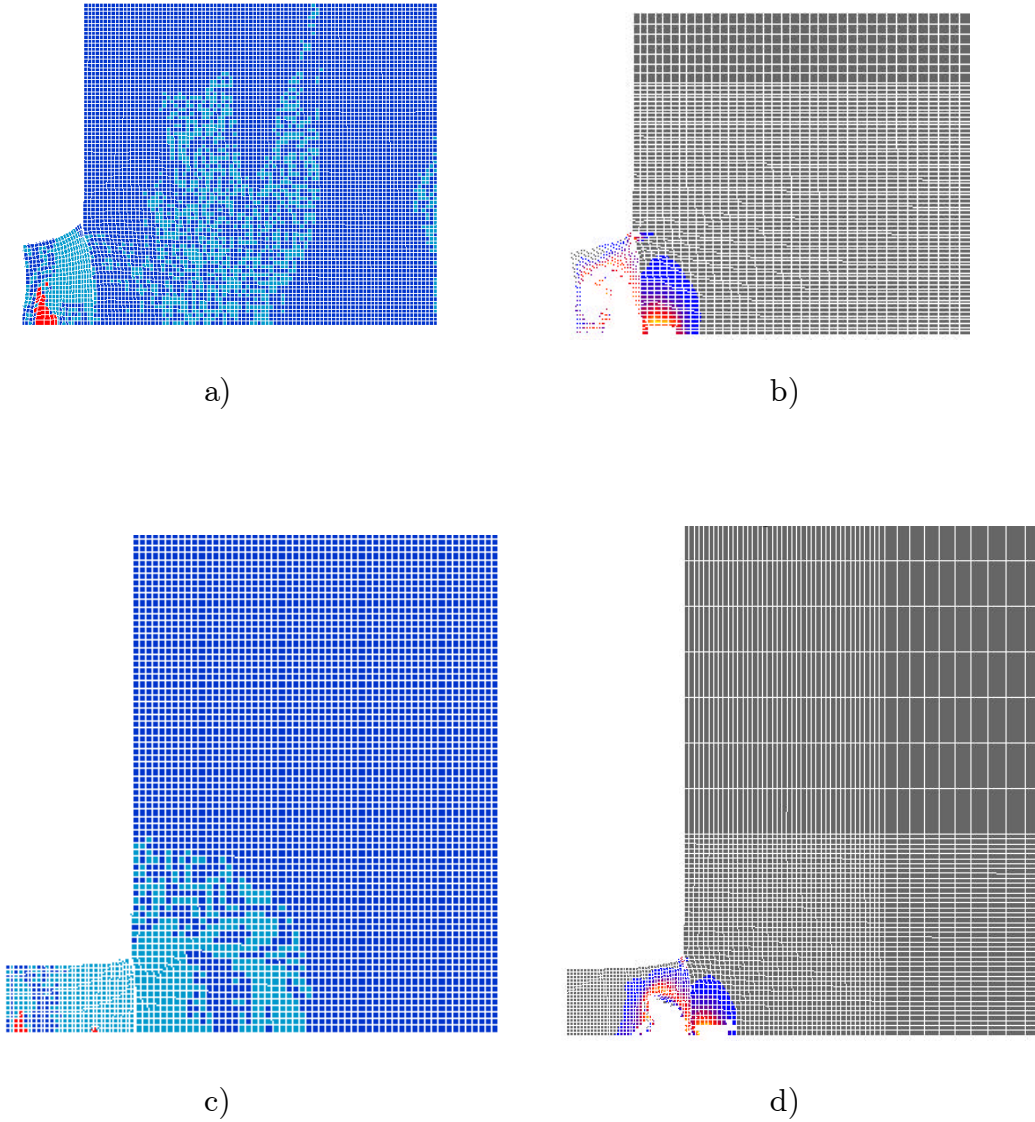


Figure 6.48 - Damage area in $D/h=2$ (a-b) and $D/h=1$ (c-d) impact configuration using both maximum pressure criterion (AUTODYN) and CDM

Spall plane location, in a symmetric impact, is determined by the flyer thickness only for a given impact velocity, thus slope of the boundary effect line can be given as:

$$h_s = (L_t - L_f) \tan(\vartheta) \quad (6.7.1)$$

where h_s is the radial distance on the spall plane measured from the flyer free corner, L_t is the target thickness, L_f is the flyer thickness and ϑ is the slope measured as depicted in Figure 6.48.

Measures of the slope of the boundary effect line have been for three different values of L_f as a function of the ratio flyer diameter/thickness. In Table 6.12 the geometrical

measured quantities relative to first spall location in OHFC copper at the constant impact velocity of 185 m/s are summarized ($L_t=9.0$ mm).

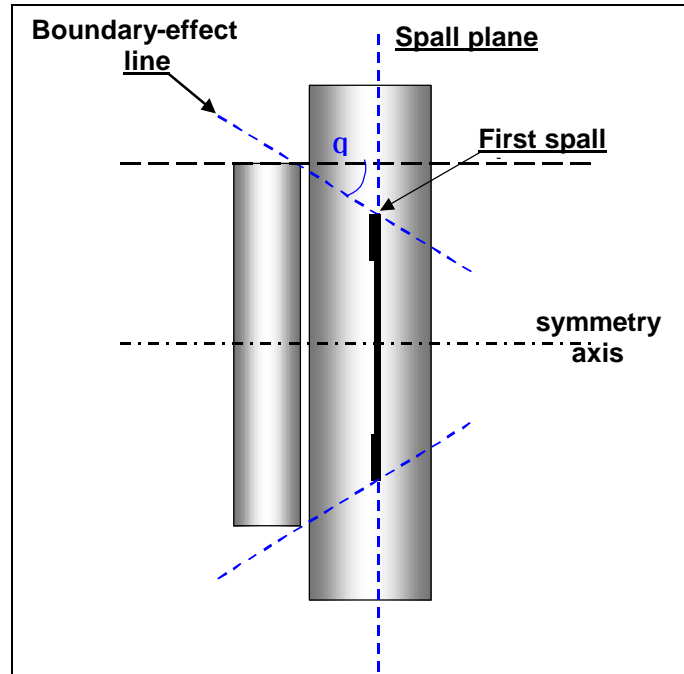


Figure 6.49 - Schematic plot of the edge effect on first spall location

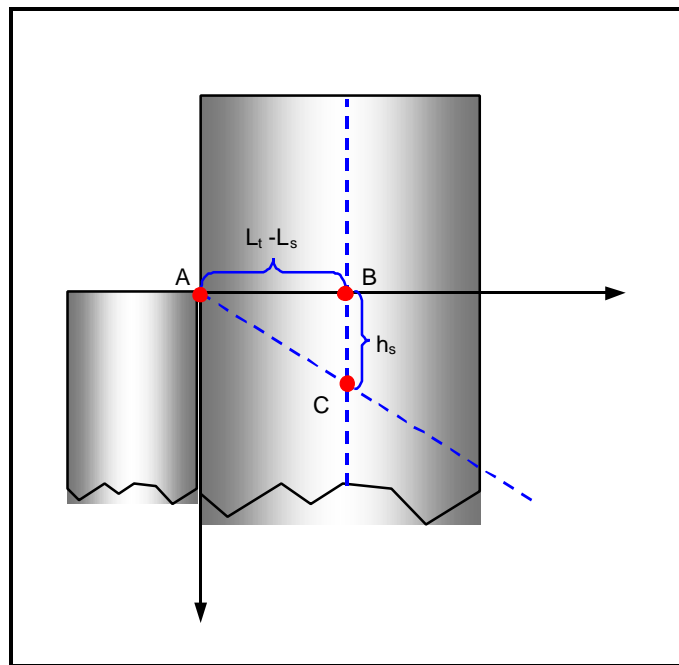


Figure 6.50 - Boundary line definition

D_f/L_f	$L_f=2 \text{ mm}$		$L_f=4 \text{ mm}$		$L_f=1 \text{ mm}$	
	h_s	L_t-L_f	h_s	L_t-L_f	h_s	L_t-L_f
	[mm]	[mm]	[mm]	[mm]	[mm]	[mm]
8	4	7.2	-	-	-	-
16	4.9	7.3	6	5.7	4.1	8.1
32	4.8	7.2	5.8	5.5	4.1	8.1
40	4.4	7.4	5.5	5.8	3.5	8.1

Table 6.12 - Geometrical co-ordinates of first spall location

These results confirm that the location of first spall occurrence is independent of the difference between flyer and target plate diameter. In addition it has been observed that the geometrical area of the triangle ABC of figure 6.48 is seems to remain also constant: i.e. changing the flyer thickness both h_s and (L_t-L_f) change but in a way that the area does not. This latter property allows one, knowing a reference solution, to estimate the location of first spall occurrence in a different flyer/target geometrical configuration using the following simple relation:

$$\tan(\vartheta) = \frac{(L_t - L_f^*)^2}{(L_t - L_f)^2} \tan(\vartheta^*) \quad (6.7.2)$$

where * indicates the reference configuration.

Simulations have also shown that there exists a geometrical condition D/L_f for which spall fracture cannot longer occur. This is the case when the intersection of the boundary effect line with the spall plane (namely point C in Figure 6.48) falls below the symmetry axis, Figure 6.45a.

The reason why spall fracture firstly initiates out of the symmetry axis can be found in the stress waves path. In fact, flyer free edge represents a region where compressive stress waves, generated just after the impact, are immediately reflected as tensile waves. Thus, the target at that location is subjected to a compressive wave followed by a tensile one. In Figure 6.49 the comparison of the stress pulse along the symmetry axis and at the flyer free edge is given. It can be clearly seen that while the compressive stress pulse is still traveling in the target material, a tensile stress wave follows after while this is not present for the path at the symmetry axis. Additionally it has to be noted that at the first spall location due to edge effects, the stress pulse becomes triangular shaped.

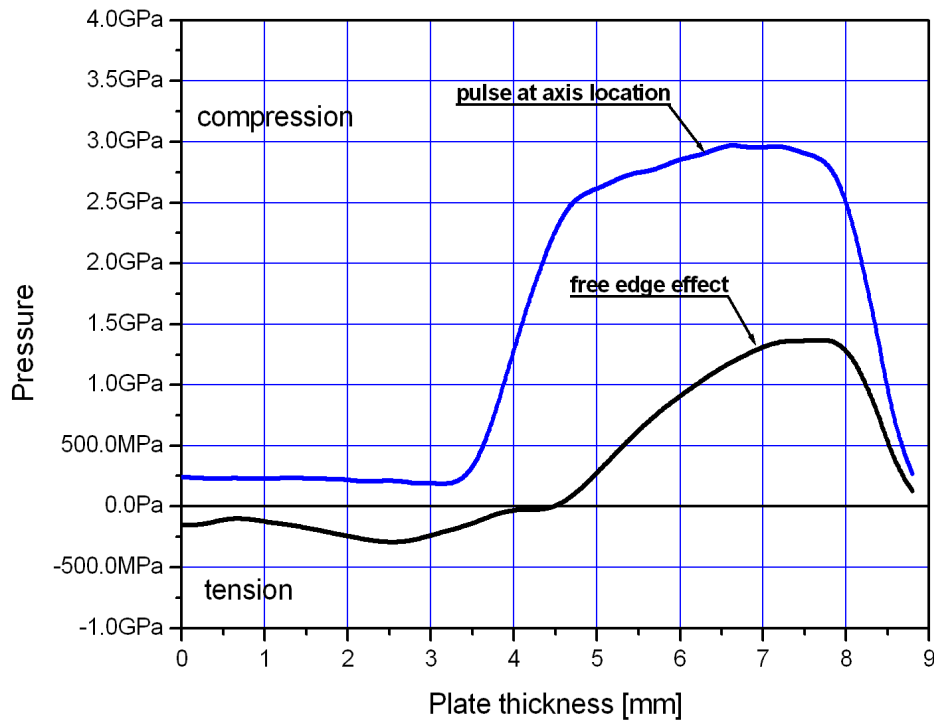


Figure 6.51 - Stress pulse at two locations: along the symmetry axis (blue), along the upper flyer edge (blue)

6.6. Flying Plate Impact Test Simulation Using Hydrocode

Hydro-codes are particularly suited to reproduce high velocity impact phenomena. As previously demonstrated, also standard finite element formulation can be used to simulate dynamic processes by means of direct integration techniques. However, this approach is limited by the impossibility to implement equations of state for the material description. The dynamic behavior of a physical system is governed by fundamental physical laws and conditions. These may be summarized as follows:

- Conservation of mass
- Conservation of momentum
- Conservation of energy
- Material models (constitutive equations)
- Initial conditions
- Boundary conditions

In AUTODYN these fundamental equations are solved using advanced numerical techniques. AUTODYN includes a multiplicity of numerical solvers, termed “processors”, each optimized for the various regimes of a physical system. The various processors may be applied independently or, uniquely, they may be coupled in a single analysis to provide an accurate and efficient solution for complex “coupled problems”. Coupled problems may include impact-penetration, fluid dynamics-structural mechanics interaction, and explosive-structure interaction. AUTODYN divides time and space into increments (discretization). Time is broken up into "time steps ". Each time step constitutes a "cycle". The user may specify the first time step, alternatively AUTODYN automatically provides the proper time step to maintain the accuracy and stability of the solution. Space is divided up or "zoned" into what are termed "cells", “zones”, or “elements”. In AUTODYN, all elements are quadrilaterals (2D) or bricks (3D). A given space or "subgrid" is organized by a structured IJ (2D) or IJK (3D) index space. The variables within a given element are then addressed by specifying an I,J (2D) or I,J,K (3D). AUTODYN allows for the definition of several independent IJK subgrids within a given problem. Moreover, each subgrid can employ a different numerical processor (Lagrange, Euler, Shell, ALE, SPH, etc.). While each subgrid has a rectangular IJK index space the use of unused cells and the functionality of multiple subgrids interacting together allows AUTODYN to describe complex non-rectangular (x,y,z) shapes and structures. Fortran subroutines allow the user to interact directly with the quantities and the variables for each cell at each time cycle. In addition, a number of modules that fulfill specific purpose, allows direct interaction with special aspects of modeling such as material, equation of state, damage, etc. The proposed damage model has been implemented using the Autodyn user subroutine Damage. Once damage has been calculated at each cell, the Young modulus is reduced and updated. Damage calculation requires the storing of damage, plastic strain, and stress triaxiality at each cell at each cycle, in order to proceed to the integration at the current time cycle. Integration is performed using standard Runge-Kutta fourth order integration scheme. During the current cycle, actual stress triaxiality is assumed constant and variation inside the cycle are neglected for simplicity purpose.

Damage model implementation benchmark test

In order to be sure that damage model was correctly implemented in AUTODYN, a number of simple benchmark tests have been performed. Here, the computed damage evolution with time and plastic strain has been compared with analytical solution.

A single four node cell with imposed symmetry boundary conditions under axis-symmetric formulation has been tested. Loading condition, in the form of initial velocity, has been imposed as depicted in Figure 6.52.

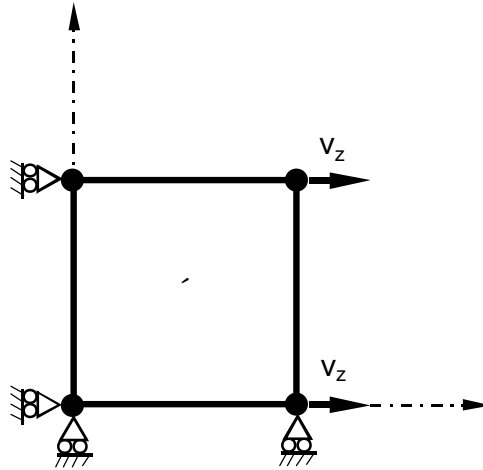


Figure 6.52 – Sketch of the single cell for damage model implementation benchmark

Several loading conditions have been examined: normal stress (uniaxial tensile), shear stress and shear strain. These configurations represent reference cases for imposed stress triaxiality levels for which damage evolution calculation can be checked. In Figure 6.53 the comparison of the calculated damage evolutions, together with the analytical reference solution, are given showing the accuracy of the numerical implementation. Additional simulations have shown that the Runge-Kutta integration scheme allows one to obtain accurate damage integration even though plastic strain step per cycle can eventually be large.

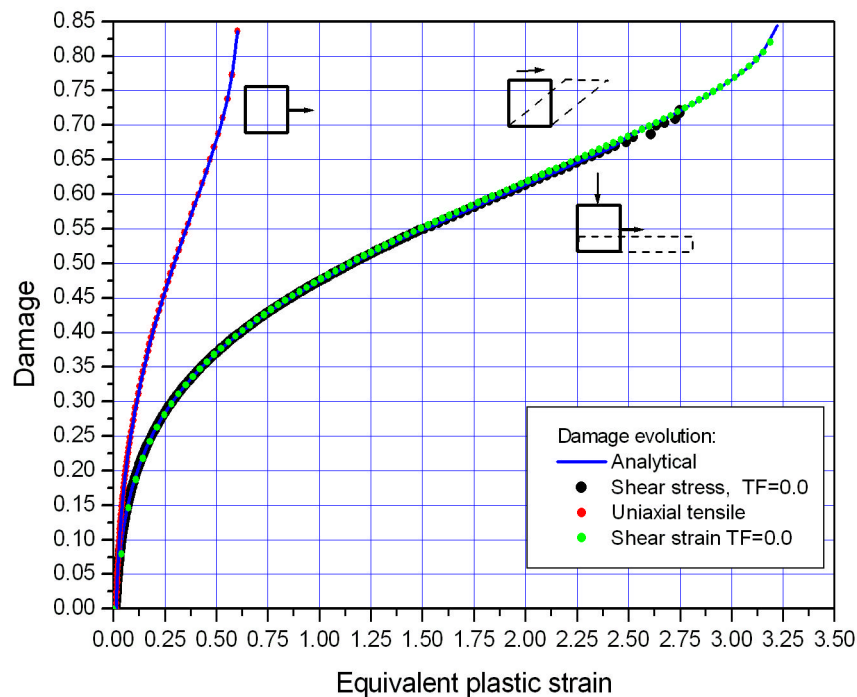


Figure 6.53 – Damage evolution under different imposed stress triaxiality levels: uniaxial (TF=0.333) and shear (TF=0.0).

Damage evolution in Flying plate impact test

The flying plate impact test in OFHC copper has been simulated. The reference configuration is a 2 mm thick flyer and 9 mm thick plate. The model has been developed building two IJ grids in axis-symmetric formulation for the plate and the flyer, respectively. A space discretization of 20 by 380 cells has been used for the flyer and 90 by 400 for the plate resulting in a cell size of 0.1 mm that corresponds to the size of the reference volume element for metals. An initial gap of 0.1 mm between the two parts has been left in order to allow correct initial contact detection. Two impact velocities have been investigated: 150 and 185 m/s.

The material has been modeled using Johnson and Cook flow stress law, Rif. 6.7. AUTODYN formulation requires that an equation of state (EOS) has to be provided, independently from the impact velocity, since stresses are explicitly formulated in separated deviatoric and pressure components. Here, the deviatoric part is formulated using standard isotropic elasticity equations and used in the strength model while EOS is used to relate pressure (the hydrostatic pressure) with cell volumetric variation. The Hook law can be written as:

$$\dot{\mathbf{s}} = \mathbf{I} \frac{\dot{V}}{V} + 2G\dot{\mathbf{e}}_i \quad (6.7.3)$$

where G and λ are the Lamé constant and $i=1,2,3$. Recalling that the stress tensor can be divided into the deviatoric and hydrostatic part, Eqn. (3.1) becomes:

$$\begin{aligned} \dot{\mathbf{s}} &= 2G \left(\dot{\mathbf{e}} - 3 \frac{\dot{V}}{V} \mathbf{I} \right) \\ p &= K \mathbf{m} \end{aligned} \quad (6.7.4)$$

where K is the bulk modulus. The second equation, is the equation of state already built in the Hook law. If severe shock or elevated pressure conditions are achieved during the impact, the second EOS should be formulated in a different form (for example: Mie-Gruneisen, etc.).

As far as concern material failure, it has been simulated according to the proposed damage model. When damage variable reaches its critical value inside a cell, the cell itself is removed and the mass is distributed to the boundary nodes of neighbor active cells. In this way failure, as well as penetration, can occur without mass loss.

Flying plate test response, plotting the free rear target surface velocity as a function of time, has been calculated and compared with experimental data, Ref. 6.5, and Fem results. In Figure 6.54 this comparison is given. Since time scale is not absolute, as a result of the fact that different initial gap distance results in a shift of the velocity plot,

calculated velocities have been shifted in order to match the initial experimental data available.

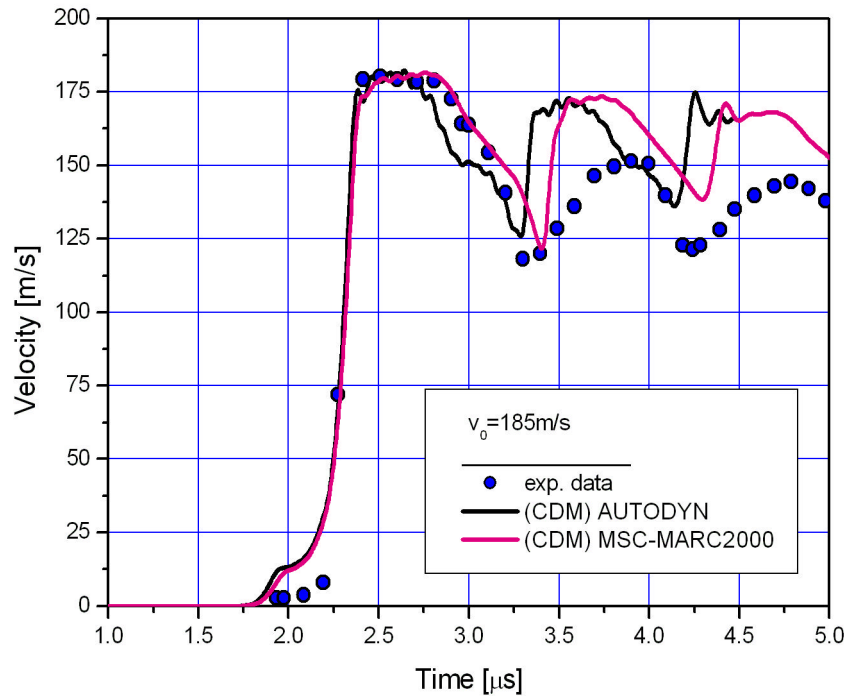


Figure 6.54 – Rear target surface velocity plot as a function of time calculated with CDM model implemented in AUTODYN: comparison with experimental data and MSC-MARC FEM code.

A number of interesting information can be obtained from this comparison. Firstly, the Hugoniot elastic limit (HEL) is clearly visible in both simulations, performed with hydrocode and standard FEM, while it is not so evident in the experimental data obtained with VISAR probably due to the lacking on enough data points in the first 0.3 μs during which the velocity rise from zero to the maximum value. Hydrocode calculated curve shows high frequency oscillations at the plateau, which results in a shorter duration of the constant velocity plateau with respect to the effective experimental one. In addition, the release wave arrival, indicated by the velocity drop, is steeper resulting in a slightly shorter spall time t_c . This is probably due to the different material internal damping formulation. In Autodyn, adjusted damping factors, other than default, would probably perform better.

Out of these differences, both calculations predict the same velocity peak values in the spall signal, while the frequency shift is mainly due to the initial difference in the estimation of t_c . This result confirms, as discussed in the above sections, that a dissipative process relative to the separation of spall plane faces, responsible for the drop of acceleration during first spall signal velocity peak, should exists.

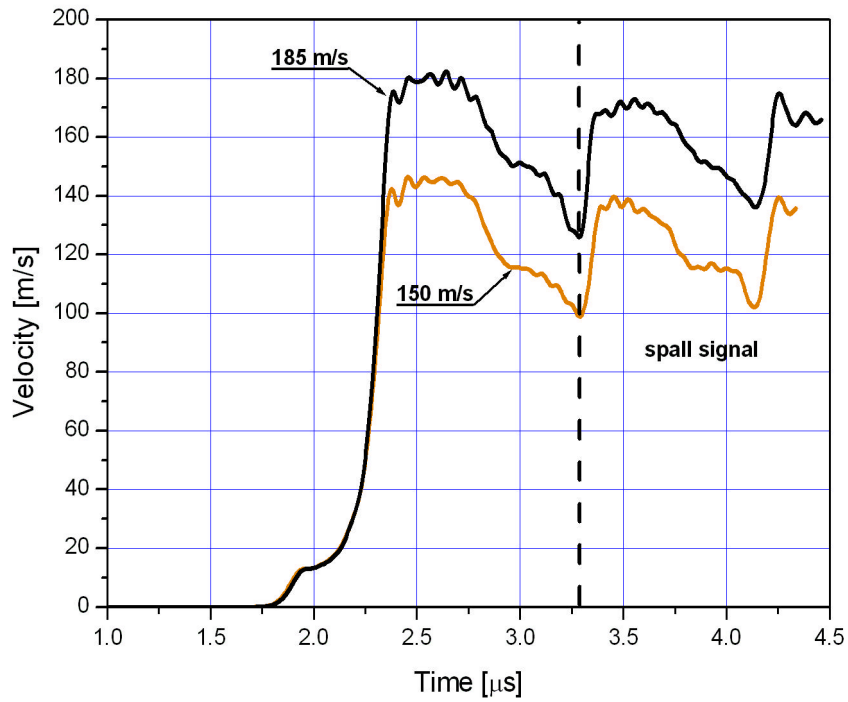


Figure 6.55 – Velocity plot calculated with Autodyn and the proposed damage model for two impact velocity conditions.

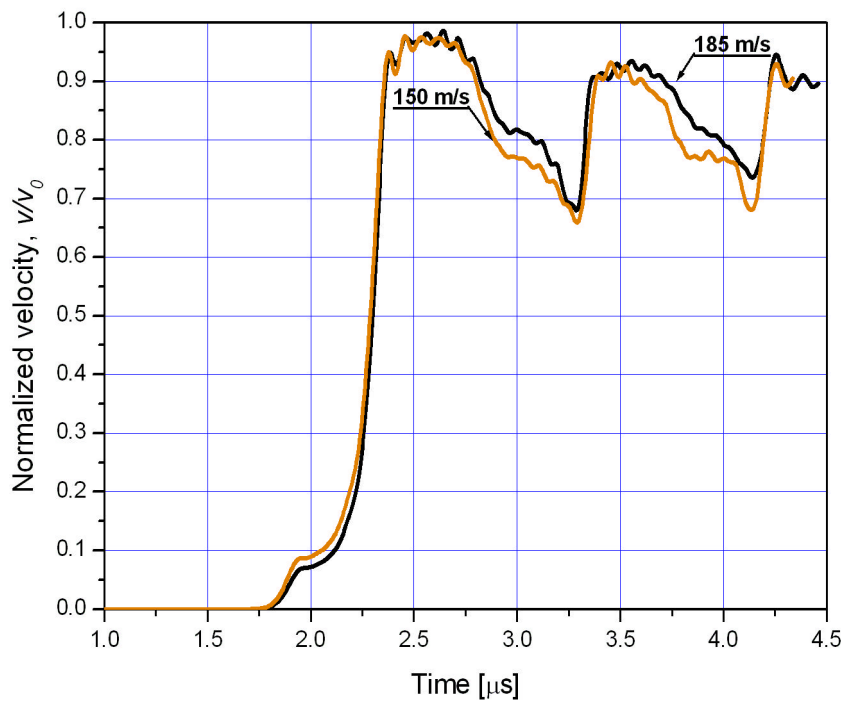
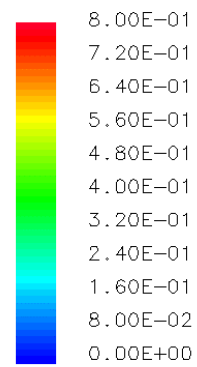
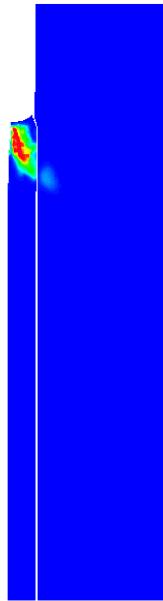


Figure 6.56 – Normalized velocity plot for 185 and 150 m/s impact in OFHC copper.

AUTODYN-2D Version 4.2.02k

Century Dynamics Incorporated

DAMAGE



AX (mm.kg.ms)

CYCLE 476

T = 3.295E-03

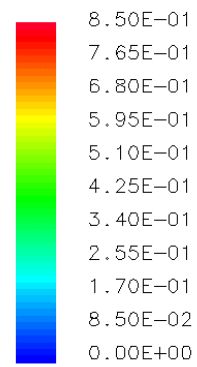
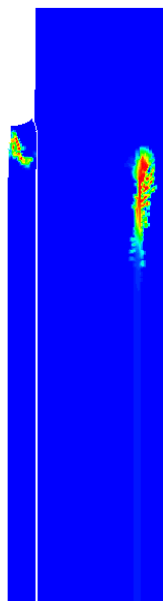
R185D0: VEL INIZ 185M/S

a)

AUTODYN-2D Version 4.2.02k

Century Dynamics Incorporated

DAMAGE



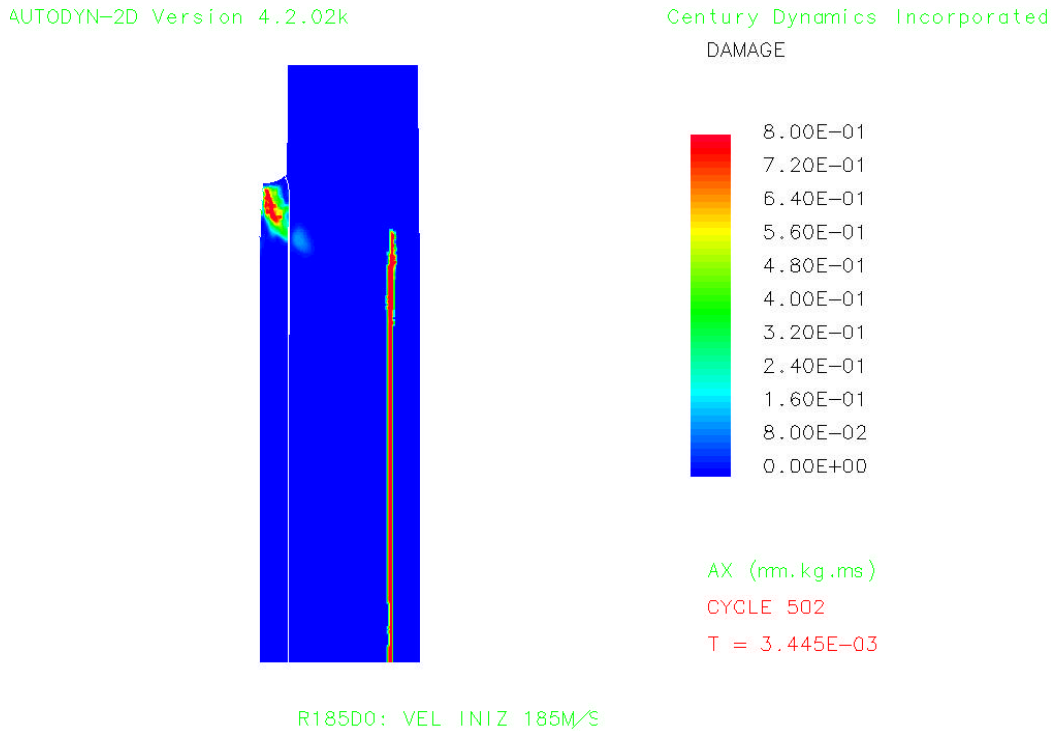
AX (mm.kg.ms)

CYCLE 490

T = 3.376E-03

R185D0: VEL INIZ 185M/S

b)



c)

Figure 6.57 – Damage evolution during spall plane formation for 185 m/s impact in OFHC copper

According to this, it can be concluded that, at least when the impact velocity is lower enough not to generate severe volume compression or shocks, both numerical formulations, explicit and implicit, using the same damage model, lead to very close results. Numerical simulations have been repeated for a lower impact velocity, 150 m/s. This value is close to the spall threshold limit. In Figure 6.55 the velocity plot showing the spall signal for different impact velocity is given. This picture clearly shows that material response in form of velocity plot maintains all the features previously discussed. Here, the velocity plot is simply scaled down to lower velocity value. In order to appreciate the differences between the two loading impact conditions the normalized velocity plot, in which each plot has been normalized by its own reference impact velocity, is shown in Figure 6.56.

Here, it can be seen how there is a direct effect of the impact velocity on the HEL, as predicted by the theory, and a steeper velocity drop due to the release wave arrival while spall time, as well as the spall signal features, remain almost unchanged.

In the present calculation half of the entire geometry has been modeled for symmetry reason while in the FEM simulation only a single element strip, where theoretical uniaxial strain condition was imposed, has been used. In addition, the attention for comparison with previous results has been focused in the development of spall region.

In Figure 6.57a-c the picture of the spall plane formation for the reference impact velocity of 185 m/s is given at different time cycles. Here it is evident how damage in the target plate is highly localized around the spall plane location. Damage development does not initiate along the symmetry axis but along the spall plane location at a radial distance close to the flyer radius. As discussed in Ref 2.1, according to the proposed damage model, this is due to the tensile release wave, that follows immediately after the compressive stress wave, at the location close to the flyer end corner. As soon as spall initiates at this location, it spreads along the entire spall plane as depicted in Figure 6.57c. It has to be noted that some damage is expected to occur at the flyer periphery, as given in Figure 6.57c. At this location, damage can be so severe to cause the fracture of the flyer plate.

Features relative to stress wave shape and interaction at different radial location have been also verified. In Figure 6.58 the stress wave at different radial location are given for $v=185$ m/s. Once again, different stress wave profiles observed in the previous study are confirmed by the present calculations.

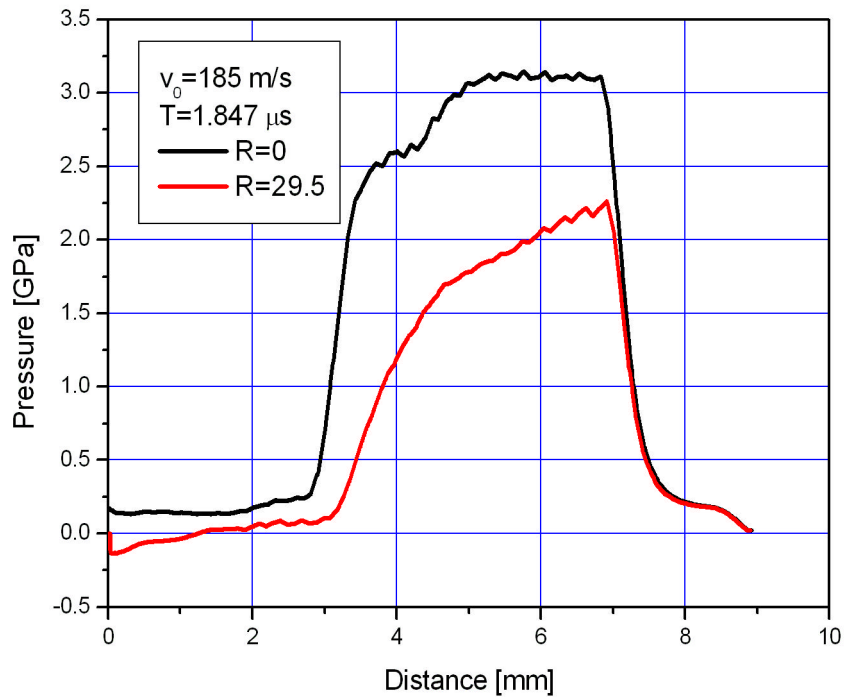
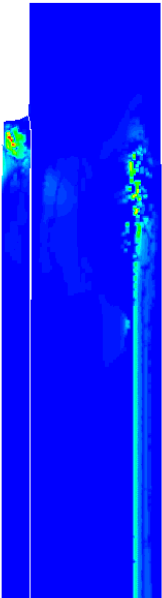


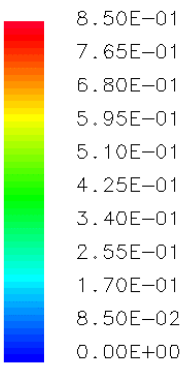
Figure 6.58 – Stress wave profile along flyer plate thickness at different radial locations.

In the following Figures 6.59a-d, damage evolution for the 150 m/s impact is given. Here it is surprising how for lower impact velocity damage extension results to be larger than for 185 m/s impact. In Figure 6.59d, for instance, damage pattern reveals that an extensive damaged area develops behind the spall plane. In addition, spall plane is not clearly identified as before resulting in a wider damaged radial section of the flyer.

AUTODYN-2D Version 4.2.02k



Century Dynamics Incorporated
DAMAGE



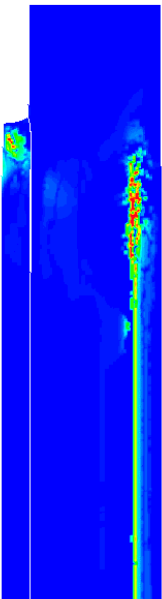
AX (mm.kg.ms)

CYCLE 420

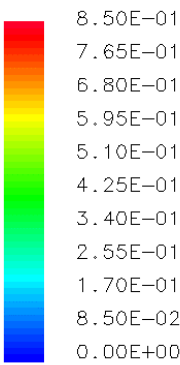
T = 3.544E-03

a)

AUTODYN-2D Version 4.2.02k



Century Dynamics Incorporated
DAMAGE



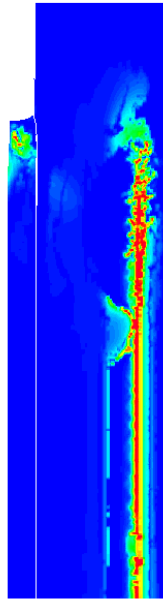
AX (mm.kg.ms)

CYCLE 425

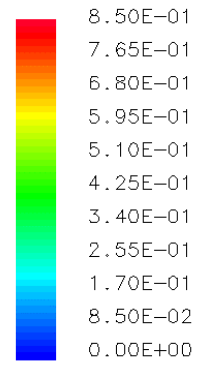
T = 3.582E-03

b)

AUTODYN-2D Version 4.2.02k



Century Dynamics Incorporated
DAMAGE



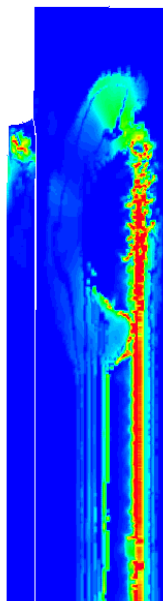
AX (mm.kg.ms)

CYCLE 480

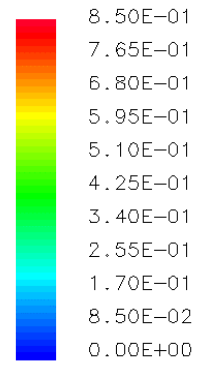
T = 4.005E-03

c)

AUTODYN-2D Version 4.2.02k



Century Dynamics Incorporated
DAMAGE



AX (mm.kg.ms)

CYCLE 610

T = 5.004E-03

d)

Figure 6.59 – Damage evolution during spall plane formation in OHFC copper. Impact velocity. 150 m/s

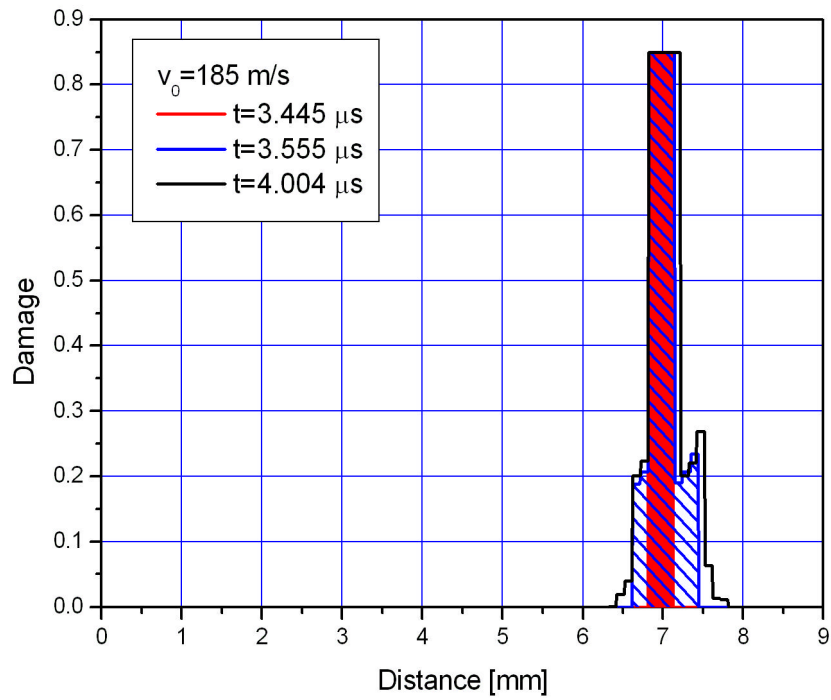


Figure 6.60 – Damage extension though flyer thickness along the symmetry axis (distance from the impact plane) at $v=185$ m/s.

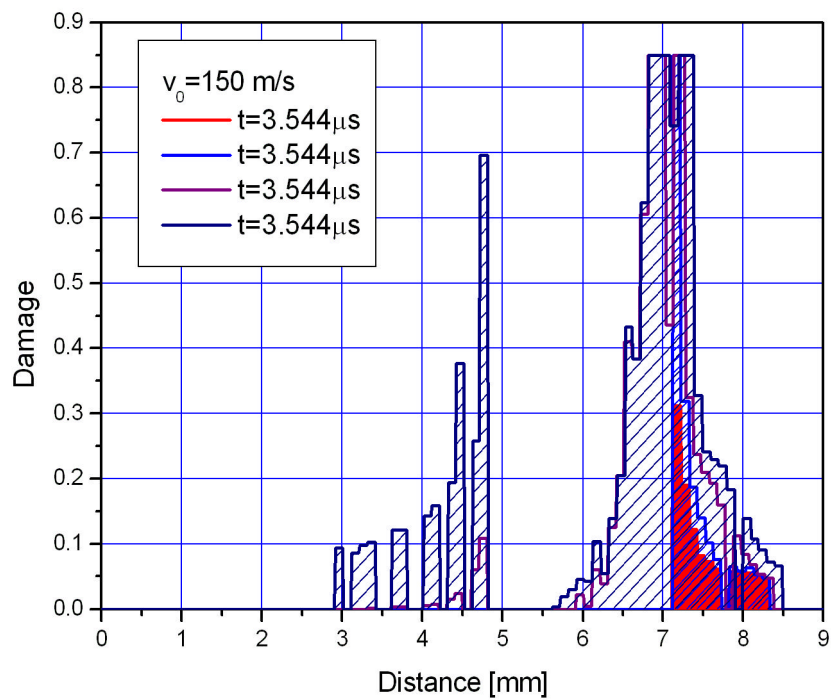


Figure 6.61– Damage extension though flyer thickness along the symmetry axis (distance from the impact plane) at $v=150$ m/s.

Even though damage pattern are so different during impacts at 150 and 185 m/s, these differences do not emerge from the velocity plot as given in Figure 6.57. Since lower impact velocity implicates lower kinetic energy that can be converted in plasticity and damage process, damage should decrease with decreasing v_0 . In Figure 6.60 and 6.61 the damage extension, along the symmetry axis, for different time cycles, is given. Results reported in Figure 6.60 can be explained as follows. For a given damage parameters set, at lower impact velocity, damage processes can evolve more as a result of a longer time for which high stress triaxiality acts on the material points. In reality, the reduction of the impact velocity causes the progressive reduction of the amount of damage in the target material for the reason that damage processes are not activated. This can be explained taking into account that the first passage of the compressive stress wave, if severe enough, can generate damage in form of pitting compacting the material microstructure during volumetric compression. From a damage point of view, this process modifies the damage threshold parameter from point to point according to the local stress history. Even though direct damage measurements for pre-shocked material are not available in the literature, it can be assumed that damage threshold may show pressure dependency.

The major consequences of this are:

- a) Since compressive stress wave is more intense along the symmetry axis than in other radial location, Figure 6.58, local damage threshold strain should be lower than in other flyer regions resulting in an early spall initiation at the symmetry axis.
- b) Spall extension should consequently decrease with decreasing impact velocity.

At the present time, pressure dependency of damage threshold strain in Autodyn is under development.

6.7. References

- 6.1 Kolsky, H., (1963), Stress waves in solids, Dover, New York
- 6.2 Wasley, R.J., (1973), Stress Wave propagation in solids: an Introduction. Marcel Dekker, New York
- 6.3 Johnson, G., (2000), I. J. of Impact Eng.,
- 6.4 Curran, D. R., Seaman, L., Shockey, D.A., in Shock Waves and High Strain Rates Phenomena in Metals, Ed. Meyers M.A. and Murr L.E., Plenum, New-York

- 6.5 Rajendran, A.M., (1988), in Dynamic Constitutive/Failure Models (ed. A.M. Rajendran, and T. Nicholas), AFWAL-TR-85-4009, Wright Patterson Afb, OH
- 6.6 Dattatraya, P.D., Williams, W.J., (1999), Int. J. of Plasticity, 15, pp. 1291-1309.
- 6.7 Johnson G.R. and Cook W.H., (1983), Proc. 7th Inter. Symp. Ballistic, Am. Def. Prep. Org. (ADPA), Netherlands.
- 6.8 Christy, S., Pak, H., and Mayers, M.A., (1986) in Metallurgical Applications of Shock Waves and High Strain Rate Phenomena (eds., Murr et al.), Marcel Dekker, New York.
- 6.9 Al-Hassani S.T.S., Chen, D., Sarumi, M., (1997), J. of Impact Engineering, 19, 493-501.
- 6.10 Nemes, J. A., and Eftis J., (1991), Computer and Structure, 38, pp. 317-328
- 6.11 Nemes, J. A., and Eftis J., (1992), Int. J. Plasticity, 8, pp.185-207
- 6.12 Razorenov, S.V. and Kanel, G.I.,(1991), Prob. Strength (USSR), 9, pp.52-55
- 6.13 Thissell, W.R., Zurek, A.K., Macdougall, D.A.S., Miller, D., Everett, R., Geltmacher, A., Brooks, R and Tonks, D., (2002), Proceedings of Shock Compression of Condensed Matter – 2001, paper n° CP620, edited by M. D. Furnish, N. N. Thadhani, and Y. Horie, American Institute of Physics.

7. Taylor Impact Test

Taylor cylinder impact test is a test configuration developed with the primary scope to identify material yield stress under dynamic loading conditions. The analysis of the impacting cylinder was initially developed by Taylor (Ref. 7.1) and Wiffin (Ref. 7.2). The method consists in impacting a right circular cylinder against a infinite rigid target and making post-impact measurements of the deformed shape. The analysis proposed by Taylor is very simple and is limited by two main assumptions that are usually not verified: a) the material is rigid elastic-perfectly plastic; b) stress wave propagation is assumed to be one-dimensional. From Taylor analysis the following expression for the dynamic yield stress can be derived:

$$\sigma_y = \rho v_0^2 \frac{(l_0 - H)}{(l_0 - l_1)} \frac{1}{\ln\left(\frac{l_0}{H}\right)} \quad (7.1.1)$$

where v_0 is the impact velocity, ρ is the cylinder material density, and H , l_0 and l_1 are the segments in the deformed configurations as given in Figure 7.1

Later, Taylor modified the previous relation introducing a correction factor in order to account for non-uniform cylinder deceleration. Indicating with $\bar{\sigma}_y$ the corrected value of σ_y , we get

$$\frac{\bar{\sigma}_y}{\sigma_y} = -\frac{(l_0 - l_1)}{(l_0 - H)} \frac{\ln\left(\frac{l_0}{H}\right)}{\left(K - \frac{c_p}{a}\right)^2} \quad (7.1.2)$$

where K and a are defined as follows,

$$a^2 = \frac{2\sigma_y}{\rho} \quad (7.1.3)$$

$$K = \frac{v_0 + c_p}{a}$$

$$c_p = \frac{v_0 (l_1 - H)}{2 (l_0 - l_1)} \quad (7.1.4)$$

In the last decades several modification have been proposed for the Taylor solution in order to account for different effects such as material hardening.

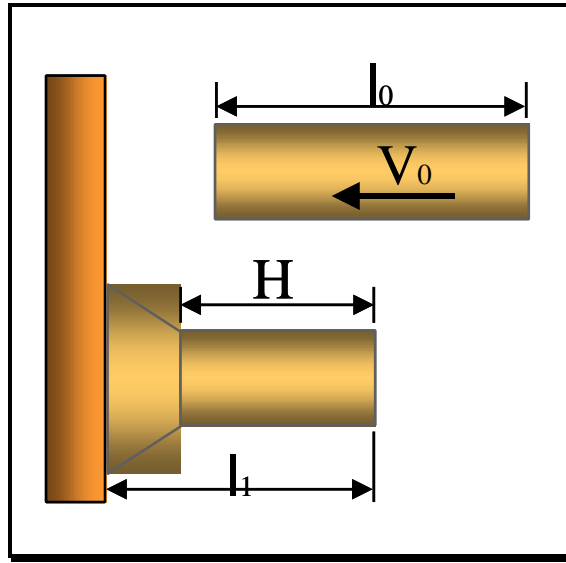


Figure 7.1- Definition of the segment for yields stress determination in the Taylor cylinder impact test

It should be recognized that the Taylor impact test involves rather complex phenomena such as two-dimensional stress wave propagation, non uniform strain rate and thermal activated softening that can make very difficult the accurate identification of effective material yield stress.

In this study, an extensive numerical investigation, incorporating the proposed damage model, has been performed in order to verify the possibility to replicate experimental features, to study the role of different effect played by strength modeling and damage distribution. Always, when possible, comparison with experimental data retrieved from the literature has been made.

7.1. Finite element modeling

Finite element modeling of Taylor cylinder is very simple in theory. However, contact between the cylinder and the wall plays a critical role. Friction condition, initial element size and mesh aspect ratio for the impacting cylinder, as well as target wall modeling, can substantially affect the finite element results. In this study MSC/MARC code in its implicit formulation, using β -newmark integration scheme has been used to simulate impact dynamics. The study has been focused on two different main aspects of the matter: a) the appropriate simulation of the target wall b) a parametric study of the strength modeling, coupled with the damage model, associated effects. Results, mainly in terms of post impact deformed shapes, have been compared with the experimental data available in the literature for copper, ARMCO iron and AISI steel.

The impacting cylinder has been simply modeled simulating only half of the entire geometry for symmetry reasons. Initial impact velocity has been provided as initial boundary condition. Since the elements in region near by the impact surface are subjected to large deformation, an initial mesh with rectangular aspect ratio has been adopted in order to have square element at the end of the deformation process. This strategy allows one to overcome problems due to excessive element distortion that can result in negative Jacobian matrix and early interruption of the analysis. On the other hand, since stress waves are expected to be mainly axial, a larger mesh in this direction would eventually allow larger time steps. In Figure 7.4 an example of the typical mesh is given. Here, the typical element size is 0.5x0.25 mm.

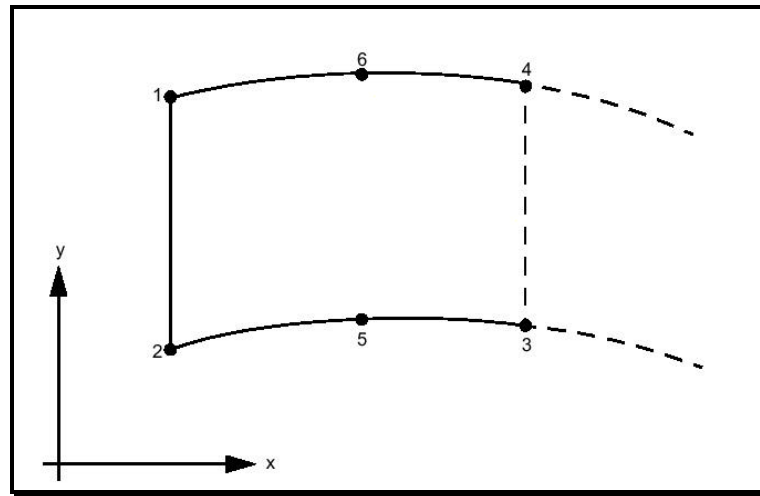


Figure 7.2- Semi-infinite elements used in modeling the infinite target wall

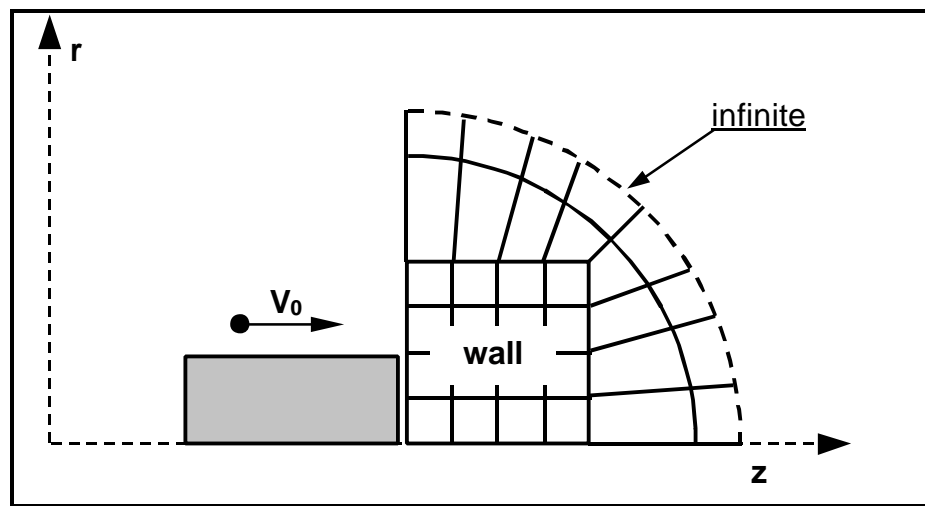
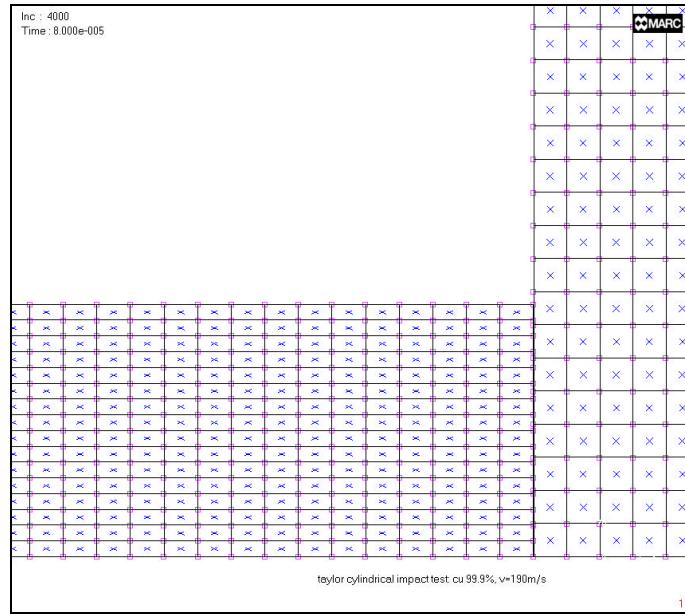
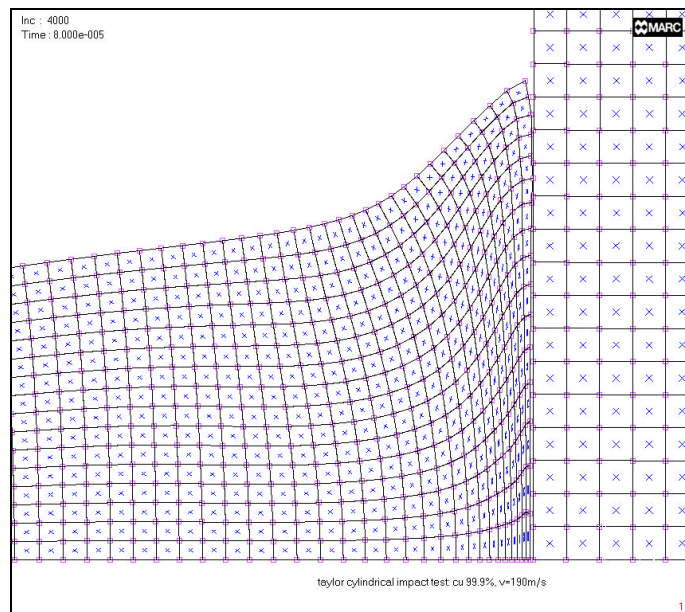


Figure 7.3 - Sketch of the finite and unbounded portions



a)



b)

Figure 7.4 - Detail of the mesh at the impact surface: a) undeformed and b) deformed mesh for copper. Here, severe element distortion is clearly visible in the near impact region

A preliminary study has been performed simulating the wall as infinitely rigid, as also reported in the literature, (J&C). However, this assumption demonstrated soon to be inadequate to describe the effective deformation process at the impact interface. In fact,

a very high frequency stress wave is generated at the interface between the body and the rigid wall resulting in contact chattering and other numerical problems.

Subsequently, the wall has been simulated much more similar to the real case, that is, a deformable body with elevated yield strength. Since the wall is now meshed as regular part of the problem its dimensions become important. In fact if only a portion of the wall is modeled, than spurious stress wave coming from reflecting finite boundaries can be generated.

Usually, a very large portion is modeled in order to avoid this even though require an additional number of elements that at the very end are not interesting from the problem point of view. An efficient alternative that has been explored is the use of semi-infinite elements. This is a six-node, axisymmetric element that can be used to model an unbounded domain in one direction. This element is used in conjunction with the usual linear element. The interpolation functions are linear in the 1-2 direction and cubic in the 2- 5-3 direction, as depicted in Figure 7.2. Mappings are such that the element expands to infinity.

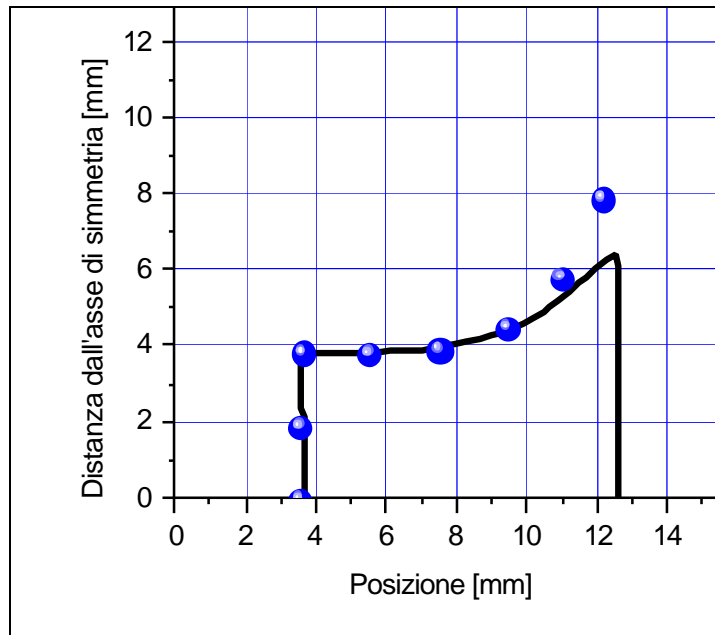
Displacements at infinity are implied to be zero; it is unnecessary to put boundary conditions at these nodes. This approach allowed to have full control on stress reflection at the target wall, Figure 7.3.

Material behavior has been modeled using Johnson and Cook strength model. Initial simulations have been performed without any strain rate and temperature effect. Subsequently, strain rate effect has been introduced and only in the final analyses both strain rate and temperature have been considered. In all calculation damage model as proposed by Bonora has been used. This parametric study allowed one to check the effect and the role of strain rate and temperature, separately, on the post impact deformed shape.

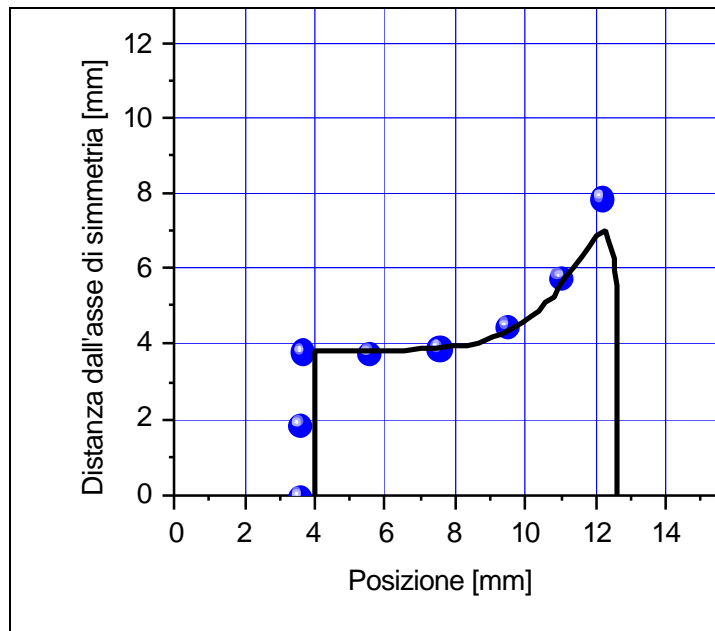
Impacts relative to three materials have been considered here. OFHC copper, Armco iron and AISI steel data are those given in the report. Here, Taylor cylinder has the same diameter (7.62 mm) for all three material while the its length (l_0) changes from 25.4 mm for copper, to 12.6 mm for Armco iron and 8.1 mm for AISI steel. Experimental data are also relative to different impact velocity: 190 m/s for copper, 279 m/s for Armco iron and 343 m/s for steel.

In Figure 7.4a-b an indicative sample of the initial mesh and the deformed one is given. Here the element distortion is clearly visible in the zone close to the impact surface.

Preliminary results using strain rate insensitive strength model, show that in all cases the normalized reduction between the final and the initial cylinder length is always lower than that found experimentally. For copper, in particular, excessive element deformation occurs just after $0.2\mu\text{s}$ over the entire expected duration time of $80\mu\text{s}$.

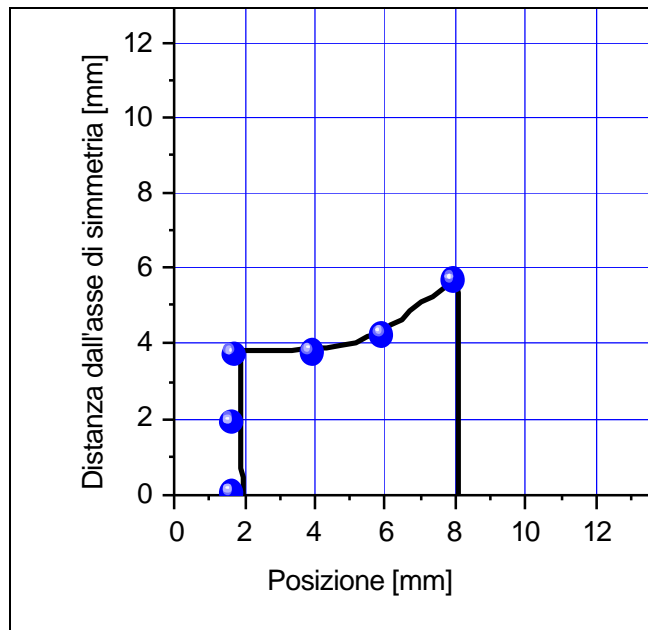


a)

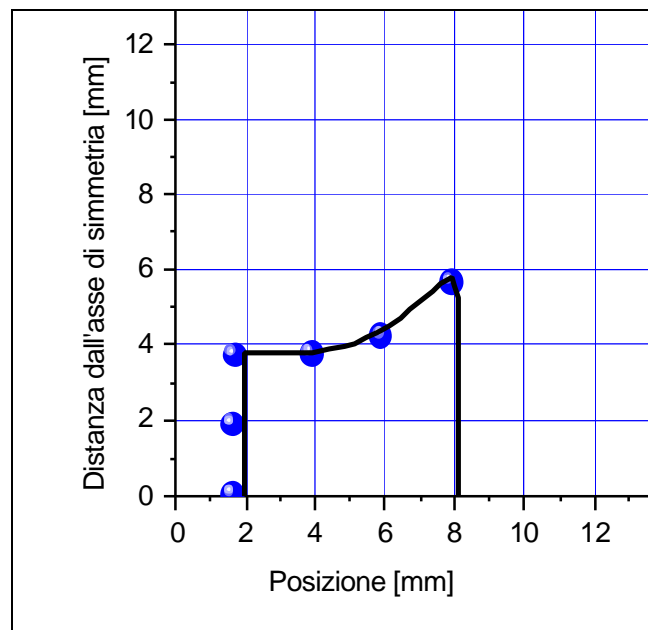


b)

Figure 7.5 - Comparison of post impact deformation with experimental data for ARMCO iron ($l_0=12,6\text{mm}$; $V_0=279\text{m/s}$): a) strain rate sensitive material, b) strain rate and temperature sensitive material.

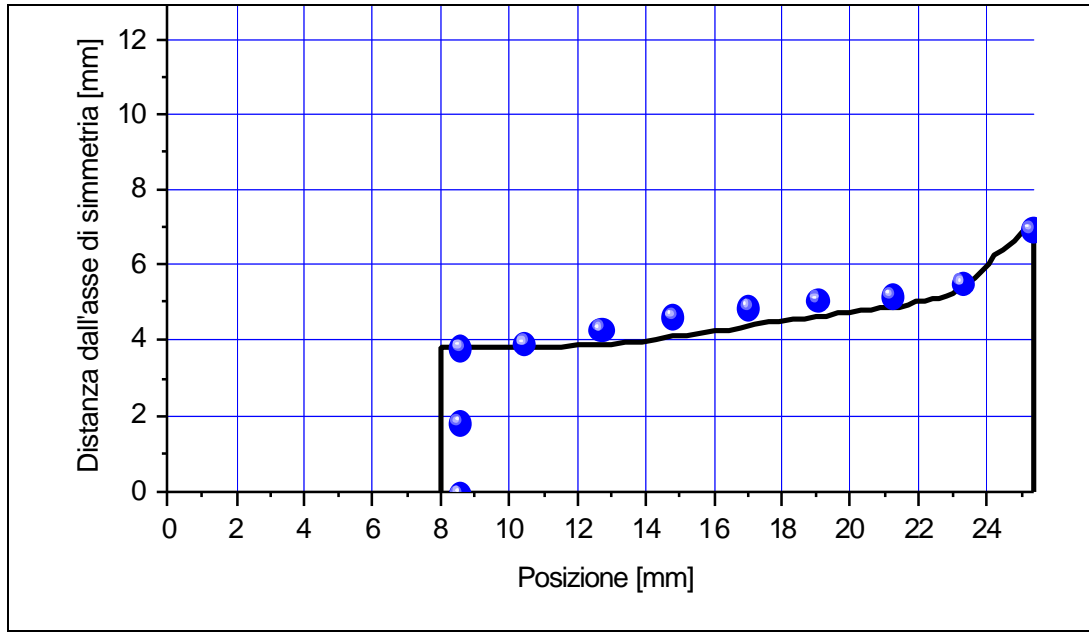


a)

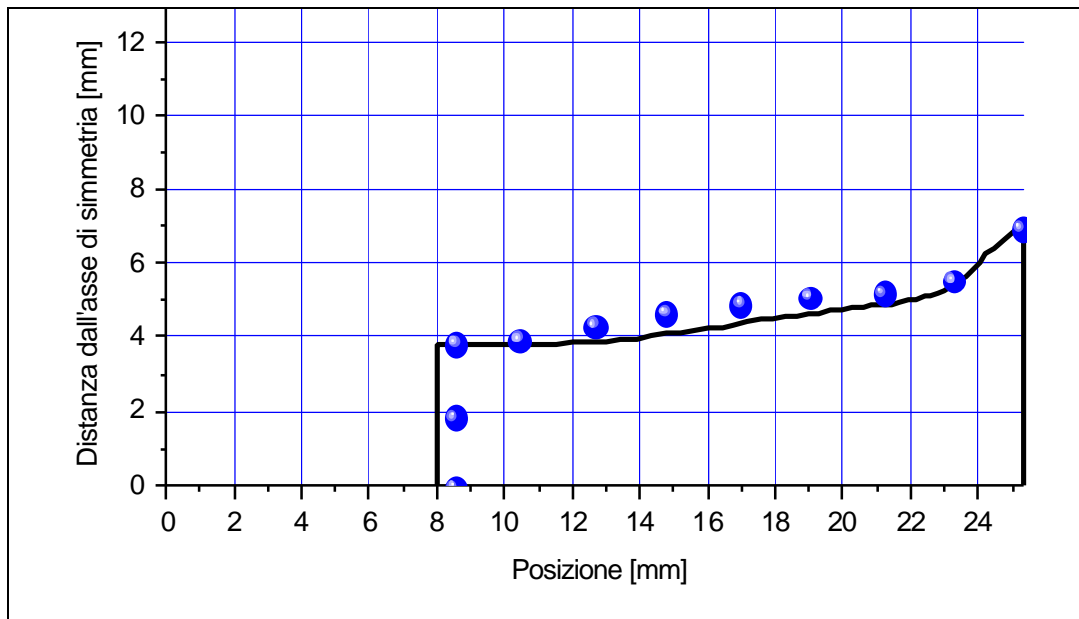


b)

Figure 7.6 - Comparison of post impact deformation with experimental data for AISI steel ($l_0=8,1\text{mm}$; $V_0=343\text{m/s}$): a) strain rate sensitive material, b) strain rate and temperature sensitive material.



a)



b)

Figure 7.7 - Comparison of post impact deformation with experimental data for OFHC copper ($l_0=24.5\text{mm}$; $V_0=190\text{ m/s}$): a) strain rate sensitive material, b) strain rate and temperature sensitive material.

The use of a strain rate sensitive strength model improve the quality of the results reducing the gap between the predicted length reduction and the experimental measurement as summarized in Table 7.1

	Exp. data	Strain rate insensitive	Strain rate sensitive	Strain rate and temperature sensitive
OFHC copper	0.68	-	0.65	0.66
ARMCO iron	0.70	0.58	0.70	0.66
AISI steel	0.73	0.80	0.77	0.61

Table 7.1 - Comparison of predicted length reduction after impact and experimental data for different strength models

In Figures 7.5-7.7 the deformed mesh compared with experimental data are given for Armco iron, AISI steel and Copper. Only ARMCO iron shows a large variation in terms of length reduction and mushroom shape with the different model formulations. In particular, the role of temperature effect is crucial for accurate post impact deformation prediction for ARMCO iron that, also from Hopkinson pressure bar tests, is known to be particularly sensible to it.

Even though deformation along the impact surface can be severe, damage calculations show that a limited damage accumulation can be found only at two location: along the symmetry axis, nearby the impact surface, and at the free upper corner. Here severe deformation occurs due to the mushrooming process. In some cases, for high velocity impact, damage indicates the possibility for erosion conditions and loss of axial symmetry.

A sample of the damage map for the copper Taylor cylinder is given in Figure 7.8. Here, as it can be seen there is no element complete failure. This latter result is consistent with the experimental observation of Johnson and Cook that did not find any visible void growth at the free surface.

Another interesting results, is that in most of the cases it is very difficult to identify the exact location for the transition between the deformed and undeformed cylinder length for yield stress measurement as given in Eqn (7.1.1). Copper shows clearly two different slopes in the deformed region (Figure 7.8). If we apply the theory tout court we get a reference dynamic yield stress of 171.6 MPa approximately. The major problem with the Taylor impact test is that the strain rate is not constant along the cylinder. In order to have a rough idea of the nominal strain rate, an average strain has been taken as the cylinder shortening, measured on the rear surface, normalized with respect to the initial length. This leads to a strain rate of the order of $185 \cdot 10^3 \text{ s}^{-1}$ to which correspond a J&C predicted value of 117 MPa. It has to be noted that in order to match the same yield stress value, a strain rate of $5.6 \cdot 10^3 \text{ s}^{-1}$ (sic!) should be inferred in the J&C strength

model. Even considering the first slope for the determination of H we get a too high yield stress value (that is 152.6 MPa)

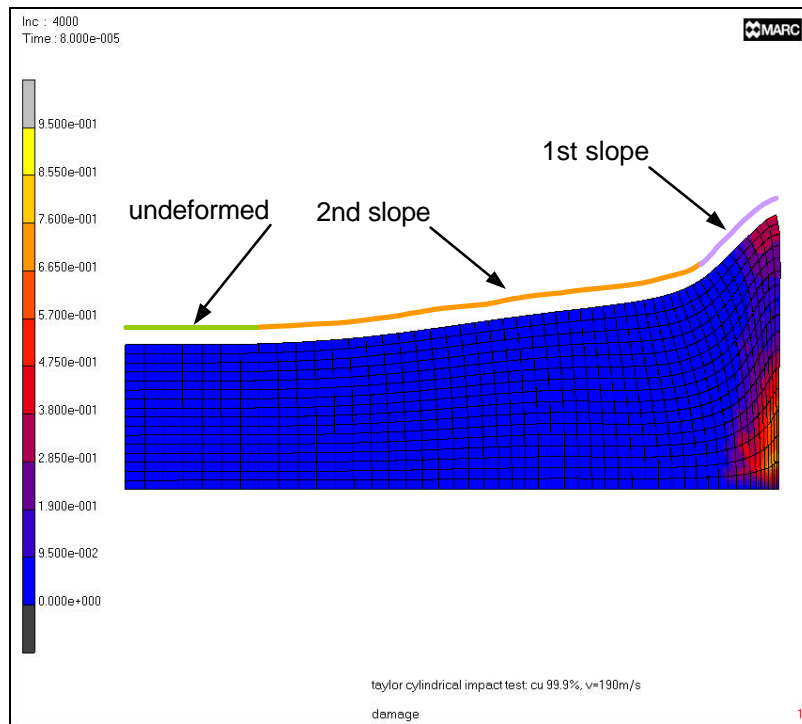


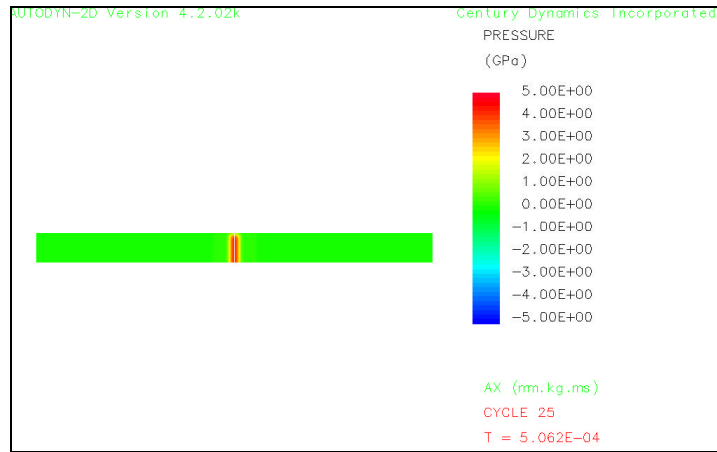
Figure 7.8 - Damage map in Taylor cylinder post impact test for copper

7.2. Rod-on-Rod (ROR) impact test

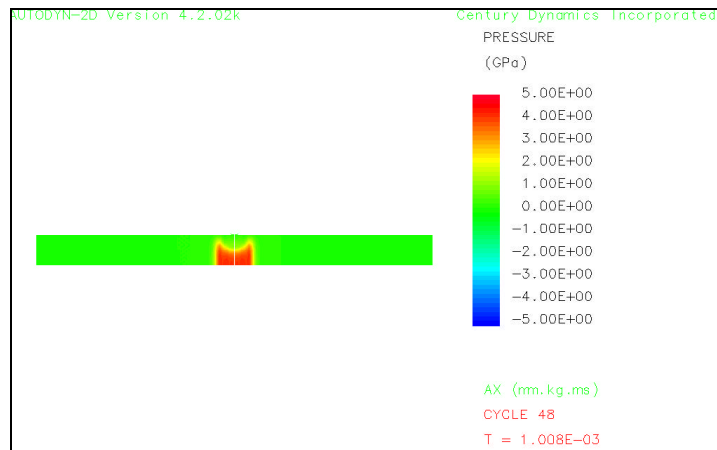
Taylor impact test is a well-known technique widely used in the past to identify material dynamic response. The major limitation of this technique is that material dynamic yield stress can be correlated to the impact velocity and not to the strain rate since there is not a unique or a reference strain rate value that can be addressed in the geometry. Standard Taylor impact test is performed shooting a rectangular cylinder made of the material under investigation against a rigid wall. The projectile/target material mismatch is responsible for shear forces that can affect the deformation of the projectile as a result of the friction forces developed along the contact surface. In addition, the presence of un-quantified friction makes difficult and arbitrary the understanding of numerical simulation results.

In order to come around these problems, the symmetric Taylor impact otherwise indicated as rod-on-rod (ROR) impact test has been proposed. In this configuration, a cylinder is shot against a steady cylinder of same dimensions and made of the same material. If the correct axial alignment is assured, thus contact will develop without friction. Today, the Taylor impact test is no longer used for its original purpose but

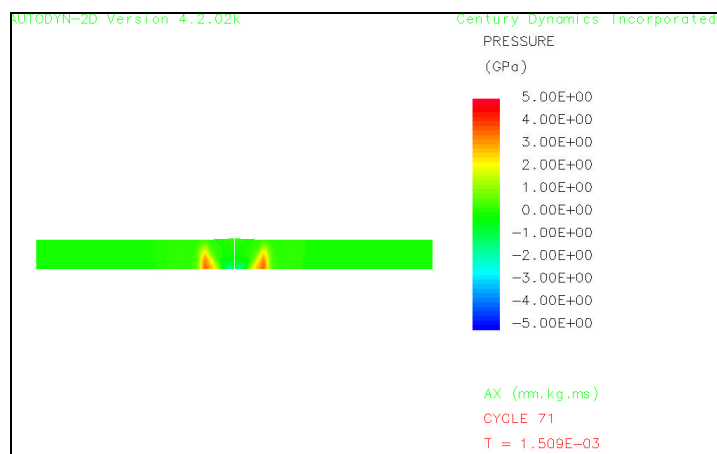
instead it is used for constitutive modeling identification through the comparison of the deformed configuration either during the impact, by means of high speed camera, or post test.



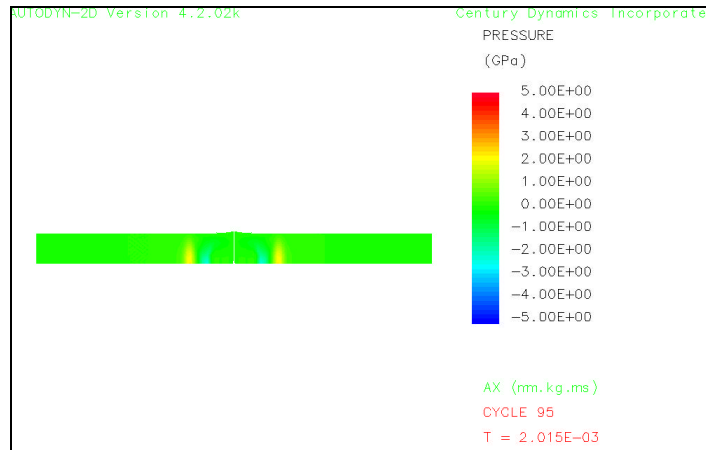
a)



b)



c)



d)

Figure 7.9 – Compressive wave formation and fading due to free boundary release wave incoming.

Following the implementation of the Bonora damage model in the hydro-code Autodyn, the ROR impact test has been simulated in order to check the effective model prediction capabilities in this impact configuration.

A ROR impact test has been modeled generating two separate grids, one for each cylinder. The target cylinder has the same dimension of the impacting one. Since in the effective test the target cylinder is simply suspended, no boundary conditions have been apply in the simulation.

In Figure 7.9a-d four different shots of the deformed shape of both cylinders is given for different time cycles. Contours plot show pressure wave development and its extension.

It has been pointed out that damage strain threshold seems to be sensitive to the compressive pressure. In order to address this issue a preliminary analysis of the intensity of pressure wave have been made. The calculated pressure during the first stage of the contact is very high. For a reference impact velocity of 232 m/s, the pressure goes up to 6.0 GPa. This value is very high even if compared with pressure generated at 185 m/s in flying plate impact.

Pressure wave shape is rectangular (top-flat) at the beginning of the contact. As soon as the stress wave starts to travel in the cylinder along its axial direction, release waves are generated at the radial free boundaries weakening the compressive wave as schematically depicted in figure 7.10. This mechanism of stress wave superposition may results in different failure process according to the material damage threshold strain as it will be discussed later.

As far as concern material damage threshold strain, it has been pointed out in the previous sections that this parameter may show pressure sensitivity. Since pressures

generated in the ROR impact configuration are well below the values of those produced in the flying plate impact test at similar velocity, the quasi static damage threshold strain has been used in the simulations.

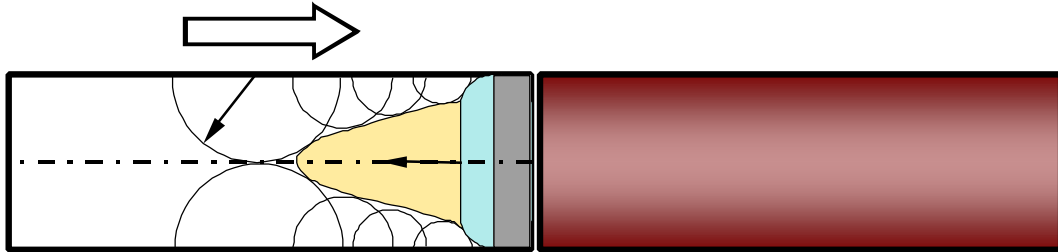


Figure 7.10- Compressive wave fading scheme in ROR impact test.

In order to allow comparison with experimental data available in the literature, the experimental configuration adopted by Mayes et al. (Ref. 7.3) and their results have been taken as reference test case. Here, two different initial grain size OFE copper were used. The larger grain material, $75\mu\text{m}$, was impacted at 300m/s and 392m/s while the finer grain copper, $40\mu\text{m}$, was impacted at 233m/s . Similarly to the Taylor impact, numerical simulation performance was checked comparing the recovered test cylinder deformed shape with the calculated one. In Table 7.2 the calculated final diameters at impact surface are compared with the experimental measurement for all velocities and microstructures showing a very good agreement at least for lower velocity impacts.

Successively, damage pattern development has been investigated and compared with photomicrographs performed on the sectioned rods.

In accordance with experimental measurements, larger damage amount is found for increasing impact velocity on large grain size microstructure. Here, damage is caused by large deformation which occurs close to the contact surface at the later stage of the impact process under low stress triaxiality level.

	Larger grain 300m/s	Larger grain 392m/s	Fine grain 233m/s
Computed diameter	12.2mm	15.0mm	10.6mm
Expeimental mesuraments [Ref. 7.3]	12.4mm	12.5mm	10.9mm

Table 7.2. Computed and experimental impact section diameter.

Surprisingly, fine grain material shows a larger amount of damage for lower impact velocity with respect to the one with large grain size. This result clearly indicates that damage parameters should differ for both materials.

A possible explanation can be given as follows. Grain size has a strengthening effect. Small grain size microstructure usually results in higher material yield strength and reduced ductility. Ductile damage can start at the inclusions (as for steels) or at the grain boundaries, as for copper. In this latter case, damage results from the impossibility of the material to accommodate, at grains level, the external imposed deformation. Consequently, in fine grain microstructure, where dislocations motion is highly constrained, ductile damage will start at lower strain level compared with large grain microstructure. In addition to this, larger damage extent is expected for the finer microstructure for a given strain level.

According to this, the threshold strain values available for different materials have been collected and plotted as a function of the average reference grain size. In Figure 7.11 the plot is given together with the interpolating fit. At this point it is important to underline how a clear relationship between ϵ_{th} and the average grain size exists independently of material.

The plot in Figure 7.11 indicates that ϵ_{th} seems to show a lower bound limit. For grain size material below this limit value the damage threshold does not exist indicating that the ductile damage processes are inhibited due to the loss of ductility. This is in accordance with recent experimental observations reporting that material behavior and failure changes from ductile to brittle when the material grain size becomes very small. In figure 7.12 the ductility expressed as elongation at fracture for nanograin materials is given. It is interesting to observe how failure data for copper are limited in the range of 18% for grain size of the order of 1 μm , while ductility of 1.5-2.0 are common for larger grain microstructures confirming the transition from ductile to brittle.

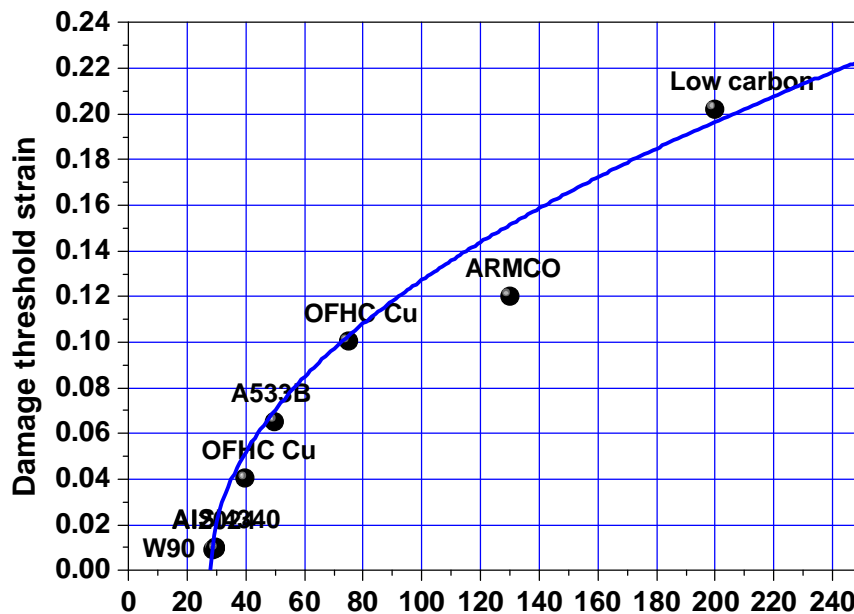
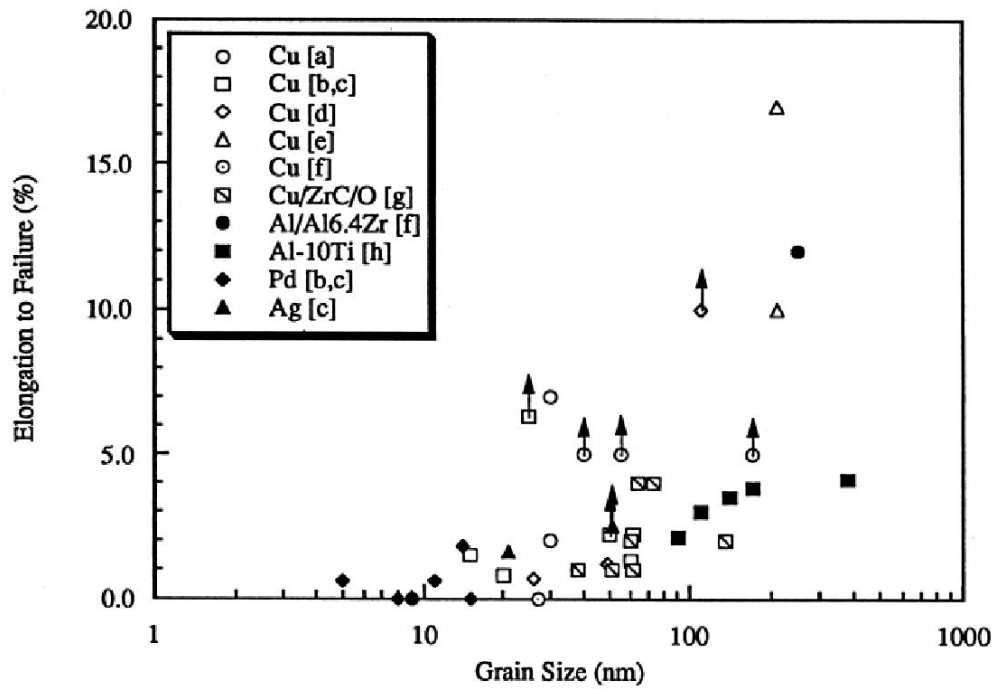


Figure 7.11- Evolution of damage threshold as a function of grain size

Another interesting result is the similarity of the trend found for the damage threshold strain as a function of the grain size with the so-called Hall-Petch effect.



Key to Sources

a. Gunther et al. 1990	e. Gertsman et al. 1994
b. Nieman et al. 1991a	f. Eastman et al. 1997, 173-182
c. Nieman et al. 1991b	g. Morris and Morris 1991
d. Sanders et al. 1996, 379-386	h. Liang et al. 1996

Figure 7.12 – Elongation to failure in nanocrystalline metals

The Hall-Petch effect states that material yield strength varies with the grain sizes as follows:

$$\sigma_y = \sigma_0 + kd^{-0.5} \quad (7.1.5)$$

where σ_0 and k are material constant. Here, it has been found that damage threshold strain as a function of material grain size is very well fitted by the following relation:

$$\varepsilon_{th} = A \cdot (d - d_0)^{0.5} \quad (7.1.6)$$

Finally in Figure 7.13, the fitting line of the damage threshold strain as a function of the square root of the grain size is also give showing the well alignment of experimental data. According to this, a new damage threshold strain value (~ 0.04) has been assumed

for the 40 μm grain size and used in the simulation of ROR at 233m/s impact velocity. This time, the final overall deformation, as well as the damage pattern, resulted to be in a very good agreement with the experiments, Figure 7.14.

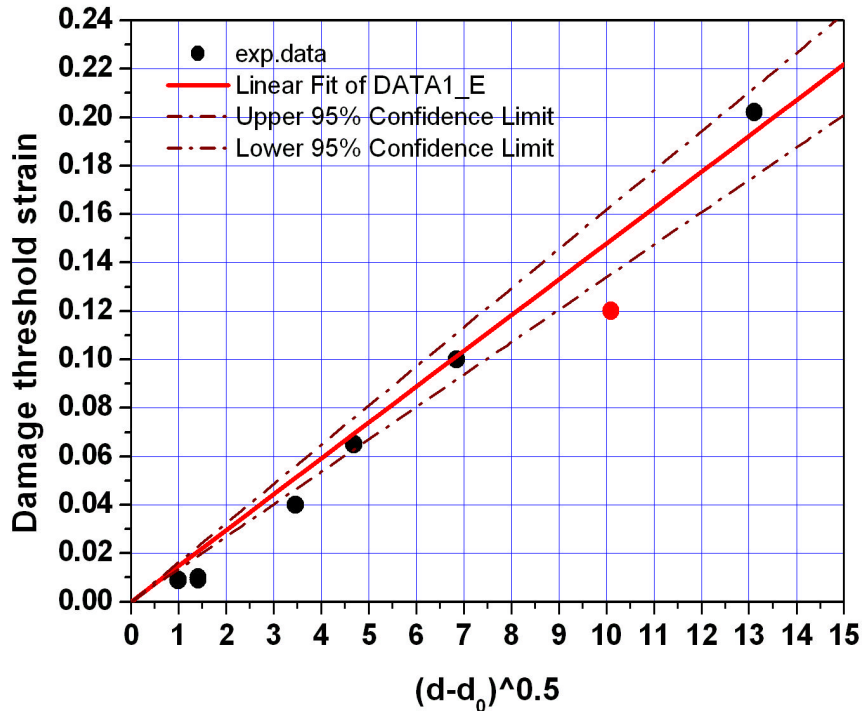


Figure 7.13 – Damage threshold strain fit as a function of grain size

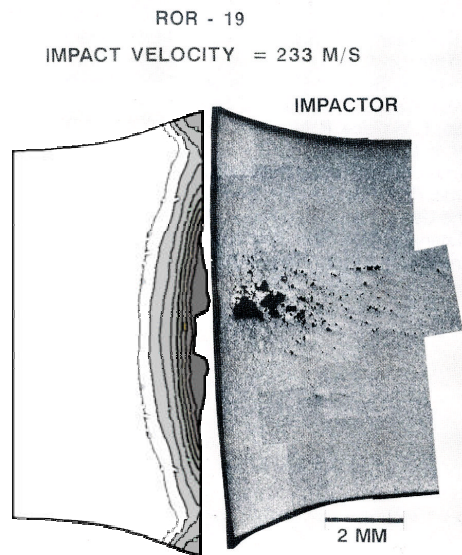


Figure 7.14- Experimental [Ref.7.3] and calculated deformed microstructure of 40mm OFE copper impacted at 233m/s.

The analysis performed with this new damage threshold strain value reveals much more about how damage develops during the impact. In fact, damage seems to occur mainly

due to the focusing of the release stress waves radially traveling from the rod free surface toward the rod axis. This process, which is characterized by low plastic strain level and high stress triaxiality, can initiate damage processes in the finer grain materials with lower damage threshold strain. Here, contrarily to the case of large grain material, this damage mechanism takes place in the early stage of the impact process, showing similarities with spall fracture in flying plate impact test.

7.3. References

Ref. 7.1 – Taylor, G. I., Proc. Roy. Soc. Lond. A., 194, p. 289, (1948)

Ref. 7.2 – Wiffin, A.C., Proc. Roy. Soc. Lond. A., 194, p. 300, (1948)

Ref. 7.3 - Mayes, J. L., Hatfield, S. L., Gillis, P. P., and House, J. W., Int. J. Impact Engng. 14, pp.503-508 (1993)

8. Numerical Investigation of Advanced Dynamic Testing Techniques for High Strain Rates Material Testing

The identification of strain rate effect on material behavior is a mandatory requirement for correct simulation of dynamically loaded components. In the last decades a number of experimental techniques have been developed. Most of them allow the identification of specific material response such as the Hugoniot elastic limit with the flying plate impact tests. The determination of the whole dynamic uniaxial stress-strain curve requires uniform stress state over a reference volume together with a strain rate constant as much as possible for the entire duration of the test. This is usually achieved with the use of cylindrical or flat specimen geometry that can allow a direct material response measurement if opportunely instrumented. The major limitation is given by the maximum strain rate achievable. In fact, according to the definition of strain rate,

$$\dot{\varepsilon} = \frac{d\varepsilon(t)}{dt} = \frac{1}{L_0} \frac{dL}{dt} = \frac{v}{L_0} \quad (8.1.1)$$

it follows that for a given imposed velocity v at one of the specimen ends, the strain rate is univocally determined by its gauge length L_0 . Even though, the specimen length can be reduced to zero, in practical application the need to grip the specimen ends define a lower bound limit below which it is impossible to go. In addition, the use of short or very short specimen geometry, which tends to look similar to a needle, open the question if the measured data can be transferred to the component dimensional scale.

Since the possibility to develop alternative new, cheap, experimental technique to determine material dynamic behavior is always welcome, two new methodologies are examined in the following sections.

The first technique investigated is the flying wedge test recently developed by Sturges and Cole (Rif. 8.1) at the University of Leeds, UK. This configuration allows one to dynamically pull the specimen from both ends at the same time, resembling in a dynamic way, the loading mechanism of standard traction test.

The second technique consists in an innovative use of the Charpy hammer test used not for traditional fracture mechanics purposes but to generate elevated strain rate as a result of the dynamic impact of the hammer on the specimen. This methodology has been conceptualized at the University of Cassino and presented here for the first time as a result of the present research.

Both methodologies have been numerically investigated in order to verify the effective stress-strain histories development in the sample and the resulting strain rates achievable.

In order to have a comparison with more traditional technique, the Hopkinson pressure bar (both in compression and in tension) has been extensively investigated. Here, the purpose of the study was twofold: to verify the finite element methodology used with the reference solution available and to compare the expected material stress-strain response, as well as the strain rate values, for the other two techniques. In addition these results have been also used to design a pure tensile Hopkinson bar at the University of Cassino and to commission the preliminary experimental tests.

8.1. Hopkinson Pressure Bar Finite Element Simulation

The Hopkinson pressure bar apparatus has been initially developed by Hopkinson in 1914. It consists in a cylindrical specimen sandwiched between two slender bars, the incident (input) and the transmitting (output) bar. A compressive uniaxial stress pulse is generated in the input bar by impacting a third bar, indicated as the striker bar, Figure 8.1

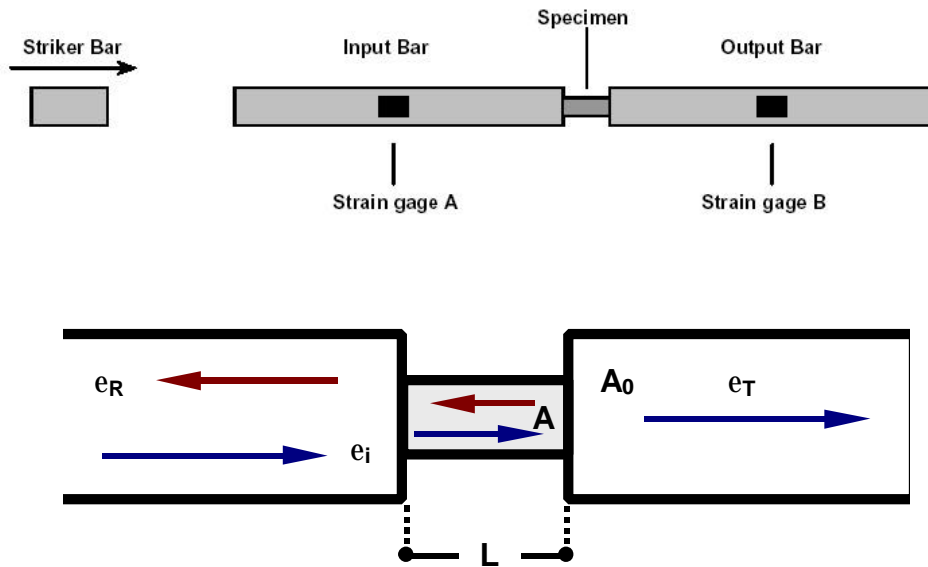


Figure 8.1- Sketch of the Hopkinson pressure bar apparatus

The compressive stress pulse generated by the impact of the striker travels through the input bar. At the interface with the specimen, the pulse is partially transmitted and partially reflected back. Similar process occurs at the second interface between the specimen and the output bar. The difference of the measured deformation as function of time at two stations in the input and output bar gives the effective deformation pulse transmitted in the specimen. So long the input and output bars remain in the elastic regime, the strain rate can be derived from the reordered strain histories. Finally,

geometrical considerations and equilibrium equations it is possible to determine the stress in specimen that are:

$$\frac{d\varepsilon_S(t)}{dt} = -\frac{2C_0}{L}\varepsilon_R(t) \quad (8.1.2)$$

$$\varepsilon_S(t) = -\frac{2C_0}{L} \int_0^t \varepsilon_R(t) dt \quad (8.1.3)$$

$$\sigma_S(t) = E \frac{A_0}{A} \varepsilon_T(t) \quad (8.1.4)$$

where the subscript _S, _R and _T indicates “specimen” “reflected” and “transmitted”, respectively; C_0 is the sound speed in the bar ($C_0=(E/\rho)^{0.5}$) and L is the specimen length, A and A_0 the section of the specimen and bar respectively.

The stress pulse generated in the input bar is function of the striker length and velocity. The generated stress amplitude, under the assumption of perfect impact, is given as:

$$\sigma = \frac{1}{2} v \rho C_0 \quad (8.1.5)$$

while the duration of the stress pulse is given according to:

$$T = \frac{2l_{stk}}{C_0} \quad (8.1.6)$$

Detailed derivation of the Hopkinson pressure bar equation can be found elsewhere, Ref. 8.1

In order to apply the above-summarized relations, it is important that the following two conditions are verified: unidimensional stress propagation and uniform deformation of the specimen. In the real cases, edge effects are always present in form of noise in the recorded signal in what so called oscillations of Pochhammer-Chree. Similarly, the second assumption of uniform stress in the specimen is only verified if appropriate relation between the specimen length and diameter are chosen. In the literature it is discussed how an optimum ratio can be found for:

$$\frac{l}{D} = \sqrt{\frac{3}{4}} \nu \quad (8.1.7)$$

where ν is the bar Poisson ratio.

As stated before, the deformation signal is recorder at two stations through the use of strain gauges. The expected signal is given in Figure 8.2.

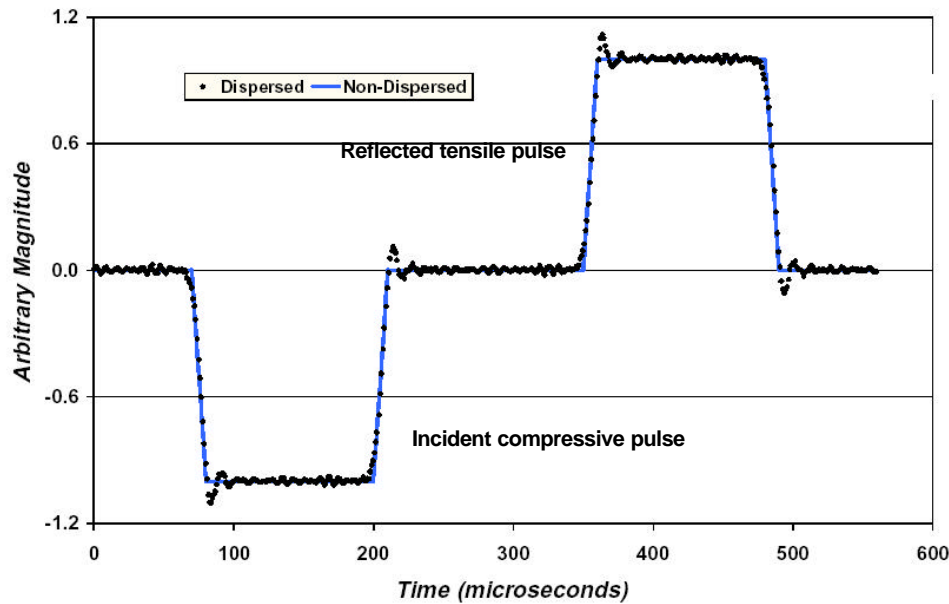


Figure 8.2- Scheme of the theoretical expected signal outputted from the Hopkinson bar

The equations that allow to determine both strain and stress in the specimen, place a limitation on the bar behavior, which has to remain elastic, and consequently, as far as concern the split Hopkinson pressure bar configuration, on the maximum striker velocity.

The split Hopkinson bar in tension requires a modification of the specimen-loading device, since the compressive pulse has to be reversed in a tensile one. In the literature there are a number of technical solutions. At the University of Cassino the idea initially developed by Staab and Gilat, has been implemented. Here, the tensile pulse is directly generated without the need to impact one bar with a striker. A portion of the input bar, opposite to the end where the specimen is positioned, is clamped and the end is pre-tensioned. The release of the clamp generates two tensile pulses one traveling toward the specimen and the second one in the opposite direction. The clamping and release fixture is critical for the cleanness of the generated signal. In order to allow instantaneous release of the clamp, a notched brittle bolt is usually employed. Tightening the bolt, the clamping stress increases together with the stress in the bolt up to failure. In Figure 8.2 a schematic plot of the Hopkinson pressure bar in tension as implemented at the University of Cassino is given.

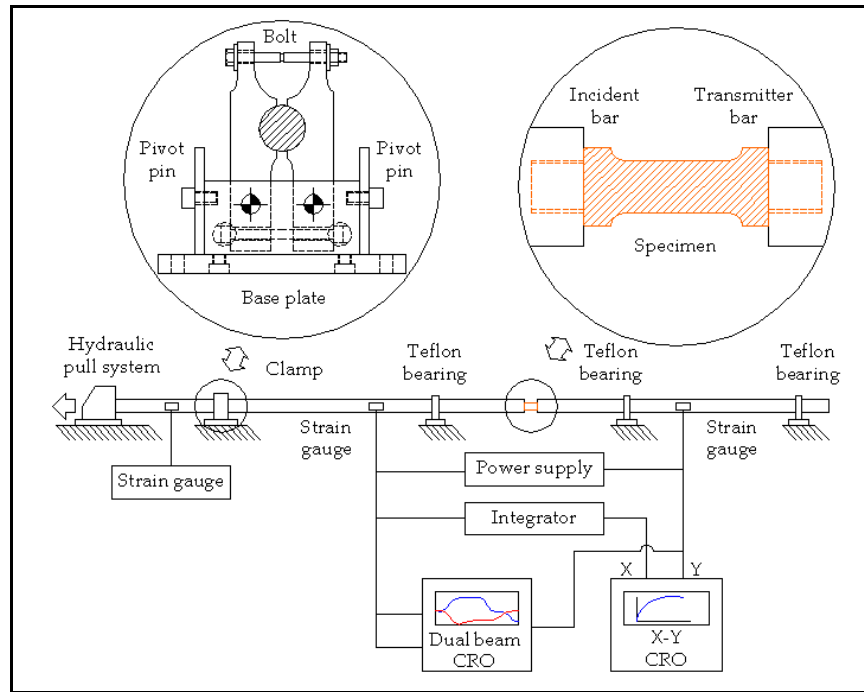


Figure 8.3- Schematics of the Hopkinson bar in tension

In order to investigate the expected signals and specimen behavior, both Hopkinson bar configurations have been simulated numerically with standard finite element method.

In order to simulate transient stress wave motion, in both bars and specimen, direct integration scheme has been used. A four node element using bilinear function has been used. Finite strain, lagrangian update and large displacement options have been used in the elastic-plastic analysis. As far as concern the split Hopkinson pressure bar in compression (SHPBC) two bars 1.1 m long and a striker 0.250 m long have been modeled, both with 10 mm in diameter. Due to the axial-symmetry, only half of the entire geometry has been modeled. The constant element mesh size of 2.0 mm long for 1.0 mm height has been used to model the bars. The compressive specimen geometry is a cylinder 8 mm in diameter and 4 mm height. Multiple contacts between deformable bodies have been implemented: striker-input bar, input bar-specimen, specimen-output bar. In figure 8.4 a detailed view of the near specimen region is given for reference

Direct integration has been performed using two different time steps: a longer one, when the pulse is traveling in the bar and smaller one when the pulse is traveling across the specimen. Natural damping has been implemented in form illustrated in the previous section. Here, a constant $\gamma=0.8$ has been used for all analyses. In order to assure the independence on the numerical integration scheme used, a comparison of Humbolt and Newmark- β method has been also performed showing no appreciable differences in the results.

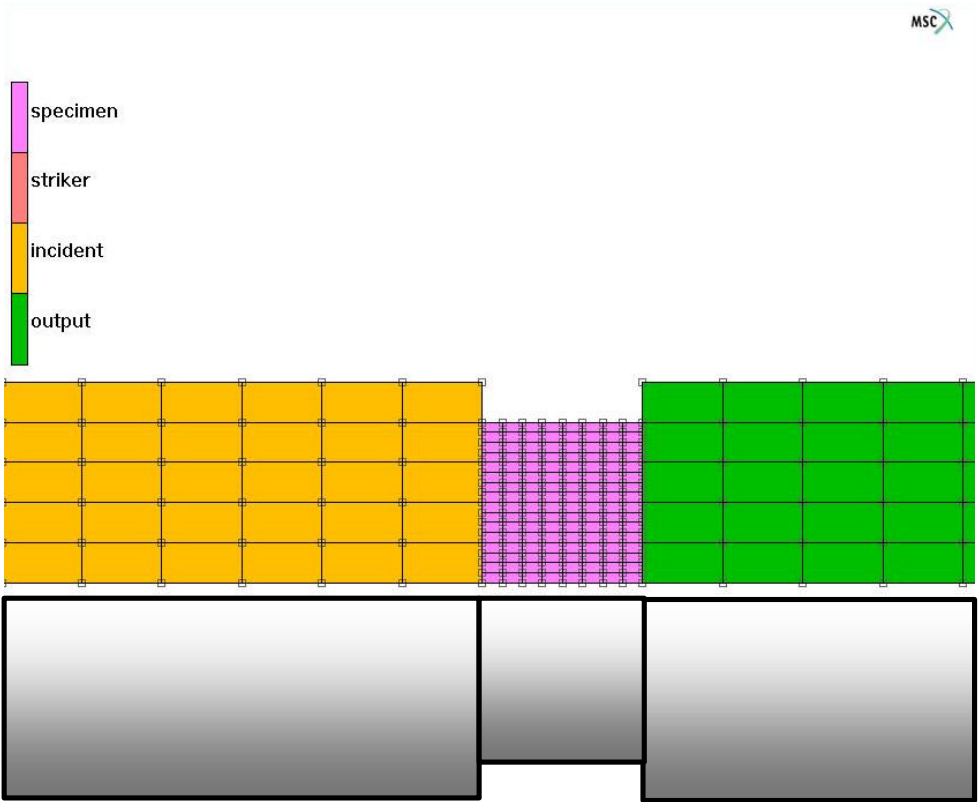


Figure 8.4 – Detail of the mesh at the specimen location

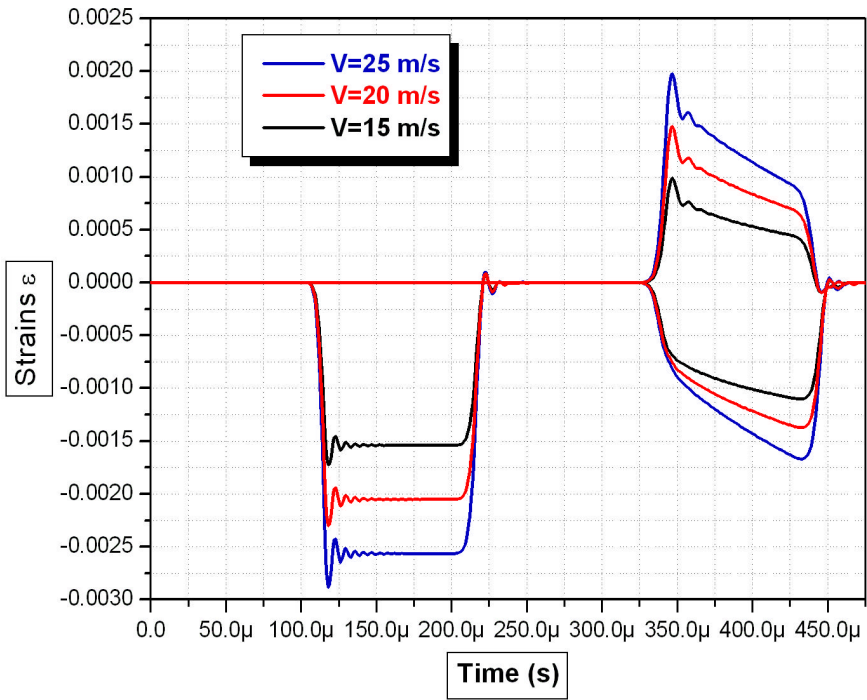


Figure 8.5- Strain signals in simulated SHPBC for three different impact velocities.

Different materials have been simulated for the specimen. The following results are those relative to OFHC copper. As for the flying plate impact test, both strain rate sensitivity, temperature effect and damage have been incorporated in the constitutive modeling.

In Figure 8.5 the strain diagram versus time, showing the three signals are given for three different striker impact velocity values.

Here, the three waves system is given. The incident strain wave is square with flat top over which the Pochhammer-Chree oscillations are clearly visible. While on the right hand side of the plot both the reflected and transmitted waves are shown. The three waves are recorder on the bars looking at the nodes, representing the strain gauges, time-histories. It is interesting to note how the increase of the initial impact velocity simply scales the maximum strain value in the incident strain pulse while, due to the material strain rate sensitivity, the transmitted wave shows an increase of the slope in the later part of the signal. If strain signal are transformed in stress, according to 8.1.4 we get the plot given in Figure 8.6

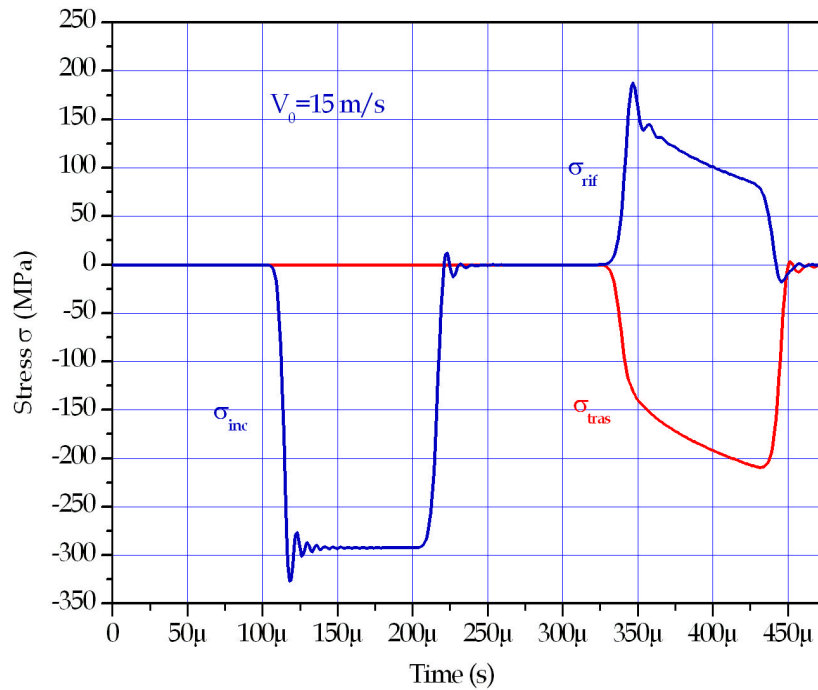


Figure 8.6- SHPBC derived stress diagram for $v=15$ m/s

Once again the Pochhammer-Chree oscillations disappear almost immediately due to the high slenderness ratio of the simulated bars ($l/d=110$). Both the stress wave intensity and pulse duration are in a very good agreement with the theory which gave:

$$\sigma = \frac{1}{2} \rho C_0 v_0 = \frac{1}{2} \rho \sqrt{\frac{E}{\rho}} v_0 \simeq 292 \text{ MPa}$$

$$\Delta t = \frac{2l}{C_0} \simeq 102 \text{ } \mu s$$
(8.1.8)

Another result is given by the occurrence at the same time of the transmitted and reflected stress wave, without appreciable delay in time. Additionally, the stress equilibrium is verified at any time increment, even though the stress waves have different shapes, for which the sum of the reflected plus the transmitted stress pulse is equal to the incident one. The shape of the reflected stress wave is peculiar of the compressive test. In fact, if we look at the equation that states:

$$\frac{d\varepsilon(t)}{dt} = -\frac{2C_0}{L} \varepsilon_r(t)$$
(8.1.9)

it follows that the strain rates cannot be constant during the compression of the specimen mainly due to the strain rate sensitivity of the material and the progressive increase of the specimen section due to the Poisson effect. It follows that reference strain rate for compressive SHPB are only averaged values. These two effects explain why a steep decreasing slopes when more intense plastic waves are induced in the specimen.

As anticipated, the role of the integration algorithm has been checked. In Figure 8.7 the comparison of the stress distribution as a function of the distance from the impact surface is given for Humbolt single step integration algorithm and Newmark- β . Here, both method gives comparable results showing no effect due to the choice of the integration scheme.

The split Hopkinson pressure bar in tension (SHPBT) has been modeled as follows. A two bars system has been modeled similarly to the SHPBC. Here, the incident bar is 1.5 m long while the output one is 1.1m long. The portion of the incident bar used to generate the tensile stress pulse is 450 mm long. The bar diameter is 9 mm while the specimen, in the typical bone cylindrical shape is 8 mm long and 4 mm in diameter. Since the specimen is tightly skewed in both bars, no contact has been necessary in the fem simulation but a continuous mesh has been generated. In Figure 8.7 a detailed picture of the mesh close to the specimen section change is given for reference.

The loading of the clamped section would require a preliminary quasi static-solution to be used as initial condition in the dynamic transient. In order to avoid complications, the following scheme has been used. The nodes along the section at which the clamp is located are initially constrained. An imposed displacement is imposed at the bar free end explicit integration is performed with a large time step in order to avoid transient evolution and to reach in a short time to the steady solution.

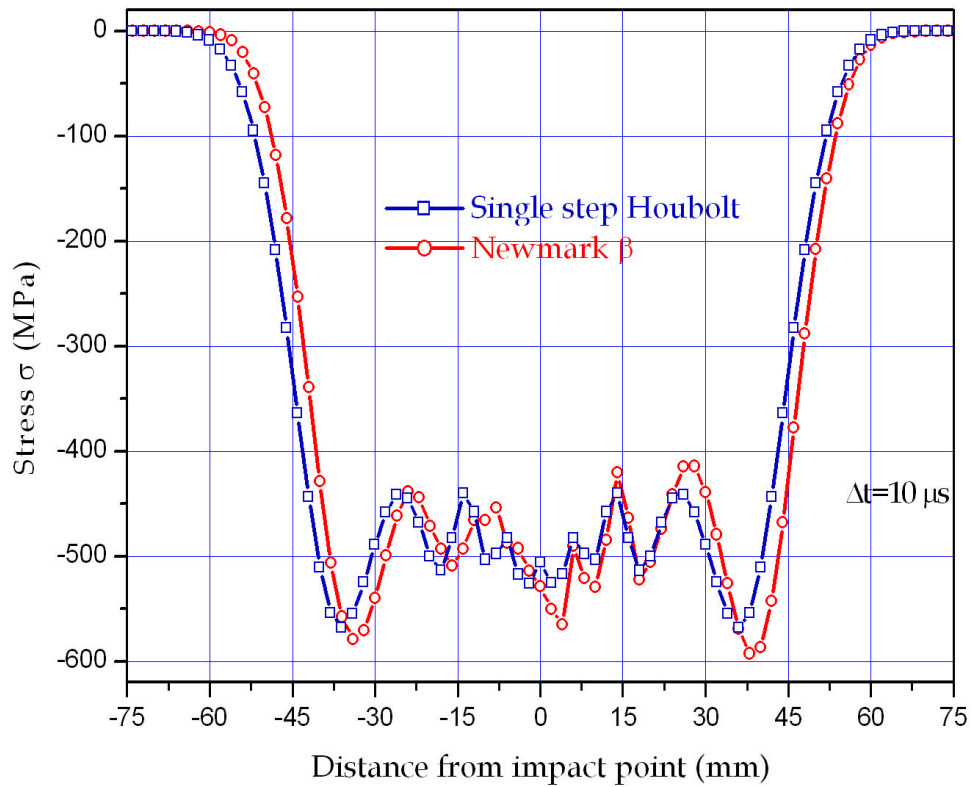


Figure 8.7 – Comparison of stress vs distance from impact with Newmark and Houbolt integration algorithms

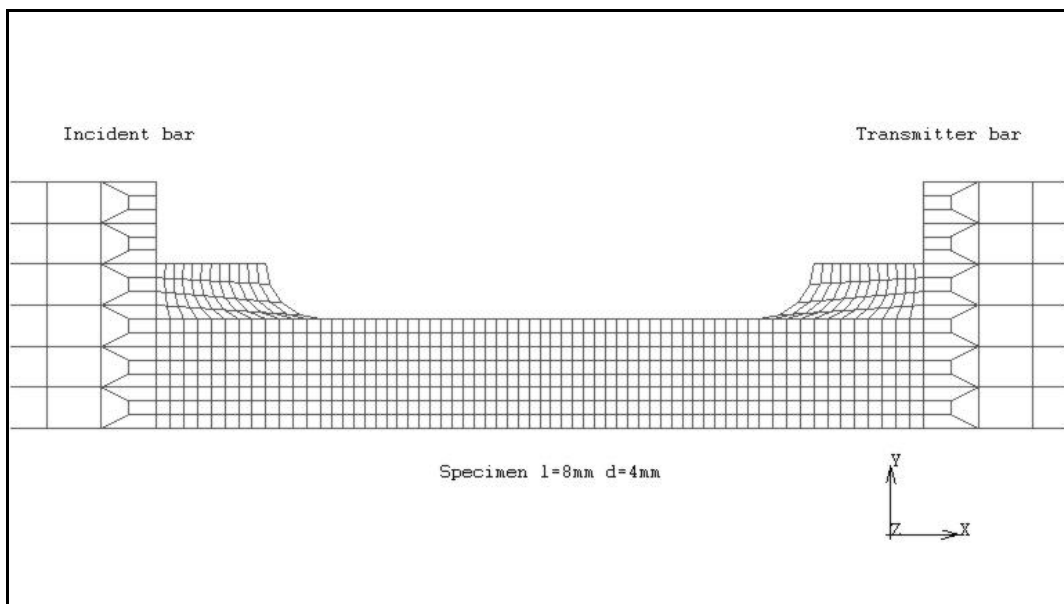


Figure 8.8- Detailed mesh for the SHPBT near the specimen section change

Since the process is purely elastic, there are no errors induced by using a large time step. In this way after few time steps the steady loading condition is reached without any bouncing stress wave in the loaded portion of the bar. At this point the boundary conditions simulating the clamps are removed in one step and the system is left free to evolve. In this way the tensile pulse is generated similarly to what happen in the real case. A time step of $2\text{E-}07$ s is used for the stress pulse traveling in the bar but it is reduced by a factor of 10 ($4.5\text{E-}08$ s) when the pulse reaches and goes through the specimen. The element minimum dimension used for the specimen mesh is 0.2×0.25 mm

In Figure 8.9 the simulated stress pulse reordered at the strain gauge stations is given similarly to Figure 8.5. In this cases three different curves for three values of the nominal imposed strain at the clamped bar portion are given for reference.

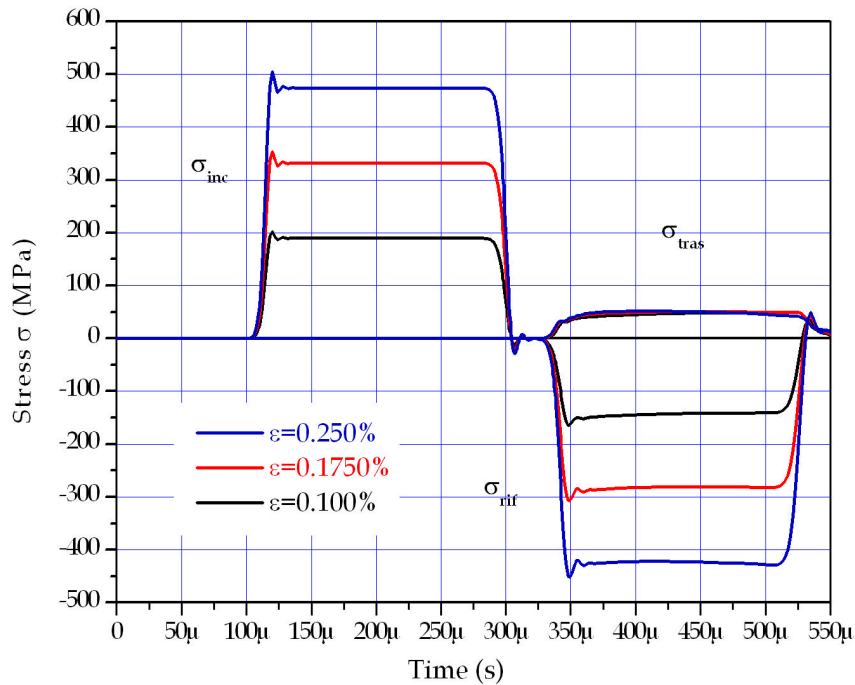


Figure 8.9- Stress pulses in SHPBT

These signals show a better regularity than those obtained in the compression tests. The regular shape of the reflected signal is a clear indicator of good strain rate versus time imposed to the specimen. Using the relation given in Eqn. 8.1.2, the strain rate, as a function of time, can be derived, Figure 8.10. The shape of the derived signal is very regular and close to the ideal square-top theoretical form. The flat-top shape is a clear indicator that the strain rate remains constant during the entire traction test. Even the tensile test shows some problems mainly related to the difficulty to explore the dynamic elastic strain range as a result of the oscillating processes, which increases with the strain rate, and the lack of uniform deformation state in the sample at the beginning of the test. In addition to that, the shape and dimensions of the specimen have an effect in

the non-homogeneous deformation distribution. The major consequence of this, is that the calculated dynamic Young modulus is lower than that extrapolated from quasi-static test data.

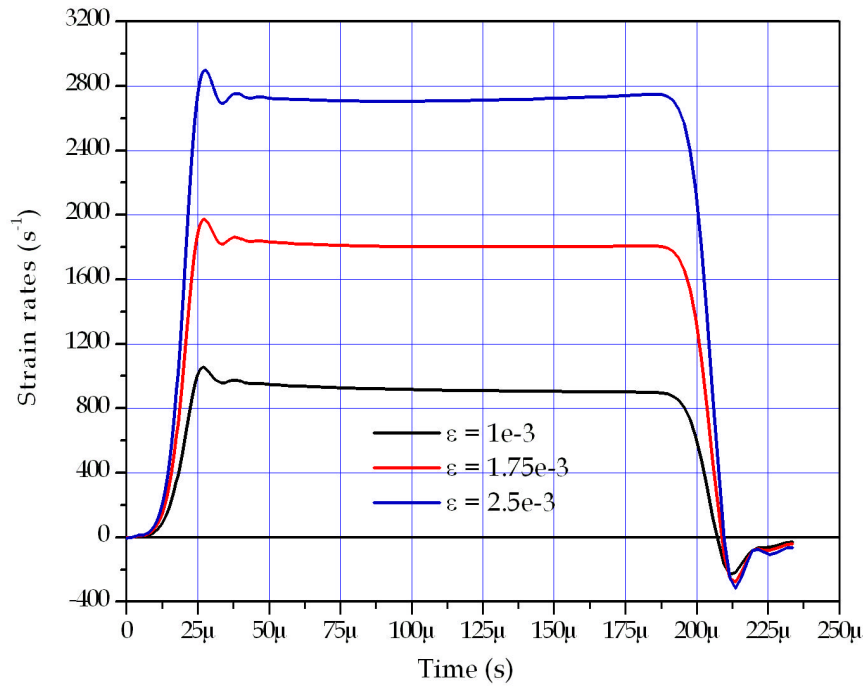


Figure 8.10- Simulated strain rate versus time signal for different strain values

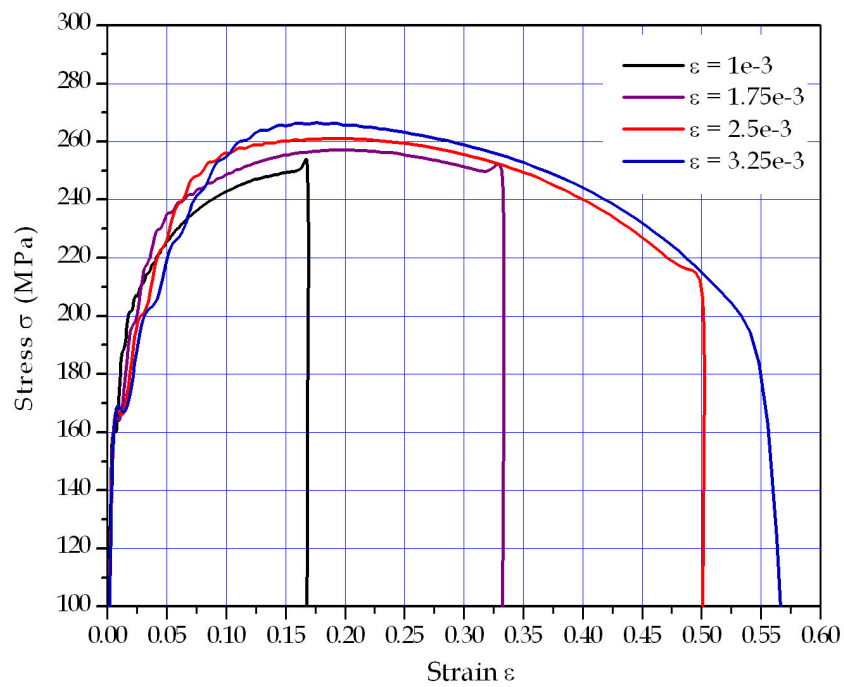


Figure 8.11- Stress-strain curve for OFHC copper using SHPBT at different strain rates

In figure 8.11 the corresponding calculated stress-strain curve obtained with different strain rates are given for OFHC copper. The SHPBT has another upper bound limit given by the value of the total accumulated strain which in ductile metals result in the formation of the necking. As a matter of fact, the one-dimensionality of the stress state is no longer verified as soon as the necking process starts to occur. During this process the value of the effective local strain rate increases amplified by the geometry changes. This value can go well off of the nominal values given by the relation in Eqn. 8.1.2. In figure 8.12 the effective strain rate measured on the specimen is given. The three curves refer to three virtual clip gauge measurements, positioned across the specimen midsection, performed with 4, 6, and 8 mm reference length, respectively. Here, it is evident how the less the reference length the more the necking effects are.

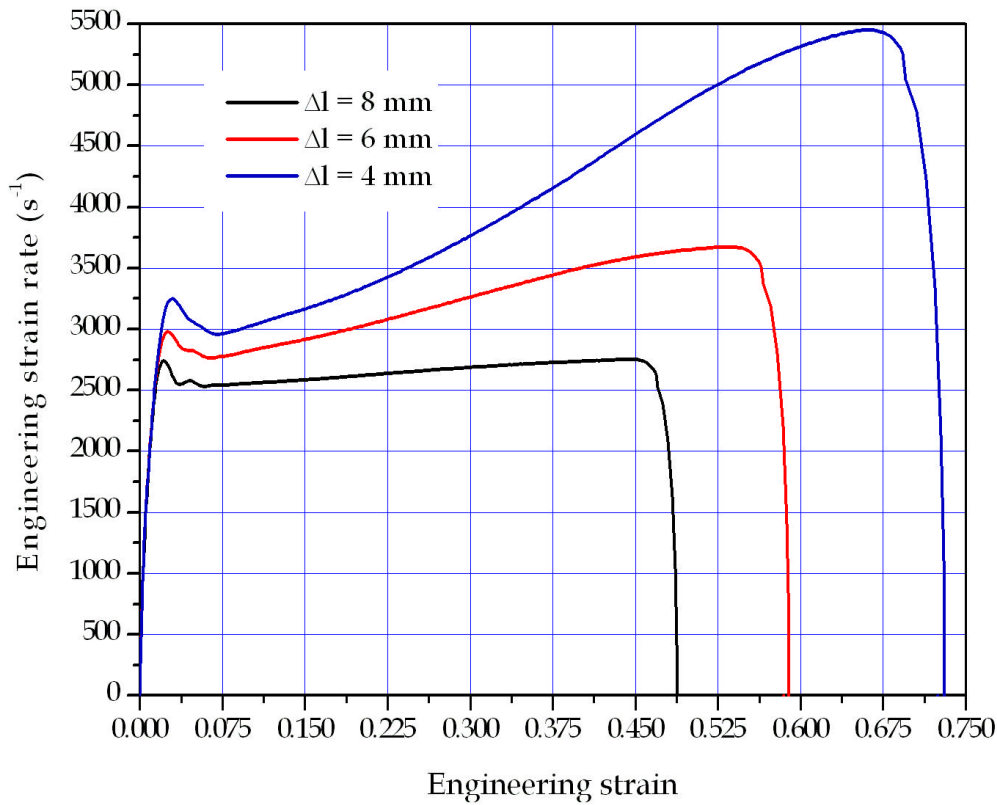


Figure 8.12- Strain rate as function increasing strain along the specimen in SHPBT using different gauge lengths

The use of a damage model together with a constitutive formulation that incorporates the strain rate and temperature is critical in order to obtain simulated signals comparable with real ones. The proposed damage model together with the element removal technique illustrated in the previous section is capable to follow both the dynamic necking process evolution together with the formation of cup-cone rupture. In figure 8.13 a sketch of the fracture evolution in dynamically tested copper is given.

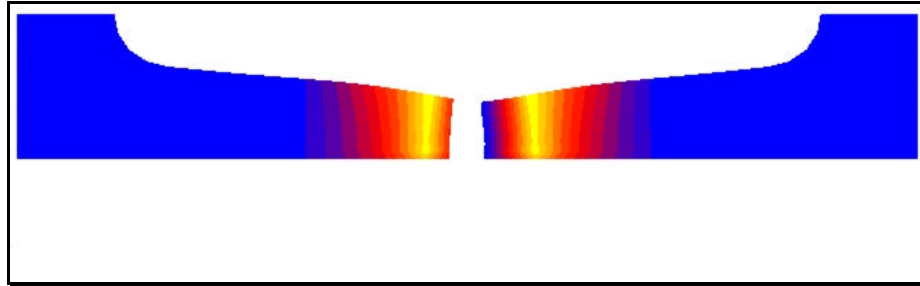


Figure 8.13- Sketch of the simulated dynamic fracture with SHPBT in copper

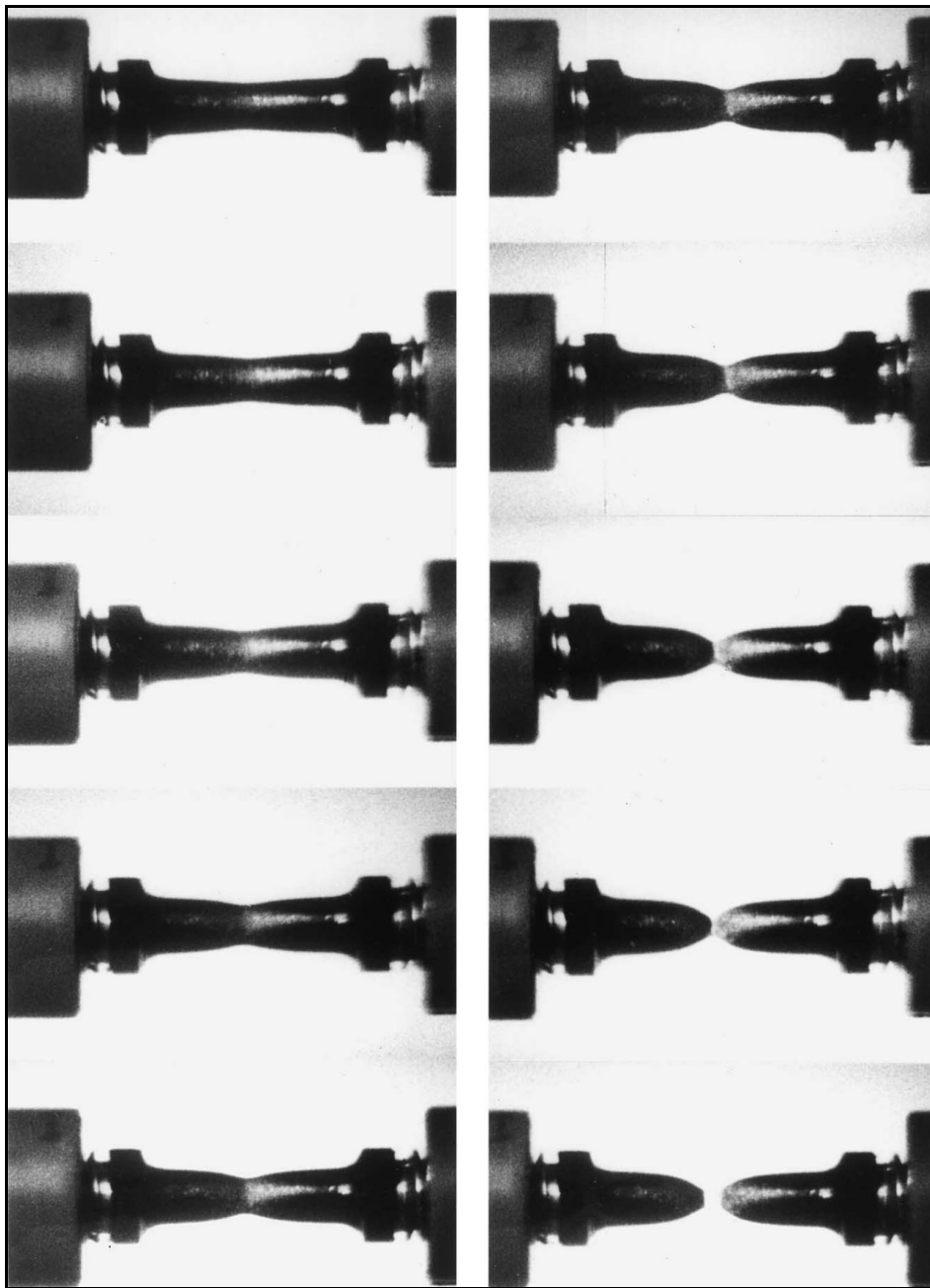


Figure 8.14- Evolution of the necking in a SHPB test.

In order to validate the numerical analyses, simulated SHPBT tests have been repeated for ARMCO iron for which experimental data were available in the literature. In this study the attention has been focused not only in the possibility to reproduce the stress and the strain rate wave signal but in the possibility to follow the evolution of local deformation process such as the progressive reduction of area together with the distribution of temperatures resulting from the conversion of the plastic work in heat.

Damage parameters as well as material properties used for simulation on ARMCO iron are the same illustrated in the previous sections. The specimen dimensions are 3 mm diameter and gauge length of 8 mm. The fem model has a uniform square mesh with a minimum element size of $0.25 \times 0.25 \text{ mm}^2$. Integration time used was $4.0\text{E}-08 \text{ s}$. In Figure 8.14 a series of pictures taken with the frequency of $10 \text{ }\mu\text{s}$ are given showing the strain localization and the progression of necking up to failure.

As usual, the effectiveness of the damping factor choice has been investigated in order to be sure not to overdamp the system response but to get rid of the high frequencies. In order to do so the different shapes of the tensile stress pulse for different damping factor values have been compared with the theoretical solution, Figure 8.15.

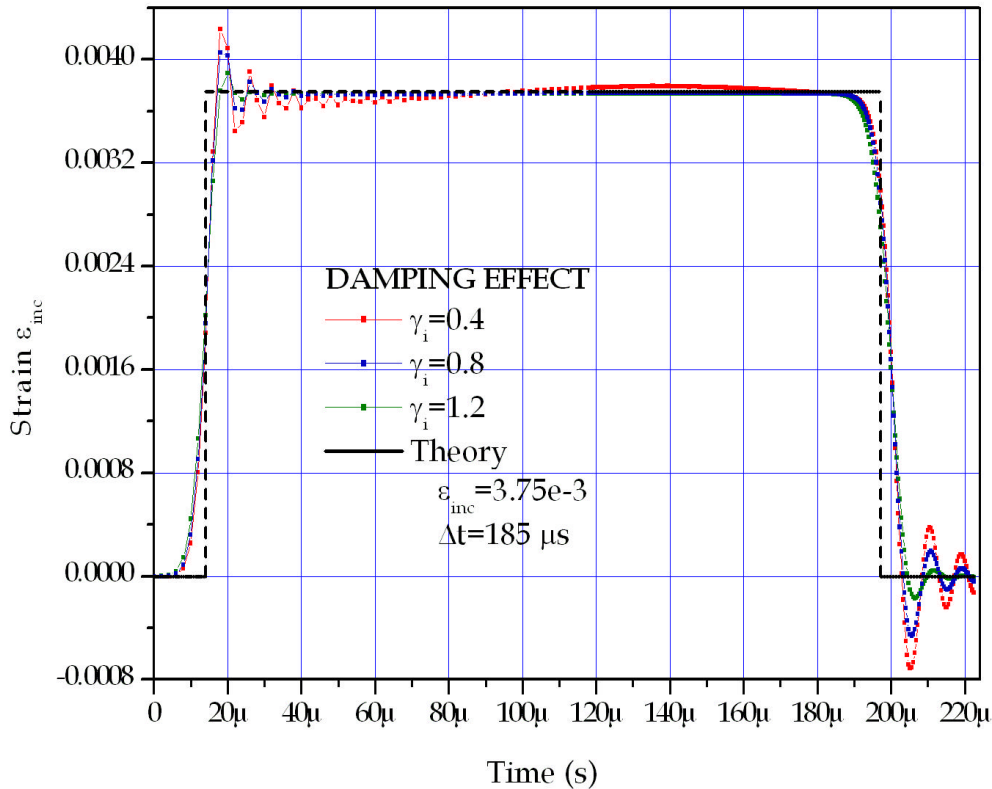


Figure 8.15- Calibration of numerical damping for ARMCO iron SHPBT test

The comparison given in Figure 8.15 show that for a choice of $\gamma=0.4-1.2$ the stress wave profiles very close showing a little dispersion with respect to the square-flat top

solution. Here the nominal duration of the stress pulse, for an incident strain wave $3.75\text{E-}03$ mm/mm amplitude, is $185\text{ }\mu\text{s}$.

Subsequently, the reduction in area as function of time has been compared with the experimental measurement as given in Figure 8.16,

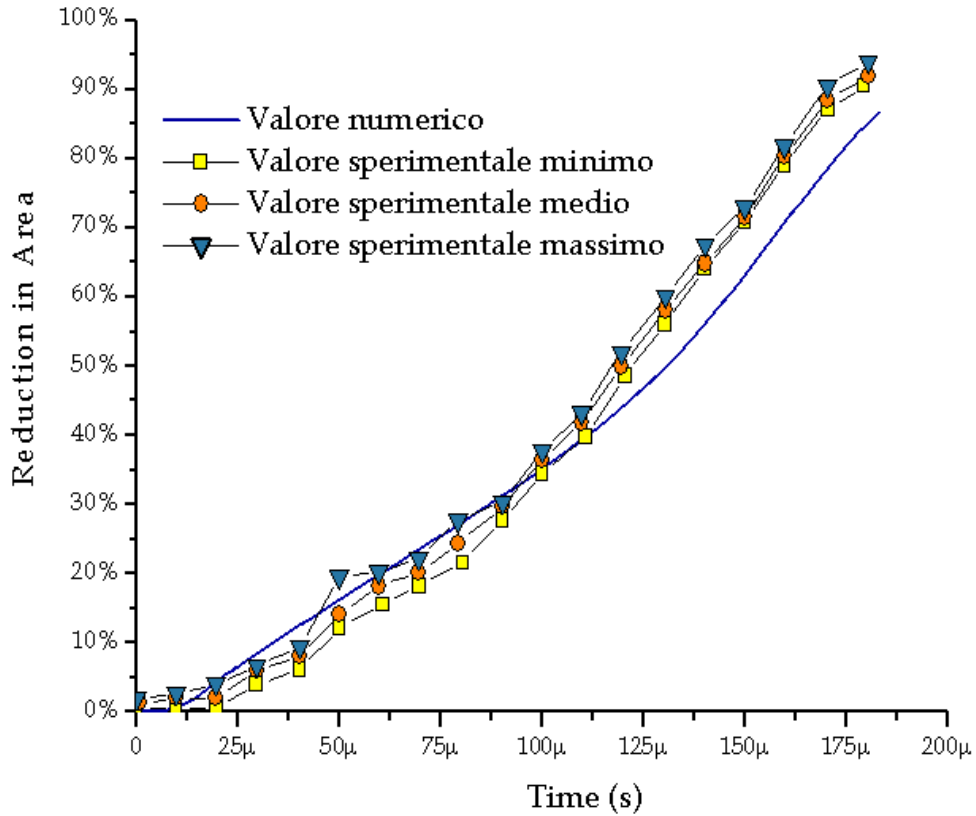


Figure 8.16- Comparison of the calculated reduction of area in the necking region as a function of time, with experimental measurements

Here, the comparison shows a very good agreement of the computational results with experimental data. It is interesting to note how the simulation is capable to catch the changing in slope for reduction of area higher than 40%.

The analysis of the location where the necking localizes showed that if no initial defect is introduced in the specimen geometry, a possible longitudinal shift, with respect to the radial symmetry axis, can occur. In Figure 8.17, a picture of the simulated dynamic traction at fracture is given showing the asymmetric fracture location.

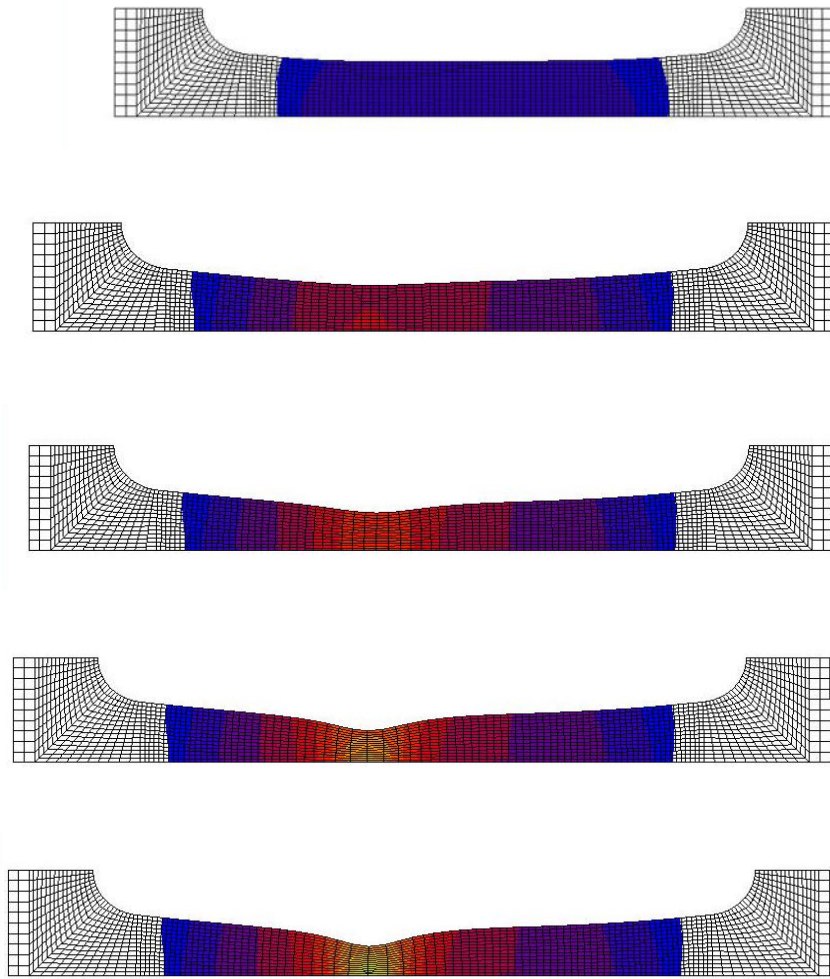


Figure 8.17- Simulated fracture in SHPBT test on ARMCO iron

An additional verification has been performed comparing the simulated strain rate as a function of strain registered along the specimen length with the experimental data measured with clip gauge technique. Once again the comparison given in Figure 8.18 is in very good agreement with the experimental data confirming the validity of the simulations together with the potential of the constitutive and damage model adopted. The final verification was the comparison of the temperature distribution along the specimen length, measured from the location of the failure section. In Figure 8.19, the comparison is given. Here the results are controversial. As a matter of fact, the simulation gives a temperature peak of 280 °C that is very close with the measured value of 250°C, approximately. Also the bulk temperature found over 3 mm from the fracture surface is comparable with the experimental value. However, consistent differences emerge as far as concern the spatial distribution that convex in the simulation and concave in the experiment. The fact that the peak temperature value is consistent with experimental value is a confirmation that the conversion of the plastic work in heat is appropriate.

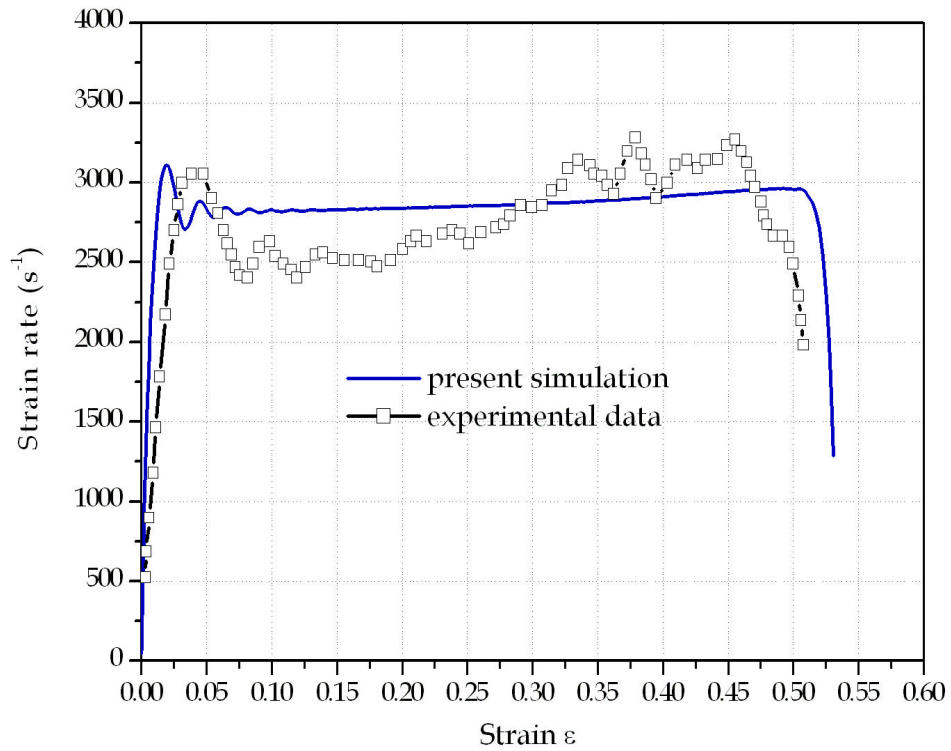


Figure 8.18 – Strain rate versus strain along the specimen: comparison between calculated and experimental data.

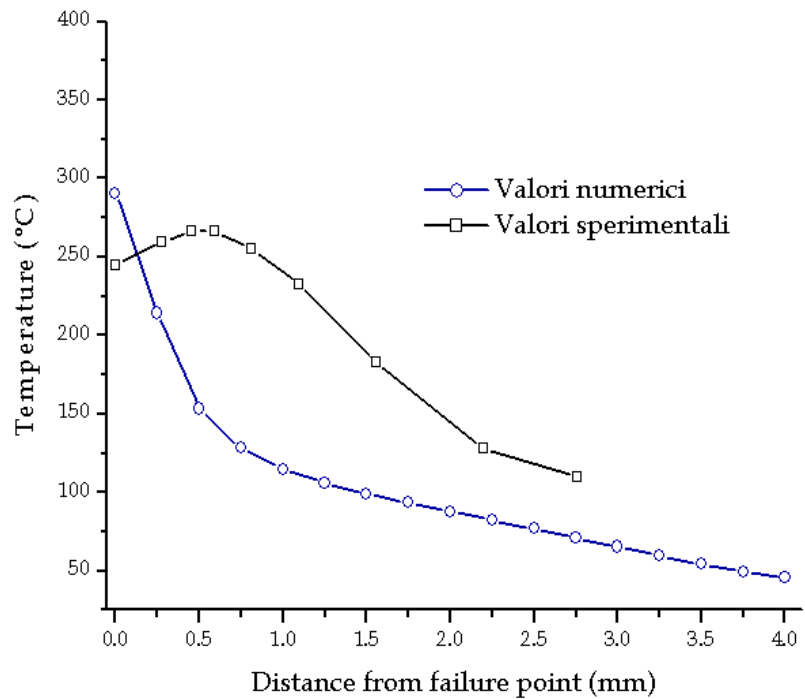


Figure 8.19- Comparison of the calculated temperature rise along the specimen with experimental data.

The amount of plastic deformation has already demonstrated to be similar to the effective experimental one since the diameter reduction along the necking section is an indirect measure of the average plastic strain according to the Bridgman solutions. Consequently, the observed differences may be due to the temperature redistribution during the transient of 200 μ s that occurred after fracture in the real experiment. In the numerical simulation presented here, heat transfer has not been taken into account. In addition to that, thermal boundary condition may also have an effect. In the simulation, adiabatic condition have been assumed. This condition is probably verified during the deformation process which lasts few microseconds, while some heat exchange may occur after fracture due to convection.

8.2. Finite Elements Modeling of Flying Wedge Device

The flying wedge tests technique consists in generating a direct tensile pulse in a round specimen by shooting a wedge in the direction normal to the specimen length. The technique is intriguing since the idea of using a wedge device to infer tensile load to the specimen bottom ends can be used in other loading equipment as well in order to generate high strain rate in tension using simple, reliable and cheap equipment.

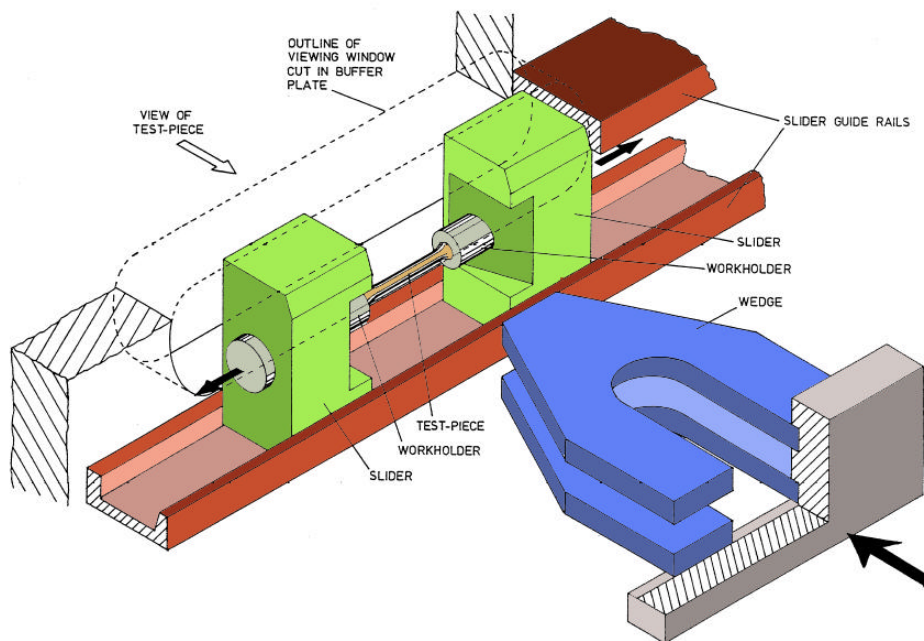


Figure 8.20 - Flying Wedge device conceptual scheme

At the present configuration, the sample is mounted over two bottom work-holders that have slanted profile in order to receive the flying wedge. The gripping system is mounted onto a slider in order to control longitudinal motion during impact. The load

is applied shooting a wedge as depicted in the Figure 8.20. The mass is mounted on the back wedge surface. One of the most interesting feature of this device is the way in which the specimen ends are mounted on the work-holder and slider.

In fact, in order to avoid that compressive waves, generated during the impact of the wedge onto the slider, would eventually enter into the specimen well before the arrival of the tensile wave, the specimen end is screwed into the work-holder that is inserted into the slider. Contact between the work holder and the slider is assured to occur only between the rears flat-end of the work holder (black arrow). To this purpose it is assumed that a small gap, not visible in the drawings, exists between the work holder and the slider.

According to the developers the following advantages can be gained with respect to other dynamic experimental devices:

- a) The device allows one to conduct of mechanical property tests on a range of materials and is not limited by material stiffness or strength.
- b) The device has the potential to generate strain rates ranging from around 25 s^{-1} up to $10,000 \text{ s}^{-1}$ in notched specimens.
- c) A simultaneous, uniform, tensile pull from both test piece ends is applied. This can be particularly useful to test particular samples such as sheet material, welded and adhesively bonded joints, etc.
- d) The entire load-time history can be obtained during testing.
- e) It is possible to record strain-time history.
- f) To conduct mechanical testing at elevated temperatures. This unit can heat the specimens via the buffer-plate window and be quickly withdrawn immediately prior to the test.
- g) To conduct testing at sub-ambient temperatures has been developed.
- h) The use of notched tension specimens with various notch profiles makes it possible to study the effects of strain rate, temperature and state-of-stress on ductile materials.

Regarding comment at point c) it has to be noted that strain rates of the order of $10,000 \text{ s}^{-1}$ can be reached in Hopkinson pressure bar with very small specimen that opens the question if the stress-strain curve measured is still valid for larger material volumes. If the flying wedge technique allows one to use larger specimen size and volume, it could be eventually used to investigate and clarify this issue. In this research an extensive numerical study has been performed in order to evaluate the effective stress wave propagation in a tensile specimen loaded with this device and the potential use of notched specimens in order to amplify the nominal strain rate. A finite element study has been performed with the twofold purpose to verify the effective pure tensile stress wave loading condition and the effective strain rates. Since no details on each piece

dimensions are given in the reference, they have been deducted from the picture given in Figure 8.20 knowing the specimen dimensions.

The role of the work-holder was completely understood only after few analyses that showed how a compressive pulse was indeed generated into the specimen due to the contact between the wedge and the slider. Only the presence of an axial gap between the slider and the work holder avoid the transmission of these waves. After few attempts the configuration given in Figure 8.21 was developed.

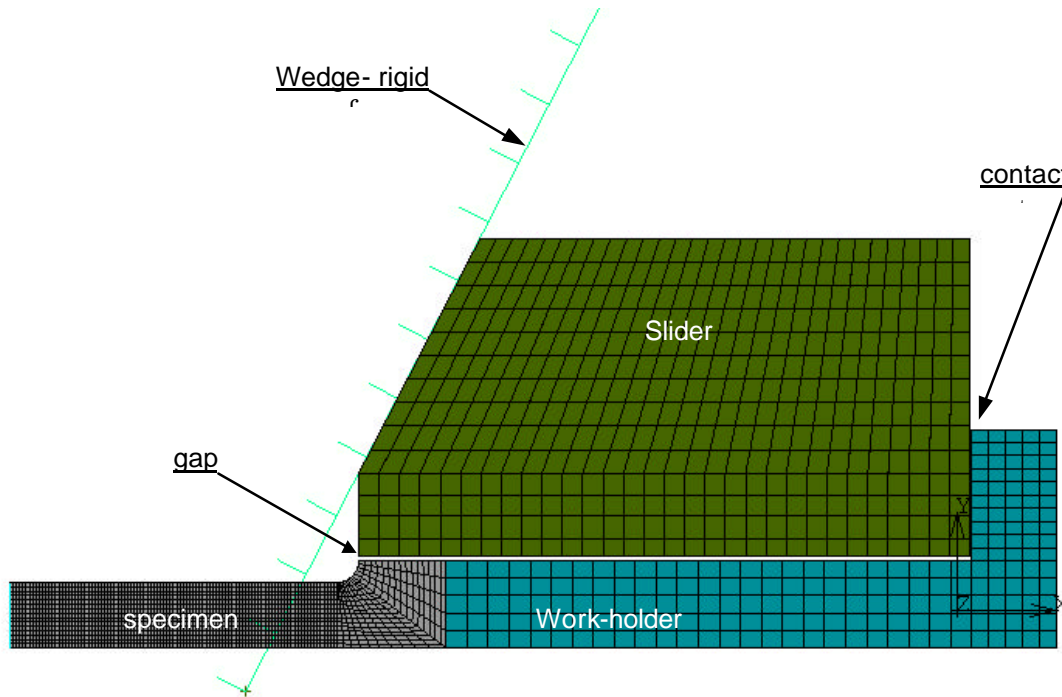


Figure 8.21 - FEM modeling of flying wedge device

In the specific, three possible technical solutions have been explored:

- a) the workholder is attached to the slider
- b) a momentum trap exist between the workholder and the slider, the whorkholder is made of steel and in contact on the back surface (contact may cease
- c) same as above with the work holder made of aluminum.

Axial symmetry applies to all pieces but the wedge. 2D Axisimmetric analysis has been performed considering a quarter of the entire geometry. The wedge has been modeled as a fully rigid surface carrying the mass and the velocity of the real wedge. All other parts are considered deformable. Selective contact has been implemented: contact can occur between the wedge and the slider and between the slider and the vertical portion of the

work holder. No contact can occur between the grip and specimen or the axial portion of the work holder. This condition avoids both the possibility of sticking contact condition between the grip and the work holder and the formation of spurious shear waves.

Case c) has been tested in order to check if there may be an effect associated to the use of different material due to the different relative sound speed. In figure 8.22 the strain rate response obtained over a smooth round specimen are given for the three cases mentioned above.

Here it is clear visible the effect due to the constrain condition and material type. The contact condition has an effect in the first 200ms of the resulting stain rate signal, while the use of different materials results in signals which differs both in amplitude and phase. On the contrary, the resulting stress strain curves measured directly onto the specimen do not show sensible differences in all cases as given in Figure 8.23.

In order to investigate the potential flexibility of the flying wedge test traction tests at different impact velocities and different specimen dimensions have been investigated.

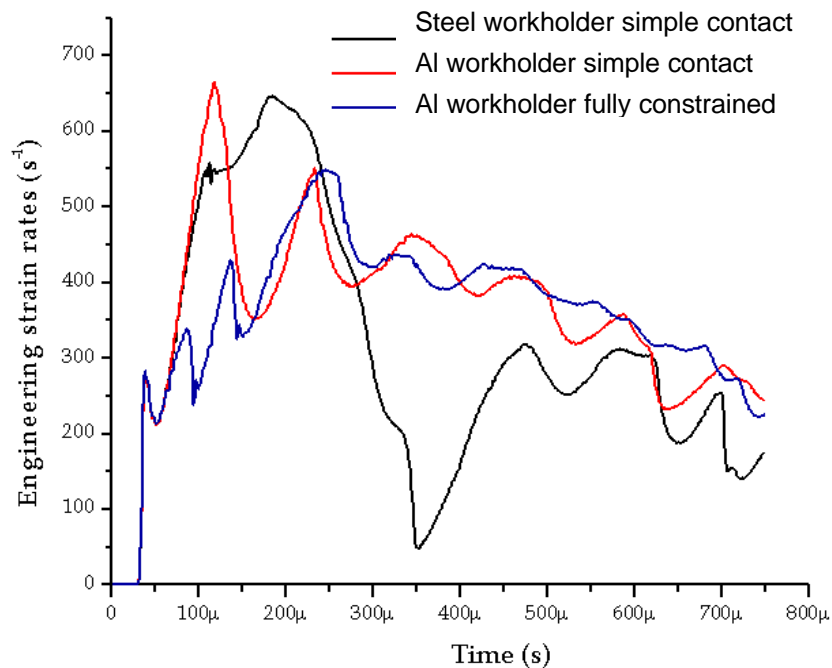


Figure 8.22 – Strain rate versus time in round smooth specimen using different whorkholder materials (steel and aluminum) and constrain condition (touching or full constrained).

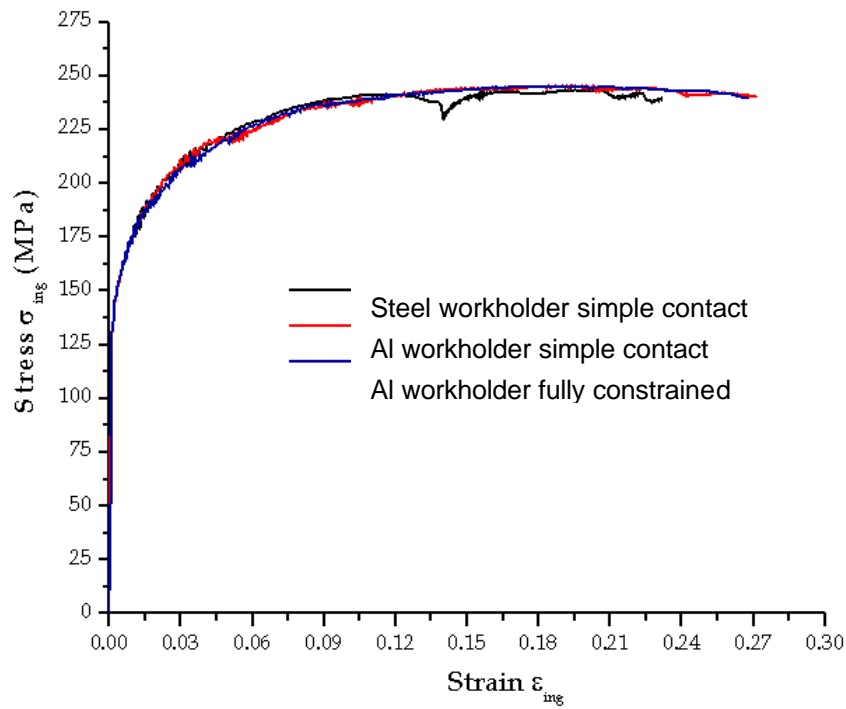


Figure 8.23 – Engineering stress-strain in round smooth specimen using different workholder materials (steel and aluminum) and constrain condition (touching or full constrained).

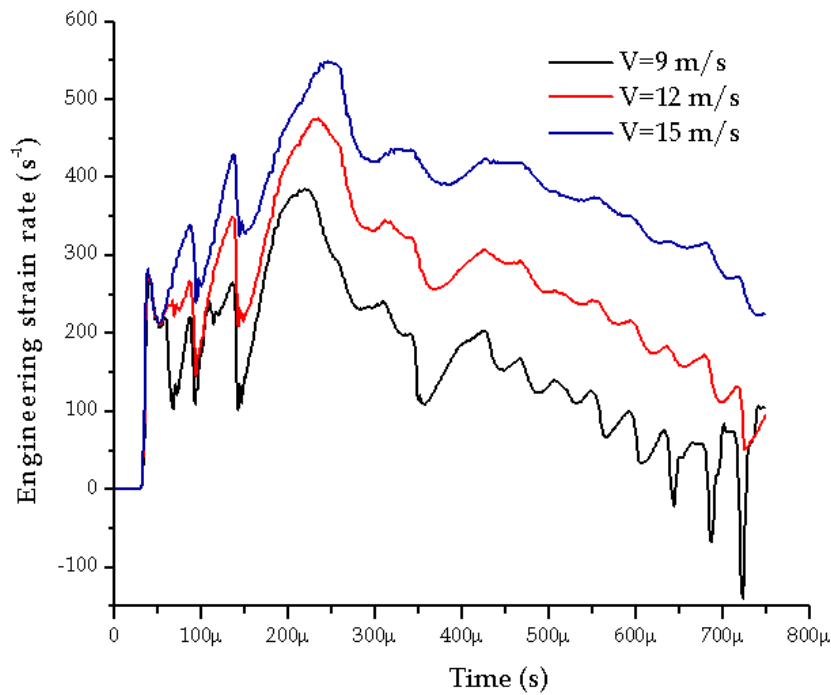


Figure 8.24 – Strain rate evolution with time in flying wedge test with different wedge impact velocities

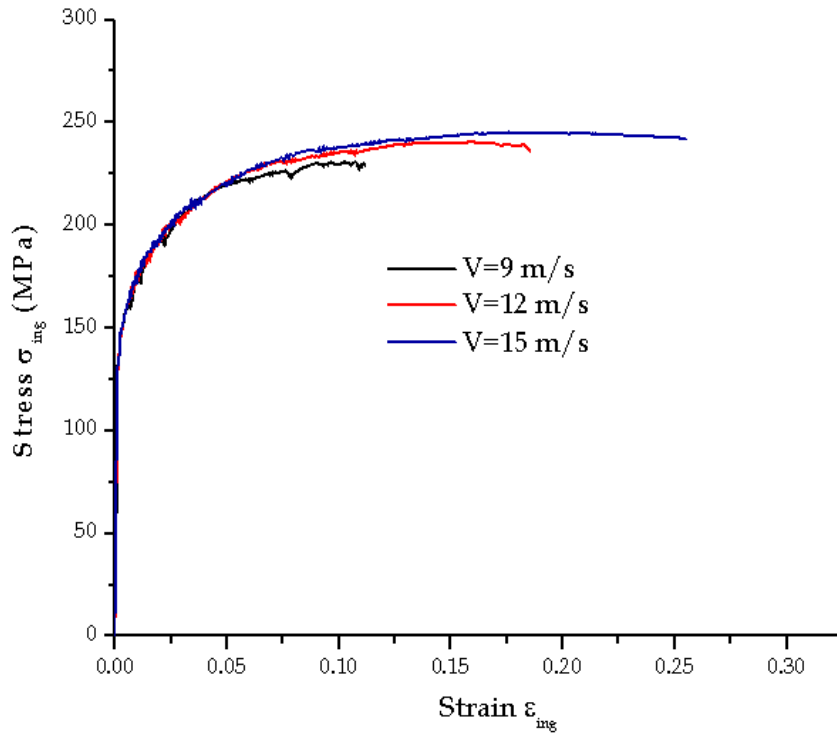


Figure 8.25 – Resulting stress-strain curves for different wedge impact velocities.

As far as concern the impact velocity, three different reference velocities have been investigated, 9, 12, and 15 m/s. Humbolt single step integration scheme has been used with a structural damping of 0.8. In figure 8.24 the strain rate versus time measured on the specimen is given showing similar trends. With specimen dimension used, the strain rate value is limited and well below the values usually obtained with the Hopkinson pressure bar. The absolute values of strain reached are also very limited and well below the necking localization limit. Similarly, the temperature increase observed in the specimen with all the impact velocities explored is of the order of 25°C which correspond to stress-strain curve very similar, as given in figure 8.25.

Standard specimen dimensions, also reported in the reference, for the smooth round bar are: 15 mm in diameter and 75 mm long with 25 mm thread. The wedge mass has been kept constant and equal to 13.7 kg. With this dimension and the maximum impact velocity of 20/ms approximately, the measured maximum strain rate is of the order of 400 s⁻¹ far away from the design values reported in the machine specifications. In order to explore the possibility to increase the strain rate reachable, different specimen dimensions have been investigated.

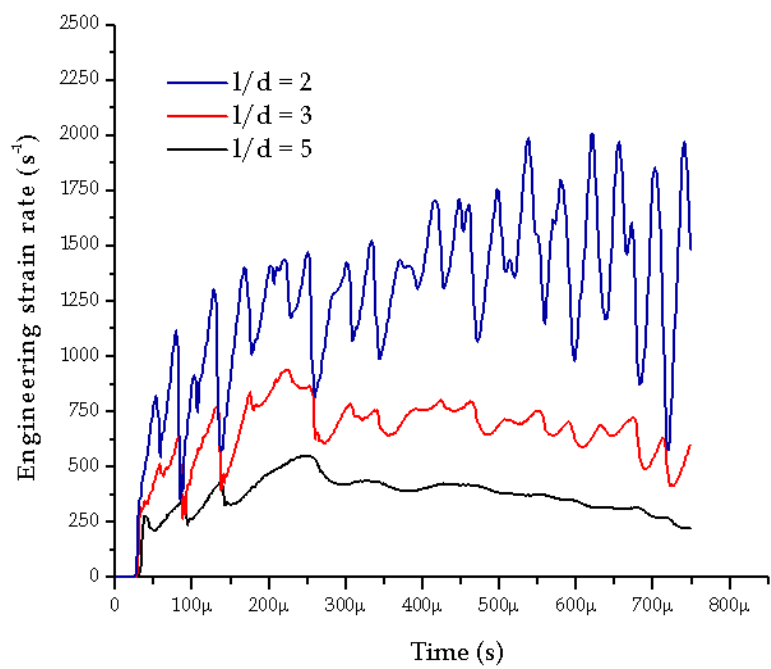


Figure 8.26 – $1/d$ effect on strain rate in flying wedge test

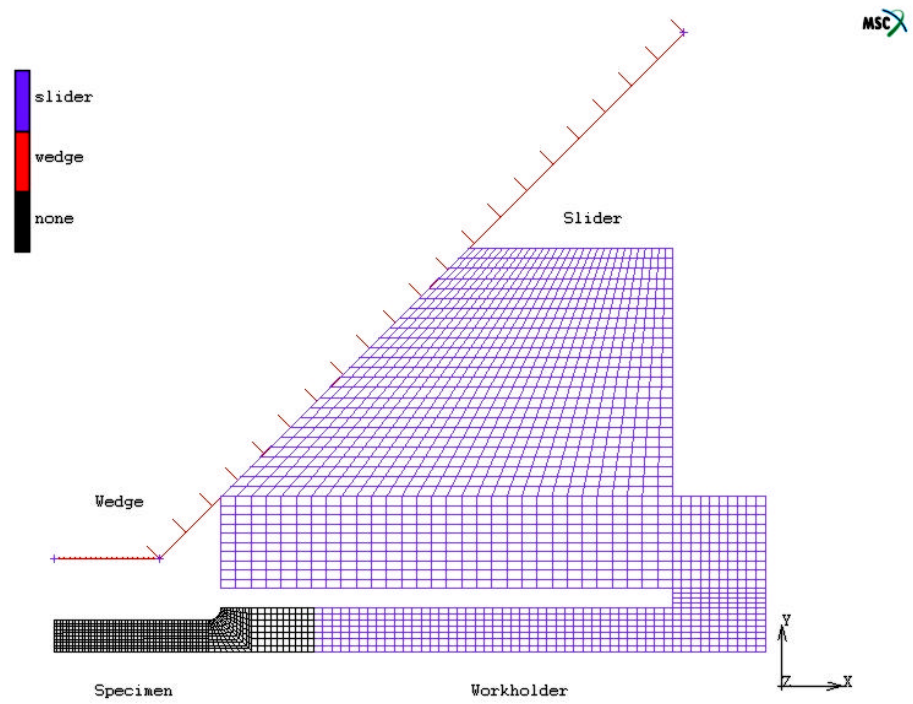


Figure 8.27 – FEM model for the flying wedge test with $d=10$ mm specimen

Three different solutions have been explored:

- a) to reduce the length to diameter ratio, l/d ;
- b) to scale the specimen dimensions keeping constant the length to diameter ratio;
- c) to employ round notch bar specimens.

Since for the case c) the notch is responsible for triaxial state of stress, three additional tests have been performed checking the response of specimen with $l/d=2,3$, and 5 respectively.

As far as concern the point a), specimen having smaller l/d ration show an increasing strain rate signal characterized by the progressive loss of regularity as depicted in figure 8.26. Here, the strain rate signal as a function of time becomes wavy and dispersed with decreasing l/d ratio. For $l/d=2$ the strain rate reached is of the order of $1300s^{-1}$. This is the only geometry for which necking initiates at the reference velocity of 15 m/s. The necking process, as also noted in the Hopkinson bar analysis, is responsible for an increase of the strain rate which holds during the test duration. On the contrary for the other geometries, where necking does not start, the strain rate decreases after reaching the maximum.

Successively, specimen dimension have been progressively reduced. The l/d ration used is 5, but the specimen diameter has been reduced to 10 mm. The reference material used in the simulation is always OFHC copper. In figure 8.27 the new fem model for the reduced specimen is given for reference. In figure 8.28 the resulting stress strain curves for 9,12 and 15 m/s are given. The major features of these simulation can be summarized as follows:

- the appearance of irregularities in the stress-strain curve where some unexpected unloading occurs;
- the appearance of double necking failure process.

The analysis of the signal on the virtual strain gauge onto the specimen reveled that a train of tensile and release waves coming from the work holder reaches the specimen resulting in a partial rapid drop of the stress in the section. The resulting strain rate is also very irregular as given in figure 8.29. The major cause of this can probably found in a the oblique contact which is responsible of clattering. The feature of the double necking is peculiar since is rarely seen during analogous experiments but it seems to be typical of the flying wedge test where , on the contrary, is commonly observed.

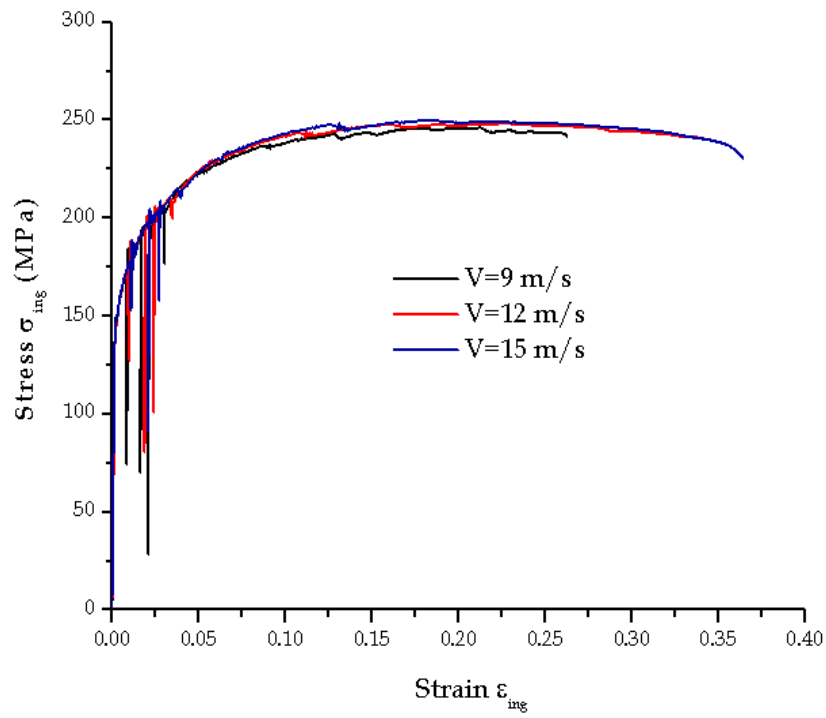


Figure 8.28 – Stress –strain response for smaller specimen dimensions at different impact velocities

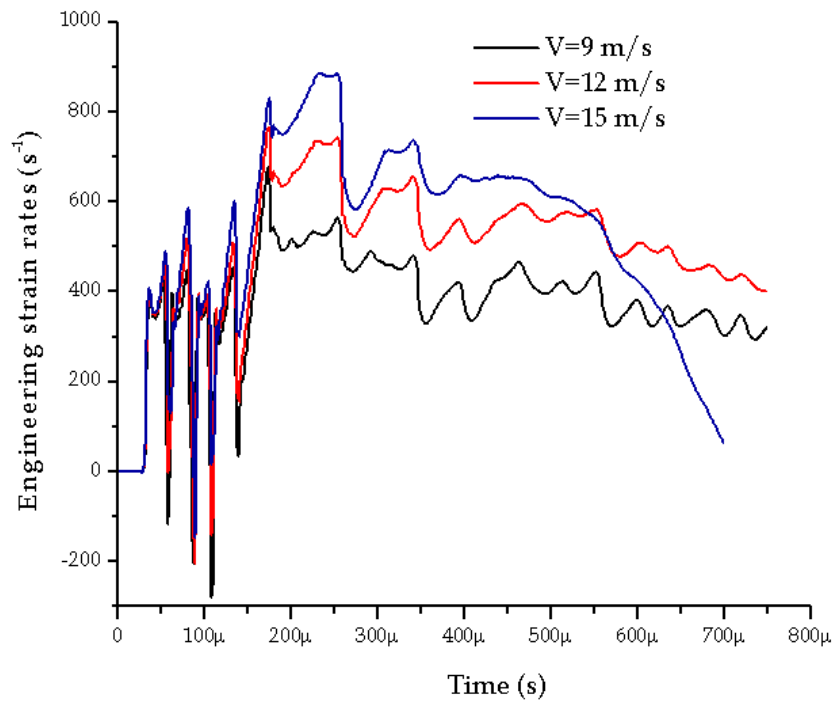


Figure 8.29 – Strain rate response in round specimen with smaller dimensions.

Our numerical simulation showed that at high impact velocity the superposition of the incoming stress waves in the specimen followed by the release ones, localizes the strain accumulation at the section change, after the specimen gripping, approximately. In figure 8.30 the picture of the double necking in OFHC copper specimen is given. Reducing the impact velocity the necking localization slowly moves toward the specimen mid section as given in figure 8.31. The same effect can be also obtained introducing a defect in the specimen midsection.

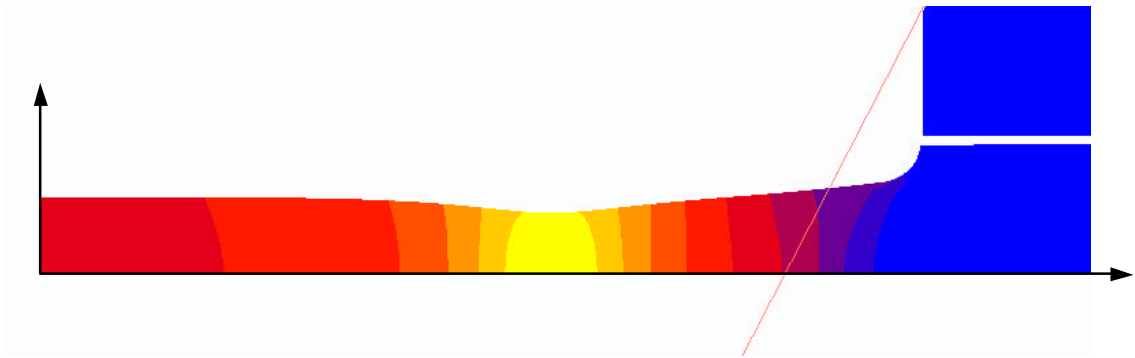


Figure 8.30 - Smooth round bar: double neck feature



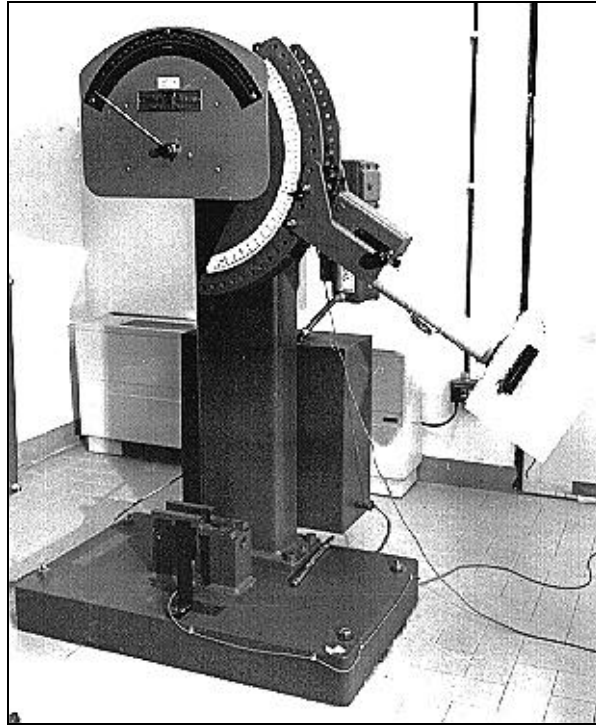
Figure 8.31- Smooth round bar: single neck feature

According to these results it can be concluded that, even though the enthusiastic potential field of application envisaged by the authors, a number of aspects seem to imitate the effective field of application of this technique:

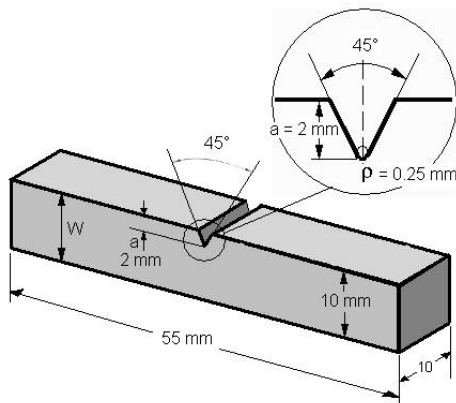
- a) strain rate signal generated in the specimen seem to everything but regular during the test duration;
- b) the resulting stress-strain curve should show rapid drops due to the incoming release waves coming from the workholder due to contact clattering.
- c) Lacking of knowledge of the influence due to equipment factors such as use of different materials, geometry, contact between impacting surfaces.

8.3. Advanced use of Charpy test for strain rate effect measurements.

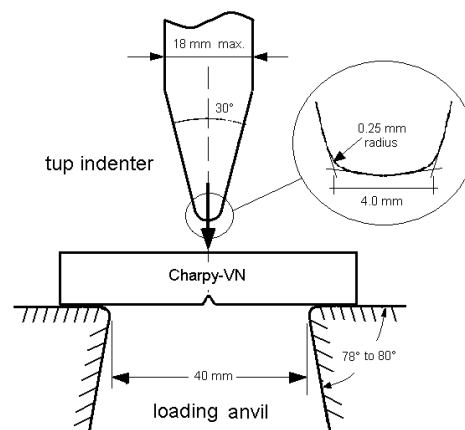
The present section treats the subject of the possible, innovative use of the Charpy pendulum to assess material properties under dynamic conditions.



(a)



(b)



(c)

Figure 8.32- (a) the Charpy pendulum, (b) CharpyV-N specimen dimensions and (c) schematic of the three-point bend loading arrangement with the specimen set on its anvil and the tup indenter.

The original idea beyond the development of this mechanical device was to assess the transition temperature from brittle to ductile behavior of steels, known as NDT, i.e. Nil Ductility Temperature.

Already two centuries ago, the occurrence of sudden, unexpected failure of coach axels, railway was the leading industry of the time, had convinced engineers that dynamic loadings could play a role in the brittle nature of the fracture. At the time, the conventional testing techniques available, namely slow rate traction tests on smooth specimens, were not capable to predict the occurrence of brittle fracture of steels. To this purpose, the British government set up in 1849 (Rif. 8.1) a commission to study the effects of dynamic loadings on steels. The commission reviewed all the cases of brittle fracture experienced in service recognizing the effect of dynamic loading, but no particular test was conceived to solve the puzzle. Almost forty years later, in 1892 the famous French scientist LeChatelier, Rif. 8.1 , better known for his researches in chemistry rather than mechanics, observed that some steels normally ductile, when tested in the form of smooth prismatic bars, shown a brittle behavior if a notch were introduced. It took a young American engineer (Rif. 8.2 , named S.B. Russel, to design a new specimen and testing device that combined the observation of the British commission with the results of LeChatelier, i.e. the dynamic loading on a specimen carrying a notch. The new specimen, in fact, was prismatic with a notch on a side and was mid-span loaded dynamically by the impact of a tup at the end of a pendulum. The specimen was struck by the tup indenter on the side opposite to that carrying the notch that was put in traction and forced to break open. By changing the falling angle of the pendulum the energy and velocity of the impacting hammer could be varied. The Russel specimen to-day is known as Charpy V-Notch, or simply CharpyV-N specimen, after Mr. Charpy who first introduced it to the international scientific community during a conference in 1901 Rif. 8.4 . Figure 8.32 shows: (a) the Charpy pendulum, (b) the CharpyV-N specimen dimensions, (c) the loading geometry with the specimen set on its anvil and the tup indenter striking it under three-point bend conditions. For some reason, the new specimen was never used and laid almost forgotten in the drawer of some research center for about forty years, till World War II brought to the attention of naval designers the problem of brittle fracture of Liberty ships and T-2 tankers (Rif. 8.5 . The studies at the Naval Research Laboratory (NRL), in Washington D.C., organized to explain the cause of those brittle fractures, again led scientists to the conclusion that dynamic loadings and notches or, better, tiny cracks were responsible for the failures. It was so that in 1945 somebody at the NRL retrieved the Russel/Charpy V-N specimen from that forgotten drawer of the time and, at last, decided to use it (Rif. 8.6). Normally, what is recorded during a conventional Charpy V-N test is the energy absorbed by the specimen at fracture, called resiliency, while the visual observation of the fracture surface morphology yields the percentage of brittle fracture (flat fracture). Since then, during the last fifty years, the Charpy V-N specimen has been successfully used to assess the NDT of carbon steels and, in general, of BCC metals and infer the fracture toughness K_{Ic} of materials and even the J-integral at initiation J_c through

suitable empirical correlations (Rif. 9.7-9.9). The Charpy testing is described by the ASTM procedures (Rif. 9.10). Figure 8.33 (Rif. 9.11) shows a set of halves of Charpy V-N specimens of A 508 Cl3 carbon steel, broken at different temperatures from which it is possible to appreciate the change in appearance of the fracture surface with temperature which, from the completely brittle one (100% brittle) at -80°C , turns into a full ductile fracture already at 20°C (100% ductile fracture). An interesting improvement of the Charpy pendulum, which our interest will focus on, has been introduced in the seventies by the insertion of two strain gauges on both sides of the tup. With this so called instrumented Charpy pendulum it is possible to assess the force acting on the specimen during the loading phase, from the beginning of the impact till fracture occurs. A trigger located at the anvil measures the time elapsed since the impact. Therefore, a complete record of force and displacement versus time is available, together with the energy absorbed, as shown in Figure 8.34. The instrumented Charpy pendulum has been originally used to measure the J_c of materials, with a pre-cracked Charpy V-N specimen in which a crack is generated by fatigue at the root of the notch. The relative procedure is defined in the book of ASTM Standards (Rif. 9.12). As it will be shown in the following paragraphs, the potential of the instrumented Charpy pendulum will be used to assess the mechanical properties of materials, in particular the yield strength, at any temperature and for a convenient range of strain rates.

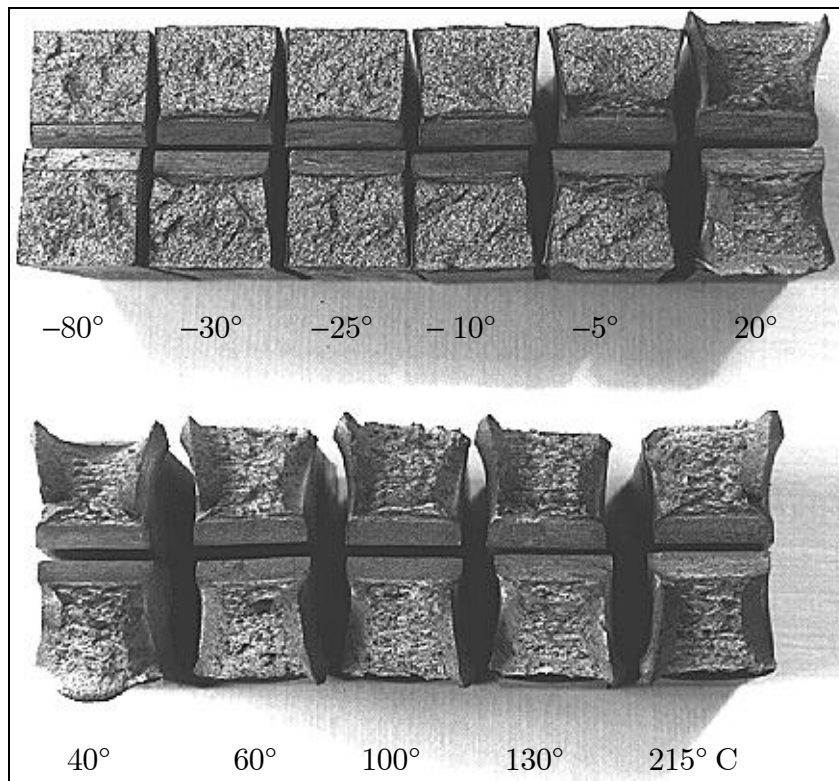


Figure 8.33 - Fracture appearance of Charpy-VN specimens broken at different temperatures (Milella).

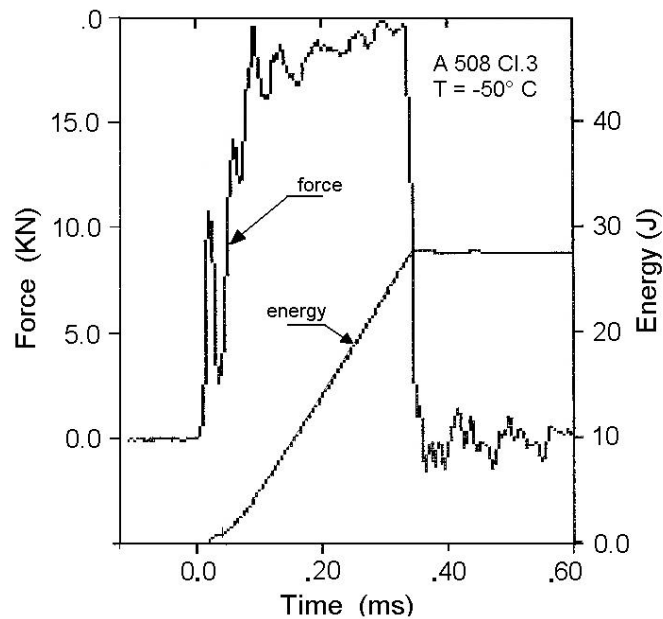


Figure 8.34 - Experimental load-displacement record obtained on a Charpy V-N specimen of A 508 Cl.B steel (Milella).

As matter of fact, already in 1978, A.L. Server(Rif.9.13), probably for the first time, presented this possible use. Yet his analysis, though very sound, was not completely accurate in the evaluation of some parameters, such as the constraint factor for a three-point bend specimen, the point of plastic hinge formation and the strain rate, that are fundamental, as we will see, in the assessment of the mechanical properties of materials. This study is aiming at performing a very accurate analysis of the Charpy V-N behavior both under static and dynamic condition, as well as under plain strain and real 3D response to provide an answer to the questions that still remain open. It is worthwhile to evidence the versatility of this small Charpy V-N specimen and the extreme simplicity and inexpensive characteristic of the testing procedure to obtain a great deal of reliable experimental data, virtually at any temperature, in a short period of time, very short if compared to any other available dynamic testing device.

8.3.1. General Yielding of Charpy V-N specimens

The use of the Charpy V-N specimen to assess the yield strength of a material stems from the slip-line theory (Rif. 8.14) that relates the load at plastic hinge formation to the yield strength of the material. The slip-line fields are described by two sets of orthogonal lines of constant shear stress (which are equivalent to lines of velocity discontinuity). The slip-line solution requires the satisfaction of equilibrium, boundary

and compatibility conditions. Moreover, which is important and must be kept in mind for the possible consequences on real cases, the theory applies to ideally perfect rigid-plastic materials under plain stress conditions. Slip-line solutions for the Charpy V-N specimen were first given by Green (Rif. 8.14 Rif. 8.15), Green and Hundy (Rif. 8.16 (Rif. 8.17), Alexander and Komoloy (Rif. 8.17), Wilshaw and Pratt, Rif. 8.18 , and by Ewing, Rif. 8.19 and experimentally verified by Knott and Cottrell, Rif. 8.20 , Wilshaw, Rif. 8.21 , and, lately, by Milella, Rif. 8.22 . The analyses refer to quasi-static or dynamic bending (Milella) either by pure moment, four-point bending (FPB), or by a central force, as in the case of the Charpy V-N test (three-point bending, Figura 8.82c).

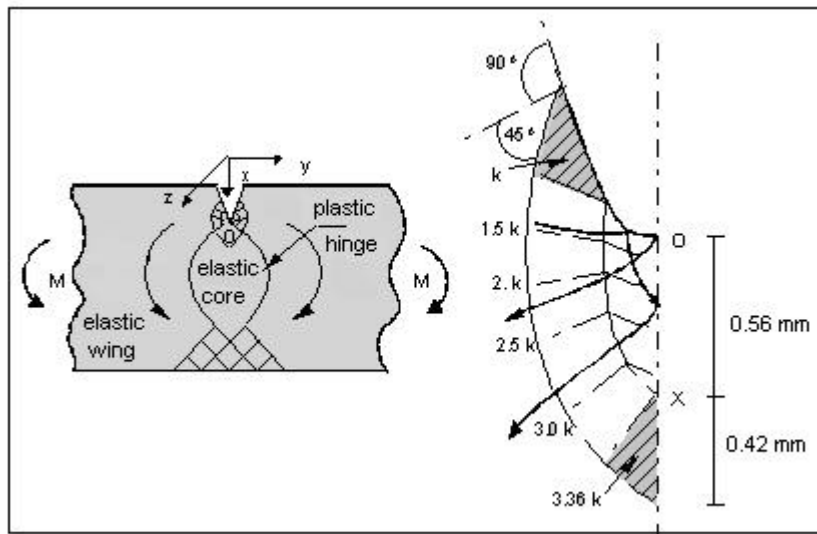


Figure 8.35 - Slip-line field solution for a Charpy V-N specimen loaded under quasi-static conditions by pure moment (four-point bending). It can be seen the plastic hinge and a detail of the stress field just behind the notch [17].

According to the slip-line solution, during the loading phase the Charpy V-N specimen undergoes a deformation field which eventually leads to the formation of a plastic hinge, also referred to as general yield (GY). The hinge starts both at the notch tip and at the point opposite to the notch and extends toward the center of the specimen, as depicted in Figure 8.35 for the four-point bending under quasi-static conditions. An experimental verification of the theory can be seen in Figure 8.36 for a Charpy V-N type specimen of high nitrogen steel of 12.7 mm cross section with a central notch of 4.2 mm depth (Rif. 8.20). The slip-line fields were evidenced by an etching technique making use of the Fry's reagent. It can be seen how the experimental evidence matches theoretical predictions (Figure 8.36.d compared to Figure 8.35). In the case of Charpy V-N specimen loaded under TPB, which is the case of interest to us, the slip-line fields are those shown in Figure 8.37. Experimental evidence of the plastic hinge formation in mild steel Charpy V-N specimens under quasi-static TPB, at different temperatures, is

presented in Figure 8.38 (Rif. 8.20). The formation of the PH leaves a central core and two wings, from both sides of the hinge, rigid-elastic.

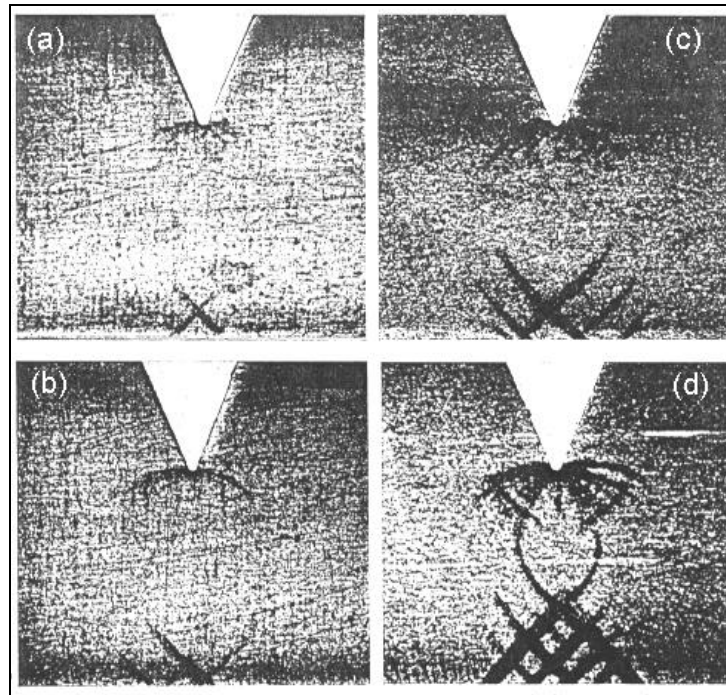


Figure 8.36 - Progression of slip-lines in a Charpy V-N type specimen subjected at room temperature to quasi-static pure bending equal to (a) 0.92, (b) 0.94, (c) 0.96 and (d) 1.00 fold the general yielding (Rif. 8.20). In (d) the plastic lines emanating from the notch tip merge those formed on the opposite face creating the plastic hinge.

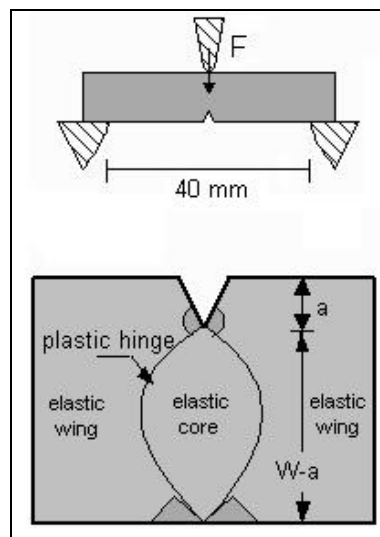


Figure 8.37 - Slipline field solution for a Charpy V-N specimen loaded under quasi-static three-point bending. It can be seen the plastic hinge emanating from the notch and the opposite point, as well.

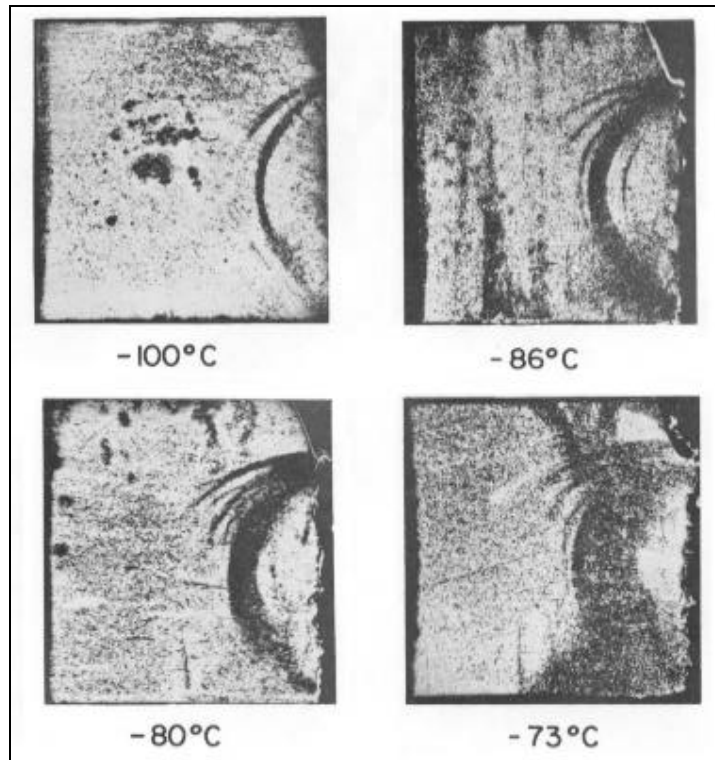


Figure 8.38 - Plastic hinge formed at different temperatures in a Charpy V-N specimen of mild steel, loaded under three-point bending, evidenced by etching with Fry's reagent (Rif. 8.20).

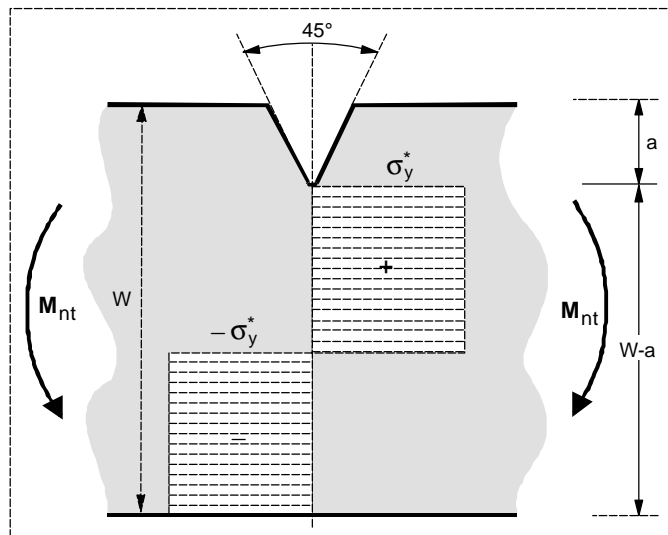


Figure 8.39 - Schematic of the internal reaction on the notched cross section that balances the external moment M_{nt} .

The reaction force at general yield, cannot increase any further, which actually means that any increase of the load applied by the tup indenter will not be carried by the specimen that will start to rotate along the PH. Let's try to analyze this limit load at general yield P_{GY} . The scheme to adopt it is depicted in Figure 8.39. Since we deal with ideal rigid-plastic materials, the stress cannot exceed the value of the yield strength \mathbf{s}_y^* . The internal reaction system, shown in Figure 8.39, must balance the applied external moment M_{nt} , where the subscript nt indicates that the specimen has a notch, therefore:

$$M_{nt} = \frac{t \cdot (W - a)^2}{4} \sigma_y^* \quad (8.10)$$

where t is the specimen thickness. It must be evidenced that \mathbf{s}_y^* in Eqn. (8.10) is not the uniaxial yield strength s_y of the material measured with a standard traction specimen, since the plain strain condition makes the former be larger than the latter. The increase of \mathbf{s}_y^* over s_y depends on the degree of triaxiality introduced by the notch. The ratio between the two, \mathbf{s}_y^* / s_y , is the constraint factor C of the Charpy V-N geometry. Its value can be inferred as the ratio of the moment M_{nt} to the moment M that would produce general yield in a specimen without notch having a section equal to the minimum section of the Charpy specimen, i.e. W -a:

$$C = \frac{\sigma_y^*}{\sigma_y} = \frac{M_{nt}}{M} \quad (8.11)$$

from which:

$$M_{nt} = C \cdot M = C \frac{t(W - a)^2}{4} \sigma_y \quad (8.12)$$

In the case of TPB, the moment M_{nt} can be also written as:

$$M_{nt} = \frac{P_{GY}l}{4} = P_{GY}W \quad (8.13)$$

where P_{GY} is the load at the moment of plastic hinge formation, that in a ideally rigid-plastic material coincides with the general yielding, and $l = 4W$ is the length of the Charpy V-N specimen (see Figure 8.32). Combining eqn. (8.13) with eq. (8.12) we finally get:

$$\sigma_y = \frac{4}{C} \frac{P_{GY}W}{t(W - a)^2} \quad (8.14)$$

Eqn. (8.14) can be used to evaluate the uniaxial yield strength of any material at any temperature from a Charpy V-N test, knowing the constraint factor C and the load P_{GY} at the formation of the plastic hinge. Furthermore, if the specimen is loaded dynamically, as it happens in a Charpy V-N test, rather than statically, as so far considered, we can infer the increase in the yield strength due to the strain rate effect, which is the target of this research. In this last case we need to assess the actual value of the strain rate $\dot{\epsilon}$, which is also part of this study, and infer the relationship $s_y = f(\dot{\epsilon})$. In any case, static or dynamic, we must know the actual value of the constraint factor C . The work by Green (Rif. 8.15), Green and Hundy (Rif. 8.16), Alexander and Komoloy, Wilshaw and Pratt and by Ewing, already cited, provides a full list of C values for different loading configuration and geometries. In particular, for the Charpy V-N specimen loaded under three-point bending the values of the constant C for a flat tup indenter of 0.5 mm and 1.0 mm half width were found to be 1.243 and 1.279, respectively. The corresponding value for the American indenter of 4 mm width (see Figure 8.21c) was extrapolated from the previous two and found to be equal to 1.336, therefore Eqn.(8.14) becomes:

$$\sigma_y = 2.99 \frac{P_{GY}W}{t(W-a)^2} = 4.678 \cdot 10^4 P_{GY} \quad (8.15)$$

The value of s_y provided by eqn. (8.15) is given in MPa. As to the second parameter in eq. (8.14) and (8.15), i.e. P_{GY} , its value shall be inferred from the load-displacement diagram. At variance with the ideally rigid-plastic material, in real materials the first formation of the plastic hinge does not coincide with the general yielding, as shown in Figure 8.40 (Rif. 8.21). Therefore, we will indicate the load associated to this event with the symbol P_{PH} or load at Plastic Hinge formation, rather than P_{GY} (General Yielding). Apparently, we now have all the elements to measure the yield strength using a Charpy V-N test, yet the task is not that simple and several questions need still to be answered. First of all, as already said, the slip-line theory applies to rigid-perfectly plastic materials. Real materials always present a certain degree of strain hardening. Secondly, the slip-line theory requires that plain strain conditions exist. A Charpy V-N specimen, because of its dimensions and, in particular, its small thickness cannot satisfy this requirement. Third, the value of the constraint factor $C = 1.336$ used in eq. (8.15) to get eq. (8.16), is not exact. As said, it has been extrapolated to a tup indenter of 4 mm width from values obtained by Ewing for indenters of 1.0 mm and 2.0 mm width, respectively. Fourth, in the theoretical analyses the indenter was assumed to have a flat tip, while the real one is rounded. Finally, the location of P_{PH} on the experimental load-displacement curve may not be so simple and straightforward in real elastic-strain hardening materials. To give an answer to all the questions just raised, a rather systematic and comprehensive study program has been organized. The program, based on FE analysis, is composed of two parts: a static analysis and a dynamic one which, in turn, will be performed both in plain strain and 3D conditions, as well, to evidence the

difference between theoretical plain strain conditions and actual ones. The overall study program is summarized in the study matrix of Figure 8.41.

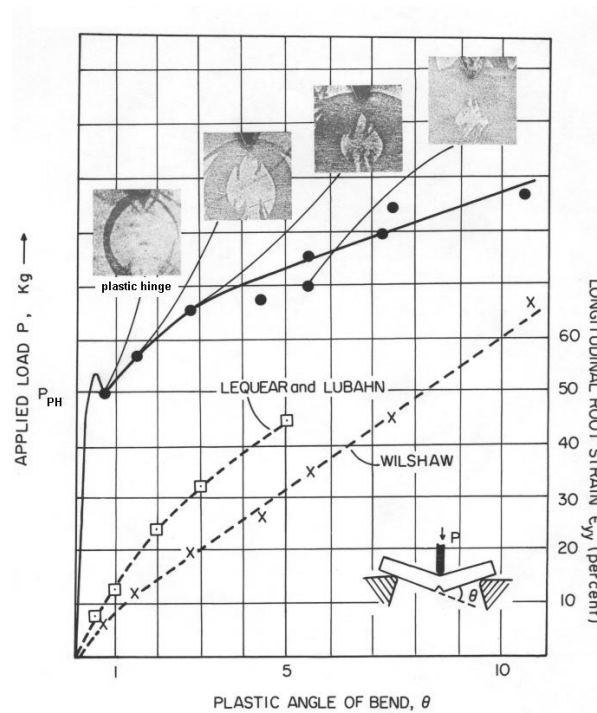


Figure 8.40 - The first formation of the plastic hinge occurs when the load-displacement diagram loses its linearity (Rif. 8.21).

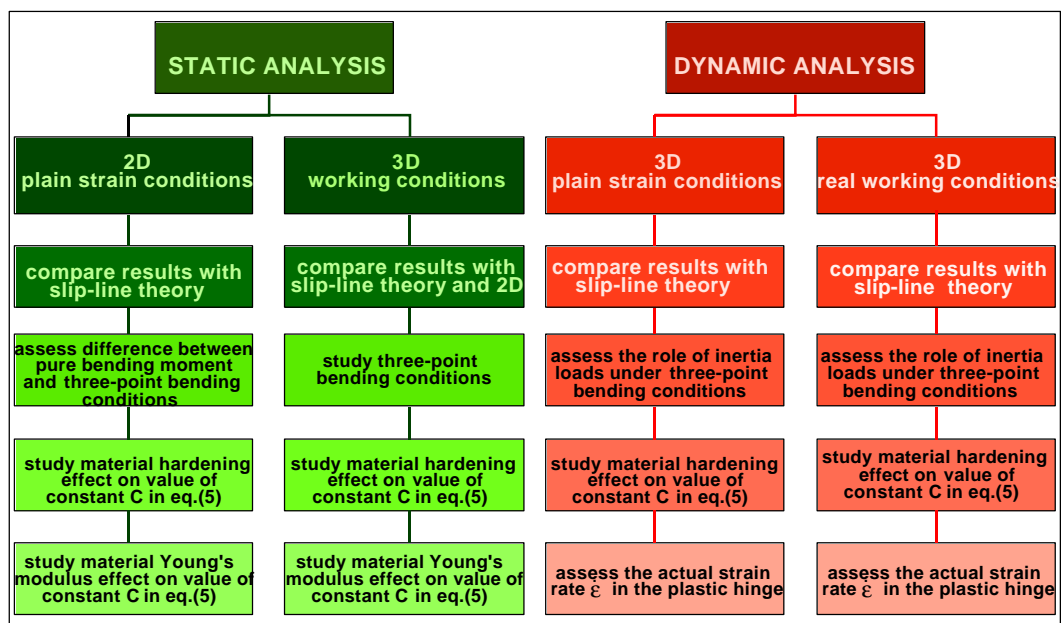


Figure 8.41 - Working matrix followed in this study.

8.3.2. 2D FE static analysis

The FE static analysis has the target to verify the predictions of the slip-line theory and infer the actual values of the constraint factor C for the real geometry (tup indenter, in particular) and real materials. Moreover, the analysis shall provide indications on where the value of the load P_{PH} , at the moment when the plastic hinge is formed, must be read on the experimental load-displacement curve. For an ideal rigid-perfectly plastic material this load, P_{GY} , is immediately inferred from the load-displacement curve (see Figure 8.43): once the hinge is formed there is no further resistance left to the specimen. Conversely, for a Charpy specimen of real material whose load-displacement curve shows a transition from the linear elastic behavior to the plastic one, with some strain hardening, it can be difficult to pin point exactly when the plastic hinge initially forms. In addition, we shall also study the influence of strain hardening n and Young's modulus E on the value of the constraint factor C and the position of the load P_{PH} on the load-displacement curve. The use of a FE static analysis for such a basic investigation will be preferable and performed first, since the dynamic one is dirtied by the superposition of inertial effects that make such an investigation more difficult. Once the static study is performed and those basic questions given an answer, then the dynamic one can be initiated aiming at assessing the effect of inertia forces and strain rate. The first calculation was performed using a rigid-plastic material in order to compare the results directly with those coming from the slip-line theory. The material considered had a yield strength s_y of 492 MPa and a Young's modulus of 196.000 MPa (A 508 B Cl.3 steel). The Charpy V-N specimen was schematized using a 2D model under plain strain condition as shown in Figure 8.42. A 1,732 quadrilateral four-nodes-element mesh was used. The smallest dimension was equal to 0.040 mm at the notch tip. Displacement step increments of 0.005 mm were used in the calculations. Both the indenter and the anvil were assumed to be rigid. The result for the half structure of Figure 8.42 is shown in Figure 8.43. The P_{GY} load for the entire specimen is twice that computed and is equal to $5596.71 \cdot 2 = 11193.4$ N. Entering this value in eq. (5) yields a constraint factor $C = 1.4219$ against a theoretical one of 1.336, which is about 6% higher. Therefore, eq. (5) yields:

$$\sigma_y = \frac{4}{1.4219} \frac{P_{GY} W}{t(W-a)^2} = 4.3955 \cdot 10^4 P_{GY} \quad (8.16)$$

In reality, we shall consider that the value 4 that appears at denominator in eq. (8.12) is relative to a beam without notch under pure bending.

In our case the specimen is loaded under three-point bending which implies the presence of a shear and, in particular, of a concentrated force on the mid-section. The constant at denominator will no longer be equal to four.

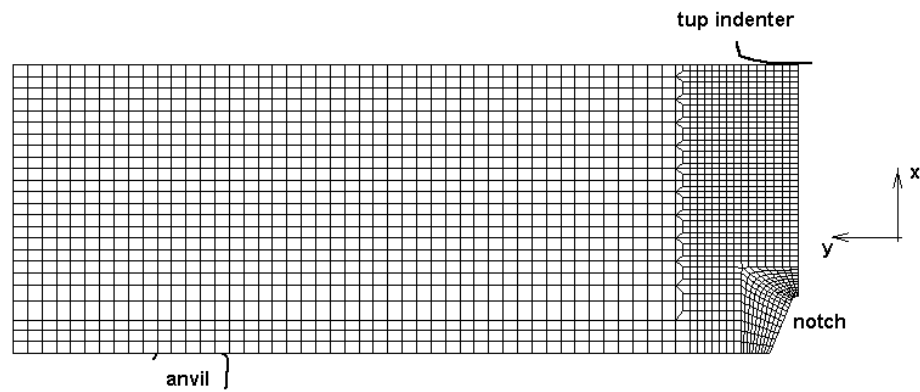


Figure 8.42 - Schematic of the mesh used in the 2D FE static analysis to simulate one half of the Charpy V-N specimen.

This will not be affecting the value of the constraint factor C , which is the ratio between to moments (see eq. 8.11), but it will have an impact on the proportionality factor between \mathbf{s}_y and P_{PH} in eq.(8.15) or eq.(8.16). A FE analysis of an un-notched Charpy specimen of width W -a having ideal rigid-plastic behavior loaded under three point bending has shown, in fact, that the plastic hinge forms when the moment M reaches the value:

$$M = \sigma_y \frac{t(W - a)^2}{3.2} \quad (8.17)$$

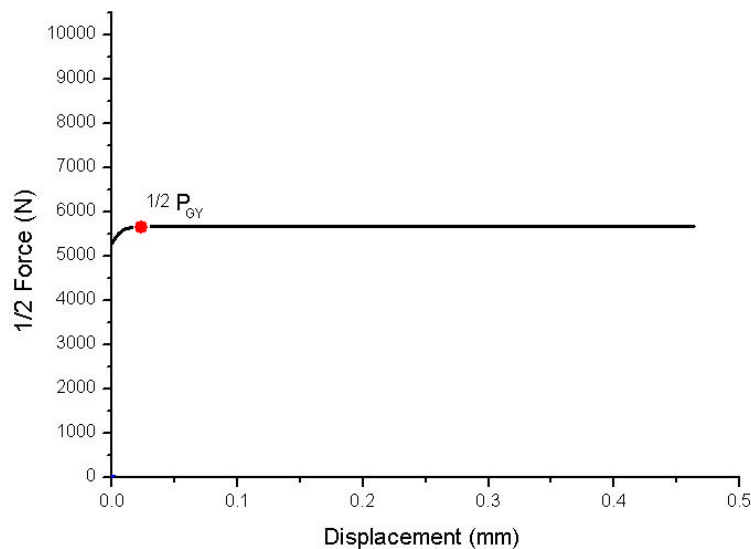


Figure 8.43 - Load vs displacement for the half Charpy specimen analyzed having either ideal rigid/plastic behavior (dashed line).

Compared to eq. (8.12) it yields a value 1.25 times higher than that obtained under pure moment. As said, this is due, as shown in Figure 8.44, to the presence of the shear stress and, in particular, to the local pressure exerted by the indenter that alters the distribution of stresses on the mid-section of the Charpy specimen, where the tup is acting, introducing a compression pike and a triaxiality, as shown in Figure 8.45. The overall moment resulting from the new stress distribution is precisely 1.25 times higher than that pertaining to pure moment, leading to a new relationship between \mathbf{s}_y and P_{GY} :

$$\sigma_y = \frac{3.2}{1.4219} \frac{P_{GY} W}{t(W-a)^2} = 3.5164 \cdot 10^4 P_{GY} \quad (8.18)$$

Equation (8.18) is valid for an ideally rigid-plastic material. For a real one showing a certain degree of strain hardening, we shall expect a different value of the constraint factor C since the hardening introduces additional strength beyond the yield point. FE calculations were, then, run for a real elastic-plastic material having the same yield strength of 492 MPa, but different strain hardening n equal to 0.0, 0.1, 0.2 and 0.3, respectively, always under plain strain conditions. The results are shown in Figure 8.46 together with the result previously obtained for the ideally rigid-plastic material (dashed line), for comparison.

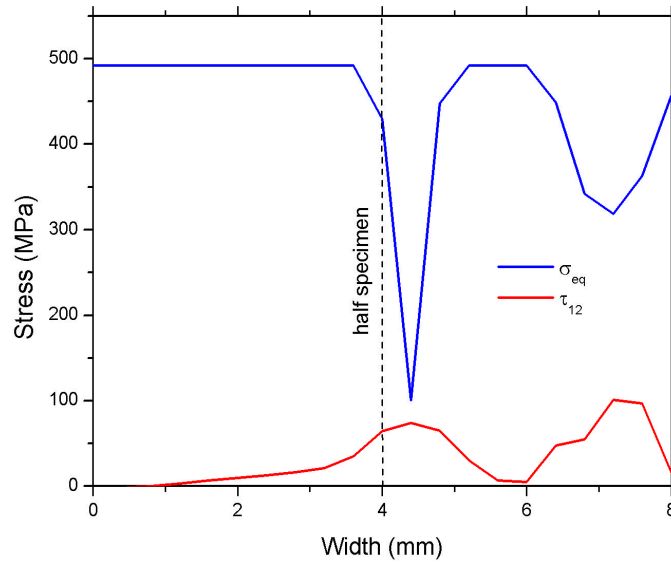


Figure 8.44 - Trend of the equivalent stress (von Mises) and shear stress at general yielding on the mid-section of un-notched Charpy specimen having ideally rigid-plastic behavior.

As it can be seen, the moment when the plastic hinge is first formed clearly depends on the value of the strain hardening n. Table 8.1 lists the results obtained. While, the displacement at which the plastic hinge first occurs varies from 0.2 mm to 0.22 mm, just two hundreds of millimeters, the corresponding change in the P_{PH} load is enormous.

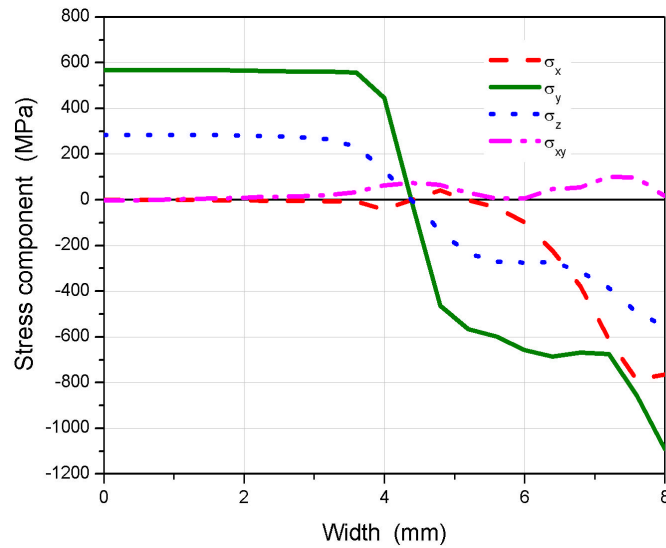


Figure 8.45 - Stress distribution on the mid-section of the un-notched Charpy specimen where the tup indenter is acting, at the moment of first plastic hinge formation.

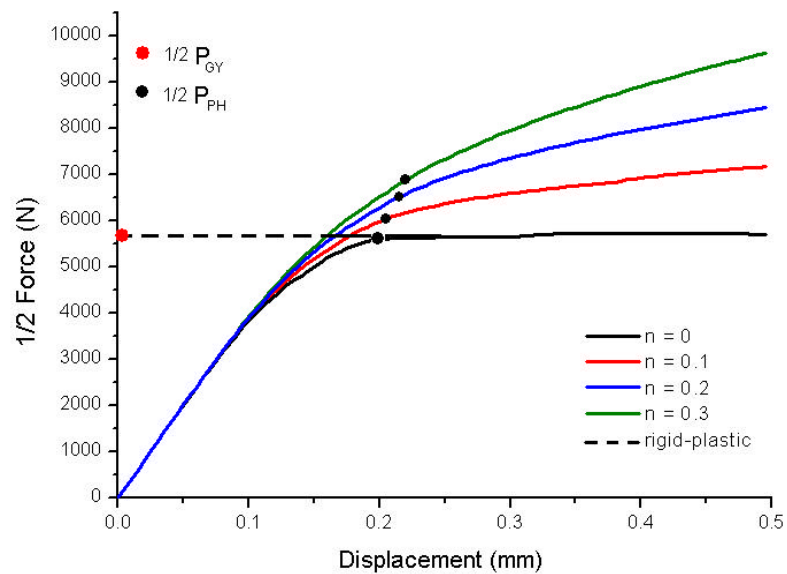


Figure 8.46 - FE results obtained for a Charpy V-N specimen of elastic-plastic material having different strain hardening. The picture shows the points (full circles) where the plastic hinge was first formed.

n	Displacement at PH (mm)	Load P_{PH} (N)	C
0	0.200	11,193.4	1.4219
0.1	0.205	12,080.4	1.5346
0.2	0.215	13,017.9	1.6546
0.3	0.220	13,915.6	1.7677

Table 8.1 Time, displacement and forces at the moment when plastic hinge first for ($E = 196,000$ MPa).

Accordingly, also the constraint factor C varies, yet the ratio between P_{PH} and C remains constant. If we plot this factor C versus the strain hardening n we obtain the graph of Figure 8.47. The trend is linear having the equation:

$$C = 1.421 + 1.156 \cdot n \quad (8.19)$$

The final static calculations were performed to check also the effect of the Young's modulus on the constraint factor C . Again, four cases were run having four different strain hardening n equal to 0.0, 0.1, 0.2 and 0.3, respectively, while the young's modulus E was reduced to 71,000 MPa. The results are shown in Figure 8.48. As in Figure 8.46 relative to a Young's modulus of 196,000 MPa, the picture is showing the moment at which the plastic hinge is first formed.

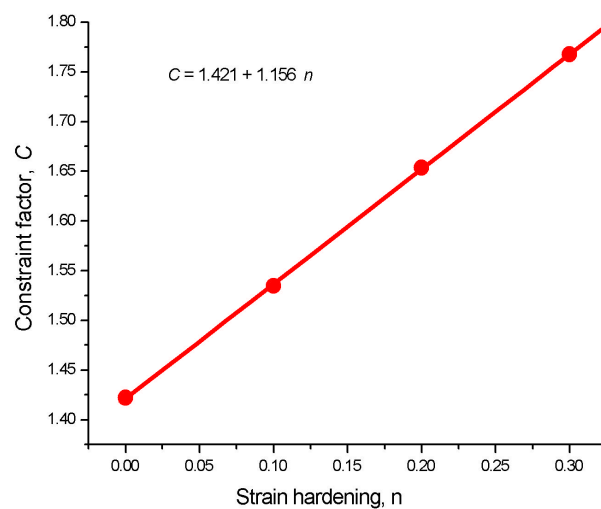


Figure 8.47 - Trend of the constraint factor C vs the hardening of the material obtained for $E = 196,000$ MPa.

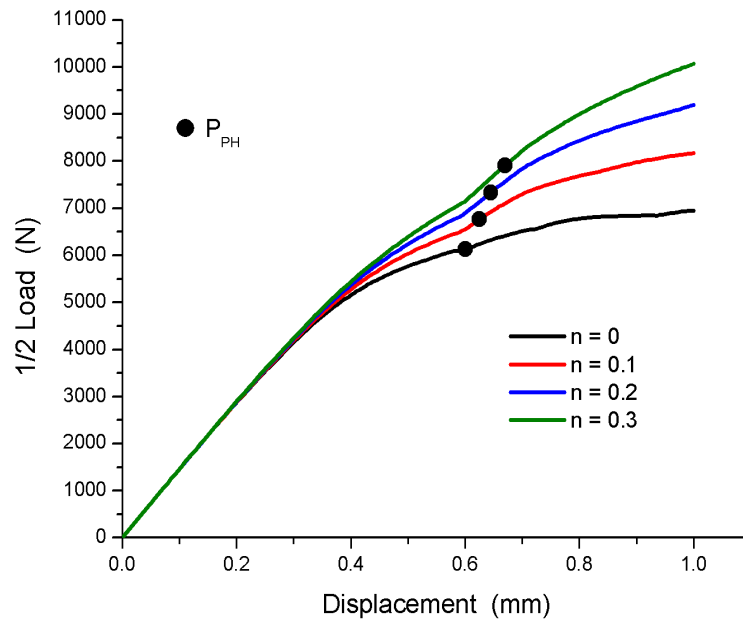


Figure 8.48 - FE results obtained for a Charpy V-N specimen of elastic-plastic material having different strain hardening, yield strength of 492 MPa and Young's modulus equal to 71,000 MPa. The picture shows the points (full circles) where the plastic hinge was first formed.

n	Displacement at Plastic hinge (mm)	$\frac{1}{2}$ Load P_{PH} (MPa)	C
0.0	0.60015	6,128.1	1.4238
0.1	0.62515	6,769.5	1.5728
0.2	0.64515	7,337.0	1.7047
0.3	0.67015	7,904.7	1.8366

Table 8.2 - Time, displacement and forces with $E = 71,000$ MPa, at the moment when plastic hinge first forms.

Table 8.2 lists the results obtained. Also in this case, the constraint factors are aligned over a straight line of equation:

$$C = 1.429 + 1.370 \cdot n \quad (8.20)$$

whose slope, shown in Figure 8.49, is very close, but just higher than that of eq.(10).

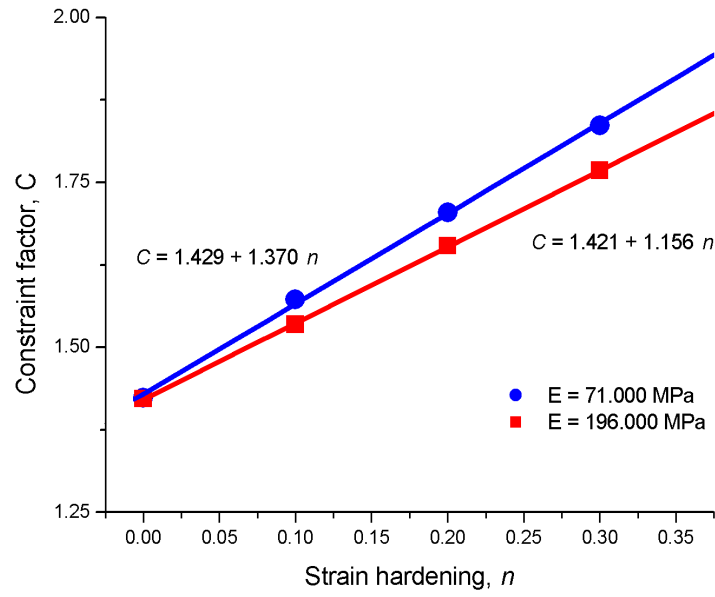


Figure 8.49 - Trend of the constraint factor C_{tpb} vs the hardening of the material obtained for $E = 71,000$ MPa compared to that for $E = 200,000$ MPa.

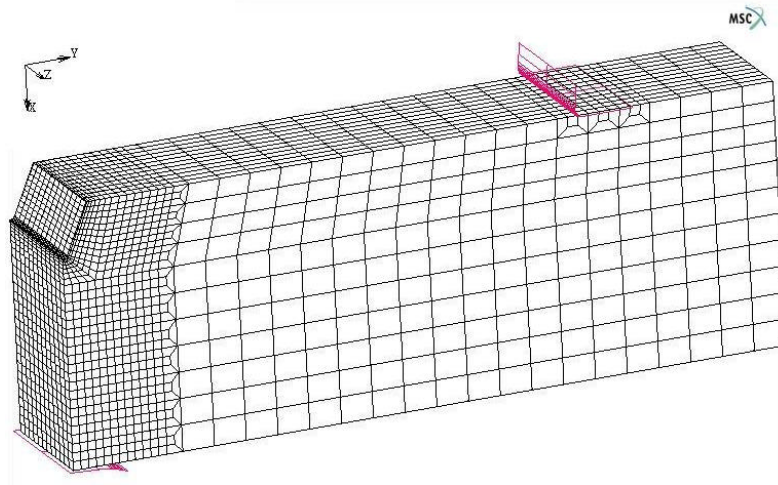


Figure 8.50 - Mesh used in the 3D static analysis. Only 1/4 of the specimen has been considered ($\frac{1}{2}$ thickness).

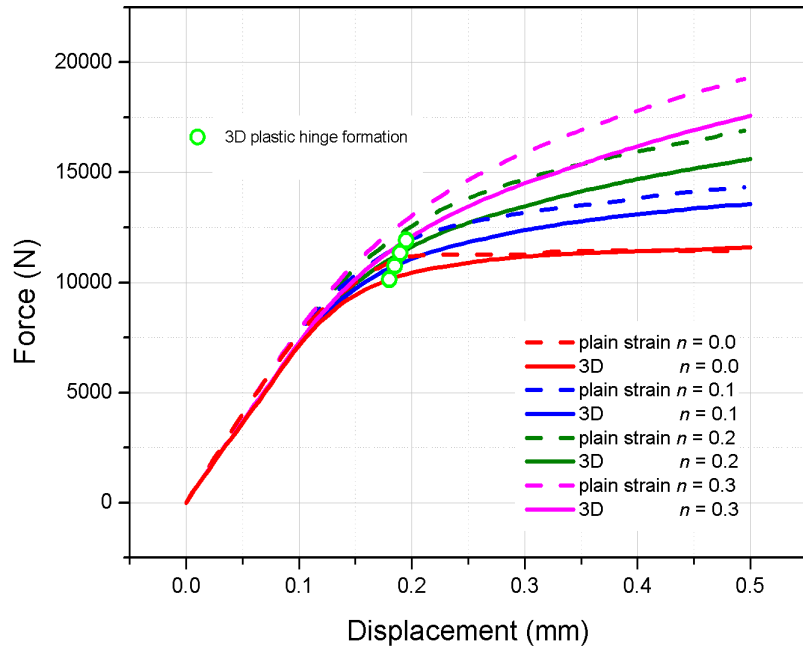


Figure 8.51 - 3D FE results obtained for $n = 0.0, 0.1, 0.2$ and 0.3 , respectively. For comparison, the 2D plain strain results are also shown.

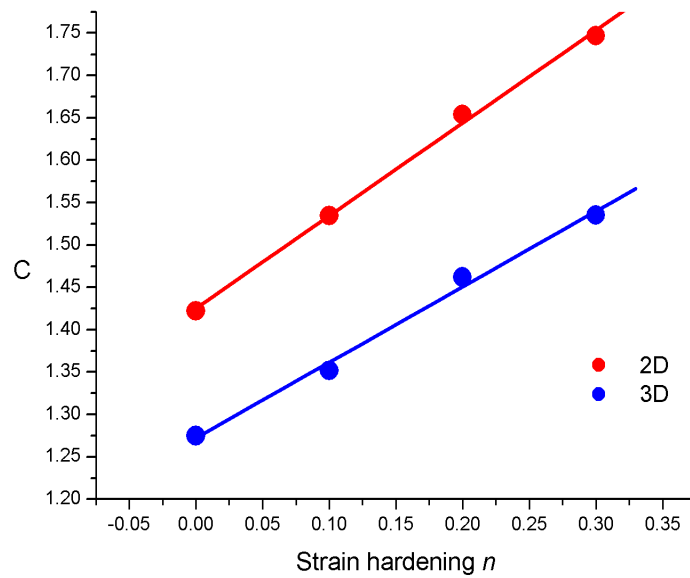


Figure 8.52 - Trend of plastic constraint factors vs strain hardening in FE 2D and 3D analyses.

8.3.3. 3D FE static analysis

We shall continue the investigation analyzing the 3D static case. The mesh used is shown in Figure 8.50.

As already said, this analysis is needed since a real Charpy V-N specimen is not thick enough for plain strain conditions to exist throughout the thickness, as assumed by the slip-lines theory. This can have an impact on the value of the constraint factor C . The results of 3D FE calculations are shown in Figure 8.51 (solid lines) together with those obtained under 2D plain strain conditions (dashed lines), for comparison. As expected, all the 3D curves lie below the corresponding 2D ones, indicating that, effectively, in real case (3D analysis) the compliance of the specimen is higher than in 2D analysis.

Consequently, also the value of the constraint factors under 3D conditions for the cases examined ($n = 0.0, 0.1, 0.2, 0.3$ and $E = 196,000$ MPa) are lower than those obtained in the 2D FE analysis. This is shown in Figure 8.52. The new equation for the 3D case is:

$$C = 1.287 + 0.89 \cdot n \quad (8.21)$$

The reduction in the values of the constraint factors C is evident. However, it must be noted that the 3D analysis indicates that in an un-notched Charpy specimen the moment M_{3D} at which the plastic hinge is formed under TPB loading, is given by:

$$M_{3D} = \sigma_y \frac{t(W-a)^2}{3.58} \quad (8.22)$$

The constant that appears at denominator is higher than 3.2 of eq.(8.17) and closer to the value of four valid for an un-notched Charpy specimen under pure moment (FPB) in plain-strain conditions, eq.(8.12). Moreover, it must be pointed out that, at variance with the 2D plain-strain case where the mesh plane is representative of any plane, in 3D conditions stresses and strains at a point vary, through the thickness, depending on the local triaxiality state. This, actually, means that the plastic hinge will not close at the same loading step, or at the same moment, on any plane. It will first form on the external surface of the Charpy V-N specimen, where plain stress conditions exist and the material is softer. When this happens, at mid-thickness the plastic zone is not closed yet. This can be immediately seen in the FE 3D calculation run on half thickness specimen (see Figure 8.50) where one plane represents the external face of the specimen and the other the mid-thickness one. Figure 8.53 presents this finding, showing the two planes of the specimen at the moment when the plastic hinge first forms on the external face, for the case n equal zero. The same result is obtained for $n = 0.1, 0.2$ and 0.3 . This last case is shown in Figure 8.54 that summarizes the results obtained for the 3D case on

the external face and on the central one, as well. The question arises as to when the plastic hinge really forms and, therefore, what value to select for the force P_{PH} .

Figure 8.55 shows the values of the C factor when the plastic hinge is completed throughout the Charpy V-N specimen, together with those already shown in Figure 8.52. It is interesting to note how the C factors relative to the case where the plastic hinge forms throughout the specimen section are very close to the 2D ones and, almost, coincide. The relative position on the force-displacement curves is shown of Figure 8.56.

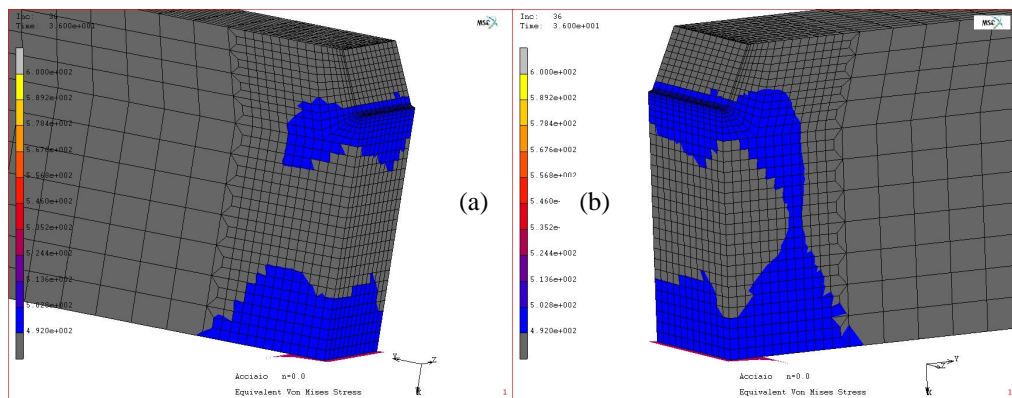


Figure 8.53 - $n = 0.0$. Plastic hinge formation on the external face of the Charpy V-N specimen (b). At the same load step the plastic hinge is not completely formed on the mid-thickness plane (a).

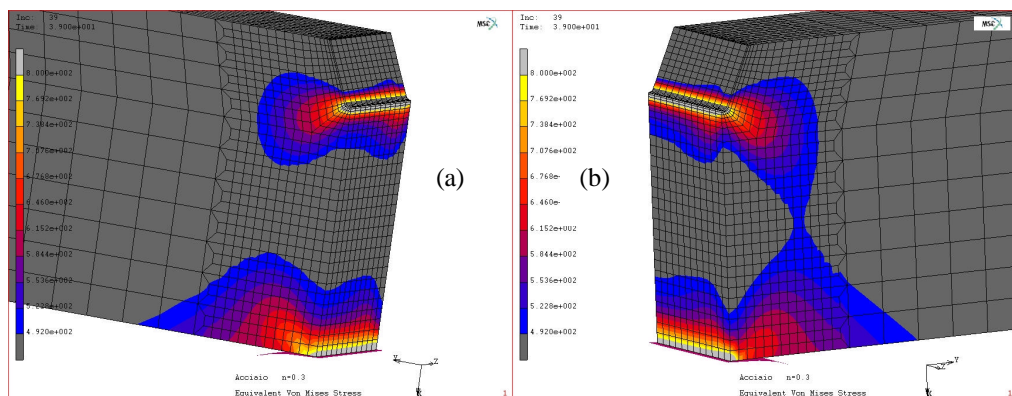


Figure 8.54 - $n = 0.3$. Plastic hinge formation on the external face of the Charpy V-N specimen (b). At the same load step the plastic hinge is not completely formed on the mid-thickness plane (a).

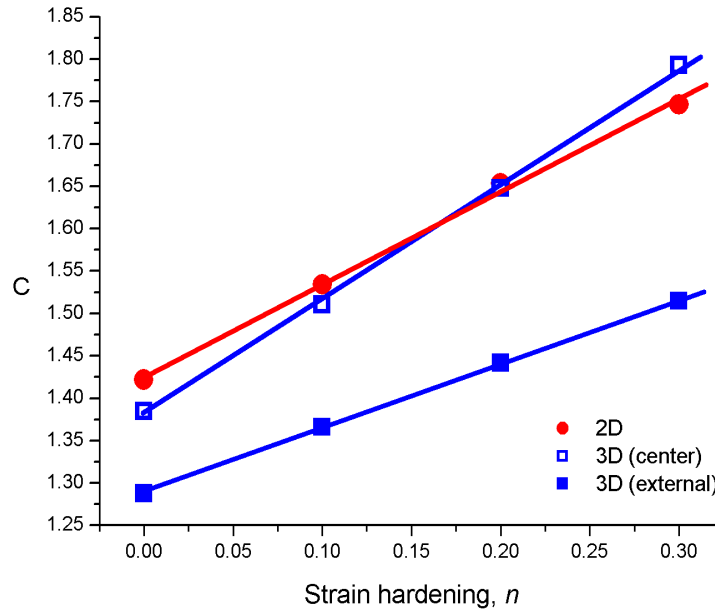


Figure 8.55 - Trend of the constraint factors versus strain hardening n under 2D and 3D conditions. As to the latter case, it is shown the trend of the C factors on both the external surface and the inner face (center of specimen).

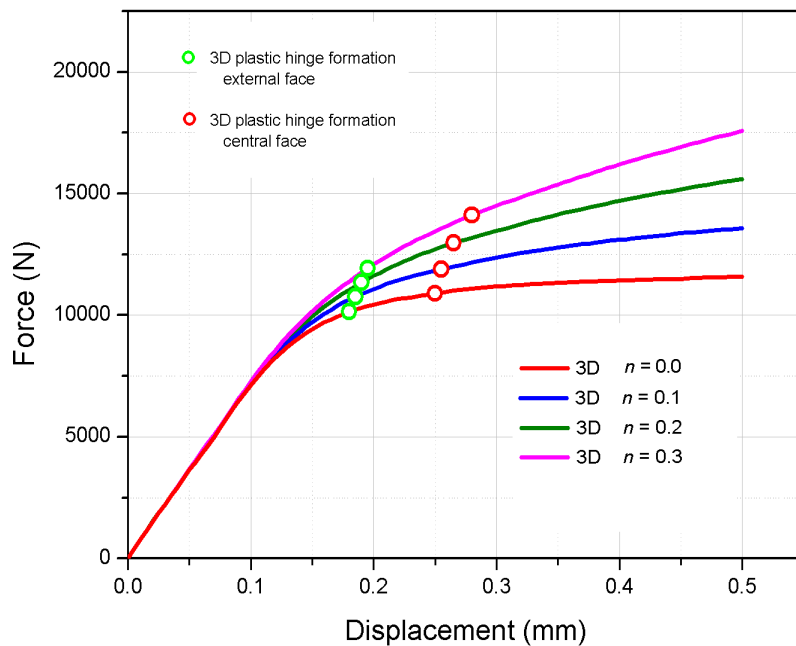


Figure 8.56 - 3D analysis. The closure of the plastic hinge on the external face and on the center face of the Charpy V-N specimen is shown on the load-displacement curves for n equal to 0.0, 0.1, 0.2 and 0.3, respectively.

n	Displacement (mm)	Load P_{PH} (N)	C	Displacement (mm)	Load P_{PH} (N)	C
	External face			Central face		
0.0	0.180	10,036.5	1.2876	0.250	10899.36	1.3846
0.1	0.185	10,640.9	1.3659	0.255	11890.64	1.5105
0.2	0.195	11,509.6	1.4414	0.265	12970.96	1.6477
0.3	0.200	12,085.4	1.5144	0.280	14111.88	1.7927

Table 8.3 - Displacement, force and constraint factor at the moment when plastic hinge forms on the external face and on the central one. ($E = 196,000$ MPa)

8.3.4. Summary of 2D-3D FE static results

We have shown that, using a Charpy V-N specimen and an instrumented Charpy pendulum, the slip-line theory provides the value of the yield strength σ_y of a material through eq.(8.14):

$$\sigma_y = \frac{4}{C} \frac{W}{t(W-a)^2} P_{GY} \quad (8.23)$$

In eq.(8.23) the factor 4 stems from the pure moment (FPB) expression:

$$M_{FPB} = \frac{t \cdot (W-a)^2}{4} \sigma_y \quad (8.24)$$

The constraint factor C for the American tup indenter is equal to 1.336, so that eq.(8.23) yields:

$$\sigma_y = \frac{4}{1.336} \frac{P_{GY} W}{t(W-a)^2} = 4.678 \cdot 10^4 P_{GY} \quad (8.25)$$

For a TPB specimen under plain strain conditions, the 2D FE analysis provides a new expression for the moment M so that eqs. (8.24) and (8.23) now become:

$$M_{TPB} = \frac{t \cdot (W-a)^2}{3.2} \sigma_y \quad (8.26)$$

$$\sigma_y = \frac{3.2}{C_{2D}} \frac{W}{t(W-a)^2} P_{GY} \quad (8.27)$$

For a rigid ideally plastic material, the constraint factor C_{2D} turns out to be equal to 1.422, so that eq.(8.17) yields:

$$\sigma_y = \frac{3.2}{1.422} \frac{W}{t(W-a)^2} P_{GY} = 3.5164 \cdot 10^4 P_{GY} \quad (8.28)$$

In a real elastic-plastic material, the constraint factor C_{2D} depends on the strain hardening n of the material according to eq.(8.19):

$$C_{2D} = 1.421 + 1.156 \cdot n \quad (8.29)$$

so that eq.(8.27) becomes:

$$\sigma_y = \frac{3.2}{(1.421 + 1.156 \cdot n)} \frac{W}{t(W-a)^2} P_{PH} \quad (8.30)$$

where P_{GY} has become P_{PH} . For a standard Charpy V-N specimen, $W = t = 10$ mm, so that eq. (8.30) can be written as:

$$\sigma_y = \frac{3.2}{(1.421 + 1.156 \cdot n)} \frac{P_{PH}}{(W-a)^2} \quad (8.31)$$

Eq.(8.31) is valid for a material with a Young's modulus $E = 196,000$ MPa. For $E = 71,000$ MPa the constraint factor C varies according to eq.(8.20) and eq.(8.30) becomes:

$$\sigma_y = \frac{3.2}{(1.429 + 1.37 \cdot n)} \frac{W}{t(W-a)^2} P_{PH} \quad (8.32)$$

Moving to a TPB specimen under real conditions, the 3D FE analysis provides a new expression for the moment M so that eqs.(8.24) and (8.23) now becomes:

$$M_{3D,TPB} = \frac{t \cdot (W-a)^2}{3.58} \sigma_y \quad (8.33)$$

$$\sigma_y = \frac{3.58}{C_{3D,TPB}} \frac{W}{t(W-a)^2} P_{PH} \quad (8.34)$$

As for the 2D plain strain case on real materials, also in 3D conditions the constraint factor $C_{3D,TPB}$ depends on the strain hardening n of the material. Yet, now the formation of the plastic hinge occurs in two steps: first it forms on the external face which is always in plain stress conditions, later it doses on the mid-section, which behaves in

plain strain conditions. Accordingly, we now have two equations for the constraint factor $C_{3D,TPB}$. The first refers to the moment when the plastic hinge appears on the surface and is given by eq.(8.21):

$$C_{3D,TPB} = 1.27 + 0.89 \cdot n \quad (8.35)$$

the second to the formation of the plastic hinge on the mid-thickness and can be assumed to be the same as in 2D plain strain conditions (see Figure 8.55) and given by eq.(8.19). Therefore the expression for the yield stress will be:

$$\begin{aligned} \sigma_y &= \frac{3.58}{C_{3D,TPB}} \frac{W}{t(W-a)^2} P_{PH} = \frac{3.58}{(1.27 + 0.89 \cdot n)} \frac{W}{t(W-a)^2} \text{ external} \\ \sigma_y &= \frac{3.58}{C_{3D,TPB}} \frac{W}{t(W-a)^2} P_{PH} = \frac{3.58}{(1.421 + 1.156 \cdot n)} \frac{W}{t(W-a)^2} \text{ mid. thick.} \end{aligned} \quad (8.36)$$

In practice, we can introduce an effective constraint factor C_{eff} for the different condition examined by rewriting eq.(8.25), (8.27) and (8.24) in the most general form:

$$\sigma_y = \frac{A}{C} \frac{P \cdot W}{t(W-a)^2} = \frac{1}{C_{eff}} \frac{P \cdot W}{t(W-a)^2} \quad (8.37)$$

with the following values of $C_{eff} = C/A$:

A) slip-line solution, pure bending (FPB):

$$C_{eff} = \frac{1.336}{4} = 0.334 \quad (8.38)$$

B) 2D TPB, $n = 0.0$:

$$C_{eff,2D} = \frac{1.42}{3.2} = 0.443 \quad (8.39)$$

C) 3D TPB, $n = 0.0$:

$$C_{eff,3D} = \frac{1.288}{3.58} = 0.359 \quad (8.40)$$

This last $C_{eff,3D}$ for TPB condition is very close to the C_{eff} coming from the slip-line solution:

$$\frac{C_{eff,3D}}{C_{eff}} = \frac{0.359}{0.334} = 1.077 \quad (8.41)$$

8.3.5. 3D FE Dynamic analysis

8.3.5.1. Plain strain condition

The first set of FE analyses were carried out over a 3D model of a 1/2 thickness Charpy V-N specimen and tup under imposed plain strain conditions, using the LS-DYNA 960 program. The mesh used had 20,240 brick elements whose minimum dimension was 0.047 mm. Figure 8.57 shows the 3D mesh for the half structure. The mesh refinement in the central region of the specimen was due to the need to pick up with great accuracy the actual moment of plastic hinge formation. Because of the symmetry of the system only a quarter mesh has been used in the analysis, as shown in Figure 8.58. The indenter was assumed to impact the specimen at a speed of 5.0 m/s, typical of a Charpy test. The constitutive equation used in the analysis for the plastic component of stress s_p has the form:

$$\sigma_p = k(\varepsilon)^n \quad (8.42)$$

Even though the analyses were dynamic, in this phase of calculations aimed at comparing static and dynamic results, the yield strength σ_y was assumed to be constant, i.e. independent of the strain rate. Four runs were done with $n = 0.0, 0.1, 0.2$ and 0.3 and k equal to 492 MPa, 892.1 MPa, 1629.38 MPa and 2965.19 MPa, respectively, to simulate the material behavior. The result relative to $n = 0.0$ case (elastic-perfect plastic, $\sigma_y = 492$ MPa) is shown in Figure 8.59 in terms of load versus time. The forces that appear in the diagram are those relative to the contact surface between tup indenter and Charpy V-N specimen and the sum of reactions on the two supports, $\Sigma R = 2 \cdot R$. The graph evidences the trend of force P and reactions during the first 10^{-4} s. It's well within that time frame that the plastic hinge forms. Therefore, what happens later is not of real interest for the present considerations. It is interesting to note how the reaction forces on the anvils start at about $0.4 \cdot 10^{-5}$ s after the first hammer-specimen contact. Considering that the anvil is about 22 mm far from the tup, this delay indicates an elastic wave speed of about 5500 m/s. The presence of inertia forces is evident. The vibration shown in Figure 8.59 has a period t of about $4 \cdot 10^{-5}$ s, equal to the experimental data, shown in Figure 8.34 for a steel A 508 Cl.B, that indicate a period of about $4 \cdot 10^{-5}$ s and frequency of about 25,000 Hz. The empirical equation, known as the Server relation:

$$t = 3.36 \frac{W}{c_o} (EtC_s)^{1/2} \quad (8.43)$$

is yielding close results. In eq.(8.43) E is the Young's modulus, W the width of the specimen, c_o the velocity of sound in the material, t the thickness and C_s the specimen compliance.

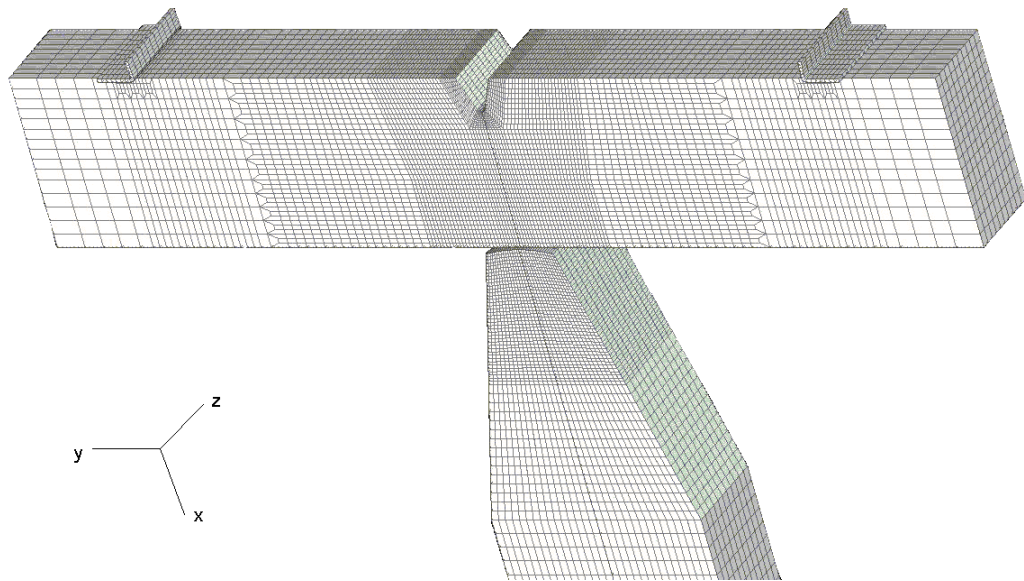


Figure 8.57 - Schematic of half thickness FE mesh.

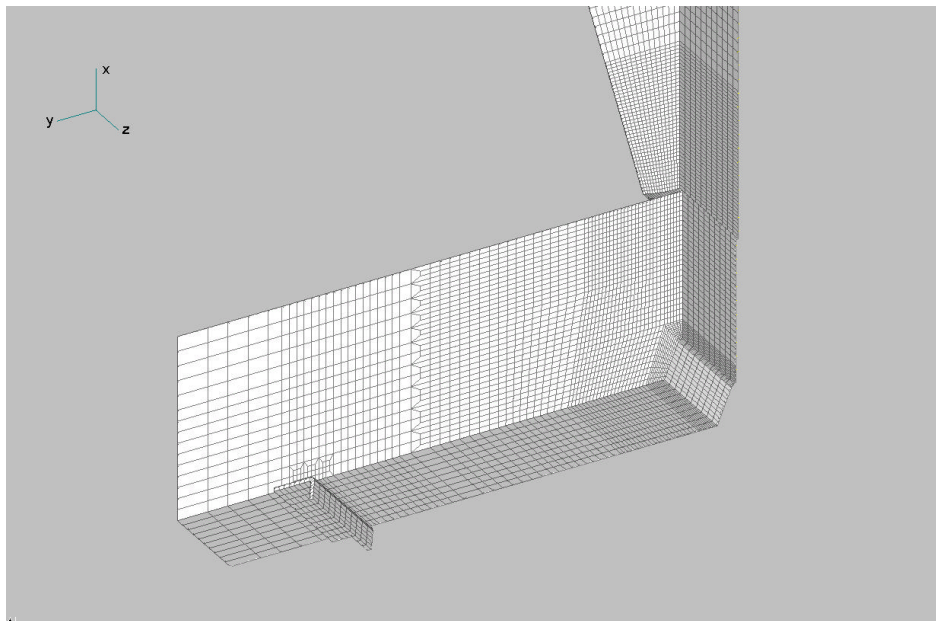


Figure 8.58 - Schematic of FE mesh used in the analysis (one quarter of the structure).

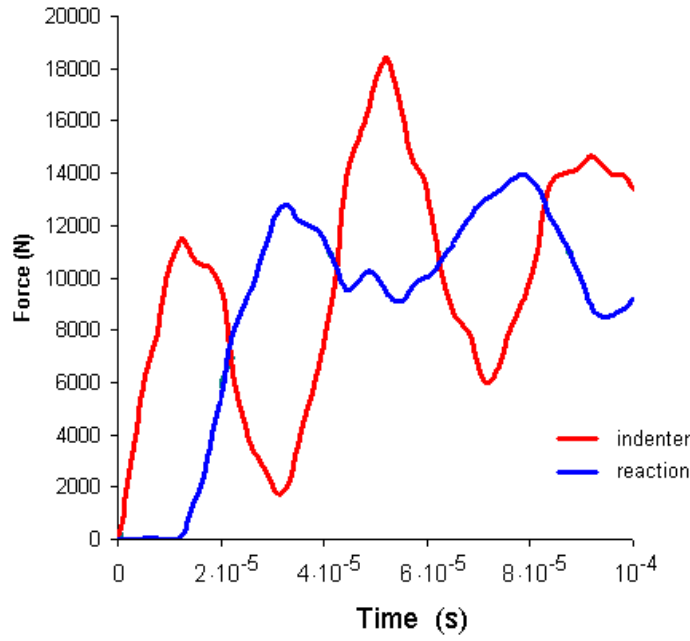


Figure 8.59 - Record of load versus time obtained in the dynamic analysis with $n = 0.0$ on the contact surface between tup indenter and Charpy V-N specimen and on the anvil as total reaction.

For the Charpy specimen, the compliance C_s is given by the relation (Ref. 8.22):

$$C_s = \frac{24.4}{Et} \quad (8.44)$$

Combining eqs.(8.43) and (8.44) yields:

$$\tau = 3.36 \frac{W}{c_o} (24.4)^{1/2} \quad (8.45)$$

Considering that the velocity of sound c_o , in a medium of density \mathbf{r} , is given by $\sqrt{E/\mathbf{r}}$, c_o is about 5000 m/s and eq.(8.45) yields a period \mathbf{t} :

$$\tau = 3.3 \cdot 10^{-5} \quad s \quad (8.46)$$

The theoretical values (vibration of beams) for a simply supported beam are given by the relation:

$$f = \lambda_n^2 \sqrt{\frac{EI}{\rho A l^4}} \quad (8.47)$$

where I is the inertia modulus, ρ the density, A the area of the cross section, l the length of the beam and λ_n are relative to the n -mode of vibration:

$$\lambda_n = n \cdot \pi, \quad n = 1, 2, \dots \quad (8.48)$$

For the first mode ($n = 1$) eq.(8.47) yields:

$$f_1 \approx 28,000 \quad Hz \quad (8.49)$$

The FE measured frequency of 25 MHz ($1/4 \cdot 10^{-5}$) corresponds to the first mode, which dominates the initial transient when the displacement is still very small. The superposition of the second mode, having a frequency four times higher, just visible in Figure 8.59, is better seen in the rigid body acceleration diagram of

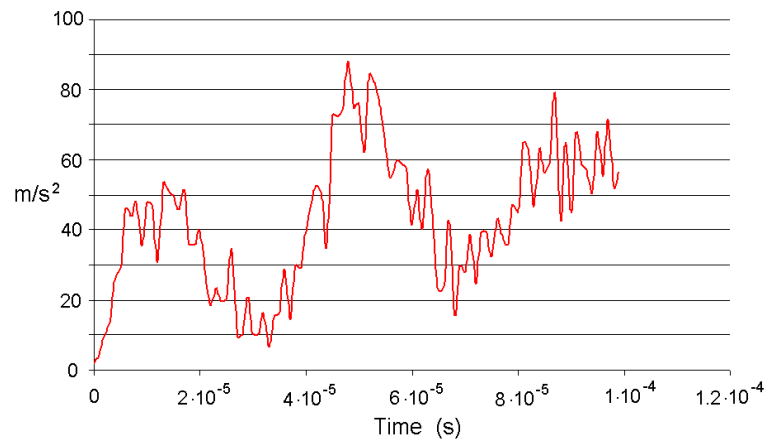


Figure 8.60 - Rigid body acceleration showing first and second mode of vibration.

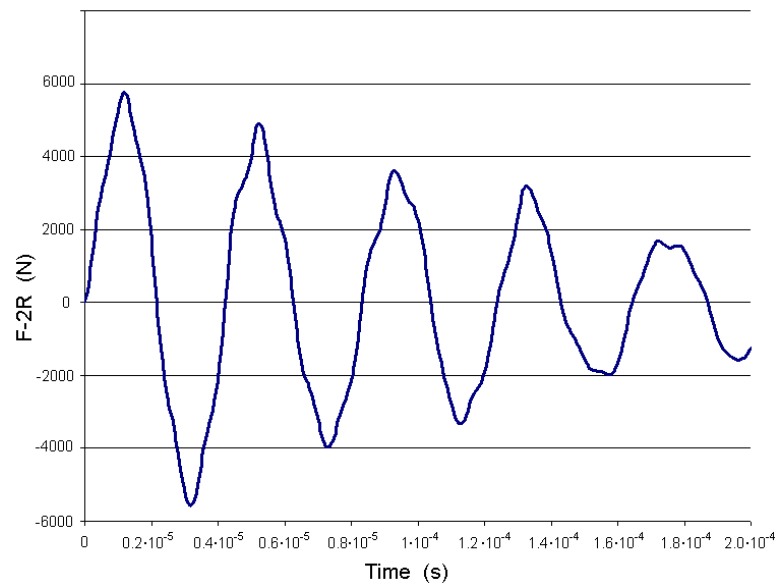


Figure 8.61 - Plot of external forces.

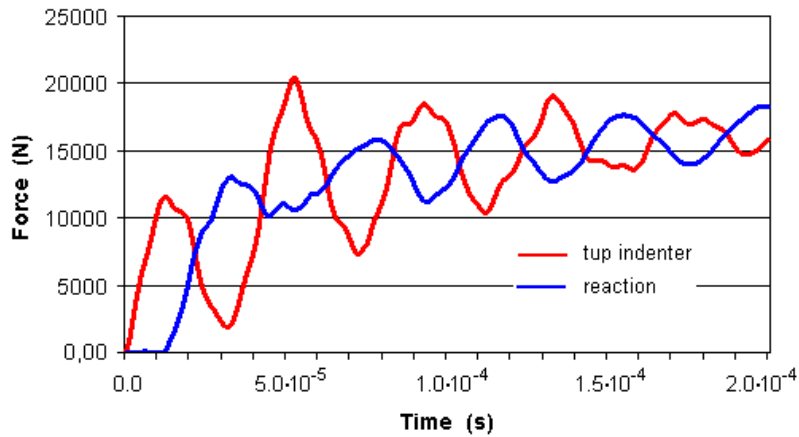


Figure 8.62 - Record of load versus time obtained in the dynamic analysis with $n = 0.1$ on the contact surface between tup indenter and Charpy V-N specimen and on the anvil as total reaction.

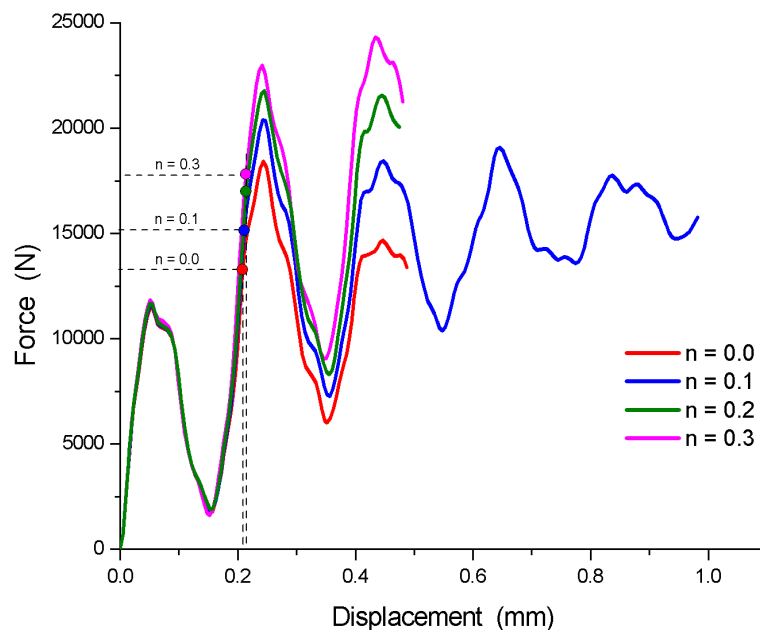


Figure 8.63 - Dynamic curves obtained in the FE analysis.

Figure 8.60. As the hammer advances, its pressure over the specimen grows continuously turning the contact surface into a node with almost full constraint. Mode one tends to diminish and the relative inertia loads to reduce and almost vanish. This can be seen by plotting the trend of external forces (sum of the tup force F and the total reaction $-2 \cdot R$) versus time, as shown in Figure 8.61. This sum, which in a static case is always zero, under dynamic conditions is balanced by the inertia forces. It's evident the

progressive reduction of that difference till the moment when it would become negligible, indicating the absence of inertia loads.

n	Time (s)	Displacement (mm)	Tup force P_{PH} (N)	Reactions 2·R (N)	$P_{PH,eq}$ (N)
0.0	$4.4 \cdot 10^{-5}$	0.208	13,198	9,648	11,022
0.1	$4.5 \cdot 10^{-5}$	0.211	15,196	10,135	11,875
0.2	$4.6 \cdot 10^{-5}$	0.214	16,977	10,895	12,665
0.3	$4.6 \cdot 10^{-5}$	0.214	17,773	11,398	13,250

Table 8.4- Time, displacement and forces at the moment when plastic hinge first forms, (E = 196,000 MPa)

In reality, inertia forces do not disappear completely since mode two becomes dominant, even though with lower amplitudes. For the case $n = 0.1$ the results of the calculations are shown in Figure 8.62. Again, the natural period is $4 \cdot 10^{-5}$ s and the frequency 25,000 Hz. Analogous results were obtained for the cases $n = 0.2$ and $n = 0.3$. Figure 8.63 compares the results obtained for all strain hardening considered in this analysis. The question arises as how to locate, on curves like those of Figure 8.59, Figure 8.62 and Figure 8.63, the moment when the plastic hinge first forms. The numerical results can provide an answer. The minimum mesh size adopted (0.047 mm) allows the use of time steps, for the FE calculations, extremely small, about $6.5 \cdot 10^{-9}$ s. This can provide a very accurate appreciation of the stress-strain state during the transient and pinpoint exactly the moment when the plastic hinge first forms.

Figure 8.64 presents a sequence of Lüder's lines emanating from the notch tip of a Charpy V-N specimen under dynamic condition with $n = 0.0$. As it can be seen, the plastic hinge first forms after $4.39 \cdot 10^{-5}$ s into the transient (Figure 8.64e), when the load at the tup-specimen contact surface has reached a value of 13,198 N with a displacement of 0.208 mm. The same procedure applied to the other cases yielded the results listed in Table 8.4.

The point of first plastic hinge formation is shown in Figure 8.63 by the solid circles. At a glance comparison between Table 8.4 and Table 8.1 indicates that the displacements at which the plastic hinge forms are rather close, but the forces and reactions are not. Since in the dynamic calculations the yield strength is not changed (so far the strain rate effect has not been considered), responsible for the elevation of forces are just the inertia loads, but these loads shall not be taken into consideration in eq.(8.18) otherwise they would artificially increase the value of the yield strength.

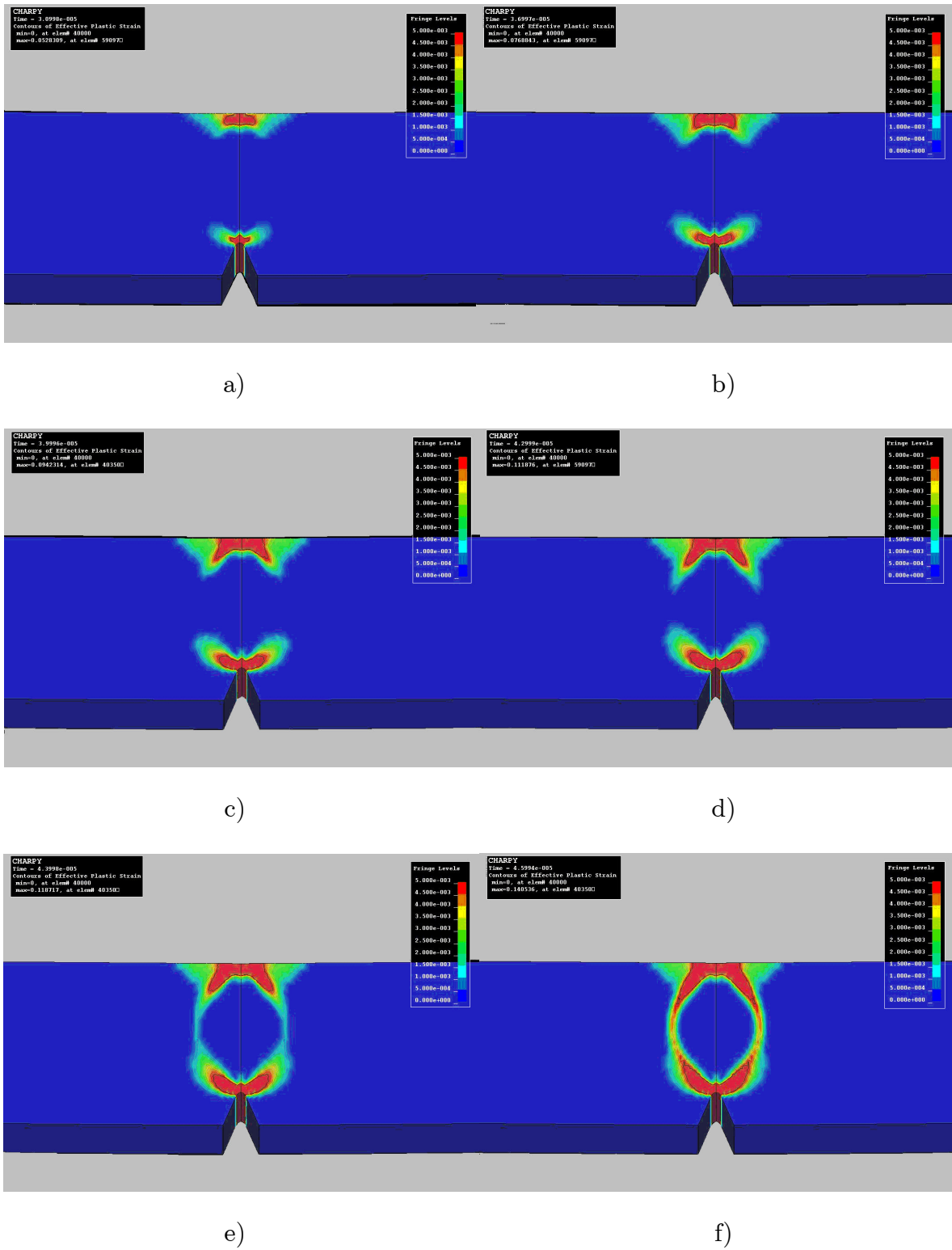


Figure 8.64 - Sequence of plastic hinge formation in a Charpy V-N specimen loaded dynamically by a tup indenter having an impact speed of 5 m/s.

Therefore, in our consideration we must refer to what we will indicate as the static equivalent curve obtained subtracting the inertia component from the dynamic response and this derived curve shall necessarily be equal to the static curve previously calculated with the FE static analysis.

This can be done in a rather simple way. With reference to Figure 8.65, from the equilibrium of moments on the section containing the notch, we have:

$$R \frac{l}{2} + \int_V f(\dot{\omega}, r, \theta) \cdot \rho \cdot dV = M_r \quad (8.50)$$

where R is the reaction, l the length of the specimen, r and θ the polar coordinates, $\dot{\omega}$ the angular acceleration, ρ the density, V the volume of half specimen and M_r the reaction moment. The integral represents the inertial component of forces. The bending moment M_r on the section containing the notch can be assessed calculating the internal reactions σ_{yy} in the y direction on the same section (see Figure 8.65). During the transient the elements on the notch section are not subjected to any acceleration in the y direction, because the section is a plane of symmetry for longitudinal vibrations and remains still. This actually means that the reaction moment M_r on the notch section is not affected by inertia forces.

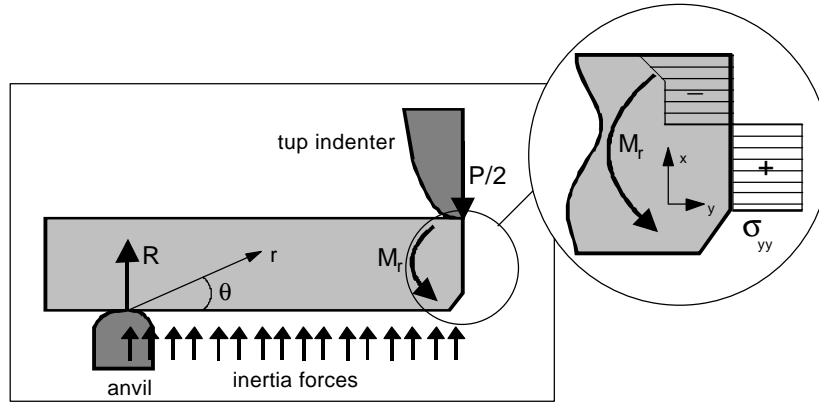


Figure 8.65 - Inertia and external forces that balance the reaction moment by internal stresses on the notch section.

This reaction moment M_r will be balanced by an equivalent static reaction force R_{eq} placed in the anvil:

$$R_{eq} \frac{l}{2} = M_r \quad (8.51)$$

Then, twice R_{eq} will be the static equivalent component P_{eq} on the tup. This procedure has led to the diagram of Figure 8.66.

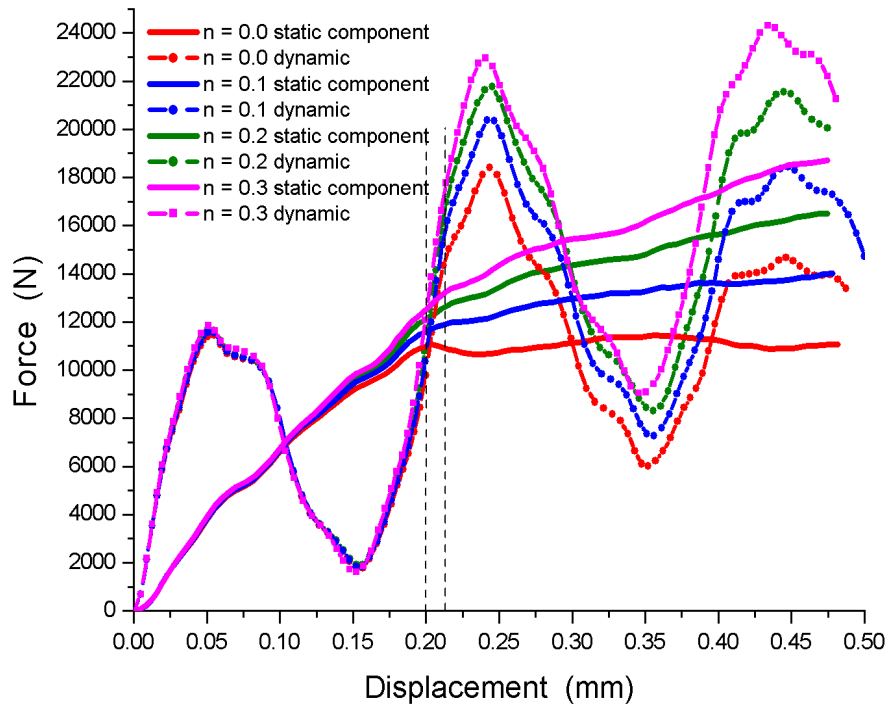


Figure 8.66- Comparison between static equivalent and dynamic forces exerted by the tup indenter on the Charpy V-N specimen, for the four values of n considered in this analysis.

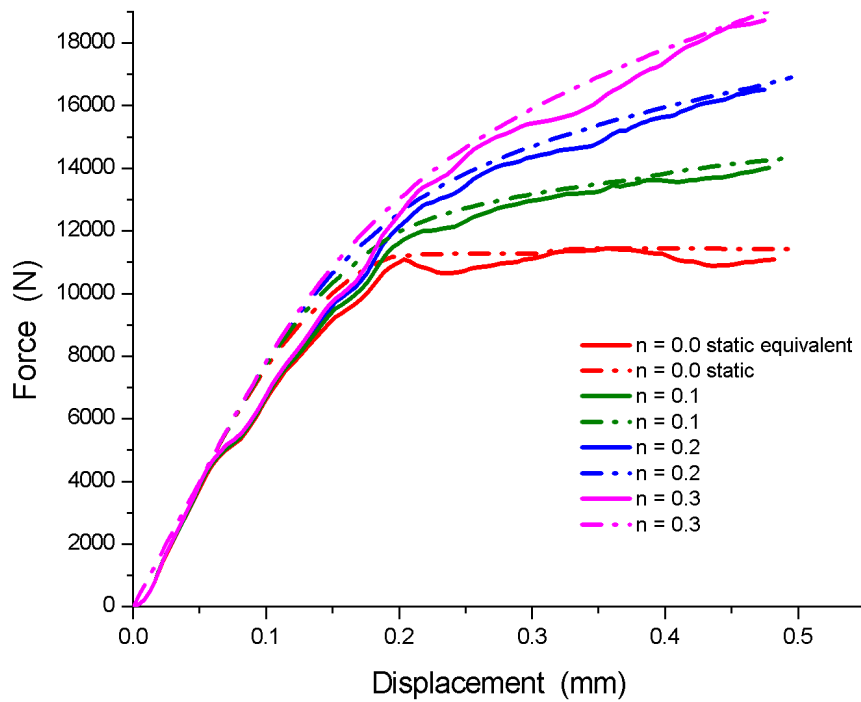


Figure 8.67 - Comparison between static and static equivalent forces at the tup indenter-specimen surface contact.

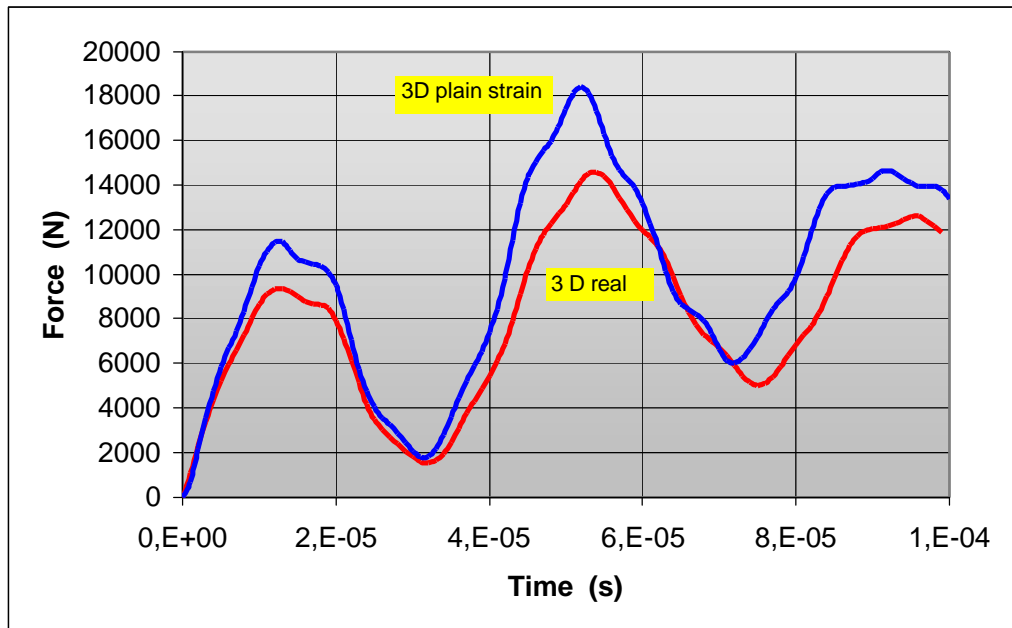


Figure 8.68 - Comparison between 3D plain strain conditions and 3D real conditions, for the tup force vs time and $n = 0.0$.

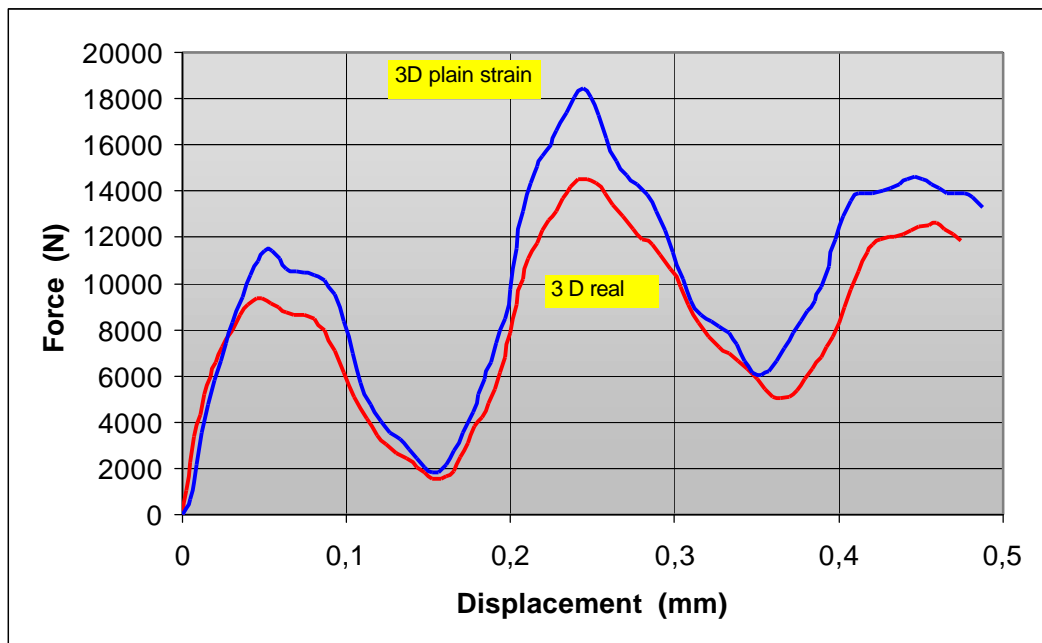


Figure 8.69 - Comparison between 3D plain strain conditions and 3D real conditions, for the tup force vs displacement and $n = 0.0$.

Here, the static equivalent forces (solid lines) are compared with those including the inertial component (dotted lines) already seen in Figure 8.63. Also shown in Figure 8.66 is the displacement interval, $0.2 \div 0.214$ mm, in which the plastic hinge is first formed. The corresponding values of the tup force, $P_{PH,eq}$, are listed in the last column of Table 8.4. The trend of the static equivalent forces P_{eq} must be equal to that computed in the static 2D FE analysis under plain strain conditions, shown in Figure 8.46. Such a comparison is presented in Figure 8.67. As it can be seen, the agreement is rather good, even though some signs of oscillations are still visible.

8.3.5.2. Real conditions

The second set of 3D calculations was run without imposing the plain strain condition. This analysis has been termed 3D real conditions. Figure 8.68 presents a comparison between 3D plain strain conditions and 3D real conditions, in terms of tup force versus time, for the case $n = 0.0$, while Figure 8.69 shows tup force versus displacement.

The softening of the specimen under real conditions can be seen, as expected. The same comparison in terms of static equivalent forces is presented in Figure 8.70, overlapped to the dynamic response under real conditions. The closed point indicates the moment when the plastic hinge is formed. For the real case there are two of such a point:

For the real case there are two of such a point: the first indicates the completion of the plastic hinge on the external surface, where it closes first, the second refers to the mid section. It is also interesting the comparison of the 3D static equivalent force to the 3D static one, where the static equivalent force has been inferred from the dynamic analysis through the method outlined in the previous section. Such a comparison is shown in Figure 8.71. The complete picture of results relative to the other strain hardening values ($n = 0.1, 0.2$ and 0.3) is shown in Figure 8.72. It is interesting to note that, at about $17 \mu s$, which corresponds to a displacement of about $6.8 \cdot 10^{-2}$ mm, the static equivalent force, at any hardening, shows a sudden softening, though of small amount, both under plain strain and real conditions, as well, which doesn't appear in the 3D static analysis.

It is not clear, at the moment, the actual reason of the softening, yet the equivalence between the two analyses, shown in Figure 8.72, is impressive. Therefore, we can consider the C coefficients developed under 3D static conditions, given by eq.(8.35), as applicable to the 3D real conditions.

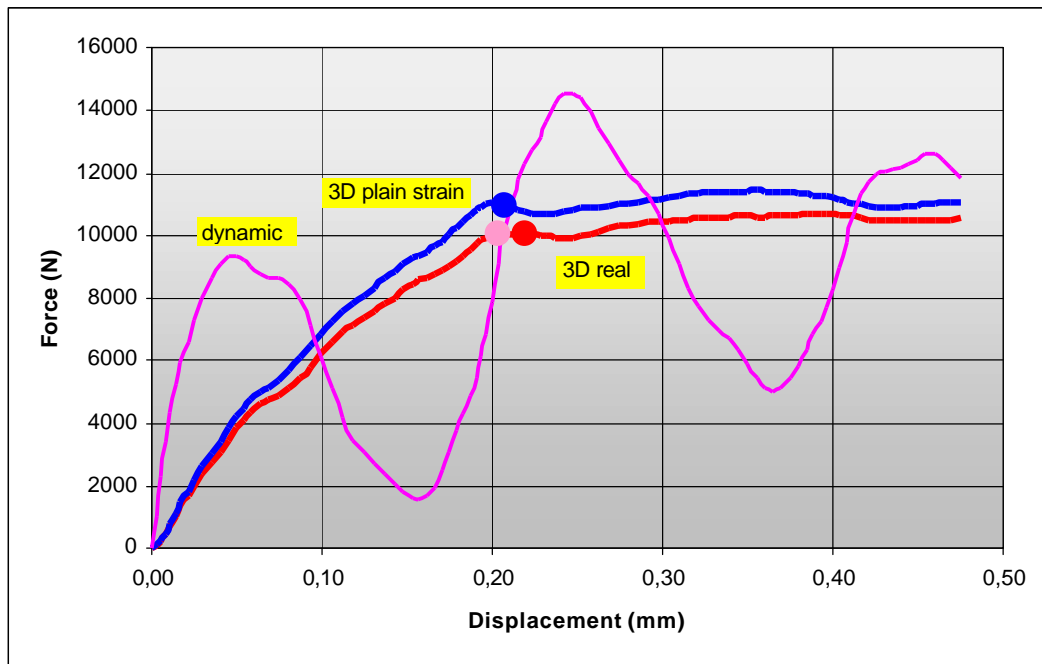


Figure 8.70 - Comparison between static equivalent tup forces under 3D plain strain conditions and 3D real conditions. The closed points indicate the moment in which the plastic hinge is formed.

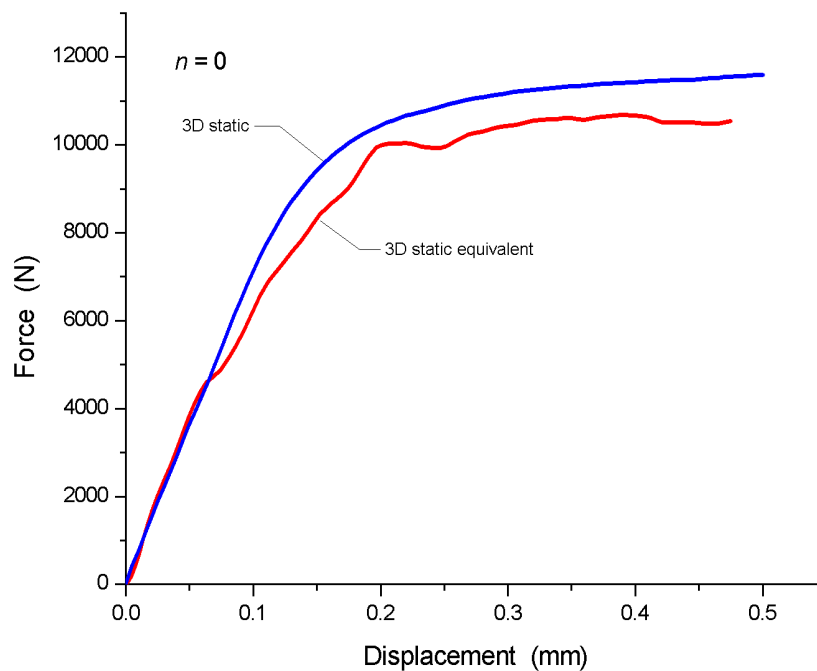


Figure 8.71 - Comparison between 3D static equivalent force (derived from the 3D dynamic calculations) on the tup and the corresponding 3D static, for the case $n = 0.0$.

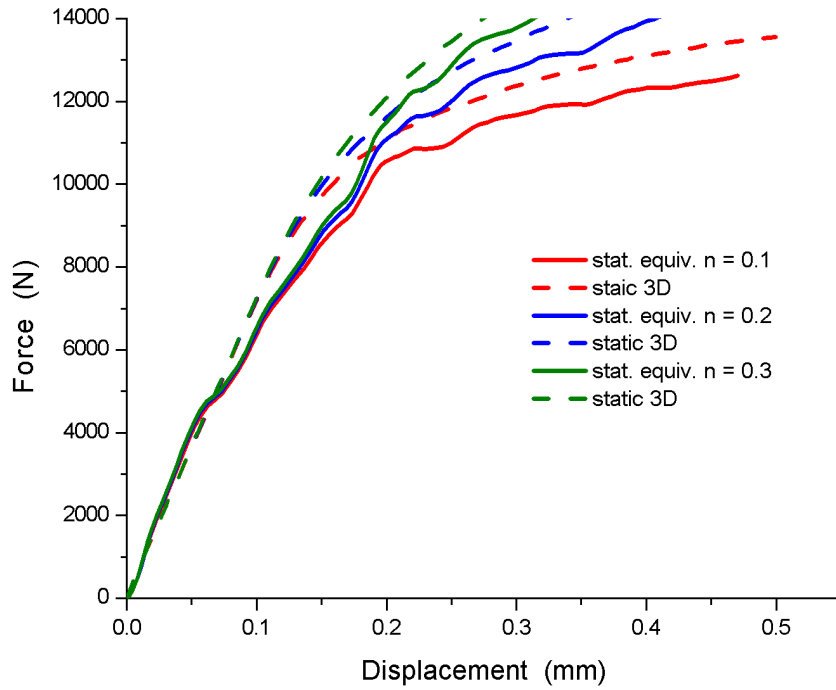


Figure 8.72 - Comparison between 3D static equivalent force (derived from the 3D dynamic calculations) on the tup and the corresponding 3D static, for the case $n = 0.1$, 0.2 and 0.3.

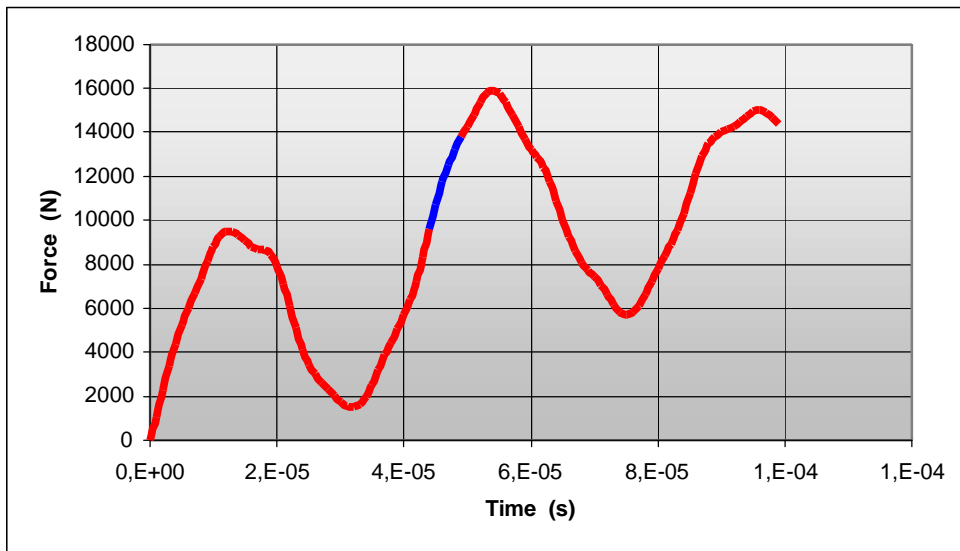


Figure 8.73 - Trend of the tup force during the transient. From about 44 μ s to about 49 μ s the plastic hinge closes on the external and internal face, respectively.

8.3.5.3. Strain rate assessment

The last point to consider, which is also the main target of the study, is the assessment of the strain rate during the plastic hinge formation, in particular. It is obvious that the

Charpy V-N specimen is suitable to measure a dynamic strain rate effect on the material properties only if the strain rate during its plastic deformation is constant. To this purpose, the plastic strain during the transient has been inferred throughout the plastic hinge that represent the actual strain rate measurement specimen. Figure 8.73 shows the trend of the tup force during the transient. The plastic hinge closes on the external face of the specimen during the second ramp at about 45 μs , while it closes on the internal face at about 50 μs . Before that time, there is no plastic hinge, but rather two lobes emanating from the notch and the tup indenter contact point. This is shown in the sequence of Figure 8.74, which refers to the internal face. The enclave between the two lobes, indicated with the letter A in Figure 8.74 (a) and (b), remains elastic till about 50 μs into the transient when the plastic hinge finally closes. From this moment

up to about 0.06 ms (see Figure 8.74c and d) the strain field in the hinge grows continuously, but with a constant strain rate $\dot{\epsilon}$, as it can be seen in Figure 8.75 by the constant slope of the various curves relative to the corresponding points in the hinge where the effective plastic strain has been computed. The caption of the letters given to each curve of Figure 8.75 is presented in Figure 8.76. From about 0.06 ms to about 0.08 ms it is $\dot{\epsilon} = 0$, i.e. the strain does not grow in the central part of the hinge. During this time, in fact, the plastic deformation extends towards the upper and lower surface of the

Charpy V-N specimen (see Figure 8.74 e and f). It is only later that $\dot{\epsilon}$ starts to grow again, as it can be seen in Figure 8.75. This particular behavior, i.e., the alternate growth and still of the strain, is characteristic of this central part of the plastic hinge, as it can be seen in Figure 8.79 for points A, D and G of Figure 8.76, in particular, that goes up to 0.2 ms. The same trend has been found along the plastic hinge, as far as the strain rate is concerned, but without any pause in plastic hinge growth. This is shown in Figure 8.78 for the points indicated by capital letters in Figure 8.77, in particular.

Again, the strain rate $\dot{\epsilon}$ appears to be constant. A precise evaluation of the strain rate during the time, for three points of the plastic hinge shown in Figure 8.79, in particular, is presented in Figure 8.80. As it can be seen, during the completion of the plastic hinge, at about 50 μs , the strain rate $\dot{\epsilon}$ is practically the same in all three points and equal to 200-250 s^{-1} . After the completion of the plastic hinge and the first pause (see Figure 8.79) it grows up to 400-450 s^{-1} and decreases down to 250 s^{-1} after 15 μs . The same trend of the plastic strain rate is seen on the side of the plastic hinge, as shown in Figure 8.81 for the points B and F of Figure 8.77. Here it can be clearly seen how the closure of the plastic hinge at point B occurs at about 10 μs later than in point F. At any rate, as the plastic hinge is formed the strain rate reaches 250-300 s^{-1} . It is interesting to note that this computed strain rate is very close to the value of 275 s^{-1} theoretically assessed by Server in 1978 (Ref. 8.12).

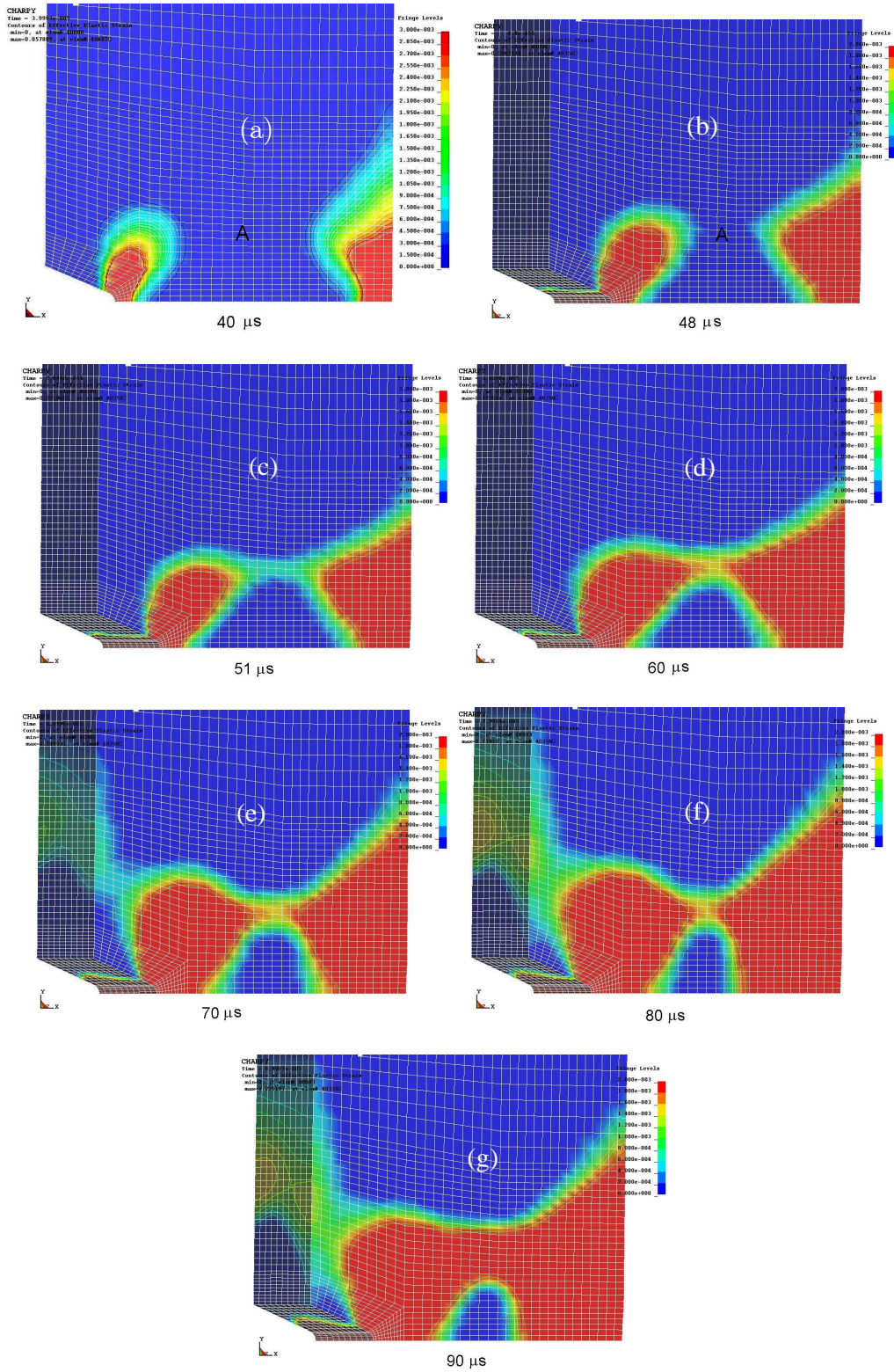


Figure 8.74 - Growth of the plastic hinge on the internal face of the Charpy V-N specimen. Till about 0.05 ms the two lobes are separated by an elastic strain field (denoted with the A letter). From about 0.05 to 0.06 ms the hinge is formed with a

growing strain field afterwards it remains constant up to about 0.08 ms, during which the strain field extends towards the upper and lower part of the specimen.

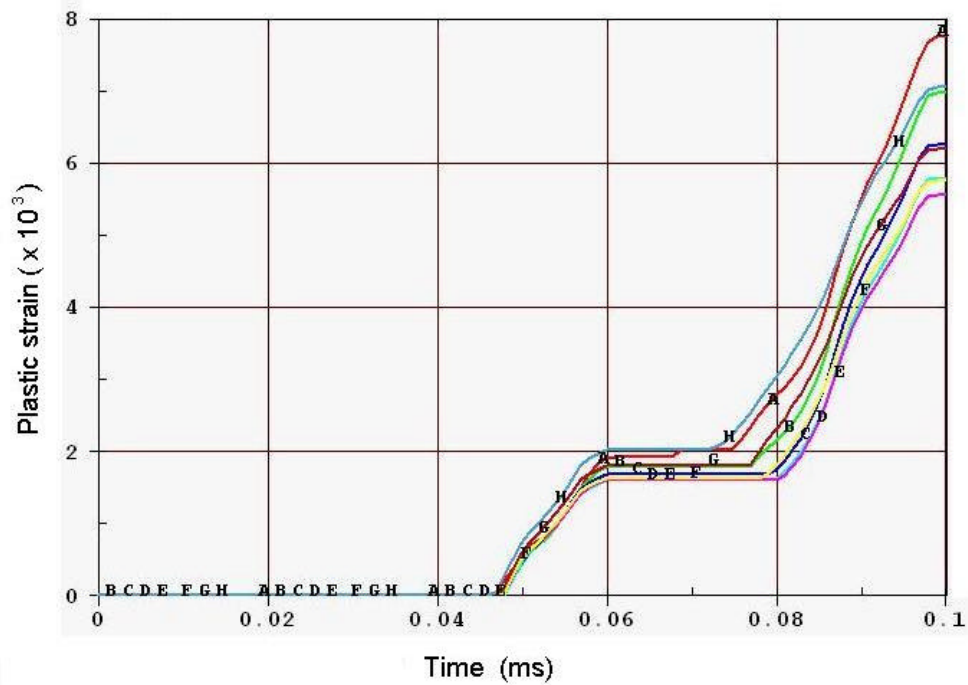


Figure 8.75 - Trend of the effective plastic strain in the plastic hinge. The letter caption is presented in Figure 8.76.

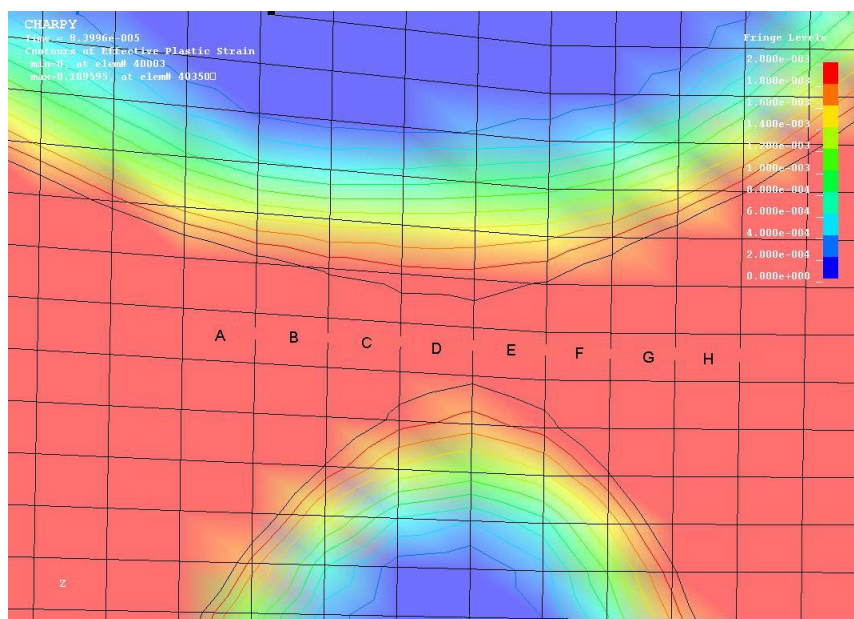


Figure 8.76 - Location of the points where the effective plastic strain of Figure 8.75 has been computed.

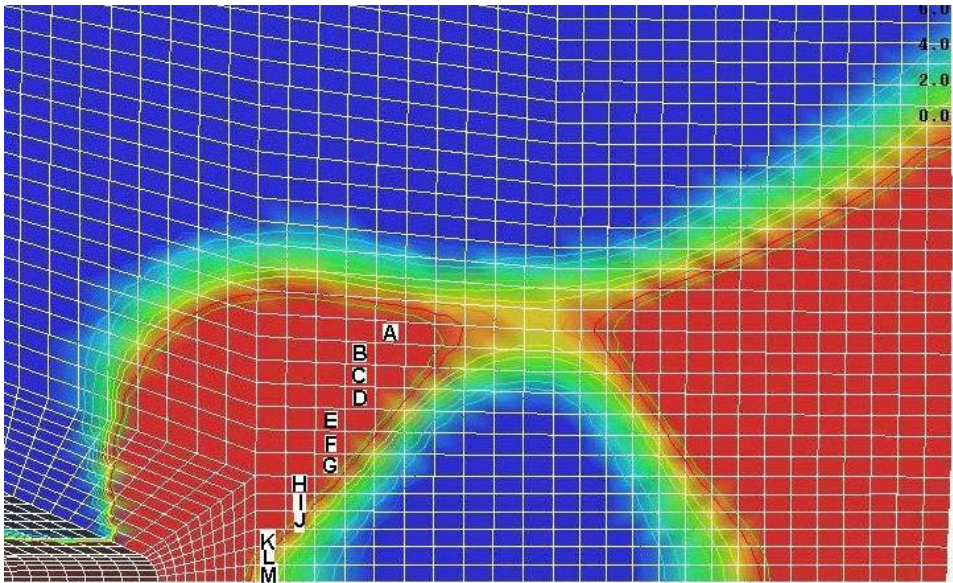


Figure 8.77 - Letters indicate the points in the plastic hinge where the effective plastic strain has been assessed.

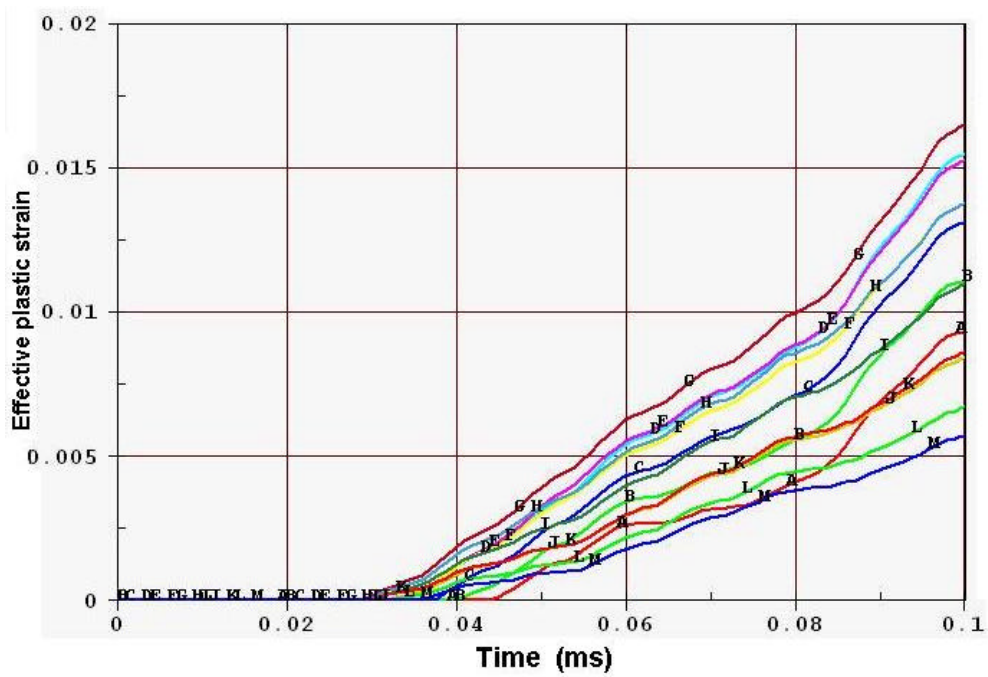


Figure 8.78 - Trend of the effective plastic strain in the plastic hinge. The letter caption is presented in Figure 8.77.

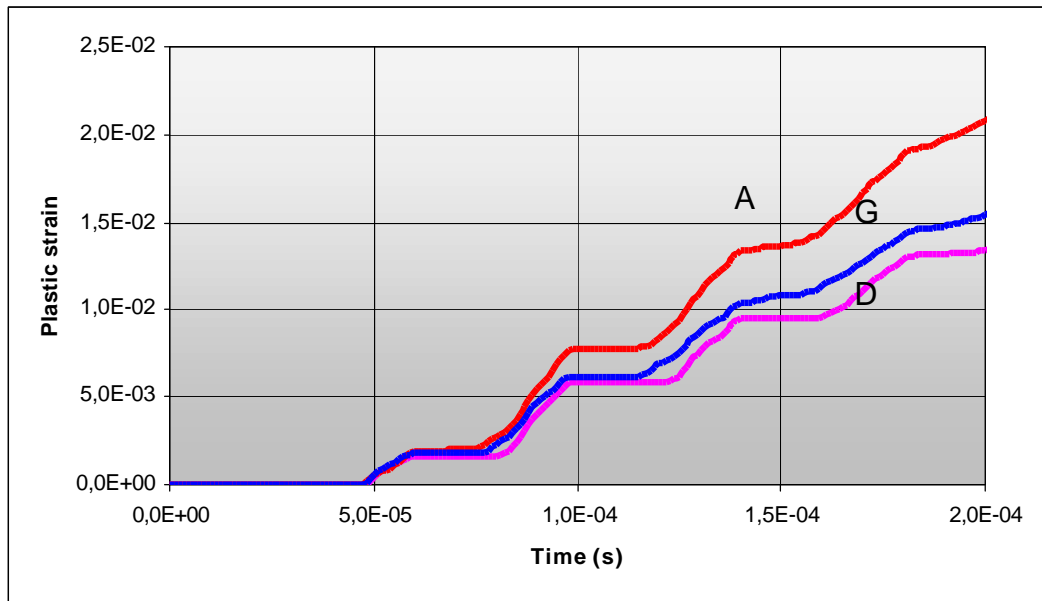


Figure 8.79 - Trend of the effective plastic strain in the plastic hinge. The letter caption is presented in Figure 8.76.

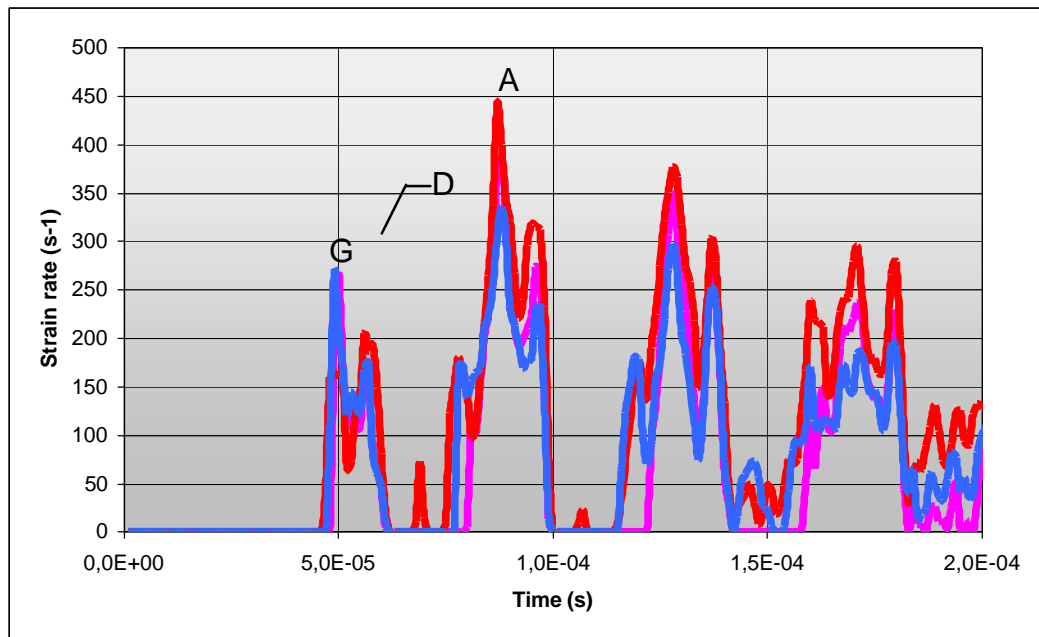


Figure 8.80 - Trend of the plastic strain rate $\dot{\epsilon}$ in points A, D and G of the plastic hinge.

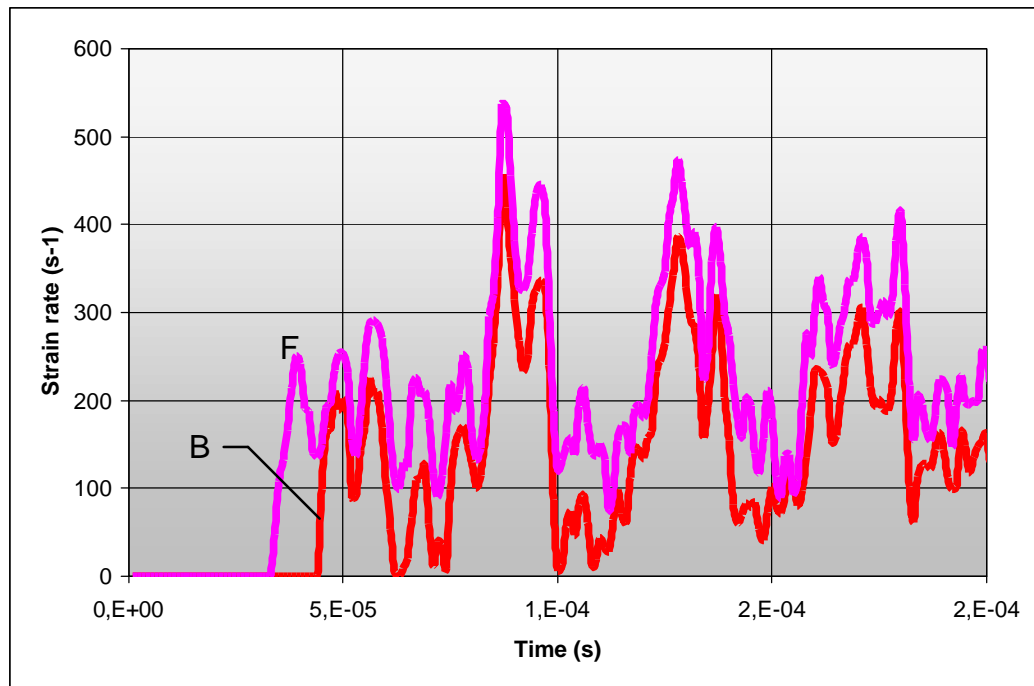


Figure 8.81 - Trend of the plastic strain rate $\dot{\epsilon}$ in points B and F of the plastic hinge (see Figure 8.77).

8.3.6. Conclusions

A comprehensive 2D-3D static and dynamic analysis of the Charpy V-N specimen has been performed in order to assess its real capabilities to measure the dependence of material properties, namely the yield stress, on strain rate. It has been shown that, in effect, the deformation along the plastic hinge occurs at constant strain rate, which is in the range of 250-300 s⁻¹, consistent with a theoretical prediction of 275 s⁻¹. This is a fundamental result, since the first condition for strain rate dependent property measurement is that $\dot{\epsilon}$ is constant during the deformation.

At variance with the ideally rigid-plastic material and plain strain conditions assumed by the flow stress theory, in real materials the plastic hinge formation occurs first on the surface and later on the mid-section of the specimen. Yet, under real conditions, the 3D dynamic analysis has shown that the constraint factor predicted by the flow stress theory still apply for a strain hardening material.

Strain hardening has the effect to change the value of the plastic constraint factor, while the young's modulus does not. The dependence of the plastic constraint factor on the strain hardening of the material has been assessed.

The 3D dynamic analysis has shown that it is possible to derive in a very simple fashion a static equivalent force-displacement curve that does not contain inertial effects and this curve is equal to the one obtained with a 3D static analysis.

The strain rate value of 250 s^{-1} is typical of a Charpy V-N specimen. Other values can be obtained by changing the notch depth or the specimen dimensions. Also the impact speed of the tup indenter on the Charpy specimen can be varied to obtain different strain rates values. This can be the targets of a possible future research aiming at developing a simple experimental procedure to assess the dependency of the yield strength on the strain rate. This finding makes the Charpy pendulum be the most efficient and simple tool to assess materials property dependence on strain rate and temperature, as well.

8.4. References

- Rif. 8.1 LeChatelier, A., "On the Fragility after Immersion in a Cold Fluid", French Testing Commission, Vol. 3, 1892.
- Rif. 8.2 Russell,S.B., "Experiments with a New Machine for Testing Materials by Impact", ASCE Transactions, No. 826, pp. 237?272, 1898.
- Rif. 8.3 White,A.E., Clark,C.L., " Bibliography of Impact Testing", Department of Engineering Research, University of Michigan, 1925.
- Rif. 8.4 Charpy,M.G., " Shock Bend Testing of Metals Using Notched Specimens", Civil Engineering Society of France, 1901.
- Rif. 8.5 Tipper,C.F., " The Brittle Fracture Story ", Cambridge University Press, New York, 1962.
- Rif. 8.6 Pellini,W.S., " Evolution of Engineering Principles for Fracture?Safe Design of Steel Structures ", U.S. NRL Report 6957, Washington, D.C., September 23, 1969.
- Rif. 8.7 Rolfe, S.T., Barsom, J.M., "Fracture and Fatigue Control in Structures-Application of Fracture Mechanics", p. 178, Prentice-Hall inc., New Jersey, 1977.

- Rif. 8.8 Dougan, J.R., “Relationship Between Charpy V-Notch Impact Energy and Fracture Toughness”, US NRC NUREG/CR-2362, 1982.
- Rif. 8.9 Eason, E.D., Nelson, E.E., “Improved Model for Predicting J-R Curves from Charpy Data, US NRC NUREG/CR-5356, 1989.
- Rif. 8.10 Standard Test Methods for Notched Bar Impact Testing of Metallic Materials, ASTM Designation: E 23 – 92, ASTM Standards Sec. 3, 1992.
- Rif. 8.11 Milella, P.P., “Meccanica della Frattura Lineare Elastica ed Elastoplastica”, Test Book in Italian, ANSALDO NUCLEARE Editor, Genova, 1999, p. 145.
- Rif. 8.12 Standard Test Methods for Determining J-R Curves, ASTM Designation: E 1152 – 87, ASTM Standards Sec. 3, 1992.
- Rif. 8.13 Hill, R., “The Mathematical Theory of Plasticity”, Oxford University Press, London, 1950, pp. 128-160.
- Rif. 8.14 Green, A.P., “ Plastic Yielding of Notched Bars Due to Bending”, Quarterly Journal of Mechanics and Applied Mathematics, Vol. 6, Part 2, 1953, pp. 223-239.
- Rif. 8.15 Green, A.P., “The Plastic Yielding of Shallow Notched Bars Due to the Bending”, Journal of the Mechanics and Physics of Solids, Vol. 4, p. 259-268, 1956.
- Rif. 8.16 Green, A.P. and Hundy, B.B., “Initial Plastic Yielding in Notch Bend Tests”, Journal of Mechanics and Physics of Solids, Vol. 4, pp. 128-144, 1956.
- Rif. 8.17 Alexander, J.M. and Komoloy, T.J., “On the Yielding of a Rigid/Plastic Bar with an Izod Notch”, Journal of Mechanics and Physics of Solids, Vol. 10, pp. 265-275, 1962.
- Rif. 8.18 Wilshaw, T.R. and Pratt, P.L., “On the Plastic Deformation of Charpy Specimens Prior to General Yielding”,
- Rif. 8.19 Ewing, D.J.F., “Calculations on the Bending of Rigid/Plastic Notched Bars”, Journal of Mechanics and Physics of Solids, Vol. 16, pp. 205-213, 1968.
- Rif. 8.20 Knott, J.F. and Cottrell, A.H., “Notch Brittleness in Mild Steels”, Journal of the Iron and Steel Institute, pp. 249-260, 1963.

- Rif. 8.21 Wilshaw, T.R., “The Deformation and Fracture of Mild Steel Charpy Specimens”, Department of Material Science, Stanford University, California, SU-DMS Report No. 66-6, January, 1966.
- Rif. 8.22 Milella, P.P., Notes on Charpy test
- Rif. 8.23 Graff, K. F., Wave Motion in Elastic Solids, New York, 1991
- Rif. 8.24 Sturges, J. L., and Cole, B. N. , (2001), Int. J. of Impact Eng., 25, pp. 251-264.

9. Conclusions

In this report the research work and the results developed during a three years research contract have been presented and discussed in details. The major outcomes are be summarized as follows.

Continuum Damage Modeling. The damage model for ductile fracture proposed by the authors has demonstrated to be an effective tool in predicting material performance under both dynamic and quasi static loading conditions confirming the geometry transferability of the damage parameters. The model requires a limited number of parameters that can be identified by means of simple quasi static tests. At the present, the damage parameters seem to be insensitive to the strain rate while a temperature dependency is expected. The present study pointed out a possible direct correlation between the damage parameters and the microstructure. This correlation seems to be independent of the specific metal. However, further investigations are necessary to clarify this issue.

Flying plate impact test. The study confirmed that the CDM modeling has a potential in the prediction not only of the basic features of the phenomenon but to give a more accurate insight on the evolution and interaction of irreversible processes that take place in the material microstructure. It has been proved that local feature such as spall plane thickness and damaged distribution can be fairly well predicted. The study on the spall signal has pointed out the need to account for the dissipation associated to the formation and separation of the spall plane faces. If this process is accounted, then the entire spall signal can be accurately predicted. The theoretical framework proposed for this process, based on fracture mechanics considerations, gives strong physical basis to the explanation of the differences observed in the spall signal simulations. The study on the edge effect in non-equal diameter impacting plates has shown the existence of some geometrical features that can lead to a reliable predictive criterion.

Taylor and ROR impact test. Simulations on Taylor cylinder has pointed out the critical role played by internal heating due to plastic work conversion. Even in this case the CDM model lead to very good results confirming the, at least in a qualitative way, both the extension and location of the most damaged areas can be predicted. The analysis confirmed the difficulty to use this experimental technique to clearly identify the material yield stress and strain rate. The simulation performed on rod-on rod impact configuration revealed the importance to account for the microstructure in the material constitutive modeling. This open a new frontier for the continuing of the present research in the developing a meso-scale modeling incorporating damage.

Hopkinson pressure bar. The simulation performed with finite element technique of the Hopkinson pressure bar equipment allowed verifying the numerical scheme adopted for

simulating dynamic stress wave propagation in solids. The numerical results are in a very good agreement with theory and represent a validation for the proposed approach. In addition these studies have been used to develop the design of a tensile pressure Hopkinson pressure bar at the University of Cassino that actually is in the stage of performance qualification.

Flying wedge test. This new experimental technique has some potential. One of the major features seems to be the possibility to use larger specimen dimension under high strain rate loading conditions. The study, together with the use of the CDM model, showed the possibility to naturally predict the occurrence of uncommon phenomenon such as double necking. The study on the effective strain rate imposed to the specimen showed that strain rate is not constant due to the multiple reflections of the stress waves along the specimen length.

Innovative use of Charpy pendulum. The investigation devoted to identify potential new experimental techniques for dynamic material testing have pointed out the use of the Charpy pendulum as a high strain rate generator device. The strain rate value of 250 s^{-1} is typical of a Charpy V-N specimen. Other values can be obtained by changing the notch depth or the specimen dimensions. Also the impact speed of the tup indenter on the Charpy specimen can be varied to obtain different strain rates values. This can be the target of a possible future research aiming at developing a simple experimental procedure to assess the dependency of the yield strength on the strain rate. This finding makes the Charpy pendulum be the most efficient and simple tool to assess materials property dependence on strain rate and temperature, as well